ISTANBUL TECHNICAL UNIVERSITY ★ GRADUATE SCHOOL

NUMERICAL SIMULATION OF AIRCRAFT ICING WITH AN ADAPTIVE THERMODYNAMIC MODEL CONSIDERING ICE ACCRETION

Ph.D. THESIS

Hadi SIYAHI

Department of Aeronautics and Astronautics Engineering

Aeronautics and Astronautics Engineering Programme

JULY 2022

ISTANBUL TECHNICAL UNIVERSITY ★ GRADUATE SCHOOL

NUMERICAL SIMULATION OF AIRCRAFT ICING WITH AN ADAPTIVE THERMODYNAMIC MODEL CONSIDERING ICE ACCRETION

Ph.D. THESIS

Hadi SIYAHI
(511152114)

Department of Aeronautics and Astronautics Engineering

Aeronautics and Astronautics Engineering Programme

Thesis Advisor: Prof. Dr. A. Cihat BAYTAŞ

JULY 2022

İSTANBUL TEKNİK ÜNİVERSİTESİ ★ LİSANSÜSTÜ EĞİTİM ENSTİTÜSÜ

BUZ BİRİKİMİNİ GÖZ ÖNÜNE ALARAK UYARLANMIŞ BİR TERMODİNAMİK MODEL İLE UÇAKTA BUZLANMANIN SAYISAL BENZETİMİ

DOKTORA TEZİ

Hadi SIYAHI
(511152114)

Uçak ve Uzay Mühendisliği Anabilim Dalı

Uçak ve Uzay Mühendisliği Programı

Tez Danışmanı: Prof. Dr. A. Cihat BAYTAŞ

TEMMUZ 2022

Hadi SIYAHI, a Ph.D. student of ITU **Graduate School**, student ID 511152114, successfully defended the dissertation entitled "NUMERICAL SIMULATION OF AIRCRAFT ICING WITH AN ADAPTIVE THERMODYNAMIC MODEL CONSIDERING ICE ACCRETION", which he prepared after fulfilling the requirements specified in the associated legislations, before the jury whose signatures are below.

Thesis Advisor :	**Prof. Dr. A. Cihat BAYTAŞ** Istanbul Technical University	.....
Jury Members :	**Prof. Dr. Can Fuat DELALE** MEF University	.....
	Prof. Dr. Mehmet ŞAHİN Istanbul Technical University	.....
	Prof. Dr. M. Adil YÜKSELEN Istanbul Gelişim University	.....
	Prof. Dr. Mustafa ÖZDEMİR Istanbul Technical University	.....

Date of Submission : **05 July 2022**
Date of Defense : **10 August 2022**

To my family,

FOREWORD

In the present research work, the icing phenomenon on aircraft's wings has been simulated. The results of our study can be useful for the cases of icing in the tail, fuselage nose, empennages, propeller blades, landing gear doors, stabilizers, nacelles, engine intakes, compressor blades, windshield, probes, sensors, pitot tube, stall warning device, fuel drainage pipe, rudder, ailerons, elevators, radio communication & navigation antenna and radar domes in the aircraft. Besides, present study may be a guideline for the cases of icing in electric lines, the blades of wind turbines, and meteorological instruments during cold seasons.

Once I started my PhD program, although I had considerable knowledge and background in the field of thermal sciences, but I was feeling a kind of inadequacy in the field of fluid dynamics. As an aeronautical engineer, I was supposed to fulfill this gap by taking proper courses during my graduate program. When my advisor offered me to select "Aircraft Icing" as a topic of my dissertation, I had to deal with the physical (deriving the governing equations), mathematical (applying the numerical methods to discretize the partial differential equations of governing equations into algebraic equations), and computational (utilizing the computational fluid dynamic techniques) aspects of the topic. Therefore, my dissertation provided me an opportunity to achieve a deeper knowledge of computational fluid dynamics.

I appreciate all the empathy and patient of my family during this period, which without their support, I did not be able to finish this commitment. Meantime, I would like to thank my advisor Professor A. Cihat Baytaş for all his support and guidance that have always been encouraging and eye-opening to me.

July 2022

Hadi SIYAHI
(Senior Mechanical and Aeronautical Engineer)

TABLE OF CONTENTS

Page

ABBREVIATIONS

TFI	**:** Transfinite Interpolation
CFD	**:** Computational Fluid Dynamics
AT	**:** Ambient Temperature
LWC	**:** Liquid Water Content
VMD	**:** Volume Median Diameter
MVD	**:** Median Volumetric Diameter
SLD	**:** Super-cooled Large Droplet
AOA	**:** Angle Of Attack
MCR	**:** Maximmum Camber Ratio
PMCR	**:** Position of Maximmum Camber Ratio
TR	**:** Thickness Ratio
FDM	**:** Finite Difference Method
FVM	**:** Finite Volume Method
QUICK	**:** Quadratic Upstream Interpolation for Convective Kinematics
LSOR	**:** Line Successive Over Relaxation
TDMA	**:** Tri Diagonal Matrix Algorithm
PDMA	**:** Penta Diagonal Matrix Algorithm
PDE	**:** Partial Differential Equation
PPE	**:** Pressure Poisson's Equation
IBL	**:** Integral Boundary Layer
SWIM	**:** Shallow Water Icing Model
PCRI	**:** Property-Constant Rime Ice
PVRI	**:** Property-Variable Rime Ice
FF	**:** Freezing Fraction
RW	**:** Run-back Water
N-S	**:** Navier-Stokes
RANS	**:** Reynolds-Averaged Navier-Stokes
SA	**:** Spalart-Allmaras

SYMBOLS

α : Volume fraction of water droplets
β : Collection efficiency
$\bar{\rho}$: Apparent density of water droplets (liquid water content)
ρ_a : Density of airflow
ρ_w : Density of water
μ_a : Dynamic viscosity of airflow
μ_w : Dynamic viscosity of water
ν : Kinematic viscosity of airflow
ν_t : Turbulent viscosity of airflow
$\mathbf{h_{conv}}$: Convective heat transfer coefficient
$\mathbf{k}$: Conductive heat transfer coefficient
$\mathbf{k_i}$: Conductive heat transfer coefficient of ice
$\mathbf{k_w}$: Conductive heat transfer coefficient of water
$\mathbf{k_s}$: Roughness height
St : Stanton number
Re : Reynolds number for a smooth surface
$\mathbf{Re_k}$: Reynolds number for a rough surface
$\mathbf{Re_t}$: Turbulent Reynolds number which defined in the present dissertation
Pr : Laminar Prandtl number of air
$\mathbf{Pr_{turb}}$: Turbulent Prandtl number of air
$\mathbf{Pr_t}$: Turbulent Prandtl number which defined in the present dissertation
M : Mach number
c : Chord
$\mathbf{C_l}$: Lift coefficient
$\mathbf{C_d}$: Drag coefficient
J : Jacobian
P,Q : Controlling terms of elliptic grid generation
R : Radius of O type grid
ω : Vorticity
ψ : Stream function
$\tilde{\nu}$: Transport (eddy) viscosity of turbulent airflow
U : Airflow velocity
V : Water-droplet velocity
$\mathbf{T_a}$: Ambient temperature
$\mathbf{T_s}$: Substrate temperature
$\mathbf{c_p}$: Specific heat coefficient at constant pressure
$\mathbf{C_p}$: Pressure coefficient
$\mathbf{C_f}$: Friction coefficient
$\mathbf{C_l}$: Lift coefficient
$\mathbf{C_d}$: Drag coefficient

D : Diameter of droplet
g : Gravitational acceleration
$\mathbf{F_D}$: Drag force
$\mathbf{F_G}$: Gravity force
δ : Thickness of viscous boundary layer
δ_1 : Displacement thickness
δ_2 : Momentum thickness
δ_t : Thickness of thermal boundary layer
Δ_2 : Enthalpy thickness
Δ_4 : Energy thickness
τ : Shear stress
$\dot{m}$: Mass flux
$\dot{Q}$: Heat flux
Le : Lewis number
$\mathbf{L_f}$: Latent heat of water fusion
$\mathbf{L_{sub}}$: Latent heat of ice sublimation
$\mathbf{L_{evap}}$: Latent heat of water evaporation
$\mathbf{e_0}$: Saturation vapor pressure constant
$\mathbf{B_g}$: Ice thickness at which glaze ice first appears
$\mathbf{t_g}$: Time at which glaze ice first appears
t : Time
B : Thickness of ice
h : Thickness of water-film
T : Temperature of ice
θ : Temperature of water-film
$\mathbf{r_{seg}}$: The independent segment ratio
Be : The dependent Bezier value

LIST OF TABLES

Page

LIST OF FIGURES

Page

NUMERICAL SIMULATION OF AIRCRAFT ICING WITH AN ADAPTIVE THERMODYNAMIC MODEL CONSIDERING ICE ACCRETION

SUMMARY

The icing phenomenon is one of the most undesirable events in aircraft. We may see this phenomenon from different points of view. The safety of flight is undoubtedly the biggest concern of designers, nowadays. The icing causes the malfunctioning or even failure of the pressure and speed measurement devices, and consequently make difficulties for controllability of the flight. Icing in rudder, ailerons, and elevators can also make control of aircraft even impossible. During landing, the icing on the pilot window along with possible failures in the landing gears may cause major catastrophes. Besides, detachment of ice particles can cause serious mechanical damage to the aircraft when they collide with the body or sometimes with internal parts such as compressor blades. The other point of view is the degradation of the performance of aircraft, and consequently the increase of fuel consumption because of icing. Icing affects the aerodynamics of an airplane in an undesirable way and puts the aircraft in a situation that is far from what the aircraft is designed for. Therefore, it is necessary to study aircraft icing to provide a safer and more efficient flight.

Since the icing in aircraft is of great importance, a precision analysis of this phenomenon should be performed. Tests in the wind tunnel and during the flight are very expensive. On contrary, the numerical-computational simulations can be cost-effective for studying aircraft icing. In the present study, the numerical-computational simulation of aircraft icing has been performed by writing a computer-code via FORTRAN. The computational simulation of aircraft icing is a modular procedure consisting of the grid generation, air solver, droplet solver and ice accretion modules.

First, the computational domain is generated via elliptic grid generation. The differential methods based on the solution of the elliptic equations are commonly used for generating of the mesh for a geometry with arbitrary boundaries. Elliptic equations are also utilized for the unstructured grids. The most popular elliptic equation is the Poisson equation, which gives the wonderful possibility to satisfy smoothness, fine spacing, and orthogonality on the body surface by means of the controlling terms.

Then, the velocity and pressure distributions of airflow around the wing have been found, and the convective heat transfer coefficient on the body will be calculated. The inviscid flow model has been selected in our simulation because it needs less effort and time in comparison with the Navier-Stokes codes. The two-dimensional, steady-state, inviscid, incompressible, irrotational flow (potential flow) model has been applied for solving airflow. The potential and stream function methods are two different models of potential flow. Because the potential method needs interpolation for the calculations of values in the inner region and it may encounter the singularity problem in sharp edges the stream function method has been preferred in our work. The potential flow gives

good approximation for the velocities of external inviscid flow next to the boundary layer. These velocities are utilized to calculate the convective heat transfer coefficient. To include the viscous and turbulent effects in the integral boundary layer method, the relevant correlations are applied.

Next, the liquid water content (apparent density) of the water droplets will be determined to know the collection efficiency of droplets on the airfoil. The aircraft icing is a special case of two-phase flow. The airflow will affect the motion of water droplets around an airfoil. On the other hand, while the diameter of a water droplet is less than 50 μm, the motion of droplets does not affect the airflow (i.e. one-way coupled flow), but when the diameter of droplets is larger than 50 μm the motion of droplets does also influence the airflow, and there is an interaction between airflow and the motion of droplets (i.e. two-way coupled flow). In our study, it is assumed that the diameter of droplets is less than 50 μm, and consequently, the two-phase flow is treated as a one-way coupled flow model. There are two main approaches namely Lagrangian and Eulerian methods to study the motion or distribution of water droplets around an airfoil. In Lagrangian method, Newton's second law of motion (force balance) is used for tracking the trajectory of water droplets. For each droplet it is checked to see whether the droplet collides with the surface of the airfoil or not. This can be a very time-consuming task. On the other hand, in the Eulerian approach, the continuity and momentum equations of water droplets are simultaneously solved for the entire grid-points around an airfoil. Since, instead of tracking individual particles, the average values of apparent density (liquid water content) and velocity components of water-droplets are calculated in all points at the same time, the Eulerian approach is time-saving in comparison to the Lagrangian approach. The other advantages are to improve the ability to model unsteady flows over the body, and the automated treatment of shadow zones (zones with no impingement). Also, this method gives better results for the complicated two-dimensional geometries. A further reason for developing the Eulerian method is the easy extension toward three-dimensional geometries. Because of these advantages of the Eulerian method, this method has benn implemented in our study.

Eventually, the thermodynamic calculations are performed by using the conservation equations of mass and energy to compute the temperature and thickness of ice, and the new iced geometry is calculated for the current time step. Predictor-Corrector and Multi-Layers methods are the well known ice accretion methods. In Predictor-Corrector approach, first, the calculations of ice accretion for the entire exposure time is performed. This is known as the predictor step. Then, by assuming a linear variation of the parameters between the solution of the clean airfoil and the iced geometry, the airflow and droplets solutions can be interpolated in time. Then, the final shape of ice is calculated by integrating from the beginning time (clean geometry) to exposure time (final ice shape). This step is known as the corrector step. Then, the solutions of flow and droplets can be re-evaluated on the corrected ice shape, consequently, a new linear interpolation can be computed and a new corrector step can be performed. This process will repeat until the difference between two corrector steps was negligible. On the other hand, in Multi-Layers approach the general process goes as follows. The grid is generated using the geometry of the clean airfoil. Then, the airflow field is solved to obtain the velocity and pressure distributions around the body, and calculate the convective heat transfer coefficient (h_{conv}) on the body. Utilizing the airflow values, the droplets equations are solved to know the collection

efficiency (β) on the body. Eventually, the thermodynamic mass and energy balances are performed to compute the surface temperature and thickness of the ice. Then, the new contaminated (iced) geometry is created and provided to the grid generator module to produce the new grid for the next time step. Finally, the whole procedure is repeated until the specified exposure time, and the final shape of the ice will be predicted. Ice accretion is inherently an unsteady problem and difficult to handle. In our study Multi-layers approach has been applied because it allows for solving the problem as a quasi-steady-state problem.

In the conventional multi-layers ice accretion models, the thickness (B_g) and time (t_g) at which the glaze ice appears for the first time, are predicted based on the thermodynamic calculations at the very beginning. Then, these values are taken as critical transient criteria to apply either the rime ice or the glaze ice calculations at each time step. To make these predictions, it is assumed that the convective heat transfer coefficient (h_{conv}) and collection efficiency (β) do not change. In reality, the geometry of the body surface changes during the icing and affects the airflow and the distribution of water droplets around the airfoil. Consequently, the convective heat transfer coefficient and the collection efficiency which playing important roles in the ice accretion change, continuously. In the proposed ice accretion model presented in this study, without the need for the predictions of the critical transient criteria at the zero time, the calculations of the ice accretion are initiated with the rime ice. If the results are plausible (until the surface temperature of ice reaches the freezing temperature of water at the ambient and the calculated thickness of ice to have a positive value) they are accepted, otherwise, the glaze ice calculation is applied. The proposed computational algorithm is the novelty contribution of present dissertation. The strength of this approach is that it enables the course of numerical computations of the icing process to proceed in the same way as the real physics of the icing phenomenon. The results of the present study show that the proposed ice accretion approach for all rime, mixed, and glaze ice-regimes gives more accurate results than the conventional ice accretion models.

Our research can meet very basic needs in analyzing the aircraft icing and even can be a guideline for providing a national computer-based program in the future. Because the icing causes high-cost damages in the aviation sector, the prepared code will also be economically beneficial. Results of our analyses can help with avoiding malfunctioning of detectors, stabilizers, and controllers. In addition, the results of the study will be useful for technological developments of unmanned aircraft. Also, more realistic and successful pilot training will be achieved by including icing prediction in the flight simulations. The most important achievements of this study are increasing the safety of flight, and reducing/eliminating the degradation of overall performance of aircraft.

BUZ BİRİKİMİNİ GÖZ ÖNÜNE ALARAK UYARLANMIŞ BİR TERMODİNAMİK MODEL İLE UÇAKTA BUZLANMANIN SAYISAL BENZETİMİ

ÖZET

Buzlanma, uçaklarda en istenmeyen olaylardan biridir. Bu olayı farklı bakış açılarından görebiliriz. Günümüzde, uçuş güvenliği şüphesiz tasarımcılar ve üreticiler için en büyük endişelerden biridir. Buzlanma basınç ve hız ölçme cihazlarının arızalanmasına sebeb olarak uçuş kontrolünü zorlaştırır. Yatay ve düşey dümenlerde meydana gelen buzlanma uçağın kontrolünü zorlaştırır hatta imkansız hale getirir. İniş sırasında, pilot penceresindeki buzlanma pilot görüşünü engeller ve yine iniş takımlarındaki muhtemel arızalar büyük facialara neden olur. Buzlanma sonucunda şekillenen buz parçacıkları, uçak yüzeyinden ayrıldığında ve gövde ya da uçak kuyruğu ile çarpıştığında veya bazen kompresör kanatları gibi iç kısımlarla çarpıştığında, uçaklarda ciddi mekanik hasarlara neden olur. Diğer bakış açısı, buzlanma etkisi ile uçak performansının azalması ve bunun neticesinde yakıt tüketiminin artmasıdır. Buzlanma, uçağın aerodinamiğini kötü biçimde ya da beklenmedik bir şekilde etkiler ve bu da uçağı tasarlanan çalışma şartlarından çok farklı şartlarda çalışmaya mecbur etmektedir. Bu nedenle, daha güvenli ve performans açısından daha verimli bir uçuş sağlamak adına buzlanma konusunda bilimsel çalışmaların yapılması gerekmektedir.

Uçaklarda buzlanma olayı bilimsel analizler yapmak istediğimizde, bir kaç seçenek ile karşıkarşıya kalmaktayız. Rüzgar tüneli ve uçuş esnasında yapılan testler yüksek maliyetli olmaktadır, buna karşılık buzlanma sayısal ve hesaplamalı benzetim ile bilgisayar ortamın da incelene bilmektedir. Mevcut çalışmada uçakta buzlanma olayın sayısal ve hesaplamalı benzetimi FORTRAN ile bir bilgisayar programı yazarak yapılmıştır. Buzlanmanın hesaplamalı benzetimi ağ üretimi, hava çözümü, damlacıkların çözümü ve buz birikim hesabı gibi temel modullerden oluşur.

İlk önce, kanat etrafında eliptik denklemleri kullanarak ağ üretilir. Eliptik denklemlerin çözümüne dayanan difransiyel metodler keyfi geometrilerin etrafındaki ağ üretiminde kullanılmaktadır. Poisson denklemi en bilinen eliptik çözümler arasında yer almaktadır. Poisson denklemi kontrol terimleri yardımıyla sıkı, düzgün ve ortogonal ağ çizgileri üretiminde çok kabiliyetli dir.

Sonra, kanat kesiti etrafında hava akışın hızları ve ısı taşınım katsayısı bulunur. Bu çalışmada viskoz olmayan hava modelleri kullanılmıştır. Viskoz olmayan çözümler Navier-Stokes kodların aksine daha az efor ve zamana ihtiyacı vardır. Bu yüzden iki boyutlu, dayimi, viskoz olmayan, sıkıştırılamaz ve girdapsız akış (potansiyel akış) modeli tercih edilmiştir. Potansiyel ve akım fonksyonu modeller, potansiyel akışların iki farklı çözümleri dir. Bizim çalışmada akım fonksyonu modeli tercih edilmiştir, çünkü potansiyel fonksyon modelinde iç noktaların değerlerini hesaplamak için interpolasyon yapmak gerekmektedir diğer yandan keskin kenarlarda tekillik problemi ile karşı karşıya kalır. Potansiyel akış çözümü sınır tabaka dışındaki viskoz olmayan akış hızları için iyi takripler vermektedir. Bu hızları integral sınır tabaka

metodunda kullanarak taşınım ısı transfer katsayısı bulunur. Viskoz ve türbülans etkileri integral sınır tabaka metoduna dahil etmek için ilgili korelasyonlar kullanılır.

Sonrasında, damlacık dağılımı saptanacaktır ve neticede damlacıkların kanat yüzeyindeki birikim verimi hesaplanır. Uçakta buzlanma olayı bir nevi iki fazlı akıştır. Hava akışı damlacıkların hareketini kanat etrafında etkiler. Diğer yandan eğer su damlacıkların çapı 50 μm'den küçük ise bu damlacıklar hava akışını etkilemez ama eğer damlacıkların çapı 50 μm'den büyük ise bu sefer su damlacıkların ataleti hava akışını etkiler ve bu etkileşimi hesaba katmak gerekiyor. Bu çalışmada su damlacıkların çapı 50 μm'den küçük olduğu varsayılmaktadır. Su damlacıkların hareketi veya dağılımını bulmak için literatürde Lagrangian veya Eulerian yöntemleri kullnılmaktadır. Lagrangian metodda Newton'nun ikinci yasasından faydalanarak her su damlacığın hareket izi (yörüngesi) takip edilir ve bu damlacığın kanat yüzeğine isabet edip etmediği kontrol edilmektedir. Eulerian metod'da ise süreklilik ve mpmentum denklemleri bütün alan için çözülür ve su damlacıkların dağılımı (yoğunluğu) bulunur. Lagrangian metod'da her damlacığın hareketi ayrıca takip edilir buna karşı Eulerian metod'da bütün alan için değerler aynı zamda çözülür ve elde edilir. Lagrangian yöntemin daha fazla zaman harcadığından dolayı bizim çalışmad Eulerian yötemi tercih edilmiştir. Ayrıca, Eulerian metodu daha karmaşık geometrilerde ve üç boyutlu geometriler için daha iyi sonuçlar verdiğini biliyoruz.

Nihayet, termodinamik hesaplamalar ile buz sıcaklığı ve kalınlığı mevcut zaman adımı için elde edilir. Tahmin-Düzeltme ve Çok-Katmanlı metodlar buz birik hesabı için bilinen metodlardır. Tahmin-Düzeltme yaklaşımda buz kalınlığı bütün maruziyet zaman için hesplanmaktadır (Tahmin aşaması). Doğrusal değişim kabulü ile bu zaman süresi için buzun kalınlığı ve sıcaklığı interpolasyon ile elde edilmektedir. İntegrasyon yaparak bütün maruziyet zamanı için buz kalınlığı hesaplanmaktadır (Düzeltme aşaması). Sonrasında yeni doğrusal değişim verileri ile hesaplamalar yeniden yapılmaktadır. Bu yaklaşımda Tahmin-Düzeltme iki son tekrardan elde edilen verilerin farkı çok küçük olduğuna kadar devam etmektedir. Diğer yandan Çok-Katmanlı yaklaşımında ise, ağ üretim sonrası, hava akışı ve taşınım ısı geçiş katsayısı (h_{conv}) yüzeyde bulunur. Bu hava etkisinde kanat etrafındaki damlacıkların dağılımı ve kanat kesitindeki su birikim verimi (β) hesaplanır. Nihayetinde, kütle ve enerji korunum denklemlerini kullanarak buz kalınlığı ve sıcaklığı elde edilir. Son olarak, yeni buzlu geometri oluşturulur ve tüm hesaplamalar bir sonraki zaman adımı için tekrarlanır. Belirlenen zamana ulaşılıncaya kadar tüm hesaplamalar tekrarlanır ve son buz şekli kanat profili üzerinde tahmin edilir. Uçakta buzlanma olayın doğası gereği dayimi durumlu çözüme sahip olmadığından dolayı hesaplaması zor dur. Bu çalışmada buz birikim hesabı için Çok-Katmanlı yaklaşım tercih edilmiştir çünkü Çok-Katmanlı buz birikim hesabı sayısal hesapların dayımı duruma yakın şekilde devam etmesini sağlamaktadır.

Geleneksel buz birikimi modellerinde, şeffaf buzun ilk meydana geleceği kalınlık ve süresi için bir tahmin edilir ve bu değerler kırağı buzdan şeffaf buz hesabına geçişi için kritik değerler olarak var sayılmaktadır. Daha sonra, bu kritik değerler dayanarak her zaman adımında termodinamik hesaplamalarda kırağı veya şeffaf buz birikimi hesaplamaların kullanılmasına karar verilir. Geleneksel modellerde bu kritik değerleri başlangıçta tahmin etmek için taşınım ısı transfer katsayısı ve su birikim veriminin bu sürede değişmemesi var sayılır. Ama gerçekte, kanat geometrisi buzlanma esnasında her zaman adımında değişmektedir ve bunun etkisinde hava

akışını ve su damlacıkların dağılımı sürekli değişir. Sonuç olarak, buz birikiminin hesabında önemli rol oynayan kanat kesitindeki taşınım ısı transfer katsayısı ve su birikim verimi devamlı olarak değişmektedir. Bu çalışmada sunulan ve önerilen buz birikimi modelinde, başlangıç zamanda kritik geçiş kriterlerinin tahminlerine ihtiyaç duymadan termodinamik hesaplamalar kırağı buz birikim hesabı ile başlatılır. Elde edilen sonuçlar mantıklı ise (buz yüzeyin sıcaklığı buzlanma sıcaklığının altında olup ve hesaplanan buz kalınlığı pozitiv ise) kabul edilir, aksi takdirde şeffaf buz birikim hesaplaması uygulanır. Sunulan hesaplamalı yöntemin algoritması bu doktora tezin özgün değeri dir. Bu yaklaşımın gücü tarafı sayısal buzlanma hesaplamalar sürecinin doğal buzlanma olayın seyri ile aynı şekilde devam etmesini sağlamasıdır. Önerilen yaklaşımın sonuçlarına göre, tüm kırağı, karışık ve şeffaf buz rejimlerinde bu yeni yaklaşım geleneksel buz birikim modellerinden daha doğru sonuçlar vermektedir.

Bu tezdeki önerilen araştırmada, uçak buzlanmasının analizinde çok temel ihtiyaç ve boşlukları karşılayabilir, ve hatta gelecekte bilgisayar tabanlı ulusal kod sağlamak konusunda öncülük edebilir. Buzlanma havacılık sektöründe yüksek maliyetli hasarlara sebep olmaktadır, bu nedenle hazırladığımız bilgisayar programı ekonomik açıdan sektöre faydalı olacaktır, zira dedektörlerde, dengeleyicilerde ve kontrolörlerde, buzlanma sebebi ile oluşacak problemler önlenecektir. Ayrıca, çalışmanın sonuçları kullanımı giderek yaygınlaşan insansız uçakların teknolojik gelişmelerine faydalı olacaktır. Diğer yandan, daha iyi uçuş simülasyonlarına yol açarak, pilot eğitimlerinin verimini ve başarı oranı artırılacaktır. Buzlanma sonucu oluşacak tehlikeleri hafifletmek ve uçağın genel performans azalmasını önlemek veya düşürmek, bu bilimsel çalışmanın en önemli amacıdır.

1. INTRODUCTION

The icing phenomenon is one of the most undesirable events in aircraft. We may see this phenomenon from different points of view. The safety of flight is undoubtedly the biggest concern of designers, nowadays. The other point of view is the degradation of the aircraft's performance. In fact, the icing badly affects the aerodynamics of an airplane and puts the aircraft in a situation that is far from what it is actually designed for.

1.1 Purpose of Dissertation

Icing is a threat during take-off, landing, climbing, descending, and cruising of aircraft. The icing causes the malfunctioning or even failure of the pressure and speed measurement devices, and consequently make difficulties for controllability of the flight. Icing in rudder, ailerons, and elevators can cause control of aircraft to even be impossible. During landing, the icing on the pilot window along with possible failures in the landing gears may cause major catastrophes. Besides, detachment of ice particles can cause serious mechanical damage to the aircraft when they collide with the body or sometimes with internal parts such as compressor blades. Furthermore, the icing will deteriorate the performance of aircraft, by distorting the aerodynamic characteristics of airplanes. Therefore, it is necessary to study aircraft icing to provide a safer and more controllable flight.

Our research can meet very basic needs in the analysis of the aircraft-icing in Turkey, and even can be a guideline for providing national computer-based code in the future. The icing causes high-cost damages in the aviation sector. Thus, the prepared computer program will also be beneficial, economically. Results of our analyses can help with increasing the controllability of aircraft, and reducing/eliminating the degradation of the performance of aircraft. Obviously, the most important achievement of this study is to decrease the life-threatening dangers caused by the icing.

1.1.1 Objectives of our research

- The geometry of the airfoil is shaped at the very beginning of the simulation procedure.
- The curvilinear body-fitted conformal coordinate transformation will be utilized to generate the O-type grid around an airfoil.
- The two-dimensional, steady-state, inviscid, incompressible, irrotational flow (potential flow) model will be applied via stream function method to calculate the velocity and pressure distributions of airflow around an airfoil.
- Using the results of airflow solution, the momentum and energy equations of boundary layers will be solved via the Integral Boundary Layer method to calculate the convection heat transfer coefficient (h).
- Knowing the nature of airflow around the airfoil, the distribution of water droplets can be modeled by the Eulerian method, and the collision efficiency (β) of the droplet will be found.
- The thermodynamic calculations are performed to compute the temperature and thickness of the ice. At each time step, either the rime or glaze ice calculation is applied based on the ambient temperature, liquid water content (LWC), and diameter of droplets. Then, the proportion of water that turns to ice is determined.
- The new iced geometry is created and provided for the next icing layer. The entire procedure is repeated until the specific exposure time, and the final shape of ice will be predicted on the airfoil.
- After verifying our computer program, the improved model of ice accretion is introduced to improve the icing simulation.

1.1.2 Uniqueness of our research work

- All modules of the simulation of aircraft-icing (i.e. grid generation, air solver, droplet solver, and ice accretion) are included in a single computer code. Simulation of aircraft-icing with a comprehensive modular computer program will give a

perfect predicting tool which has a very important capability and can be used by authorized organizations who give necessary certificates to aircraft to flight in harsh atmospheric conditions.

- Generally, the available icing codes provide satisfactory results for the rime ice regime. However, there is a need for developing better models of the mixed and glaze ice regimes. Our proposed model improves the disadvantages of conventional ice accretion models.

1.1.3 Motivations of study of aircraft icing

Benefiting from the computational fluid dynamics (CFD), heat transfer, and thermodynamic tools for the simulation of aircraft icing, it is anticipated that the present study to be useful:

- To provide a better understanding of aircraft behavior under icing situation.
- To introduce the mitigating solutions to the possible hazards for airplanes.
- To avoid malfunctioning of detectors, stabilizers, and controllers which otherwise will lead to misreading of technical data via these instruments.
- For omitting/reducing the degradation of the overall performance of aircraft.
- For increasing of technological advances of the unmanned aircraft which their usage is ever increasing.
- For enhancing the quality of future pilot training equipment, by providing more realistic flight simulation under icing conditions.

Besides, what have been mentioned above:

- The important achievement of our study is to develop a comprehensive modular computer program that best anticipates icing on the aircraft.
- Our research can meet very basic needs in analyzing of the aircraft-icing in Turkey and even can also be a guideline for providing national computer-based code in the future.

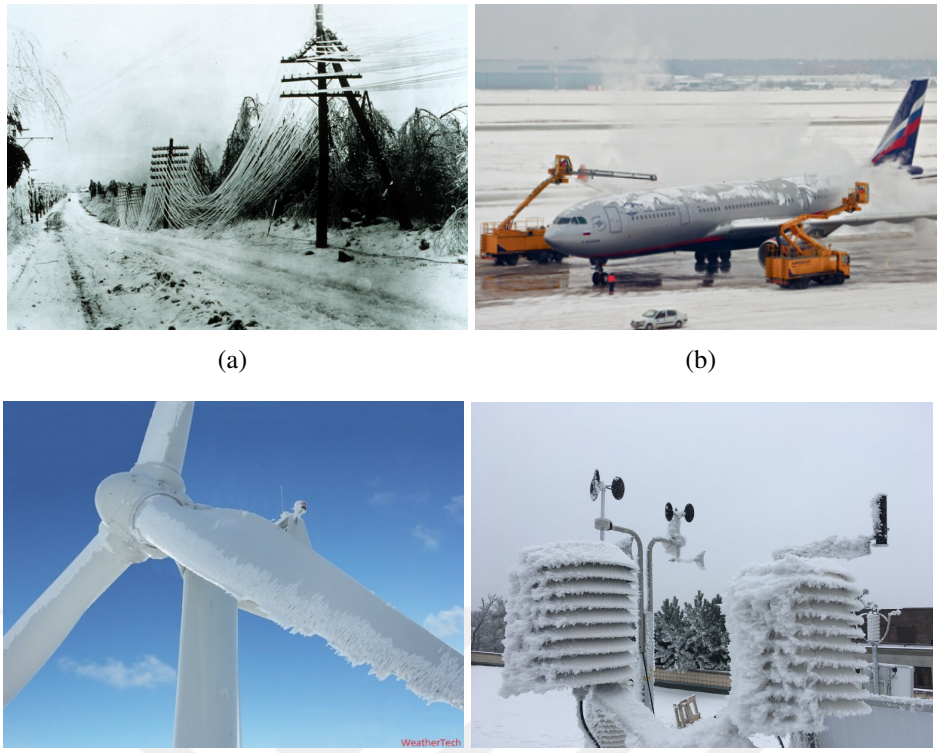

Figure 1.1 : Samples of ground icing (Gro, 2008).

- The icing causes high-cost damages in the aviation sector. Thus, the prepared code also is economically beneficial.

- The most important effect of this study is to decrease the life-threatening dangers caused by aircraft icing.

1.2 Hypothesis and General Concepts of Icing

The different type of icing will be explained in this section. The important parameters that influence the icing are revealed and various disadvantages are also described.

1.2.1 Different icing samples

Atmospheric icing occurs when water vapor in humid air or water droplet of the rain freezes into the cold body surfaces. This can be observed in electrical lines, ground icing of aircraft, the blades of wind turbines, and meteorological instruments during cold seasons (Figure 1.1).

On the other hand, the in-flight icing is different from the ground icing. The super-cooled water droplets in clouds remain in a liquid state even at temperatures

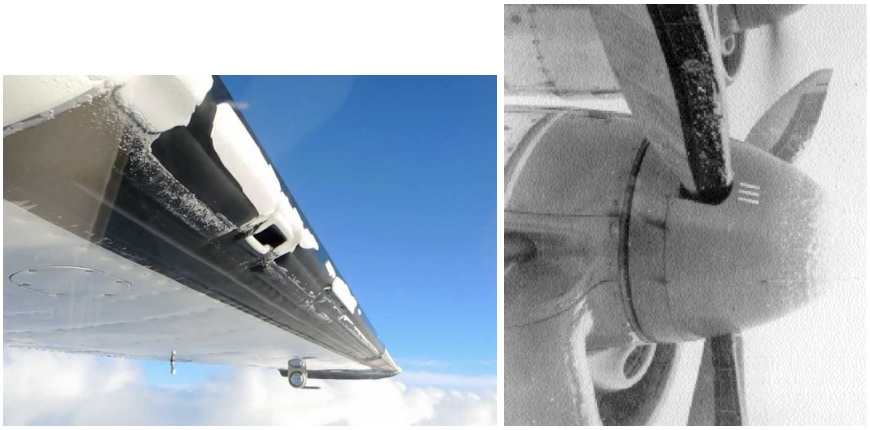

(a) (b)

Figure 1.2 : Samples of in-flight icing (Oleskiw, 2001).

below freezing temperature. Therefore, although the freezing point of water is $0°C$, it may be more accurate to say that the melting point of ice is $0°C$. This is because, for some complex reasons, water exists in liquid form well below $0°C$. Super-cooled water exists because it cannot complete the nucleation process. Two of the factors influencing the freezing of super-cooled droplets are releasing of the latent heat and forming of nuclei.

In-flight icing happens when super-cooled water droplets within clouds freeze on the impact with any external part of an aircraft during flight (Figure 1.2). If the surface temperature of an aircraft body is below zero, the moisture within the air may immediately or gradually turn to ice. The amount of super-cooled water droplets decreases as the static temperature of ambient air drops about $-40°C$ (except in cumulonimbus cloud where super-cooled water may exist at even lower temperatures). The size of a super-cooled water droplet and the momentum of the airflow around the aircraft surface determine whether these droplets will impinge on the surface or not. The size of a droplet will also affect what happens after impingement, and if they stick, rebound, spread or splash. The size of a water droplet also determines the required time for the phase change from liquid (water) to solid (ice).

1.2.2 Clouds types

There are two type of clouds namely dry and wet clouds. Dry clouds have relatively little moisture, and as a result, the potential for aircraft icing is low. On contrary, any cloud containing liquid water (wet cloud) can cause a significant ice accretion if

its temperature was $0°C$ or less. Generally, cumuli-form clouds (Figure 1.3) contain relatively large droplets and can cause very rapid ice formation. Strati-form clouds (Figure 1.4) usually contain much smaller droplets, but if the exposure time in icing conditions within a strati-form cloud was long enough, the ice accretion would be considerable.

Figure 1.3 : Cumuli-form cloud.

Figure 1.4 : Strati-form cloud.

The liquid water content of cumuli-form clouds ranging from 0.1 g/m^3 to 3.9 g/m^3. Whereas, this range for strati-form clouds extends from 0.1 g/m^3 to 0.9 g/m^3.

Freezing rain and drizzle can drastically roughen large surface areas or distort airfoil shapes and make flight extremely dangerous in few minutes. Freezing rain occurs when precipitation from warmer overhead air falls into below freezing air. A freezing drizzle is commonly formed when droplets collide with other droplets in the cloud. As the droplets grow in size, they begin to fall as drizzle. Both freezing rain and drizzle can fall below and cause ice to form on aircraft surfaces during ground operations, takeoff, and landing if the surface temperature is below freezing.

The icing risk due to different types of cloud and precipitation are show in Figure 1.5.

Icing Risk

Cumulus Clouds		Stratiform Clouds		Rain and Drizzle
0° to -20°C 32° to -4°F	High	0° to -15°C 32° to 5°F	High	0°C and below 32°F and below
-20° to -40°C -4° to -40°F	Med.	-15° to -30°C 5° to -22°F	Med.	
< than -40°C <than -40°F	Low	< than -30°C <than -22°F	Low	

Figure 1.5 : Icing risk (Landsberg, 2010).

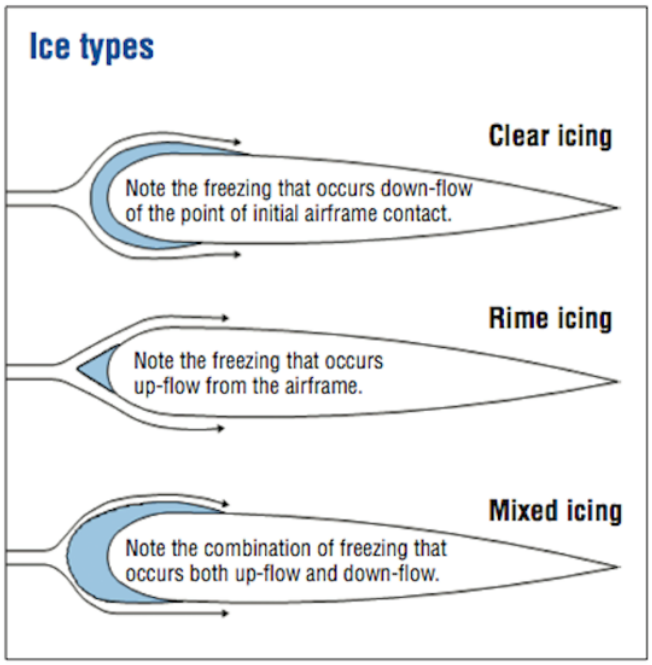

Figure 1.6 : Types of aircraft icing (Alemour et al., 2019).

Snow is a solid phase of water and solely does not count as an icing threat. However, when the snow mix with the droplets inside clouds, it starts melting and can reform as an ice.

Eventually, the inter-cycle ice is the icing case that may form in the aircraft between activation and deactivation period of the thermal deicing systems.

1.2.3 Icing types

There are two major types of icing namely glaze (clear) and rime (opaque). Meanwhile, mixed icing is a combination of the two (Figure 1.6).

Rime ice is formed when small super-cooled water droplets freeze immediately in contact with a surface below freezing temperature. This takes place because the droplets are small, and the latent heat can release faster, and air bubbles will be trapped in ice particles. The resulting ice is rough, crystalline, opaque, and brittle. It appears white when viewed from a distance. Rime ice may begin to form from a leading-edge and continues toward flow stream.

Clear or Glaze ice is formed when super-cooled droplets with larger diameters freeze gradually. The slow pattern of icing will cause in the run-back water film and progressive freezing of the remaining liquid. Thus, the resulting ice relatively few

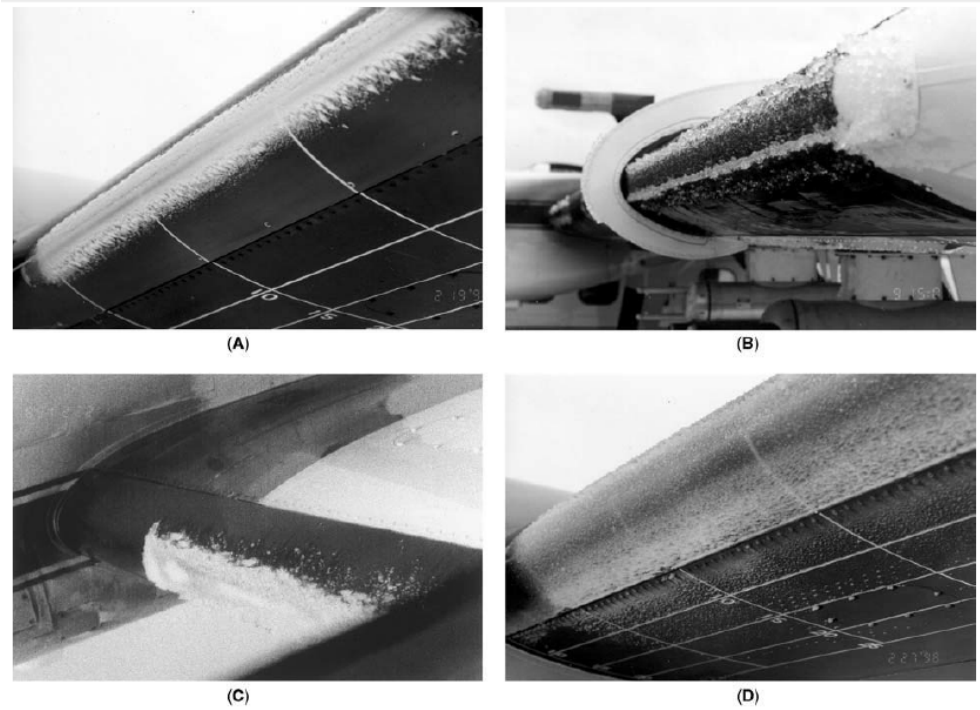

Figure 1.7 : Observations of different icing types: (A) light rime ice, (B) severe glaze ice, (C) moderate mixed ice, (D) super-cooled large droplet ice (Politovich, 2003).

air bubbles. Consequently, the glaze ice is transparent or translucent, and difficult to detect. Since the glaze ice has stronger structure than the rime ice and contains spreading water film, it can reach the larger sizes.

The combination of the rime and glaze ices is named the mixed ice. Mixed icing often occurs in layers, similar to wet and dry hailstone growth, as a result of transition from of the rime into glaze ice. The different icing types can be seen in Figure 1.7.

1.2.4 Important parameters which affect the aircraft icing

The different flow and flight parameters like the outside air temperature, droplet diameter, LWC, airspeed, and altitude can influence the severity of icing (Gent et al., 2000).

- Ambient Temperature (AT): The most important parameter that influences the accretion of ice is the temperature of ambient air. Although the static temperature of ambient can easily be available for pilots, the body temperature under the influence of the ambient temperature plays the most important role in indicating whether the ice accretion is possible or not, and what would be the rate of this accretion.

Actually, in thermal protection systems, the main goal is to remain the temperature of the surface above zero, either temporarily (deicing) or permanently (anti-icing). Then, using anti-icing and deicing techniques, even if the ambient temperature was below freezing temperature the ice will not form.

On the other hand, the lower the AT was, the higher the potential for convective cooling (releasing of the latent heat), and the greater tendency to freeze the impinging droplets will be.

The other effect of AT is because of the link between droplet size and the temperature of super-cooled droplets. Generally, as the ambient temperature reduces, the probability of the existence of the larger droplets also decreases.

- Liquid Water Content (LWC): This is the mass of water in a cloud. The apparent density $(\bar{\rho})$ is the other equivalent interpretation of the liquid water content.

  The LWC affects the type of accretion and the rate at which the ice may form. If the LWC and the AT were larger, the latent heat that releases during freezing will also be larger. Consequently, the freezing process takes more time and the glaze ice will form. Besides, the low LWC along with the low AT will lead to the formation of the rime ice.

  On the other hand, although the larger LWC near a body will increase the potential for the ice formation, the order of magnitude of collision efficiency has the most important effect in the determination of the actual amount of water that impinges on the surface. In other words, a large apparent density of droplets with a small diameter droplet has no or little probability of the ice accretion.

- Droplet Diameter: The mass of a water droplet is directly proportional to its diameter, whereas the influence of the airflow on the droplet is directly proportional to the square of the diameter. The droplets with large diameters have large mass and inertia, and will be less affected by the aerodynamics of surrounding flow. Therefor, the larger droplets will tend to follow a straighter trajectory, and have a higher tendency to impinge on the surface. On contrary, droplets with smaller diameters have low mass, and will likely follow the free-stream, and in most cases may not impinge on the surface.

- Airspeed: Airspeed indefinitely affects the icing. The faster speed of air will accelerate the motion of droplets. This is a necessary but not an sufficient condition. The higher airspeed along with the larger LWC and larger droplets will increase the impingement of droplets on the surface (collection efficiency), and consequently, the ice accretion will increase.

- Altitude: The altitude of flight does indirectly affect the severity of ice accretion. Since the air temperature bears an indirect relation with the altitude, the probability of aircraft icing will increase at the higher altitude.

Generally, the type of icing is related to the altitude, ambient temperature, liquid water content (LWC), size of the droplets, speed of flow, total exposure time, angle of attack, shape and size of body. Glaze ice is generally associated with higher temperatures (close and below zero degree Celsius), higher super-cooled liquid water contents and larger-size droplets. On the other hand, rime ice usually occurs at lower temperature, low LWC, and small droplet sizes.

1.2.5 Location and frequency of aircraft icing

Since icing can occur in clouds or precipitation at temperatures below $0°C$, any icing climatology should be considered as a possible icing conditions. Meanwhile, the average altitude of icing environments is around 3000 m above mean sea level, with few encounters above 6000 m. The cumuli-form clouds, with their greater depth and transport of significant liquid contents to higher altitudes, have the higher average altitude coverage than the strati-form clouds.

Most of icing situations have been reported by pilots during the daytime. About 60-70 % of all reports report the light icing. Severe icing which indicates a condition that flight cannot be sustained, is reported in only a few percent of cases. Rime icing is reported much more frequently than glaze or mixed ice, comprising 70-75 % of reports (Politovich, 2003).

1.2.6 Adverse effects of icing on aircraft

The icing can affect both the rotary and stationary parts in an aircraft. The ice accretion will worsen the aerodynamic characteristics of airfoil by decreasing lift, increasing

drag, and deteriorating pitching moment and stall margins. Decreasing of the lift with increasing drag will increase the required thrust. On the other hand, deteriorating pitching moment and stall margins will harden the control of aircraft. Under the icing condition, the wing will stall at a lower angle of attack and higher speed. Along with the serious controllability problems, the wing stall will also degrade the aerodynamics characteristics of an aircraft. When the tail stalls, the downward lift that is needed for horizontal balance, is lessened or removed and the nose of the airplane can severely pitch down. Because the tail has a smaller radius and length than the wings, it can collect proportionately two to three times more ice than the wings. Therefore, the tail stall in icing is harsh. Apart from what has been mentioned about the nature of wing and tail stall in icing, the recovery from a tail stall is exactly the opposite of the traditionally taught wing stall recovery. In a tail stall recovery, the airflow must be corrected to the tail's lower surface, whereas in a wing stall recovery, the airflow must be corrected to the wing's upper surface. The influence of extra loads imposed by the ice weight on an aircraft is insignificant when it is compared to the total weight of aircraft and the aerodynamic degradation that icing causes (Landsberg, 2010).

On the whole, the icing is bad for an aircraft because:

- Icing increases total weight.
- Ice disrupts aerodynamic characteristics by increasing drag, and decreasing lift.
- Both wing and tail stalls can occur, the tail stall is more severe than the wing stall.
- Stall speed increases, and stall angle decreases considerably.
- Icing causes malfunctioning of pressure and velocity probes, and lead to misreading of data by them, and consequently controlling of aircraft becomes very difficult.
- Pitch and roll behaviors become unpredictable, possibly uncontrollable. Recovery from stall or spin may be impossible.
- Icing may cause engine stoppage by icing the carburetor or blocking the engine's air inlet (induction/carburetor icing).
- Iced windscreen/shield may restrict or even block forward vision, especially during landing.

Structure and systems at risk:

- Wings
- Tail
- Fuselage nose
- Empennages
- Propeller blades
- Landing gear doors
- Horizontal and vertical stabilizers
- Nacelles, engine intakes, air intake scoops, compressor blades
- Cockpit glass
- Probes and sensors: pitot tube, temperature probe, static port, angle of attack vane, stall warning device and fuel drainage pipe
- Rudder, ailerons and elevators
- Radio communication & navigation antenna
- Radar domes

Generally, the icing tends to affect large-scale aircraft less than small-scale aircraft. There are several reasons for this. The smaller aircraft in the general aviation category tend to fly at lower altitudes where icing is more prevalent. The small aircraft may have not deicing capability, and their pilots may also have less experience of operating under icing conditions. On contrary, larger aircraft tend to quickly pass wet clouds on ascent and descent, and cruise at altitudes far above those at which icing occurs. Besides, large aircraft are more likely equipped by anti-icing and deicing tools.

1.3 Literature Review

To investigate the aircraft icing, it is possible to perform new experimental tests or relying on the results of empirical correlations. Since performing the new tests will be time-consuming and expensive, the other option is to analyze the icing problems through a numerical simulation via computational fluid dynamics methods.

In this section, the statistical, analytical and numerical researches have been mentioned from the early days of the beginning of the study of aircraft icing up to the present. A chronological look has been taken at the modeling of aircraft icing. Also, the well-known research centers that deal with the icing of aircraft have been announced.

1.3.1 General concept

Cao et al. (2018) have done a comprehensive study for aircraft icing. In this case study different and most important aspects of icing, like causes of icing on aircraft, types & severity of icing, environmental & aircraft-related parameters, and aerodynamic & controllability effects on aircraft have been considered for both take-off and cruise flight phases. Besides, estimating methods of iced aerodynamic parameters have been discussed. The following summarizes some important conclusions from this research work. (1) Ice accretion on aircraft is classified into rime ice, glaze ice, and mixed ice based on its property. Because of its streamlined or spear-like shape, rime ice has a limited effect on the flow-field of aircraft, so the harm is less than the latter two. Most glaze ice has double or multiple horns, and it has the greatest impact on the flow-field and aerodynamic performance. Mixed ice is one of the most common icing forms in reality. It has a mediate impact on aircraft aerodynamic performance. (2) When the aircraft is cruising or approaching, accidents are most likely to occur under the state of icing. (3) Conditions that possibly lead to severe icing are specific temperature (about $-4°C$) and specific altitude, super-cooled water droplets with a larger diameter, high liquid water content, a period of flight under icing conditions (at least 15 minutes). (4) Icing of Super-cooled Large Droplets (SLD) caused by freezing rain (droplet diameter larger than 50 microns) and freezing drizzle (droplet diameter between 40 and 500 microns) often leads to fatal accidents.

1.3.2 Safety aspect of aircraft icing

The icing causes instability problems that leads to the controllability issues in aircraft (BFU, 2001; Cao et al., 2018; COLE and SAND, 1991).

In the period 1990 - 2000, a total of 3,230 aircraft accidents were recorded by the Air Safety Foundation. Twelve percent of those were related to icing (Green, 2006). In-flight icing problems led to a total of 803 aviation accidents and incidents from 1975 to 1988 (NTS, 1996a,b).

Green (2006) has studied U. S. in-flight icing accidents and incidents from 1978 to 2002. The principal conclusion shows that the stall that is followed by loss of control is the most common occurrences. Ice protection systems on smaller aircraft may delay an event but not prevent it. Smaller aircraft which are not equipped with ice protection systems, experience the majority of the events. However, the more severe events experienced by this fleet tend to occur during the descending and landing periods. On the other hand, it is generally observed that the icing effects mitigate on the larger aircraft. This may be because of the greater percentage of bigger aircraft equipped with ice protection systems, or due to a greater power margin.

1.3.3 Icing impact on aircraft performance

Aircraft icing increases the overall weight of an aircraft and degrades its aerodynamic performance. Besides, the icing causes controllability issues because icing disrupts the smoothness of flow around the body surface. The excessive icing accretion even can lead to the separation of flow and cause more drag and less lift, loss of control, and eventually, aircraft crashes (Reehorst et al., 1999). The effect of ice accretion on aircraft has been systematically observed and investigated since the 1940s (Kanter, 1945). The early studies mainly focused on the changes of aerodynamic forces and moment of an aircraft under icing conditions (Gray and Von Glahn, 1953; Gray and vonGlahn, 1958; Yi et al., 2010). Later, the performance, stability, and controllability of aircraft after icing became the main interests (Chengtao, 2008; Ranaudo et al., 1984; Zhang et al., 2011). Ice accumulation on the aircraft causes unsteadiness and

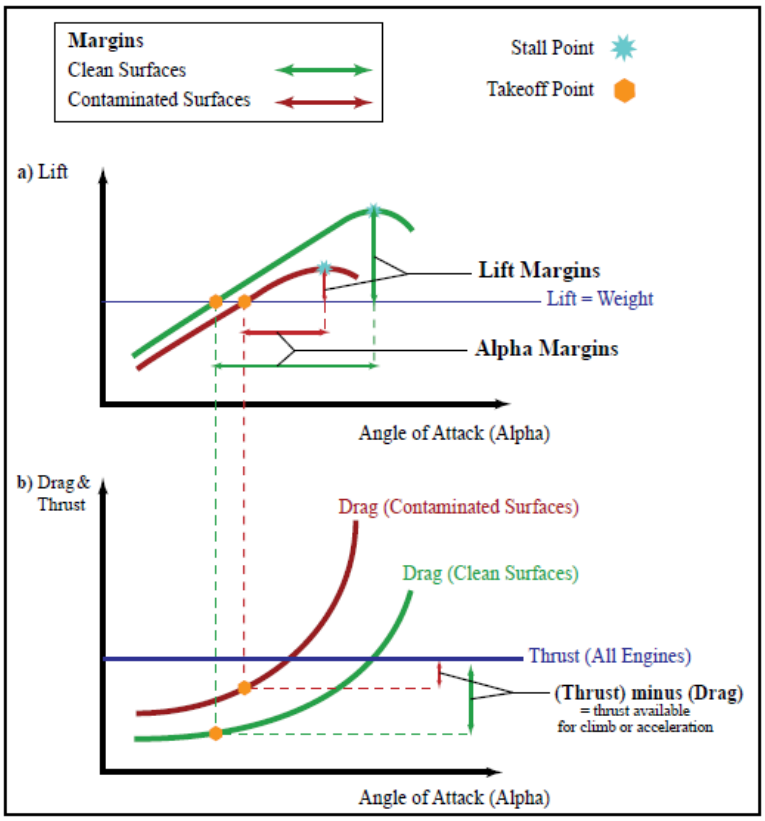

Figure 1.8 : Lift and thrust are severely degraded by icing contaminants (Gro, 2008).

instability. Also, the icing degrades the performance. Under the icing conditions, the aircraft will stall at higher speeds, and the stall angle decreases (Whalen et al., 2002).

The stall happens when the angle of attack reaches a certain point, and the flow no longer moves smoothly over a wing or tail surface. Consequently, the flow separates from the surface leading to generating the extra drag and the decreased lift remarkably. Actually, a small amount of ice over an airfoil reduces the angle of attack at which the stall occurs, consequently, the maximum available lift decreases extremely.

The wind tunnel test shows that only 0.4 mm ice thickness on the wing with a chord length of 1.5 m will reduce the maximum lift by approximately 30 % (Figure 1.8. (a)). Also, the test data (Figure 1.8. (b)) shows that the drag of the aircraft can increase more than double (Gro, 2008). Also, these results show that the angle of attack at which the stall occurs will lessen.

In the stall happening, this is the flow separation that causes the escalation of lift and drag coefficients. If the stall and resulting separation take place earlier the larger area will be affected. Figure 1.9 shows that the stall occurrence in the leading edge limits the maximum accessible lift more than the trailing edge stall. Therefore, the smaller

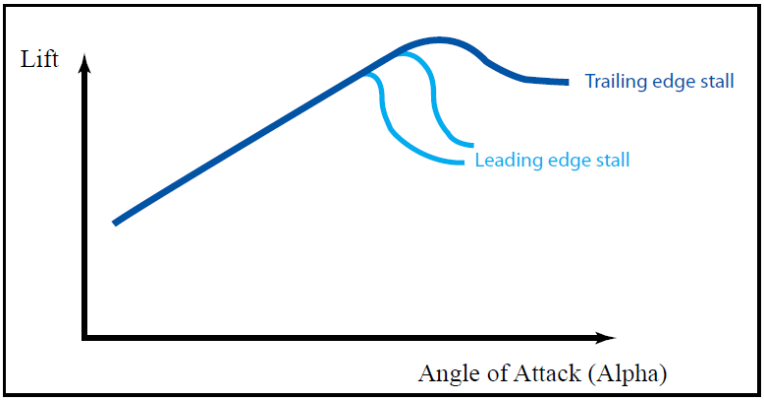

Figure 1.9 : Leading edge stalls are more abrupt than trailing edge stalls (Gro, 2008).

stall angle in the icing will follow the serious performance degradation. On the other hand, the icing will increase the stall occurrence speed which is undesirable in aircraft (Gro, 2008).

One of the earliest performance investigations during flight performed by Preston and Blackman (1948) shows that the additional 81 % drag and almost a complete loss of control were seen during the flight. A large data set has been reported by NASA Glenn Research Center based on the tests in natural icing situations, as well as artificial icing conditions to investigate the stability behavior of aircraft. Results show that the ice accretion badly affects the longitudinal and lateral static stability, and makes difficulties in the controllability of an aircraft. A 10 % reduction in stability and controllability was observed. There is also evidence that the effects of ice are more significant at a smaller stall angle where early flow separation occurs Bragg et al. (2000).

Acker and Kleinknecht (1950) conducted a flight test to study the icing effects on the inlets of a turbojet engine. They found that the ice accretion on the engine inlet resulted in a 9 to 26 % reduction of engine thrust.

Most of the ice accretions simulations at the NASA Glenn Icing Research Tunnel (IRT) based on a full-scale model indicate that runback ice accretion can significantly degrade the aerodynamic performance of airfoils, particularly for the icing cases located near the leading edge of airfoil (Broeren and Bragg, 2005; Busch et al., 2008; Calay et al., 1997; Gray and Von Glahn, 1953; Lee and Bragg, 1999, 2003; Lee et al., 2005; Papadakis and Gile Laflin, 2001; Whalen et al., 2006, 2008). They found that the drag coefficient increases up to approximately 0.011, while the maximum lift

coefficient decreases up to 0.35 during icing. Results also show that the Reynolds number has more significant effects in the icing simulation, On the other hand, the geometric scaling did not reproduce the same aerodynamics of the full-scale wing. Therefore, the empirical methods are more accurate to develop aerodynamically equivalent shapes that represented the full-scale iced-wing.

1.3.4 Modeling of aircraft icing

Although the experimental tests within icing wind tunnel are accurate tools to investigate the ice accretion, these tests are very expensive and time-consuming. Instead, using numerical simulations via computational methods are low expense and reliable. With the considerable progress in computational tools and methods, the numerous numerical studies have been done in recent years to predict the icing process.

The numerical-computational icing simulation consists of the following procedure for computing the ice shapes around wings, (1) grid generation, (2) calculation of the airflow field and calculation of the convective heat transfer coefficient, (3) droplets' trajectories (Lagrangian approach) or droplets' distribution (Eulerian approach) and calculation of the collision efficiencies, and (4) the ice accretion (Figure 1.10).

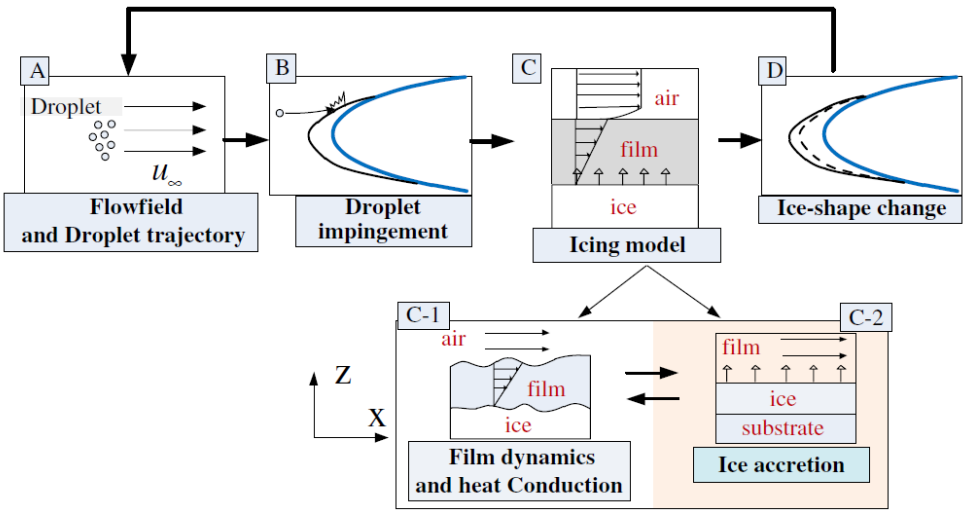

Figure 1.10 : Computational simulation of icing (Kong and Liu, 2014).

The classical numerical approach to predicting ice accretion on an unheated icing surface is Messinger (1953) model which is based on the energy and mass balance in each control volume. The main idea is that there is a balance of energy, between

heat losses and heat gains on the icing surface. This method was updated by Cansdale and Gent (1983) to include the air compressibility effects.

Myers (2001); Myers and Charpin (2004) also made some improvements to Messinger model for developing a general ice-accretion code to three-dimensional flows. Besides, this extension to Messinger model, partly, improves the deficit of the simple Messinger model in the modeling of glaze ice. The main advantages of using the extended model are that it provides the temperature profiles in the ice-water interface, and a formula for the ice thickness at which glaze ice is first observed.

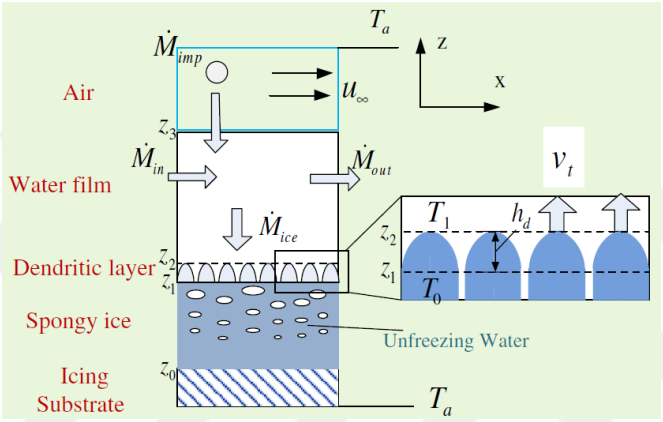

Figure 1.11 : Spongy ice (Kong and Liu, 2014).

The Messinger approach is the base of most today ice-accretion codes that have been used widely such as ICECREMO (Myers, 2001) and FENSAP-ICE (Beaugendre et al., 2003). Messinger model supposes a homogeneous ice and a constant zero $^{\circ}C$ freezing temperature at the water-ice interface. However, the experimental investigations show that the temperature at the ice surface will fall below the freezing temperature (List, 1990), then impinging water droplets can be entrapped in the ice matrix, and form the spongy ice. Many efforts have been made by Karev et al. (2007); Yanxia et al. (2010) to investigate these phenomena. Recently, Kong and Liu (2014); Li et al. (2014) proposed a spongy icing model with better prediction to account the entrapped liquid within ice formation, and to improve the determination of the surface temperature (Figure 1.11).

There are three differences between traditional models and the spongy icing model. The first difference is the definition of the surface temperature. In traditional models, it has been assumed that the temperature of the ice-water interface is at the freezing point, while in the spongy icing model, the temperature of the interface is super-cooled. The second difference is the capability of describing icing regimes. The spongy model

can describe four different regimes while traditional models can only describe three at best. The third difference is the capability of describing the sponginess of ice. The computational results are in good agreement with the experimental data. Although the spongy model has good agreement with experiments in predicting icing thickness and temperature, the spongy model assumes that the unfrozen liquid continuously flows over the ice surface, then omitting the droplets retention phenomena which observed in the icing experiments Olsen and Walker (1986).

It has been found that the unfrozen liquid water may come together with the little droplets (which remain on the ice surface) and gradually freeze that consequently affect the entire icing process (Olsen and Walker, 1986). To be more specific, the droplets between the smooth and rough zone caused by the water film and ice can bring an air transition from laminar to turbulent flow, and enhancing the heat transfer. This accelerates the droplets freezing rate, consequently influencing the ice accretion morphology. With considering the effect of water droplets retention on the icing process Lian et al. (2018) have modified the existing spongy icing model.

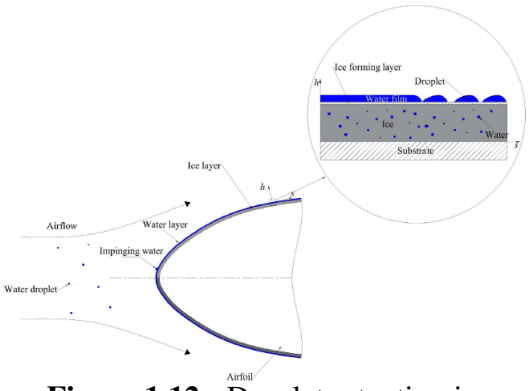

Figure 1.12 : Droplet retention in modified spongy model (Lian et al., 2018).

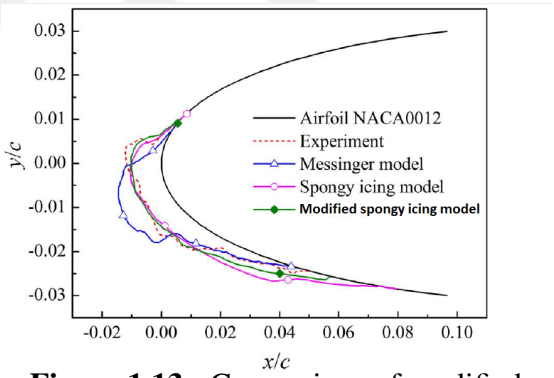

Figure 1.13 : Comparison of modified spongy model with others in $10°C$ (Lian et al., 2018).

The results indicate that the modified spongy model has a better agreement with the experiment on the ice accretion morphology than the former spongy icing model (Figure 1.12 and Figure 1.13), when there is liquid water in ice at not much low air temperature, demonstrating the necessity of consideration of droplets retention on the ice surface in the simulation of glaze ice accretion.

1.3.5 Worldwide research centers which deal with aircraft icing

Some of the most important centers and labs that studying the icing in aircraft are mentioned here.

- The National Aeronautics and Space Administration (NASA), USA.
- Aircraft Icing Research, Wichita State University, USA.
- Aircraft Icing & Aerodynamics Research Group, University of Washington, USA.
- Aircraft Icing Physics and Anti-/De-icing Technology Laboratory, Iowa State University, USA.
- National Research Council of Canada (NRC), Canada.
- Polytechnique Montréal, Canada.
- McGill University, Canada.
- University of Ottawa, Canada.
- Concordia University, Canada.
- Defense Research Agency (DRA), UK.
- Defense Evaluation and Research Agency (DERA), UK.
- Defense Science and Technology Laboratory (DSTL), UK.
- Icing Tunnel, Cranfield University, UK.
- Research Impact, University College London, UK.
- The Office National d'Etudes et de Recherches Aérospatiales (ONERA), The French Aerospace Lab, France.
- The Advanced Diagnosis and Warning System for aircraft Icing Environments (ADWICE), Germany.
- Das Institut für Flugsystemtechnik (FT), The Institute of Flight Systems at the DLR site Braunschweig, Germany

- Italian Aerospace Research Center (CIRA), Italy.
- RHEA group.
- Japanese-European Deicing Aircraft Collaborative Exploration (JEDI ACE).
- Department of Civil Aviation Engineering, School of Aeronautics, Northwestern, Poly-technical University, China.

1.4 Structure of Dissertation

In the 1st chapter, the main concepts of the icing phenomenon are mentioned earlier, then, the literature survey provides an overview of the most important research that deals with the aircraft icing. The geometry of the aircraft's wing is revealed in the 2nd chapter. Chapter 3 explains how the grid is generated around the airfoil. The airflow is determined in the 4th chapter, then, the convective heat transfer coefficient is obtained in chapter 5. Based on the values of airflow, the water droplets distribution is calculated in the 6th chapter to calculate the collision efficiency. In chapter 7 the conventional ice accretion models are implemented to validate our icing simulation. In the 8th chapter, the uniqueness of our study is announced by introducing the proposed ice accretion model to improve the simulation of aircraft icing, consequently, the results of numerical and computational simulation of aircraft icing are shown. Finally, in chapter 9 the conclusions of our research work are discussed, and recommendations will be given for the future works.

2. GEOMETRY

The different types of airfoils can be selected in the icing simulation. Among them, the NACA 0012 airfoil is selected in the present study because lots of verification in the literature are reported for this airfoil.

2.1 NACA 4-Digits Airfoil Specification

Many references explain the x and y coordinates of NACA wings with four digits. The geometry of the NACA wing will be calculated via these digits. The geometry of NACA airfoil is determined via 4 digits which designate the maximum camber ratio (MCR), position of the maximum camber (PMCR), and thickness ratio (TR).

If an airfoil number be NACA MPXX:

The maximum camber ratio (MCR) is M divided by 100. In the case of NACA 0012, M=0 so the camber is 0.0 or 0 % of the chord which means airfoil is symmetric.

The position of the maximum camber ratio is PMCR divided by 10. In the case of NACA 0012, P=0 thus the maximum camber is at 0. or 0 % of the chord.

XX is the thickness divided by 100. In the case of NACA 0012, XX=12 so the thickness ratio (TR) is 0.12 or 12 % of the chord.

Then, the NACA airfoil body is created from a camber line and a thickness distribution plotted perpendicular to the camber line.

2.2 X Coordinate of Airfoil

One way to plot the airfoil is to iterate through a cosine spacing with uniform increments of $cos(n\frac{2\pi}{NE})$ which NE is the number of elements that form the airfoil. Then, the x coordinate of the nth increment will be (Bramantya and Ginting, 2020):

$$x_c = 0.5\left[1 + cos(n\frac{2\pi}{NE})\right] \tag{2.1}$$

$$x = chord(x_c) \tag{2.2}$$

2.3 Y Coordinate of Airfoil

The Y coordinates of the camber line are considered separately along two sections on either side of the position of maximum camber ratio (PMCR). Then, the position of the upper and lower surfaces of the airfoil envelope later by adding/subtracting the thickness of the camber line to/from the Y values of the camber line. The relevant equations are (Bramantya and Ginting, 2020):

$$\begin{cases} y_c = \frac{(MCR)}{(PMCR)^2}\left[2(PMCR)x_c - x_c^2\right] & ,for\ x_c \leq (PMCR) \\ y_c = \frac{(MCR)}{(1-PMCR)^2}\left[1 - 2(PMCR) + 2(PMCR)x_c - x_c^2\right] & ,for\ x_c > (PMCR) \end{cases} \tag{2.3}$$

For a symmetric airfoil the y_c value of camber is always zero.

The thickness of airfoil for a closed trailing edge is (Bramantya and Ginting, 2020):

$$y_T = 5.TR\left[0.2969x_c^{0.5} - 0.1260x_c - 0.3516x_c^2 + 0.2843x_c^3 - 0.1036x_c^4\right] \tag{2.4}$$

then,

$$y = chord(y_c \pm y_T) \tag{2.5}$$

The slop of upper and lower surfaces of an airfoil ($tan\theta = \frac{dy}{dx} = \frac{d(y_c \pm y_T)}{dx}$) can be easily calculated by differentiation of the mentioned coordinate equations of the airfoil, then the angle of camber of surface on the airfoil will be $\theta = Arctan\left(\frac{dy}{dx}\right)$.

2.4 Shifting Center of Coordinate from Leading Edge into Half-Chord

In order to generate O type grid around an airfoil, the center of coordinate will be transferred into the half of the chord as follows:

$$x = x - \frac{chord}{2} \tag{2.6}$$

$$y = y \tag{2.7}$$

3. GRID

The grid generation can be classified into two categories known as structured and unstructured, based on the topology of the elements or volumes that fill the domain. The grid generation methods should be able to meet the especial properties via specific control tools. The mesh spacing (stretching), skewness, smoothness, and aspect ratio are among these properties. Also, these methods should be computationally reliable, efficient, and easy to code (Liseikin, 2017).

One of the common ideas to all structured grid generation methods is the transformation (mapping) of a physical domain into a computational domain. The most efficient structured grids are the boundary-fitted grids. First, a body-fitted grid line is generated on the body, then the grid lines successively extended from the body to the interior region to reach outer boundary. On this basis, three basic groups of mapping methods of grid generation are as follows:

1. The algebraic grid generation approach relies on an explicit construction of coordinate transformations through the transfinite interpolation.

2. Variational methods are performed through the optimization of a grid quality via minimization of the combination of functionalities.

3. Differential methods, are mainly based on the solution of parabolic, elliptic, and hyperbolic equations in a selected transformed region.

The differential methods based on solution of the elliptic equations are commonly used for generating of the mesh for a geometry with arbitrary boundaries. The elliptic equations can generate smooth grids, allow for full specification of grid nodes on the boundary, do not allow the boundary singularities spread into interior region, and have not the cell overlapping problem. Elliptic equations are also utilized for the unstructured grids (Liseikin, 2017). The most popular elliptic equation is the Poisson

equation, which gives the wonderful possibility to apply controlling terms to satisfy smoothness, fine spacing, and orthogonality on the body surface.

3.1 Elliptic Grid Generation

For the most practical problems, the geometry of the body is usually curved and the flow exhibits regions of strong gradients just near the body, and to accommodate these effects, the grid needs to be: body-fitted which grid wrapped around the airfoil, curvilinear which cells are "rotated" relative to the x-y coordinates, and orthogonal which grid collide the body in a nearly normal fashion. In such cases, the conventional finite difference quotients, are difficult to express, and hence, the grid has to be transformed from the curvilinear non-uniform x,y coordinates (physical domain) to the rectangular uniform ξ ,η coordinates (computational domain).

The elliptic grid generation has been preferred frequently because it contains all desired features of grid generation techniques, including (i) Gridlines of the same family, that do not cross each other, (ii) Smoothness of the grid point distribution, (iii) Orthogonality or nearly orthogonal fashion of the grid lines and (iv) Options for grid point clustering (Hoffmann, 2000). In this chapter, Thomson's grid-generation approach is used (Thames et al., 1977; Thompson et al., 1974, 1977a,b, 1982, 1985) which is the extension of elliptic partial differential equations (Laplace equation) to the Poisson equations with the definition of the controlling functions (controlling terms) to satisfy the smoothness, fine-spacing, and orthogonality of mesh on the body. In particular, the automatic controlling functions concept introduced by Steger and Sorenson (1979) has been extended to generate an O-type grid around a NACA airfoil as a sample of a curvilinear boundary.

The elliptic body-fitted curvilinear conformal coordinate transformation can be useful in the areas like Aerodynamics and computational fluid dynamic applications (such as fluid dynamics modeling/simulation and optimal shape design of airfoil based on pressure distribution on its surface), thermal science applications transfer, and Heating Ventilation and Air Conditioning (HVAC) applications (such as design and calculations of air handling units and air ducts). Apart from the applications which are mentioned, elliptic grid generation can be also used in computational physics and computational solid mechanics.

The main idea of this chapter is to provide an elliptic grid generation method to transport problems from the physical domain to the computational domain which allows for the simple use of computational methods in a way that decreases the time and cost of computer-based calculations. The most important advantage of its body-fitted aspect is its ability to clearly define the spatial boundary conditions just on the body. Also, space controlling of grid lines and their orthogonality near the body allows for defining the physical concept of the problem very well just in the area that the large variations and sharp gradients of flow and thermal properties exist.

Numerical results show the satisfactory performance of elliptic grid generation by its coupling effectiveness in achieving orthogonality and smoothness of the grid on the boundaries. Besides, it will be applied very well for arbitrary-shaped bodies, and also can be used for multiple-element bodies, easily.

3.2 O Type Grid

To calculate the velocity and pressure distributions at any point in the flow region, a grid should be generated over the region. The grid generation method considered in this research is the elliptic grid generation, which was proposed by Thompson. The O-type elliptic grid generation technique is employed in this section which will be resulted in a smooth, fine, and orthogonal grid over the airfoil surface. The O-type grid is a doubly-connected domain, this is a shape in which there are two paths between any two points, and those paths are distinct and can't be smoothly deformed into each other. As an example, consider the airfoil shown in Figure 3.1. An outer boundary will be selected by specifying some geometrical configuration such as the circle, elliptic, rectangular, etc. To unwrap this physical domain such that a rectangular computational domain can be created, two branch cuts, shown as lines AB and CD in Figure 3.1, are introduced. An intermediate step is also shown in this figure.

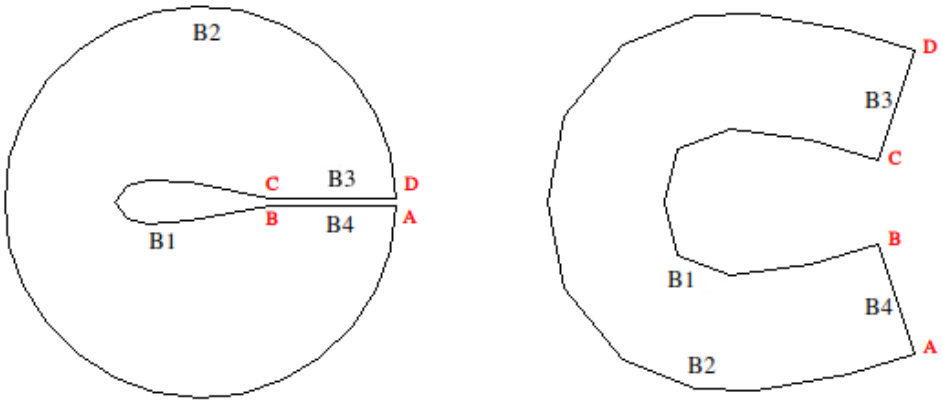

Figure 3.1 : O type grid.

The domain is stretched and deformed to create a rectangular shape computational domain as shown in Figure 3.2.

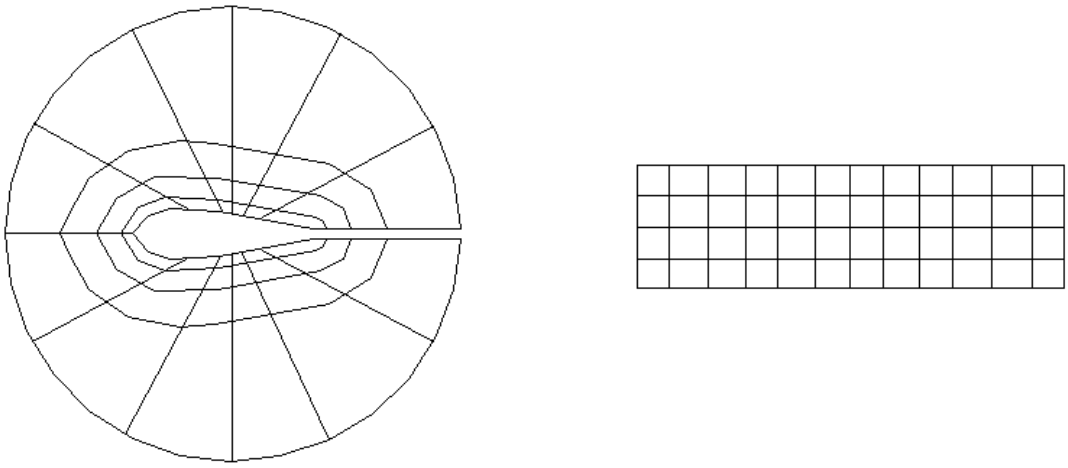

Figure 3.2 : Coordinate transformation from $x-y$ physical domain (left hand side) to $\xi-\eta$ computational domain (right hand side).

The boundaries of the domain are identified by B_1, B_2, B_3 *and* B_4. A uniformly distributed grid system is constructed in the computational space; therefore, the location of every grid in the computational domain, including the boundaries, is known. Then the object is to employ the elliptic grid generator to determine the location of grid points in the physical space. Thus, the elliptic equations should be solved. The procedure is similar to the one used for simply-connected regions. that is, the grid point distribution on the boundaries of the physical domain must be defined and an initial guess grid point distribution for the interior region must be provided. One distinct difference is the treatment of grid points on the boundaries B_3 *and* B_4, i.e. on the

branch cuts. These points must be free to float, i.e. the location of the grids along line AC should be updated. This update is accomplished by computing new values of x, and y after each iteration. It is not necessary to compute the values of x,y for $\xi = \xi_{Max}$, because grid lines $\xi = 0$ and $\xi = \xi_{Max}$ are coincident, therefore, $x(\xi_{Max}, \eta) = x(0, \eta)$ and $y(\xi_{Max}, \eta) = y(0, \eta)$ (Hoffmann, 2000).

3.2.1 Poisson equation

To generate an elliptic grid the Poisson equation will be solved by applying controlling terms of P and Q which meet the basic requirements of space-controlling, orthogonality, and smoothness near the body. The basic Poisson equation in the physical domain is:

$$\nabla^2 \xi = \xi_{xx} + \xi_{yy} = P(\xi, \eta) \tag{3.1}$$

$$\nabla^2 \eta = \eta_{xx} + \eta_{yy} = Q(\xi, \eta) \tag{3.2}$$

The terms of $\frac{\partial \xi}{\partial x}$, $\frac{\partial \xi}{\partial y}$, $\frac{\partial \eta}{\partial x}$, $\frac{\partial \eta}{\partial y}$ should be expressed in terms of $\frac{\partial x}{\partial \xi}$, $\frac{\partial x}{\partial \eta}$, $\frac{\partial y}{\partial \xi}$, $\frac{\partial y}{\partial \eta}$. for that consider the identities as:

$$x = x\Big(\xi(x,y), \eta(x,y)\Big) \tag{3.3}$$

$$y = y\Big(\xi(x,y), \eta(x,y)\Big) \tag{3.4}$$

By differentiating both sides of equations 3.3 , 3.4 with respect to x the following results is obtained:

$$\begin{cases} 1 = \frac{\partial x}{\partial \xi}\frac{\partial \xi}{\partial x} + \frac{\partial x}{\partial \eta}\frac{\partial \eta}{\partial x} \\ 0 = \frac{\partial y}{\partial \xi}\frac{\partial \xi}{\partial x} + \frac{\partial y}{\partial \eta}\frac{\partial \eta}{\partial x} \end{cases} \tag{3.5}$$

Similarly by differentiating both sides of equations 3.3 , 3.4 with respect to y the following results is obtained:

$$\begin{cases} 0 = \frac{\partial x}{\partial \xi}\frac{\partial \xi}{\partial y} + \frac{\partial x}{\partial \eta}\frac{\partial \eta}{\partial y} \\ 1 = \frac{\partial y}{\partial \xi}\frac{\partial \xi}{\partial y} + \frac{\partial y}{\partial \eta}\frac{\partial \eta}{\partial y} \end{cases} \tag{3.6}$$

Equation 3.5 can be written as:

$$\begin{bmatrix} \frac{\partial x}{\partial \xi} & \frac{\partial x}{\partial \eta} \\ \frac{\partial y}{\partial \xi} & \frac{\partial y}{\partial \eta} \end{bmatrix} \begin{bmatrix} \frac{\partial \xi}{\partial x} \\ \frac{\partial \eta}{\partial x} \end{bmatrix} = \begin{bmatrix} 1 \\ 0 \end{bmatrix} \tag{3.7}$$

this equation can be rewritten as:

$$\begin{bmatrix} \frac{\partial \xi}{\partial x} \\ \frac{\partial \eta}{\partial x} \end{bmatrix} = \begin{bmatrix} \frac{\partial x}{\partial \xi} & \frac{\partial x}{\partial \eta} \\ \frac{\partial y}{\partial \xi} & \frac{\partial y}{\partial \eta} \end{bmatrix}^{-1} \begin{bmatrix} 1 \\ 0 \end{bmatrix} = \frac{1}{\begin{vmatrix} \frac{\partial x}{\partial \xi} & \frac{\partial x}{\partial \eta} \\ \frac{\partial y}{\partial \xi} & \frac{\partial y}{\partial \eta} \end{vmatrix}} \begin{bmatrix} \frac{\partial y}{\partial \eta} & -\frac{\partial x}{\partial \eta} \\ -\frac{\partial y}{\partial \xi} & \frac{\partial x}{\partial \xi} \end{bmatrix} \begin{bmatrix} 1 \\ 0 \end{bmatrix} = \frac{1}{J} \begin{bmatrix} \frac{\partial y}{\partial \eta} \\ -\frac{\partial y}{\partial \xi} \end{bmatrix} \tag{3.8}$$

which, J is the jacobian of the coordinate transformation,

$$\Delta x \Delta y = J \Delta \xi \Delta \eta \tag{3.9}$$

$$J = \begin{vmatrix} \frac{\partial x}{\partial \xi} & \frac{\partial x}{\partial \eta} \\ \frac{\partial y}{\partial \xi} & \frac{\partial y}{\partial \eta} \end{vmatrix} = (\frac{\partial x}{\partial \xi}\frac{\partial y}{\partial \eta} - \frac{\partial x}{\partial \eta}\frac{\partial y}{\partial \xi}) = (x_\xi y_\eta - x_\eta y_\xi) \tag{3.10}$$

from the equation 3.8:

$$\frac{\partial \xi}{\partial x} = \frac{1}{J}\frac{\partial y}{\partial \eta} \rightarrow \xi_x = \frac{y_\eta}{J} \tag{3.11}$$

$$\frac{\partial \eta}{\partial x} = -\frac{1}{J}\frac{\partial y}{\partial \xi} \rightarrow \eta_x = -\frac{y_\xi}{J} \tag{3.12}$$

Similar treatment of equation 3.6 gives:

$$\frac{\partial \xi}{\partial y} = -\frac{1}{J}\frac{\partial x}{\partial \eta} \rightarrow \xi_y = -\frac{x_\eta}{J} \tag{3.13}$$

$$\frac{\partial \eta}{\partial y} = \frac{1}{J}\frac{\partial x}{\partial \xi} \rightarrow \eta_y = \frac{x_\xi}{J} \tag{3.14}$$

The double derivative of $\frac{\partial^2 \xi}{\partial x^2}$ can be written as:

$$\begin{aligned} \frac{\partial^2 \xi}{\partial x^2} = \frac{\partial\left(\frac{\partial \xi}{\partial x}\right)}{\partial x} = \frac{\partial\left(\frac{\partial \xi}{\partial x}\right)}{\partial \xi}\frac{\partial \xi}{\partial x} + \frac{\partial\left(\frac{\partial \xi}{\partial x}\right)}{\partial \eta}\frac{\partial \eta}{\partial x} = \\ \frac{\partial\left(\frac{1}{J}\frac{\partial y}{\partial \eta}\right)}{\partial \xi}\frac{1}{J}\frac{\partial y}{\partial \eta} + \frac{\partial\left(\frac{1}{J}\frac{\partial y}{\partial \eta}\right)}{\partial \eta}\frac{-1}{J}\frac{\partial y}{\partial \xi} = \\ \left(\frac{1}{J}\frac{\partial^2 y}{\partial \xi \partial \eta} - \frac{1}{J^2}\frac{\partial J}{\partial \xi}\frac{\partial y}{\partial \eta}\right)\frac{1}{J}\frac{\partial y}{\partial \eta} + \left(\frac{1}{J}\frac{\partial^2 y}{\partial \eta \partial \eta} - \frac{1}{J^2}\frac{\partial J}{\partial \eta}\frac{\partial y}{\partial \eta}\right)\frac{-1}{J}\frac{\partial y}{\partial \xi} \end{aligned} \tag{3.15}$$

Remembering that $J = \left(\frac{\partial x}{\partial \xi}\frac{\partial y}{\partial \eta} - \frac{\partial x}{\partial \eta}\frac{\partial y}{\partial \xi}\right)$, now $\frac{\partial J}{\partial \xi}$, $\frac{\partial J}{\partial \eta}$ are written as:

$$\frac{\partial J}{\partial \xi} = \frac{\partial^2 x}{\partial \xi \partial \xi}\frac{\partial y}{\partial \eta} + \frac{\partial x}{\partial \xi}\frac{\partial^2 y}{\partial \xi \partial \eta} - \frac{\partial^2 x}{\partial \xi \partial \eta}\frac{\partial y}{\partial \xi} - \frac{\partial x}{\partial \eta}\frac{\partial^2 y}{\partial \xi \partial \xi} \tag{3.16}$$

$$\frac{\partial J}{\partial \eta} = \frac{\partial^2 x}{\partial \xi \partial \eta}\frac{\partial y}{\partial \eta} + \frac{\partial x}{\partial \xi}\frac{\partial^2 y}{\partial \eta \partial \eta} - \frac{\partial^2 x}{\partial \eta \partial \eta}\frac{\partial y}{\partial \xi} - \frac{\partial x}{\partial \eta}\frac{\partial^2 y}{\partial \xi \partial \eta} \tag{3.17}$$

Substituting equations 3.16 , 3.17 in equation 3.15 gives:

$$\begin{aligned}
\frac{\partial^2 \xi}{\partial x^2} &= \Big(\frac{1}{J}\frac{\partial^2 y}{\partial \xi \partial \eta} - \frac{1}{J^2}\big(\frac{\partial^2 x}{\partial \xi \partial \xi}\frac{\partial y}{\partial \eta} + \frac{\partial x}{\partial \xi}\frac{\partial^2 y}{\partial \xi \partial \eta} - \frac{\partial^2 x}{\partial \xi \partial \eta}\frac{\partial y}{\partial \xi} - \frac{\partial x}{\partial \eta}\frac{\partial^2 y}{\partial \xi \partial \xi}\big)\frac{\partial y}{\partial \eta}\Big)\frac{1}{J}\frac{\partial y}{\partial \eta} \\
&+ \Big(\frac{1}{J}\frac{\partial^2 y}{\partial \eta \partial \eta} - \frac{1}{J^2}\big(\frac{\partial^2 x}{\partial \xi \partial \eta}\frac{\partial y}{\partial \eta} + \frac{\partial x}{\partial \xi}\frac{\partial^2 y}{\partial \eta \partial \eta} - \frac{\partial^2 x}{\partial \eta \partial \eta}\frac{\partial y}{\partial \xi} - \frac{\partial x}{\partial \eta}\frac{\partial^2 y}{\partial \xi \partial \eta}\big)\frac{\partial y}{\partial \eta}\Big)\frac{-1}{J}\frac{\partial y}{\partial \xi} \\
&= \frac{1}{J^3}\Big[-\big(\frac{\partial y}{\partial \eta}\big)^3\frac{\partial^2 x}{\partial \xi \partial \xi} + 2\frac{\partial y}{\partial \xi}\big(\frac{\partial y}{\partial \eta}\big)^2\frac{\partial^2 x}{\partial \xi \partial \eta} - \big(\frac{\partial y}{\partial \xi}\big)^2\frac{\partial y}{\partial \eta}\frac{\partial^2 x}{\partial \eta \partial \eta}\Big] \\
&+ \frac{1}{J^3}\Big[\frac{\partial x}{\partial \eta}\big(\frac{\partial y}{\partial \eta}\big)^2\frac{\partial^2 y}{\partial \xi \partial \xi} + \Big(\frac{\partial x}{\partial \xi}\big(\frac{\partial y}{\partial \eta}\big)^2 - \frac{\partial x}{\partial \eta}\frac{\partial y}{\partial \xi}\frac{\partial y}{\partial \eta} - \frac{\partial x}{\partial \xi}\big(\frac{\partial y}{\partial \eta}\big)^2 - \frac{\partial x}{\partial \eta}\frac{\partial y}{\partial \xi}\frac{\partial y}{\partial \eta}\Big)\frac{\partial^2 y}{\partial \xi \partial \eta} \\
&+ \Big(-\frac{\partial x}{\partial \xi}\frac{\partial y}{\partial \xi}\frac{\partial y}{\partial \eta} + \frac{\partial x}{\partial \eta}\big(\frac{\partial y}{\partial \xi}\big)^2 + \frac{\partial y}{\partial \eta}\frac{\partial x}{\partial \xi}\frac{\partial y}{\partial \xi}\Big)\frac{\partial^2 y}{\partial \eta \partial \eta}\Big]
\end{aligned} \tag{3.18}$$

after simplification it will be:

$$\begin{aligned}
\frac{\partial^2 \xi}{\partial x^2} &= \frac{1}{J^3}\frac{\partial y}{\partial \eta}\Big[-\big(\frac{\partial y}{\partial \eta}\big)^2\frac{\partial^2 x}{\partial \xi \partial \xi} + 2\frac{\partial y}{\partial \xi}\frac{\partial y}{\partial \eta}\frac{\partial^2 x}{\partial \xi \partial \eta} - \big(\frac{\partial y}{\partial \xi}\big)^2\frac{\partial^2 x}{\partial \eta \partial \eta}\Big] \\
&+ \frac{1}{J^3}\frac{\partial x}{\partial \eta}\Big[\big(\frac{\partial y}{\partial \eta}\big)^2\frac{\partial^2 y}{\partial \xi \partial \xi} - 2\frac{\partial y}{\partial \xi}\frac{\partial y}{\partial \eta}\frac{\partial^2 y}{\partial \xi \partial \eta} + \big(\frac{\partial y}{\partial \xi}\big)^2\frac{\partial^2 y}{\partial \eta \partial \eta}\Big]
\end{aligned} \tag{3.19}$$

After similar derivation with respect to y, it is derived that:

$$\begin{aligned}
\frac{\partial^2 \xi}{\partial y^2} &= \frac{1}{J^3}\frac{\partial y}{\partial \eta}\Big[-\big(\frac{\partial x}{\partial \eta}\big)^2\frac{\partial^2 x}{\partial \xi \partial \xi} + 2\frac{\partial x}{\partial \xi}\frac{\partial x}{\partial \eta}\frac{\partial^2 x}{\partial \xi \partial \eta} - \big(\frac{\partial x}{\partial \xi}\big)^2\frac{\partial^2 x}{\partial \eta \partial \eta}\Big] \\
&+ \frac{1}{J^3}\frac{\partial x}{\partial \eta}\Big[\big(\frac{\partial x}{\partial \eta}\big)^2\frac{\partial^2 y}{\partial \xi \partial \xi} - 2\frac{\partial x}{\partial \xi}\frac{\partial x}{\partial \eta}\frac{\partial^2 x}{\partial \xi \partial \eta} + \big(\frac{\partial x}{\partial \xi}\big)^2\frac{\partial^2 y}{\partial \eta \partial \eta}\Big]
\end{aligned} \tag{3.20}$$

By summation of equations 3.19 and 3.20 gives:

$$
\begin{aligned}
P(\xi,\eta) = \frac{\partial^2\xi}{\partial x^2} + \frac{\partial^2\xi}{\partial y^2} = \\
\frac{1}{J^3}\frac{\partial y}{\partial \eta}\Big[-\{(\frac{\partial x}{\partial \eta})^2 + (\frac{\partial y}{\partial \eta})^2\}\frac{\partial^2 x}{\partial \xi \partial \xi} + \\
2\{\frac{\partial x}{\partial \xi}\frac{\partial x}{\partial \eta} + \frac{\partial y}{\partial \xi}\frac{\partial y}{\partial \eta}\}\frac{\partial^2 x}{\partial \xi \partial \eta} - \{(\frac{\partial x}{\partial \xi})^2 + (\frac{\partial y}{\partial \xi})^2\}\frac{\partial^2 x}{\partial \eta \partial \eta}\Big] \\
+\frac{1}{J^3}\frac{\partial x}{\partial \eta}\Big[\{(\frac{\partial x}{\partial \eta})^2 + (\frac{\partial y}{\partial \eta})^2\}\frac{\partial^2 y}{\partial \xi \partial \xi} \\
-2\{\frac{\partial x}{\partial \xi}\frac{\partial x}{\partial \eta} + \frac{\partial y}{\partial \xi}\frac{\partial y}{\partial \eta}\}\frac{\partial^2 y}{\partial \xi \partial \eta} + \{(\frac{\partial x}{\partial \xi})^2 + (\frac{\partial y}{\partial \xi})^2\}\frac{\partial^2 y}{\partial \eta \partial \eta}\Big]
\end{aligned}
\tag{3.21}
$$

by definition of the coefficients of coordinate transformation as:

$$a = x_\eta^2 + y_\eta^2 \tag{3.22}$$

$$b = x_\xi x_\eta + y_\xi y_\eta \tag{3.23}$$

$$c = x_\xi^2 + y_\xi^2 \tag{3.24}$$

the corresponding equation for ξ will be restated as:

$$
\begin{aligned}
\frac{\partial^2\xi}{\partial x^2} + \frac{\partial^2\xi}{\partial y^2} = -\frac{1}{J^3}\frac{\partial y}{\partial \eta}\Big[a\frac{\partial^2 x}{\partial \xi \partial \xi} - 2b\frac{\partial^2 x}{\partial \xi \partial \eta} + c\frac{\partial^2 x}{\partial \eta \partial \eta}\Big] \\
+\frac{1}{J^3}\frac{\partial x}{\partial \eta}\Big[a\frac{\partial^2 y}{\partial \xi \partial \xi} - 2b\frac{\partial^2 y}{\partial \xi \partial \eta} + c\frac{\partial^2 y}{\partial \eta \partial \eta}\Big] = P(\xi,\eta)
\end{aligned}
\tag{3.25}
$$

On similar lines for η the equivalent equation can be written as:

$$
\begin{aligned}
\frac{\partial^2\eta}{\partial x^2} + \frac{\partial^2\eta}{\partial y^2} = \frac{1}{J^3}\frac{\partial y}{\partial \xi}\Big[a\frac{\partial^2 x}{\partial \xi \partial \xi} - 2b\frac{\partial^2 x}{\partial \xi \partial \eta} + c\frac{\partial^2 x}{\partial \eta \partial \eta}\Big] \\
-\frac{1}{J^3}\frac{\partial x}{\partial \xi}\Big[a\frac{\partial^2 y}{\partial \xi \partial \xi} - 2b\frac{\partial^2 y}{\partial \xi \partial \eta} + c\frac{\partial^2 y}{\partial \eta \partial \eta}\Big] = Q(\xi,\eta)
\end{aligned}
\tag{3.26}
$$

$\frac{\partial x}{\partial \xi}$.Eq 3.25 + $\frac{\partial x}{\partial \eta}$.Eq 3.26 gives:

$$
\begin{aligned}
&-\frac{\partial x}{\partial \xi}\frac{\partial y}{\partial \eta}\Big[a\frac{\partial^2 x}{\partial \xi \partial \xi}-2b\frac{\partial^2 x}{\partial \xi \partial \eta}+c\frac{\partial^2 x}{\partial \eta \partial \eta}\Big]\\
&+\frac{\partial x}{\partial \xi}\frac{\partial x}{\partial \eta}\Big[a\frac{\partial^2 y}{\partial \xi \partial \xi}-2b\frac{\partial^2 y}{\partial \xi \partial \eta}+c\frac{\partial^2 y}{\partial \eta \partial \eta}\Big]\\
&+\frac{\partial x}{\partial \eta}\frac{\partial y}{\partial \xi}\Big[a\frac{\partial^2 x}{\partial \xi \partial \xi}-2b\frac{\partial^2 x}{\partial \xi \partial \eta}+c\frac{\partial^2 x}{\partial \eta \partial \eta}\Big]\\
&-\frac{\partial x}{\partial \eta}\frac{\partial x}{\partial \xi}\Big[a\frac{\partial^2 y}{\partial \xi \partial \xi}-2b\frac{\partial^2 y}{\partial \xi \partial \eta}+c\frac{\partial^2 y}{\partial \eta \partial \eta}\Big]=\\
&J^3\frac{\partial x}{\partial \xi}P(\xi,\eta)+J^3\frac{\partial x}{\partial \eta}Q(\xi,\eta)
\end{aligned}
\tag{3.27}
$$

by simplification this equation will be:

$$
\begin{aligned}
&\Big(-\frac{\partial x}{\partial \xi}\frac{\partial y}{\partial \eta}+\frac{\partial x}{\partial \eta}\frac{\partial y}{\partial \xi}\Big)\Big[a\frac{\partial^2 x}{\partial \xi \partial \xi}-2b\frac{\partial^2 x}{\partial \xi \partial \eta}+c\frac{\partial^2 x}{\partial \eta \partial \eta}\Big]=\\
&J^3\frac{\partial x}{\partial \xi}P(\xi,\eta)+J^3\frac{\partial x}{\partial \eta}Q(\xi,\eta)
\end{aligned}
\tag{3.28}
$$

Again, remembering that $J=\big(\frac{\partial x}{\partial \xi}\frac{\partial y}{\partial \eta}-\frac{\partial x}{\partial \eta}\frac{\partial y}{\partial \xi}\big)$, this equation can be restated as:

$$
-J\Big[a\frac{\partial^2 x}{\partial \xi \partial \xi}-2b\frac{\partial^2 x}{\partial \xi \partial \eta}+c\frac{\partial^2 x}{\partial \eta \partial \eta}\Big]=J^3\Big[\frac{\partial x}{\partial \xi}P(\xi,\eta)+\frac{\partial x}{\partial \eta}Q(\xi,\eta)\Big] \tag{3.29}
$$

which can be simplified as system of Poisson equation as:

$$
a\frac{\partial^2 x}{\partial \xi \partial \xi}-2b\frac{\partial^2 x}{\partial \xi \partial \eta}+c\frac{\partial^2 x}{\partial \eta \partial \eta}=-J^2\Big(\frac{\partial x}{\partial \xi}P(\xi,\eta)+\frac{\partial x}{\partial \eta}Q(\xi,\eta)\Big) \tag{3.30}
$$

By repeating all the process has been mentioned so far for the y the similar Poission equation will be achieved as:

$$
a\frac{\partial^2 y}{\partial \xi \partial \xi}-2b\frac{\partial^2 y}{\partial \xi \partial \eta}+c\frac{\partial^2 y}{\partial \eta \partial \eta}=-J^2\Big(\frac{\partial y}{\partial \xi}P(\xi,\eta)+\frac{\partial y}{\partial \eta}Q(\xi,\eta)\Big) \tag{3.31}
$$

Finally, the Poisson equations (3.1 and 3.2) which transformed into the computational domain are described as (Liseikin, 2017):

$$
ax_{\xi\xi}-2bx_{\xi\eta}+cx_{\eta\eta}=-J^2(Px_{\xi}+Qx_{\eta}) \tag{3.32}
$$

$$ay_{\xi\xi} - 2by_{\xi\eta} + cy_{\eta\eta} = -J^2(Py_{\xi} + Qy_{\eta}) \tag{3.33}$$

To solve the Poisson equations all of the coefficients (i.e. $a,\ b,\ c,\ J,\ x_{\xi},\ x_{\eta},\ y_{\xi},\ y_{\eta},\ x_{\xi\xi},\ x_{\eta\eta},\ y_{\xi\xi},\ y_{\eta\eta},\ x_{\xi\eta},\ y_{\xi\eta},\ P\ and\ Q$) should be found in each iteration.

$P(\xi,\eta)$ and $Q(\xi,\eta)$ are controlling terms, and all difficulty about elliptic grid generation is to find out these terms, properly.

3.3 Applying of Computational Method

3.3.1 Initial grid generation via trans finite interpolation (TFI)

The initial guess values for the elliptic grid generation are provided using the transfinite interpolation (TFI) method. Since TFI method is an algebraic technique and does not need much computational time, it will give an appropriate guess-values for the elliptic grid generation and speed up the convergence time (Mohebbi and Sellier, 2014).

Note that $\xi_{max} = 1$ and $\eta_{max} = 1$.

$$\begin{aligned} x(\xi,\eta) = +\frac{\xi-0}{1-0}x(1,\eta) + \frac{1-\xi}{1-0}x(0,\eta) + \frac{\eta-0}{1-0}x(\xi,1) + \frac{1-\eta}{1-0}x(\xi,0) - \\ \frac{\xi-0}{1-0}\times\frac{\eta-0}{1-0}x(1,1) - \frac{\xi-0}{1-0}\times\frac{1-\eta}{1-0}x(1,0) - \\ \frac{1-\xi}{1-0}\times\frac{\eta-0}{1-0}x(0,1) - \frac{1-\xi}{1-0}\times\frac{1-\eta}{1-0}x(0,0) \end{aligned} \tag{3.34}$$

$$\begin{aligned} y(\xi,\eta) = +\frac{\xi-0}{1-0}y(1,\eta) + \frac{1-\xi}{1-0}x(0,\eta) + \frac{\eta-0}{1-0}y(\xi,1) + \frac{1-\eta}{1-0}y(\xi,0) - \\ \frac{\xi-0}{1-0}\times\frac{\eta-0}{1-0}y(1,1) - \frac{\xi-0}{1-0}\times\frac{1-\eta}{1-0}y(1,0) - \\ \frac{1-\xi}{1-0}\times\frac{\eta-0}{1-0}y(0,1) - \frac{1-\xi}{1-0}\times\frac{1-\eta}{1-0}y(0,0) \end{aligned} \tag{3.35}$$

3.3.2 Updating x and y values on "Branch Cuts" (i.e. reentrants)

The grid-points on branch cuts must be free to float, i.e. the location of the grids along line AC should be updated (Hoffmann, 2000) as:

$$x(0,\eta) = \left\{ \frac{a}{(\Delta\xi)^2}\left[x(\Delta\xi,\eta)+x(1-\Delta\xi,\eta)\right] + \frac{c}{(\Delta\eta)^2}\left[x(0,\eta+\Delta\eta)+x(0,\eta-\Delta\eta)\right] - \right.$$
$$\left. \frac{b}{2\Delta\xi\Delta\eta}\left[x(\Delta\xi,\eta+\Delta\eta)-x(\Delta\xi,\eta-\Delta\eta)+x(1-\Delta\xi,\eta-\Delta\eta)-x(1-\Delta\xi,\eta+\Delta\eta)\right] \right\}$$
$$\left[\frac{a}{2(\Delta\xi)^2}+\frac{c}{2(\Delta\eta)^2}\right] \tag{3.36}$$

$$y(0,\eta) = \left\{ \frac{a}{(\Delta\xi)^2}\left[y(\Delta\xi,\eta)+y(1-\Delta\xi,\eta)\right] + \frac{c}{(\Delta\eta)^2}\left[y(0,\eta+\Delta\eta)+y(0,\eta-\Delta\eta)\right] - \right.$$
$$\left. \frac{b}{2\Delta\xi\Delta\eta}\left[y(\Delta\xi,\eta+\Delta\eta)-y(\Delta\xi,\eta-\Delta\eta)+y(1-\Delta\xi,\eta-\Delta\eta)-y(1-\Delta\xi,\eta+\Delta\eta)\right] \right\}$$
$$\left[\frac{a}{2(\Delta\xi)^2}+\frac{c}{2(\Delta\eta)^2}\right] \tag{3.37}$$

Note that for O type grid the values of y remain constant (i.e. zero) on branch cuts.
It is not necessary to compute the values of x,y for $\xi = 1$, because grid lines $\xi = 0$ and $\xi = 1$ are coincident, therefore:

$$\begin{aligned} x(1,\eta) &= x(0,\eta) \\ y(1,\eta) &= y(0,\eta) \end{aligned} \tag{3.38}$$

3.3.3 Satisfying fine-spacing and orthogonality on body surface

The Laplace or Poisson equations satisfy the smoothness of the generated grid by their nature. Then, remembering that:

$$\Delta\xi = \frac{1-0}{i_{Max}-1} \tag{3.39}$$

$$\Delta\eta = \frac{1-0}{j_{Max}-1} \tag{3.40}$$

fine spacing in the normal direction will be satisfied by:

$$\Delta n = \sqrt{\Delta x^2+\Delta y^2} = \sqrt{(x_\xi\Delta\xi + x_\eta\Delta\eta)^2+(y_\xi\Delta\xi+y_\eta\Delta\eta)^2} = \Delta\eta\sqrt{x_\eta^2+y_\eta^2}$$

$$n_\eta = \frac{dn}{d\eta} \simeq \frac{\Delta n}{\Delta\eta} = \sqrt{x_\eta^2+y_\eta^2} \tag{3.41}$$

orthogonality will be satisfied by:

$$\Delta\xi\Delta\eta = |\Delta\xi||\Delta\eta| cos\left(\frac{\pi}{2}\right) = 0$$

$$x_\xi x_\eta + y_\xi y_\eta = 0 \tag{3.42}$$

which i_{Max} and j_{Max} are the maximum number of grid points in ξ and η directions, respectively. n is the normal direction to the body and dn is the normal distance of the grid-loop just next to the body.

Generally, for the low Reynolds number dn=0.005 (m) and for higher Reynolds number dn=0.00001 (m) are preferred which dn is the distance of the mesh loop just next to the body of airfoil (Kim et al., 2009; Steger and Sorenson, 1979). The most important factor in this section is to find derivatives with respect to η in a way that satisfies fine spacing and orthogonality on the body.

Note that $x_{\xi F}$, $y_{\xi F}$, $x_{\xi B}$ and $y_{\xi B}$ are the only terms needed for the calculation of $x_{\xi\eta}$ and $y_{\xi\eta}$.

Derivatives with respect to ξ:

$$x_\xi(\xi,0) = \frac{x(\xi+\Delta\xi,0) - x(\xi-\Delta\xi,0)}{2\Delta\xi} \tag{3.43}$$

$$y_\xi(\xi,0) = \frac{y(\xi+\Delta\xi,0) - y(\xi-\Delta\xi,0)}{2\Delta\xi} \tag{3.44}$$

$$x_{\xi\xi}(\xi,0) = \frac{x(\xi+\Delta\xi,0) + x(\xi-\Delta\xi,0) - 2x(\xi,0)}{\Delta\xi^2} \tag{3.45}$$

$$y_{\xi\xi}(\xi,0) = \frac{y(\xi+\Delta\xi,0) + y(\xi-\Delta\xi,0) - 2y(\xi,0)}{\Delta\xi^2} \tag{3.46}$$

and with considering the equations 3.41 , 3.42 derivatives with respect to η will be:

$$x_\eta(\xi,0) = -n_\eta \frac{y_\xi(\xi,0)}{\sqrt{x_\xi^2(\xi,0) + y_\xi^2(\xi,0)}} \tag{3.47}$$

$$y_\eta(\xi,0) = +n_\eta \frac{x_\xi(\xi,0)}{\sqrt{x_\xi^2(\xi,0) + y_\xi^2(\xi,0)}} \tag{3.48}$$

$$x_{\eta\eta}(\xi,0) = \frac{-7x(\xi,0) + 8x(\xi,\Delta\eta) - x(\xi,2\Delta\eta)}{2(\Delta\eta)^2} - \frac{3x_\eta(\xi,0)}{\Delta\eta} \tag{3.49}$$

$$y_{\eta\eta}(\xi,0) = \frac{-7y(\xi,0) + 8y(\xi,\Delta\eta) - y(\xi,2\Delta\eta)}{2(\Delta\eta)^2} - \frac{3y_\eta(\xi,0)}{\Delta\eta} \tag{3.50}$$

and,

$$x_{\xi F} = \frac{x(\xi+\Delta\xi,0) - x(\xi,0)}{\Delta\xi} \tag{3.51}$$

$$y_{\xi F} = \frac{y(\xi + \Delta\xi, 0) - y(\xi, 0)}{\Delta\xi} \tag{3.52}$$

$$x_{\xi B} = \frac{x(\xi, 0) - x(\xi - \Delta\xi)}{\Delta\xi} \tag{3.53}$$

$$y_{\xi B} = \frac{x(\xi, 0) - x(\xi - \Delta\xi)}{\Delta\xi} \tag{3.54}$$

$$x_{\eta F}(\xi, 0) = -n_\eta \frac{y_{\xi F}(\xi, 0)}{\sqrt{x_{\xi F}^2(\xi, 0) + y_{\xi F}^2(\xi, 0)}} \tag{3.55}$$

$$x_{\eta B}(\xi, 0) = -n_\eta \frac{y_{\xi B}(\xi, 0)}{\sqrt{x_{\xi B}^2(\xi, 0) + y_{\xi B}^2(\xi, 0)}} \tag{3.56}$$

$$y_{\eta F}(\xi, 0) = +n_\eta \frac{x_{\xi F}(\xi, 0)}{\sqrt{x_{\xi F}^2(\xi, 0) + y_{\xi F}^2(\xi, 0)}} \tag{3.57}$$

$$y_{\eta B}(\xi, 0) = +n_\eta \frac{x_{\xi B}(\xi, 0)}{\sqrt{x_{\xi B}^2(\xi, 0) + y_{\xi B}^2(\xi, 0)}} \tag{3.58}$$

therefore,

$$x_{\xi\eta}(\xi, 0) = \frac{x_{\eta F} - x_{\eta B}}{\Delta\xi} \tag{3.59}$$

$$y_{\xi\eta}(\xi, 0) = \frac{y_{\eta F} - y_{\eta B}}{\Delta\xi} \tag{3.60}$$

construction of “controlling terms”:

$$R_1(\xi, 0) = -\frac{a(\xi, 0)x_{\xi\xi}(\xi, 0) - 2b(\xi, 0)x_{\xi\eta}(\xi, 0) + c(\xi, 0)x_{\eta\eta}(\xi, 0)}{J^2(\xi, 0)} \tag{3.61}$$

$$R_2(\xi, 0) = -\frac{a(\xi, 0)y_{\xi\xi}(\xi, 0) - 2b(\xi, 0)y_{\xi\eta}(\xi, 0) + c(\xi, 0)y_{\eta\eta}(\xi, 0)}{J^2(\xi, 0)} \tag{3.62}$$

then,

$$P_1(\xi, 0) = \frac{+y_\eta(\xi, 0)R_1(\xi, 0) - x_\eta(\xi, 0)R_2(\xi, 0)}{J(\xi, 0)} \tag{3.63}$$

$$Q_1(\xi, 0) = \frac{+y_\xi(\xi, 0)R_1(\xi, 0) - x_\xi(\xi, 0)R_2(\xi, 0)}{J(\xi, 0)} \tag{3.64}$$

Assuming that the i and j represent the number of ith and jth lines equivalent to ξ and η values, respectively, it is more explanatory to introduce P_1 and Q_1 as functions of i, and P and Q as functions of i and j.

Therefore,

$$P_1(i) = \frac{+y_\eta(i, 1)R_1(i, 1) - x_\eta(i, 1)R_2(i, 1)}{J(i, 1)} \tag{3.65}$$

$$Q_1(i) = \frac{+y_\xi(i,1)R_1(i,1) - x_\xi(i,1)R_2(i,1)}{J(i,1)} \tag{3.66}$$

All terms in the right hand sides are calculated at the first loop of grid i.e. $j = 1$,

and finally

$$P(i,j) = +P_1(i)e^{-m_1|j-1|} \tag{3.67}$$

$$Q(i,j) = +Q_1(i)e^{-m_2|j-1|} \tag{3.68}$$

The magnitudes of $m_1 = 1$ and $m_2 = 1$ have been selected and made sense, in our cases.

It will be more accurate to say that the resulted grid has a nearly orthogonal fashion, and as the number of grid-points on the surface of the body increases, this fashion also will be enhanced.

3.3.4 Calculations for inner region

Outer boundary is the circle with the radius of $R = 2 \times chord$, and inner boundary is the surface of NACA airfoil.

To calculate x and y values of inner region, Finite Difference Method (FDM) will be applied for discretization and equations rearranged using Line Successive Over Relaxation (LSOR) method in η direction as follows:

$$A_{S1}(\eta)x(\xi,\eta-\Delta\eta) + A_{P1}(\eta)x(\xi,\eta) + A_{N1}(\eta)x(\xi,\eta+\Delta\eta) = b_1 \tag{3.69}$$

$$A_{S2}(\eta)y(\xi,\eta-\Delta\eta) + A_{P2}(\eta)y(\xi,\eta) + A_{N2}(\eta)y(\xi,\eta+\Delta\eta) = b_2 \tag{3.70}$$

The coefficients for x equation are calculated as follows:

$$A_{N1}(\eta) = \big[\frac{c(\xi,\eta)}{\Delta\eta^2} + J^2(\xi,\eta)\frac{Q(\xi,\eta)}{2\Delta\eta}\big] \tag{3.71}$$

$$A_{P1}(\eta) = \big[-\frac{2a(\xi,\eta)}{\Delta\xi^2} - \frac{2c(\xi,\eta)}{\Delta\eta^2}\big] \tag{3.72}$$

$$A_{S1}(\eta) = \big[\frac{c(\xi,\eta)}{\Delta\eta^2} - J^2(\xi,\eta)\frac{Q(\xi,\eta)}{2\Delta\eta}\big] \tag{3.73}$$

$$\begin{aligned} b_1(\eta) = {} & \big[-\frac{a(\xi,\eta)}{\Delta\xi^2} + J^2(\xi,\eta)\frac{P(\xi,\eta)}{2\Delta\xi}\big]x(\xi-\Delta\xi,\eta) + \\ & \big[-\frac{a(\xi,\eta)}{\Delta\xi^2} - J^2(\xi,\eta)\frac{P(\xi,\eta)}{2\Delta\xi}\big]x(\xi+\Delta\xi,\eta) + \\ & \big[\frac{2b(\xi,\eta)}{4\Delta\xi\Delta\eta}\big](x(\xi+\Delta\xi,\eta+\Delta\eta) + x(\xi-\Delta\xi,\eta-\Delta\eta) - \\ & x(\xi+\Delta\xi,\eta-\Delta\eta) - x(\xi-\Delta\xi,\eta+\Delta\eta)) \end{aligned} \tag{3.74}$$

which for $j = 2$ these coefficients are as:

$$A_{N1}(\eta) = \big[\frac{c(\xi,\eta)}{\Delta\eta^2} + J^2(\xi,\eta)\frac{Q(\xi,\eta)}{2\Delta\eta}\big] \tag{3.75}$$

$$A_{P1}(\eta) = \big[-\frac{2a(\xi,\eta)}{\Delta\xi^2} - \frac{2c(\xi,\eta)}{\Delta\eta^2}\big] \tag{3.76}$$

$$A_{S1}(\eta) = 0 \tag{3.77}$$

$$\begin{aligned} b_1(\eta) = {} & \big[-\frac{a(\xi,\eta)}{\Delta\xi^2} + J^2(\xi,\eta)\frac{P(\xi,\eta)}{2\Delta\xi}\big]x(\xi-\Delta\xi,\eta)+ \\ & \big[-\frac{a(\xi,\eta)}{\Delta\xi^2} - J^2(\xi,\eta)\frac{P(\xi,\eta)}{2\Delta\xi}\big]x(\xi+\Delta\xi,\eta)+ \\ & \big[\frac{2b(\xi,\eta)}{4\Delta\xi\Delta\eta}\big](x(\xi+\Delta\xi,\eta+\Delta\eta)+x(\xi-\Delta\xi,\eta-\Delta\eta)- \\ & x(\xi+\Delta\xi,\eta-\Delta\eta)-x(\xi-\Delta\xi,\eta+\Delta\eta))- \\ & \big[\frac{c(\xi,\eta)}{\Delta\eta^2} - J^2(\xi,\eta)\frac{Q(\xi,\eta)}{2\Delta\eta}\big]x(\xi,\eta-\Delta\eta) \end{aligned} \tag{3.78}$$

and for $j = j_{Max} - 1$ the coefficients will be:

$$A_{N1}(\eta) = 0 \tag{3.79}$$

$$A_{P1}(\eta) = \big[-\frac{2a(\xi,\eta)}{\Delta\xi^2} - \frac{2c(\xi,\eta)}{\Delta\eta^2}\big] \tag{3.80}$$

$$A_{S1}(\eta) = \big[\frac{c(\xi,\eta)}{\Delta\eta^2} - J^2(\xi,\eta)\frac{Q(\xi,\eta)}{2\Delta\eta}\big] \tag{3.81}$$

$$\begin{aligned} b_1(\eta) = {} & \big[-\frac{a(\xi,\eta)}{\Delta\xi^2} + J^2(\xi,\eta)\frac{P(\xi,\eta)}{2\Delta\xi}\big]x(\xi-\Delta\xi,\eta)+ \\ & \big[-\frac{a(\xi,\eta)}{\Delta\xi^2} - J^2(\xi,\eta)\frac{P(\xi,\eta)}{2\Delta\xi}\big]x(\xi+\Delta\xi,\eta)+ \\ & \big[\frac{2b(\xi,\eta)}{4\Delta\xi\Delta\eta}\big](x(\xi+\Delta\xi,\eta+\Delta\eta)+x(\xi-\Delta\xi,\eta-\Delta\eta)- \\ & x(\xi+\Delta\xi,\eta-\Delta\eta)-x(\xi-\Delta\xi,\eta+\Delta\eta))- \\ & \big[\frac{c(\xi,\eta)}{\Delta\eta^2} + J^2(\xi,\eta)\frac{Q(\xi,\eta)}{2\Delta\eta}\big]x(\xi,\eta+\Delta\eta) \end{aligned} \tag{3.82}$$

The equivalent coefficients for y equation are calculated as follows:

$$A_{S2}(\eta) = \big[\frac{c(\xi,\eta)}{\Delta\eta^2} - J^2(\xi,\eta)\frac{Q(\xi,\eta)}{2\Delta\eta}\big] \tag{3.83}$$

$$A_{P2}(\eta) = \big[-\frac{2a(\xi,\eta)}{\Delta\xi^2} - \frac{2c(\xi,\eta)}{\Delta\eta^2}\big] \tag{3.84}$$

$$A_{N2}(\eta) = \big[\frac{c(\xi,\eta)}{\Delta\eta^2} + J^2(\xi,\eta)\frac{Q(\xi,\eta)}{2\Delta\eta}\big] \tag{3.85}$$

$$
\begin{aligned}
b_2(\eta) = \big[-\frac{a(\xi,\eta)}{\Delta\xi^2} + J^2(\xi,\eta)\frac{P(\xi,\eta)}{2\Delta\xi}\big] y(\xi-\Delta\xi,\eta) + \\
\big[-\frac{a(\xi,\eta)}{\Delta\xi^2} - J^2(\xi,\eta)\frac{P(\xi,\eta)}{2\Delta\xi}\big] y(\xi+\Delta\xi,\eta) + \\
\big[\frac{2b(\xi,\eta)}{4\Delta\xi\Delta\eta}\big] (y(\xi+\Delta\xi,\eta+\Delta\eta) + y(\xi-\Delta\xi,\eta-\Delta\eta) - \\
y(\xi+\Delta\xi,\eta-\Delta\eta) - y(\xi-\Delta\xi,\eta+\Delta\eta))
\end{aligned}
\tag{3.86}
$$

which for $j = 2$ these coefficients are as:

$$A_{S2}(\eta) = 0 \tag{3.87}$$

$$A_{P2}(\eta) = \big[-\frac{2a(\xi,\eta)}{\Delta\xi^2} - \frac{2c(\xi,\eta)}{\Delta\eta^2}\big] \tag{3.88}$$

$$A_{N2}(\eta) = \big[\frac{c(\xi,\eta)}{\Delta\eta^2} + J^2(\xi,\eta)\frac{Q(\xi,\eta)}{2\Delta\eta}\big] \tag{3.89}$$

$$
\begin{aligned}
b_2(\eta) = \big[-\frac{a(\xi,\eta)}{\Delta\xi^2} + J^2(\xi,\eta)\frac{P(\xi,\eta)}{2\Delta\xi}\big] y(\xi-\Delta\xi,\eta) + \\
\big[-\frac{a(\xi,\eta)}{\Delta\xi^2} - J^2(\xi,\eta)\frac{P(\xi,\eta)}{2\Delta\xi}\big] y(\xi+\Delta\xi,\eta) + \\
\big[\frac{2b(\xi,\eta)}{4\Delta\xi\Delta\eta}\big] (y(\xi+\Delta\xi,\eta+\Delta\eta) + y(\xi-\Delta\xi,\eta-\Delta\eta) - \\
y(\xi+\Delta\xi,\eta-\Delta\eta) - y(\xi-\Delta\xi,\eta+\Delta\eta)) - \\
\big[\frac{c(\xi,\eta)}{\Delta\eta^2} - J^2(\xi,\eta)\frac{Q(\xi,\eta)}{2\Delta\eta}\big] y(\xi,\eta-\Delta\eta)
\end{aligned}
\tag{3.90}
$$

and for $j = j_{Max} - 1$ the coefficients will be:

$$A_{S2}(\eta) = \big[\frac{c(\xi,\eta)}{\Delta\eta^2} - J^2(\xi,\eta)\frac{Q(\xi,\eta)}{2\Delta\eta}\big] \tag{3.91}$$

$$A_{P2}(\eta) = \big[-\frac{2a(\xi,\eta)}{\Delta\xi^2} - \frac{2c(\xi,\eta)}{\Delta\eta^2}\big] \tag{3.92}$$

$$A_{N2}(\eta) = 0 \tag{3.93}$$

$$
\begin{aligned}
b_2(\eta) = \big[-\frac{a(\xi,\eta)}{\Delta\xi^2} + J^2(\xi,\eta)\frac{P(\xi,\eta)}{2\Delta\xi}\big] y(\xi-\Delta\xi,\eta) + \\
\big[-\frac{a(\xi,\eta)}{\Delta\xi^2} - J^2(\xi,\eta)\frac{P(\xi,\eta)}{2\Delta\xi}\big] y(\xi+\Delta\xi,\eta) + \\
\big[\frac{2b(\xi,\eta)}{4\Delta\xi\Delta\eta}\big] (y(\xi+\Delta\xi,\eta+\Delta\eta) + y(\xi-\Delta\xi,\eta-\Delta\eta) - \\
y(\xi+\Delta\xi,\eta-\Delta\eta) - y(\xi-\Delta\xi,\eta+\Delta\eta)) - \\
\big[\frac{c(\xi,\eta)}{\Delta\eta^2} + J^2(\xi,\eta)\frac{Q(\xi,\eta)}{2\Delta\eta}\big] y(\xi,\eta+\Delta\eta)
\end{aligned}
\tag{3.94}
$$

Thomas Algorithm (TDMA) is utilized to calculate the resulted matrix. In order to guarantee the stability, all of the coefficients of A_N, A_P, A_S and b may be multiplied

by -1. The magnitude of 0.04 can be applied as relaxation factors for both x and y directions. It must be mentioned here that all first and second order derivative for calculations of the inner region are central based differences.

3.4 Algorithm of Iterative Solution for Grid Generation

The following algorithm is used in the computer program for the calculating x and y values:

1. Construction of initial grid between outer boundary (i.e. perimeter of circle radius of R=2) and inner boundary (i.e. surface of a NACA airfoil) via the "Transfinite Interpolation" algebraic method.

2. Updating x and y values on "Branch Cuts".

3. Satisfying "Smoothness" and "Orthogonality" on the inner boundary (body) via controlling terms (i.e. $P(\xi, \eta)$ and $Q(\xi, \eta)$).

4. Forming coefficient matrix of x and y values in the inner region by applying "Line Successive Over Relaxation" (LSOR) in η direction, and computing the x and y values of inner grid points via "Thomas Algorithm" (i.e. Tri Diagonal Matrix Algorithm: TDMA, see appendix 2).

5. Checking convergence criteria for the residuals of x and y values, if the problem was not converged then repeat the entire iteration method procedure from the second step (i.e. "Updating x and y values on branch cuts"), otherwise the grid generation has been done.

6. To help and guarantee convergence the magnitude of dn=0.01 is been set before the beginning of the iteration-loop (i.e. updating x and y values on branch cuts), and just after satisfying the convergence criteria the magnitude of dn=dn-dn/2 has been reset and all these steps will be repeated until achieving to the desired magnitude of dn. The dn=0.005 for low Reynolds numbers and dn=0.00001 for high Reynolds numbers.

3.5 Results

In this section, the results of elliptic grid generation have been presented for different grid points.

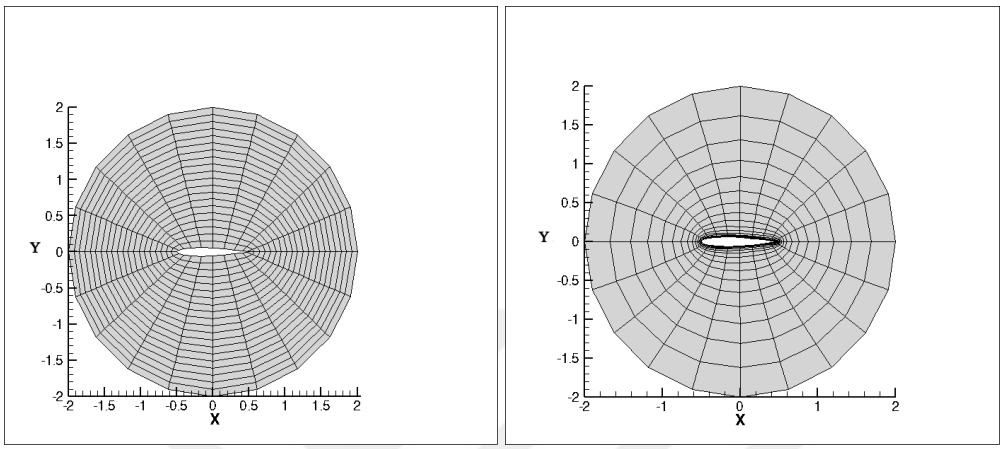

(a) (b)

Figure 3.3 : Initial algebraic transfinite (left hand side) and final elliptic grids (right hand side) for 21×21 grid points.

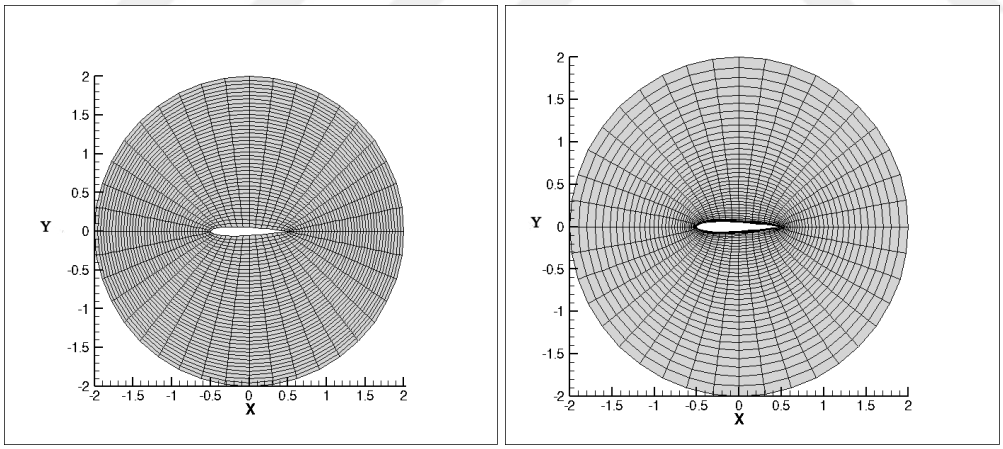

(a) (b)

Figure 3.4 : Initial algebraic transfinite (left hand side) and final elliptic grids (right hand side) for 41×41 grid points.

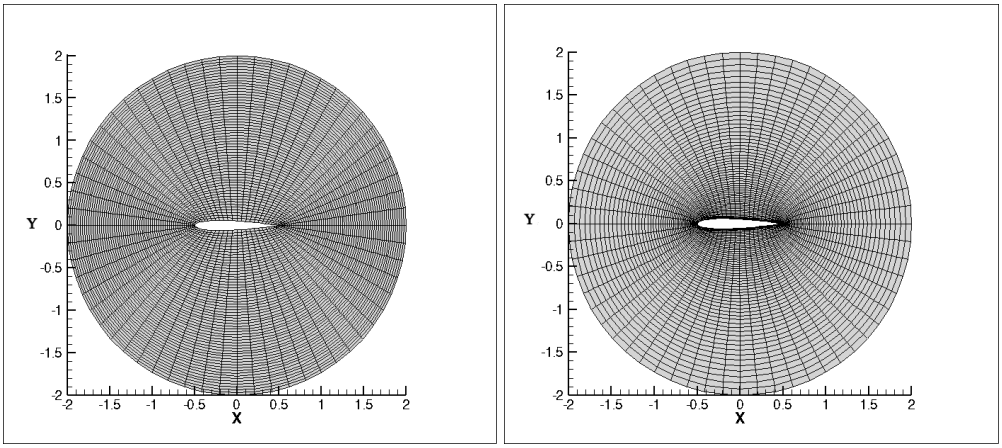

(a) (b)

Figure 3.5 : Initial algebraic transfinite (left hand side) and final elliptic grids (right hand side) for 61×61 grid points.

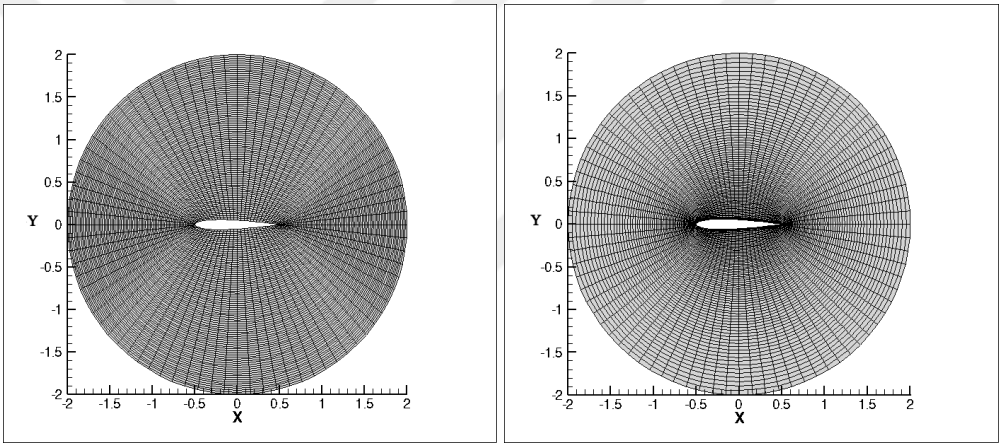

(a) (b)

Figure 3.6 : Initial algebraic transfinite (left hand side) and final elliptic grids (right hand side) for 81×81 grid points.

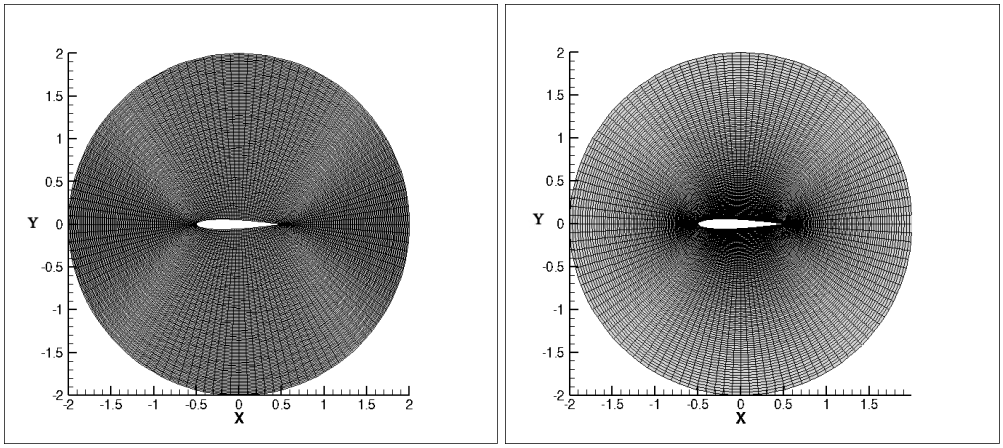

(a) (b)

Figure 3.7 : Initial algebraic transfinite (left hand side) and final elliptic grids (right hand side) for 121×121 grid points.

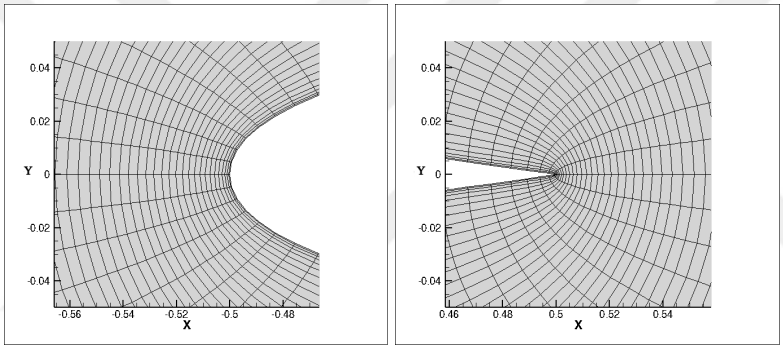

(a) (b)

Figure 3.8 : Leading edge (left hand side) and trailing edge (right hand side) for 121×121 grid points.

The leading edge and trailing edge of the elliptic grid have been shown in Figure 3.8 for 121×121 grid point. It shows that orthogonality and fine-spacing have been satisfied properly around an airfoil.

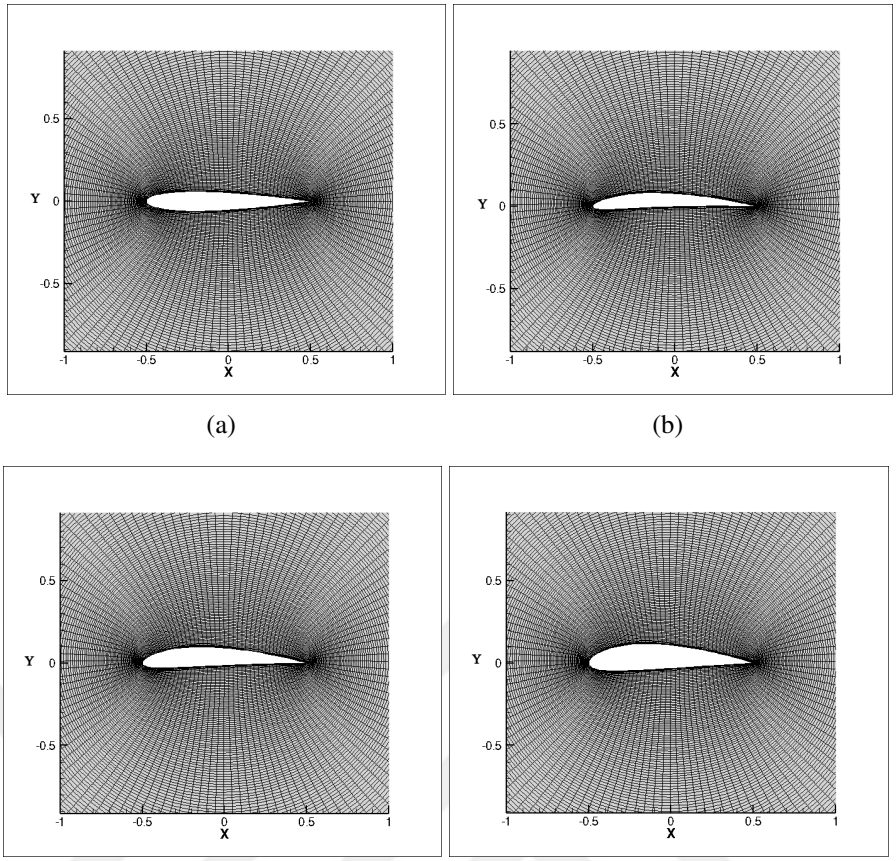

Figure 3.9 : O type elliptic grid for different NACA airfoils, NACA 0012 (up left hand side), NACA 4409 (up right hand side), NACA 4412 (down left hand side) and NACA 4416 (down right hand side) for 121 × 121 grid points.

Figure 3.9 shows that our generated O type elliptic grid is successfully practical and perfectly works for different types of NACA airfoil series.

4. AIRFLOW

Generally, the inviscid or viscous flow models may be implemented for the calculation of airflow values around the icing airfoil. In the next section, the inviscid flow model has been explained for airflow solver.

4.1 Potential Airflow Around Airfoil

The majority of two-dimensional aircraft-icing codes use the potential airflow solver (Gent et al., 2000; Lavoie, 2017). For the two-dimensional, steady-state, inviscid, incompressible, irrotational flow (potential flow) model two methods are applied in the literature, namely the panel method and stream-function method. Although both methods attempt to convert the surface of an airfoil to a streamline, the panel method does not need grid generation. Once, the values of the potential function (ϕ) are found on the body, the values for inner region can be calculated via extrapolation which may cause kind of inaccuracy. Despite the panel method in the stream function method, after the grid is generated, the Laplace equation of stream function (resulting from the combination of the continuity and momentum equations) is solved for each inner grid-point to find the values of the stream function (ψ) of airflow for the entire grid-points. Eventually, the velocity and pressure distributions have been calculated. Furthermore, in panel methods, the airfoil surface is divided into the straight line segments (panels), and calculations of the vortex panel strength and circulation quantities can lead to singularity issues. On the other hand, because the stream-function method does not consider the vortex panel strength and circulation it does not face the the singularity problems. Therefore, the panel method is numerically much more complex than the stream-function method and requires high programming effort (Mohebbi and Sellier, 2014).

4.1.1 Stream function equation

The main equation of stream function method in the physical domain is in the form of Laplace equation (Anderson Jr, 2010):

$$\psi_{xx} + \psi_{yy} = 0 \tag{4.1}$$

To simplify the calculations the stream equation will be transformed from physical domain (i.e. x, y coordinate) into computational domain (i.e. ξ, η coordinate).

The 4.1 equation can be restate as:

$$\frac{\partial(\frac{\partial\psi}{\partial x})}{\partial x} + \frac{\partial(\frac{\partial\psi}{\partial y})}{\partial y} = 0 \tag{4.2}$$

assuming that x and y are functions of ξ and η, the former equation can be as:

$$\frac{\partial\left[\frac{\partial\psi}{\partial\xi}\frac{\partial\xi}{\partial x} + \frac{\partial\psi}{\partial\eta}\frac{\partial\eta}{\partial x}\right]}{\partial x} + \frac{\partial\left[\frac{\partial\psi}{\partial\xi}\frac{\partial\xi}{\partial y} + \frac{\partial\psi}{\partial\eta}\frac{\partial\eta}{\partial y}\right]}{\partial y} = 0 \tag{4.3}$$

by extending partial derivatives with respect to x and y, we have:

$$\begin{aligned} &\frac{\partial^2\psi}{\partial\xi^2}(\frac{\partial\xi}{\partial x})^2 + \frac{\partial^2\psi}{\partial\xi\partial\eta}\frac{\partial\xi}{\partial x}\frac{\partial\eta}{\partial x} + \frac{\partial\psi}{\partial\xi}\frac{\partial^2\xi}{\partial x^2} + \\ &\frac{\partial^2\psi}{\partial\xi\partial\eta}\frac{\partial\eta}{\partial x}\frac{\partial\xi}{\partial x} + \frac{\partial^2\psi}{\partial\eta^2}(\frac{\partial\eta}{\partial x})^2 + \frac{\partial\psi}{\partial\eta}\frac{\partial^2\eta}{\partial x^2} + \\ &\frac{\partial^2\psi}{\partial\xi^2}(\frac{\partial\xi}{\partial y})^2 + \frac{\partial^2\psi}{\partial\xi\partial\eta}\frac{\partial\xi}{\partial y}\frac{\partial\eta}{\partial y} + \frac{\partial\psi}{\partial\xi}\frac{\partial^2\xi}{\partial y^2} + \\ &\frac{\partial^2\psi}{\partial\xi\partial\eta}\frac{\partial\eta}{\partial y}\frac{\partial\xi}{\partial y} + \frac{\partial^2\psi}{\partial\eta^2}(\frac{\partial\eta}{\partial y})^2 + \frac{\partial\psi}{\partial\eta}\frac{\partial^2\eta}{\partial y^2} = 0 \end{aligned} \tag{4.4}$$

by factorization this equation will be simplified as:

$$\begin{aligned} \left[(\frac{\partial\xi}{\partial x})^2 + (\frac{\partial\xi}{\partial y})^2\right]\frac{\partial^2\psi}{\partial\xi^2} + 2\left[\frac{\partial\xi}{\partial x}\frac{\partial\eta}{\partial x} + \frac{\partial\xi}{\partial y}\frac{\partial\eta}{\partial y}\right]\frac{\partial^2\psi}{\partial\xi\partial\eta} + \left[(\frac{\partial\eta}{\partial x})^2 + (\frac{\partial\eta}{\partial y})^2\right]\frac{\partial^2\psi}{\partial\eta^2} + \\ \left[\frac{\partial^2\xi}{\partial x^2} + \frac{\partial^2\xi}{\partial y^2}\right]\frac{\partial\psi}{\partial\xi} + \left[\frac{\partial^2\eta}{\partial x^2} + \frac{\partial^2\eta}{\partial y^2}\right]\frac{\partial\psi}{\partial\eta} = 0 \end{aligned} \tag{4.5}$$

using P, Q, ξ_x, ξ_y, η_x, η_y and J concepts by 3.1, 3.2, 3.11, 3.12, 3.13, 3.14 and 3.10 the stream equation can be written as:

$$\begin{aligned} \left[\frac{y_\eta^2}{J^2} + \frac{y_\eta^2}{J^2}\right]\frac{\partial^2\psi}{\partial\xi^2} - 2\left[\frac{y_\eta}{J}\frac{y_\xi}{J} + \frac{x_\eta}{J}\frac{x_\xi}{J}\right]\frac{\partial^2\psi}{\partial\xi\partial\eta} + \left[\frac{y_\xi^2}{J^2} + \frac{x_\xi^2}{J^2}\right]\frac{\partial^2\psi}{\partial\eta^2} + \\ P\frac{\partial\psi}{\partial\xi} + Q\frac{\partial\psi}{\partial\eta} = 0 \end{aligned} \tag{4.6}$$

remembering the definitions of a, b and c from 3.22, 3.23 and 3.24 this equation will be restated as:

$$a\frac{\partial^2\psi}{\partial\xi^2} - 2b\frac{\partial^2\psi}{\partial\xi\partial\eta} + c\frac{\partial^2\psi}{\partial\eta^2} = -J^2\left(P\frac{\partial\psi}{\partial\xi} + Q\frac{\partial\psi}{\partial\eta}\right) \tag{4.7}$$

Finally, the stream function equation transformed into the computational domain is (Mohebbi and Sellier, 2014):

$$a\psi_{\xi\xi} - 2b\psi_{\xi\eta} + c\psi_{\eta\eta} = -J^2(P\psi_\xi + Q\psi_\eta) \tag{4.8}$$

The coefficients of a, b, c, J, P and Q are the same as what were defined for the elliptic grid generation (see chapter 3).

4.1.2 Applying of computational method

The main idea is to transform of the problem from physical domain into computational domain to simply the solution of the problem.

$\xi_{Min} = 0$, $\xi_{Max} = 1$, $\eta_{Min} = 0$ and $\eta_{Max} = 1$.

4.1.2.1 Outer boundary condition for farfield ($j = j_{Max}$ or $\eta = 1$)

If the outer boundary is far enough from the airfoil, the velocity on the outer boundary equals the free stream velocity, and consequently, the x and y components of velocity are just equal to the x and y components of the uniform free stream velocity ($U_{\infty x}$, $U_{\infty y}$). Then referring to the definition of stream function, it is known that:

$$U_x(\xi,1) = \frac{\partial\psi(\xi,1)}{\partial y} = U_\infty cos(AOA) \tag{4.9}$$

$$U_y(\xi,1) = -\frac{\partial\psi(\xi,1)}{\partial x} = U_\infty sin(AOA) \tag{4.10}$$

by integration of stream function with respect to x and y, stream function at outer boundary is derived:

$$\psi(\xi,1) = U_\infty\left[y(\xi,1).cos(AOA) - x(\xi,1).sin(AOA)\right] \tag{4.11}$$

4.1.2.2 Kutta condition and inner boundary condition on airfoil ($j = 1$ or $\eta = 0$)

The Kutta condition states that the flow leaves the sharp trailing edge of an airfoil smoothly (Mohebbi and Sellier, 2014). To apply the Kutta condition in our calculation, we need to consider two possible configurations of the trailing edge. The trailing edge can have a finite-angle or can be cusped (Figure 4.1).

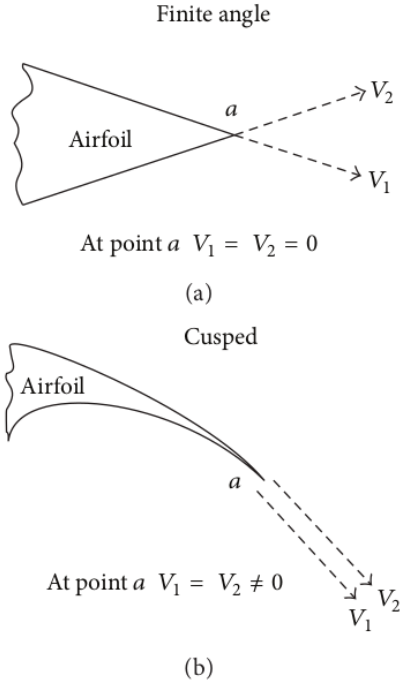

Figure 4.1 : Different possible shapes of the trailing edge and their relation to the Kutta condition (Mohebbi and Sellier, 2014).

Suppose that the velocities along the top surface and bottom surface are $U_1(0,0)$ and $U_2(1,0)$, respectively. For a finite-angle trailing edge, having two finite velocities in two different directions at the same point is physically impossible (Figure 4.1 (a)) and, therefore, the only possibility is that both velocities should be zero ($U_1(0,0) = U_2(1,0) = 0$). For the cusped trailing edge (Figure 4.1 (b)), having two velocities in the same directions at point a shows that both $U_1(0,0)$ and $U_2(1,0)$ can be finite. However, the pressure at point a is unique and the Bernoulli equation states that:

$$P_a + \frac{\rho U_1^2(0,0)}{2} = P_a + \frac{\rho U_2^2(1,0)}{2} \tag{4.12}$$

or

$$U_1(0,0) = U_2(1,0) \tag{4.13}$$

To obtain relationships for the Kutta condition in terms of stream function ψ, consider the finite-angle trailing edge in the O-type grid scheme shown in Figure 4.2.

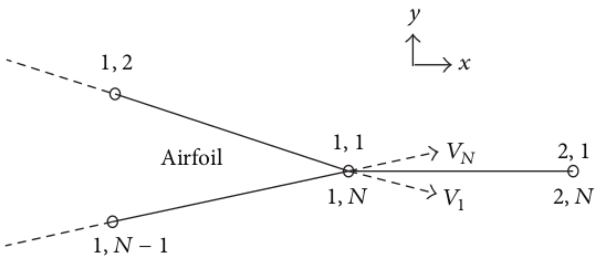

Figure 4.2 : Finite angle trailing edge and the associated grid notation (Mohebbi and Sellier, 2014).

From equation 4.9, we have:

$$U_x = \psi_y \tag{4.14}$$

from the transformation relationship, (equation),

$$\psi_y = \frac{1}{J}\left[-x_\eta \psi_\xi + x_{xi}\psi_\eta\right]. \tag{4.15}$$

If $U_1(0,0)$ and $U_2(1,0)$ be the velocities of the first and last grid points on the airfoil, respectively, the Kutta condition $U_1(0,0) = U_2(1,0) = 0$ gives:

$$\begin{gathered} U_1(0,0) = U_2(1,0) = 0 \;\rightarrow\; U_{x,1}(0,0) = U_{x,2}(1,0) = 0 \\ \frac{1}{J}\left[-x_\eta \psi_\xi + x_\xi \psi_\eta\right]\Big|_{(0,0)} = \frac{1}{J}\left[-x_\eta \psi_\xi + x_\xi \psi_\eta\right]\Big|_{(1,0)} = 0 \\ consequently \\ -x_\eta \psi_\xi + x_\xi \psi_\eta\Big|_{(0,0)} = 0 \end{gathered} \tag{4.16}$$

By discretization of the above equation in computational domain, we get:

$$x_\eta \psi_\xi = x_\xi \psi_\eta$$

$$[x(\Delta\xi,0) - x(0,0)]\,[\psi(0,\Delta\eta) - \psi(0,0)] = [x(0,\Delta\eta) - x(0,0)]\,[\psi(\Delta\xi,0) - \psi(0,0)]$$

and consequently

$$\psi(0,0) = \frac{\psi(0,\Delta\eta)\,[x(\Delta\xi,0) - x(0,0)] - \psi(\Delta\xi,0)\,[x(0,\Delta\eta) - x(0,0)]}{x(\Delta\xi,0) - x(0,\Delta\eta)} \tag{4.17}$$

By considering the wall boundary condition ($\psi(0,0) = \psi(\Delta\xi,0)$, we can simplify this to get:

$$\psi(0,0) = \psi(0,\Delta\eta) \tag{4.18}$$

Since the grid points (0,0) and (1,0) are the same points in the physical domain, we have:

$$\psi(0,0) = \psi(1,0) = \psi(0,\Delta\eta) \tag{4.19}$$

Since in potential flow, the value of stream function (ψ) is constant on the airfoil surface due to wall boundary condition, from the combination of Kutta condition and boundary condition we have:

$$\psi(\xi,0) = \psi(0,\Delta\eta) \tag{4.20}$$

On the other hand, the derivation of an equation for the cusped trailing edge is more complicated. Consider the cusped trailing edge and the associated grid notation shown in 4.3.

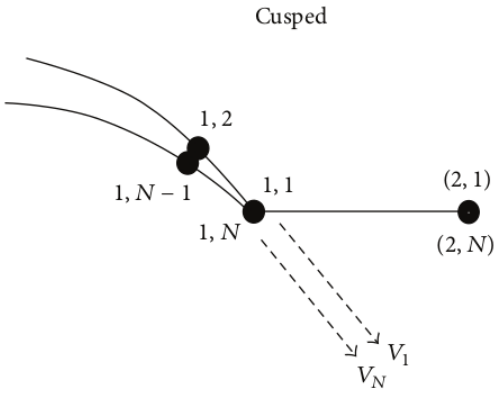

Figure 4.3 : Cusped trailing edge and the associated grid notation (Mohebbi and Sellier, 2014).

Since for the cusped trailing edge both vectors $U(1,1)$ and $U(i_{Max},1)$ are equal in the magnitude and direction, from the Kutta condition for the cusped trailing edge $(U(1,1)=U(i_{Max},1))$ we can write:

$$\begin{gathered} U(0,0)=U(1,0) \;\rightarrow\; U_x(0,0)=U_x(1,0) \\ \frac{1}{J}\left[-x_\eta\,\psi_\xi+x_\xi\,\psi_\eta\right]\Big|_{(0,0)}=\frac{1}{J}\left[-x_\eta\,\psi_\xi+x_\xi\,\psi_\eta\right]\Big|_{(1,0)} \end{gathered} \tag{4.21}$$

But

$$\begin{aligned} x_\xi\Big|_{(0,0)} &= x(0,\Delta\eta)-x(0,0) \\ x_\xi\Big|_{(1,0)} &= x(1,\Delta\eta)-x(1,0) \end{aligned} \tag{4.22}$$

Since $x(1,\Delta\eta)=x(0,\Delta\eta)$ and $x(1,0)=x(0,0)$ we have:

$$x_\xi\Big|_{(0,0)}=x_\xi\Big|_{(1,0)} \tag{4.23}$$

In similar approach, we have:

$$y_\xi\Big|_{(0,0)}=y_\xi\Big|_{(1,0)} \tag{4.24}$$

Furthermore, $\psi_\xi\Big|_{(0,0)}=\psi(0,\Delta\eta)-\psi(0,0)$ and $\psi_\xi\Big|_{(1,0)}=\psi(1,\Delta\eta)-\psi(1,0)$. Since $\psi(0,0)=\psi(1,0)$ and $\psi(0,\Delta\eta)=\psi(1,\Delta\eta)$ then:

$$\psi_\xi\Big|_{(0,0)}=\psi_\xi\Big|_{(1,0)} \tag{4.25}$$

Moreover, $\psi_\eta\Big|_{(0,0)}=\psi(\Delta\xi,0)-\psi(0,0)$ and $\psi_\eta\Big|_{(1,0)}=\psi(1,0)-\psi(1-\Delta\xi,0)$. Since $\psi(0,0)=\psi(\Delta\xi,0)=\psi(1-\Delta\xi,0)=\psi(1,0)$ i.e. wall boundary condition, we obtain:

$$\psi_\eta\Big|_{(0,0)}=\psi_\eta\Big|_{(1,0)}=0 \tag{4.26}$$

By substituting equations 4.23 through 4.26 into 4.21, we have:

$$\begin{gathered} \frac{1}{[x(0,\Delta\eta)-x(0,0)]\,[y(\Delta\xi,0)-y(0,0)]-[x(\Delta\xi,0)-x(0,0)]\,[y(0,\Delta\eta)-y(0,0)]} \\ \Big(-[x(\Delta\xi,0)-x(0,0)]\,[\psi(0,\Delta\eta)-\psi(0,0)]+0\Big)= \\ \frac{1}{[x(0,\Delta\eta)-x(0,0)]\,[y(1,0)-y(1-\Delta\xi,0)]-[x(1,0)-x(1-\Delta\xi,0)]\,[y(0,\Delta\eta)-y(0,0)]} \\ \Big(-[x(1,0)-x(1-\Delta\xi,0)]\,[\psi(0,\Delta\eta)-\psi(0,0)]+0\Big) \end{gathered} \tag{4.27}$$

By solving this equation for $\psi(0,0)$ using Maple software, we get:

$$\psi(0,0) = \psi(0,\Delta\eta) \tag{4.28}$$

Since the grid points (0,0) and (1,0) are the same points in the physical domain, we have:

$$\psi(0,0) = \psi(1,0) = \psi(0,\Delta\eta) \tag{4.29}$$

Again since in potential flow, the value of stream function (ψ) is constant on the airfoil surface due to wall boundary condition, from the combination of Kutta condition and boundary condition we have:

$$\psi(\xi,0) = \psi(0,\Delta\eta) \tag{4.30}$$

All in all, in 2-D potential flow, for both finite angle and cusped shape trailing edge to simultaneously satisfy Kutta condition (flow must leave an airfoil in a smooth pattern) and boundary condition (the surface of airfoil should convert to a streamline), there should be (Mohebbi and Sellier, 2014):

$$\psi(\xi,0) = \psi(0,\Delta\eta) \tag{4.31}$$

4.1.2.3 Updating ψ values on "branch cuts" (reentrants)

The ψ values on "Branch Cuts" will be updated at the beginning of each iteration as follows:

$$\psi(0,\eta) = \frac{\psi(\Delta\xi,\eta) + \psi(1-\Delta\xi,\eta)}{2} \tag{4.32}$$

$$\psi(1,\eta) = \frac{\psi(\Delta\xi,\eta) + \psi(1-\Delta\xi,\eta)}{2} \tag{4.33}$$

4.1.2.4 Calculations for inner region

Finally, the transferred stream function equation is discretized by Finite Difference Method (FDM) and rearranged by applying Line Successive Over Relaxation (LSOR) in η direction as:

$$A_{S3}(\eta)\psi(\xi,\eta-\Delta\eta) + A_{P3}(\eta)\psi(\xi,\eta) + A_{N3}(\eta)\psi(\xi,\eta+\Delta\eta) = b_3(\eta) \tag{4.34}$$

The $A_{S3}(\eta)$, $A_{P3}(\eta)$, $A_{N3}(\eta)$ and $b_3(\eta)$ coefficients are:

$$A_{S3}(\eta) = \big[\frac{c(\xi,\eta)}{\Delta\eta^2} - \frac{J^2(\xi,\eta)Q(\xi,\eta)}{2\Delta\eta}\big] \tag{4.35}$$

$$A_{P3}(\eta) = \big[-\frac{2a}{\Delta\xi^2} - \frac{2c(\xi,\eta)}{\Delta\eta^2}\big] \tag{4.36}$$

$$A_{N3}(\eta) = \big[\frac{c(\xi,\eta)}{\Delta\eta^2} + \frac{J^2(\xi,\eta)Q(\xi,\eta)}{2\Delta\eta}\big] \tag{4.37}$$

$$\begin{aligned} b_3(\eta) = \big[-\frac{a(\xi,\eta)}{\Delta\xi^2} + \frac{J^2(\xi,\eta)P(\xi,\eta)}{2\Delta\xi}\big]\psi(\xi-\Delta\xi,\eta)+ \\ \big[-\frac{a(\xi,\eta)}{\Delta\xi^2} - \frac{J^2(\xi,\eta)P(\xi,\eta)}{2\Delta\xi}\big]\psi(\xi+\Delta\xi,\eta)+ \\ \big[\frac{2b(\xi,\eta)}{4\Delta\xi\Delta\eta}\big](\psi(\xi+\Delta\xi,\eta+\Delta\eta)+\psi(\xi-\Delta\xi,\eta-\Delta\eta)- \\ \psi(\xi+\Delta\xi,\eta-\Delta\eta)-\psi(\xi-\Delta\xi,\eta+\Delta\eta)) \end{aligned} \tag{4.38}$$

which for $j = 2$ these coefficients are as:

$$A_{S3}(\eta) = 0 \tag{4.39}$$

$$A_{P3}(\eta) = \big[-\frac{2a}{\Delta\xi^2} - \frac{2c(\xi,\eta)}{\Delta\eta^2}\big] \tag{4.40}$$

$$A_{N3}(\eta) = \big[\frac{c(\xi,\eta)}{\Delta\eta^2} + \frac{J^2(\xi,\eta)Q(\xi,\eta)}{2\Delta\eta}\big] \tag{4.41}$$

$$\begin{aligned} b_3(\eta) = \big[-\frac{a(\xi,\eta)}{\Delta\xi^2} + \frac{J^2(\xi,\eta)P(\xi,\eta)}{2\Delta\xi}\big]\psi(\xi-\Delta\xi,\eta)+ \\ \big[-\frac{a(\xi,\eta)}{\Delta\xi^2} - \frac{J^2(\xi,\eta)P(\xi,\eta)}{2\Delta\xi}\big]\psi(\xi+\Delta\xi,\eta)+ \\ \big[\frac{2b(\xi,\eta)}{4\Delta\xi\Delta\eta}\big](\psi(\xi+\Delta\xi,\eta+\Delta\eta)+\psi(\xi-\Delta\xi,\eta-\Delta\eta)- \\ \psi(\xi+\Delta\xi,\eta-\Delta\eta)-\psi(\xi-\Delta\xi,\eta+\Delta\eta))- \\ \big[\frac{c(\xi,\eta)}{\Delta\eta^2} - \frac{J^2(\xi,\eta)Q(\xi,\eta)}{2\Delta\eta}\big]\psi(\xi,\eta-\Delta\eta) \end{aligned} \tag{4.42}$$

and for $j = j_{Max} - 1$ the coefficients will be:

$$A_{S3}(\eta) = \big[\frac{c(\xi,\eta)}{\Delta\eta^2} - \frac{J^2(\xi,\eta)Q(\xi,\eta)}{2\Delta\eta}\big] \tag{4.43}$$

$$A_{P3}(\eta) = \big[-\frac{2a}{\Delta\xi^2} - \frac{2c(\xi,\eta)}{\Delta\eta^2}\big] \tag{4.44}$$

$$A_{N3}(\eta) = 0 \tag{4.45}$$

$$
\begin{aligned}
b_3(\eta) = \big[-\frac{a(\xi,\eta)}{\Delta\xi^2} + \frac{J^2(\xi,\eta)P(\xi,\eta)}{2\Delta\xi} \big] \psi(\xi-\Delta\xi,\eta) + \\
\big[-\frac{a(\xi,\eta)}{\Delta\xi^2} - \frac{J^2(\xi,\eta)P(\xi,\eta)}{2\Delta\xi} \big] \psi(\xi+\Delta\xi,\eta) + \\
\big[\frac{2b(\xi,\eta)}{4\Delta\xi\Delta\eta} \big] (\psi(\xi+\Delta\xi,\eta+\Delta\eta) + \psi(\xi-\Delta\xi,\eta-\Delta\eta) - \\
\psi(\xi+\Delta\xi,\eta-\Delta\eta) - \psi(\xi-\Delta\xi,\eta+\Delta\eta)) - \\
\big[\frac{c(\xi,\eta)}{\Delta\eta^2} + \frac{J^2(\xi,\eta)Q(\xi,\eta)}{2\Delta\eta} \big] \psi(\xi,\eta+\Delta\eta)
\end{aligned}
\tag{4.46}
$$

The values of stream function will be calculated for the inner region by utilizing Thomas Algorithm (TDMA) (Sebben and Baliga, 1995), (see appendix 2 for TDMA explanation).

4.1.3 Algorithm of iterative solution for air solver

The following algorithm is used in the computer program for the calculating ψ values:

1. At the outer boundary, the values of airflow are set equal to the values of free-stream flow.
2. On the airfoil, the Mohebbi's boundary condition (Mohebbi and Sellier, 2014) is applied.
3. The V_ξ, V_η and $\bar{\rho}$ values are updated on the branch cuts.
4. The coefficient matrix of ψ values is formed in the inner region by applying "Line Successive Over Relaxation" (LSOR) in η direction, and these values are computed via Tri Diagonal Matrix Algorithm: TDMA, see appendix 2).
5. The convergence criteria are checked for the residuals of values, if the problem was not converged then the entire iteration method procedure is repeated from the second step (i.e. "the boundary condition on the body").

4.1.4 Calculation of velocity and pressure distributions

To know velocity and pressure distributions in all of the grid points, the values of stream function which have been found during previous section are utilized to calculate the derivatives of ψ_ξ and ψ_η at those points:

$$U_x = +\frac{\partial \psi}{\partial y} \tag{4.47}$$

$$U_y = -\frac{\partial \psi}{\partial x} \tag{4.48}$$

In general, the derivatives of stream function with respect to ξ and η are obtain via the chain rule in calculus and the coordinate transforming relationships:

$$\begin{aligned} \frac{\partial \psi}{\partial x} &= \frac{\partial \psi}{\partial \xi}\frac{\partial \xi}{\partial x} + \frac{\partial \psi}{\partial \eta}\frac{\partial \eta}{\partial x} = \frac{\partial \psi}{\partial \xi}\xi_x + \frac{\partial \psi}{\partial \eta}\eta_x \\ \frac{\partial \psi}{\partial y} &= \frac{\partial \psi}{\partial \xi}\frac{\partial \xi}{\partial y} + \frac{\partial \psi}{\partial \eta}\frac{\partial \eta}{\partial y} = \frac{\partial \psi}{\partial \xi}\xi_y + \frac{\partial \psi}{\partial \eta}\eta_y \end{aligned} \tag{4.49}$$

which,

$$\begin{aligned} \frac{\partial \psi}{\partial \xi} &= \frac{\partial \psi}{\partial x}\frac{\partial x}{\partial \xi} + \frac{\partial \psi}{\partial y}\frac{\partial y}{\partial \xi} = \frac{\partial \psi}{\partial x}x_\xi + \frac{\partial \psi}{\partial y}y_\xi \\ \frac{\partial \psi}{\partial \eta} &= \frac{\partial \psi}{\partial x}\frac{\partial x}{\partial \eta} + \frac{\partial \psi}{\partial y}\frac{\partial y}{\partial \eta} = \frac{\partial \psi}{\partial x}x_\eta + \frac{\partial \psi}{\partial y}y_\eta \end{aligned} \tag{4.50}$$

and, the coordinate transforming relationships are:

$$y_\eta = +J\xi_x \tag{4.51}$$

$$x_\eta = -J\xi_y \tag{4.52}$$

$$y_\xi = -J\eta_x \tag{4.53}$$

and

$$x_\xi = +J\eta_y \tag{4.54}$$

In details, the derivatives of stream function with respect to ξ and η are:

derivatives on the outer boundary ($j = j_{Max}$ *or* $\eta = 1$):

$$\psi_\xi(0,1) = \frac{1}{2\Delta\xi}[-3\psi(0,1) + 4\psi(\Delta\xi,1) - \psi(2\Delta\xi,1)] \tag{4.55}$$

$$\psi_\xi(1,1) = \frac{1}{2\Delta\xi}[+3\psi(1,1) - 4\psi(1-\Delta\xi,1) + \psi(1-2\Delta\xi,1)] \tag{4.56}$$

$$\psi_\xi(\xi,1) = \frac{1}{2\Delta\xi}[\psi(\xi+\Delta\xi,1) - \psi(\xi-\Delta\xi,1)] \tag{4.57}$$

$$\psi_\eta(\xi,1) = \frac{1}{2\Delta\eta}[+3\psi(\xi,1) - 4\psi(\xi,1-\Delta\eta) + \psi(\xi,1-2\Delta\eta)] \tag{4.58}$$

derivatives on the inner boundary ($j = 1$ *or* $\eta = 0$):

$$\psi_\xi(\xi,0) = 0 \tag{4.59}$$

$$\psi_\eta(\xi,0) = \frac{1}{2\Delta\eta}[-3\psi(\xi,0) + 4\psi(\xi,+\Delta\eta) - \psi(\xi,+2\Delta\eta)] \tag{4.60}$$

derivatives on the branch cuts ($i = 1, i_{Max}$ *or* $\xi = 0,1$):

$$\psi_\xi(0,\eta) = \frac{1}{2\Delta\xi}[-3\psi(0,\eta) + 4\psi(\Delta\xi,\eta) - \psi(2\Delta\xi,\eta)] \tag{4.61}$$

$$\psi_\xi(1,\eta) = \frac{1}{2\Delta\xi}[+3\psi(1,\eta) - 4\psi(1-\Delta\xi,\eta) + \psi(1-2\Delta\xi,\eta)] \tag{4.62}$$

$$\psi_\eta(0,\eta) = \frac{1}{2\Delta\eta}[\psi(0,\eta+\Delta\eta) - \psi(0,\eta-\Delta\eta)] \tag{4.63}$$

$$\psi_\eta(1,\eta) = \frac{1}{2\Delta\eta}[\psi(1,\eta+\Delta\eta) - \psi(1,\eta-\Delta\eta)] \tag{4.64}$$

and, derivatives in the inner region are:

$$\psi_\xi(\xi,\eta) = \frac{1}{2\Delta\xi}[\psi(\xi+\Delta\xi,\eta) - \psi(\xi-\Delta\xi,\eta)] \tag{4.65}$$

$$\psi_\eta(\xi,\eta) = \frac{1}{2\Delta\eta}[\psi(\xi,\eta+\Delta\eta) - \psi(\xi,\eta-\Delta\eta)] \tag{4.66}$$

besides, by using coordinate transforming relashionships (i.e. equations of 4.51 , 4.52 , 4.53 and 4.54, the velocity components of U_x and U_y in x,y coordinate will be calculated as:

$$U_x(x,y) = \frac{-[x_\eta(\xi,\eta)][\psi_\xi(\xi,\eta)] + [x_\xi(\xi,\eta)][\psi_\eta(\xi,\eta)]}{J(\xi,\eta)} \tag{4.67}$$

$$U_y(x,y) = \frac{-[y_\eta(\xi,\eta)][\psi_\xi(\xi,\eta)] + [y_\xi(\xi,\eta)][\psi_\eta(\xi,\eta)]}{J(\xi,\eta)} \tag{4.68}$$

consequently, the velocity distribution is:

$$U(x,y) = \sqrt{[U_x(x,y)]^2 + [U_y(x,y)]^2} \tag{4.69}$$

and the pressure distribution will be obtained from the Bernoulli's principle for the inviscid flow as:

$$P(x,y) = P_\infty + \frac{\rho_a[U(x,y)]^2}{2} \tag{4.70}$$

which pressure coefficient on the surface of airfoil is obtained:

$$C_p(s) = 1 - \left[\frac{U(x,y)\big|_{On\ The\ Airfoil}}{U_\infty}\right]^2 \tag{4.71}$$

Because x value of the center of geometry has been already shifted to $\frac{chord}{2}$, then the C_p will plot with respect to $\frac{x}{chord} + 0.5$ which leads to values of horizontal axis vary from the 0 to 1.

4.1.5 Assumptions

Since there are lots of parameters that affect the icing phenomenon in aircraft, therefore to be able to do an engineering analysis on the topic, does require taking some considerations, constraints, and limitations into account. Thus, some assumptions are included in our study as follows:

1. The diameters of the water droplets are small enough to neglect the influence of the droplets on the airflow (i.e. one-way coupled flow), therefore the governing equations of the airflow are solved independently from water-droplet equations.

2. It is assumed that airflow is the two-dimensional, steady-state, inviscid, incompressible, irrotational flow (potential flow).

4.1.6 Validation

Result of C_p values has been validated for present study for NACA 0012 airfoil with respect to Anderson Jr (2010).

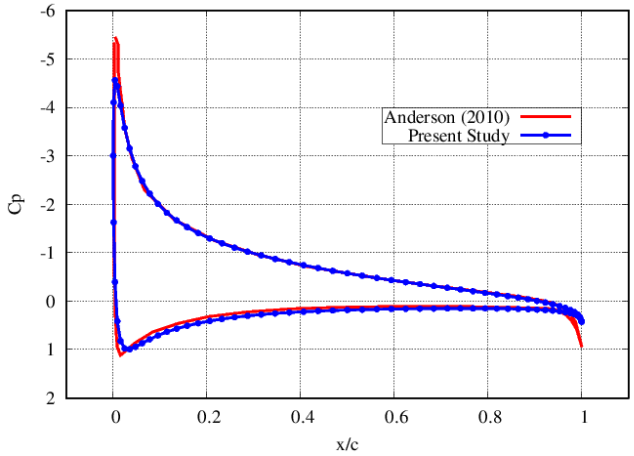

Figure 4.4 : Validation of C_p value of present study for 121×121 grid points with respect to Anderson Jr (2010), for chord=1.0 m, $U_\infty = 70\ m/s$, and $AOA = 9\ ^\circ$.

The mesh independence study shows that for the 121×121 grid size and $dn = 5\ mm$ (dn is the normal distance of the grid-loop just next to the body) results are in a good agreement with the literature (Figure 4.4).

4.1.7 Results

Results of stream lines and velocity vectors of the airflow have been shown in the following figures for different angle of attacks for present study.

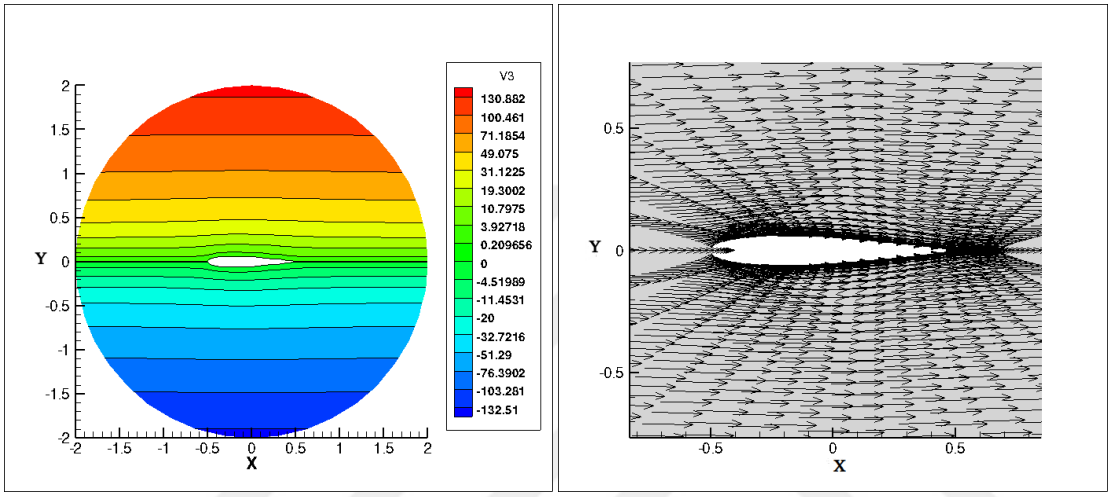

(a) (b)

Figure 4.5 : Stream lines (left hand side) and velocity vectors (right hand side) for 121×121 grid points, chord=1 m, $U_\infty = 70\ m/s$, and $AOA = 0\ ^\circ$.

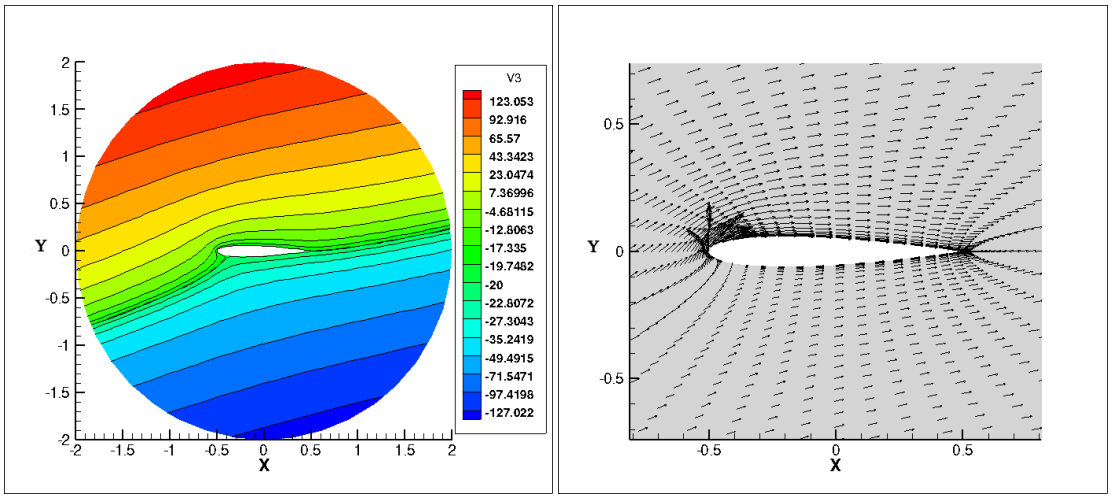

(a) (b)

Figure 4.6 : Stream lines (left hand side) and velocity vectors (right hand side) for 121×121 grid points, chord=1 m, $U_\infty = 70\ m/s$, and $AOA = 15\ ^\circ$.

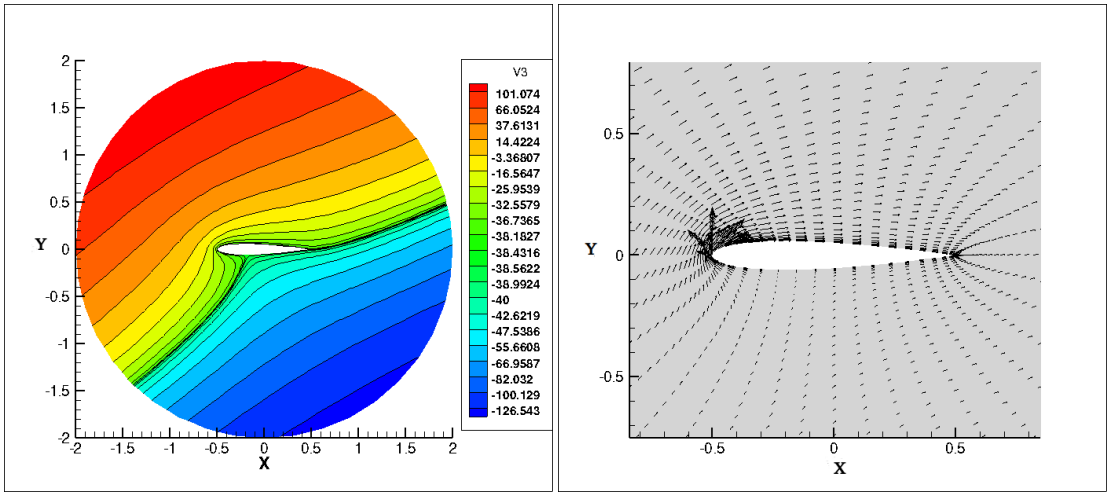

(a) (b)

Figure 4.7 : Stream lines (left hand side) and velocity vectors (right hand side) for 121×121 grid points, chord=1 m, $U_\infty = 70\ m/s$, and $AOA = 30\ ^\circ$.

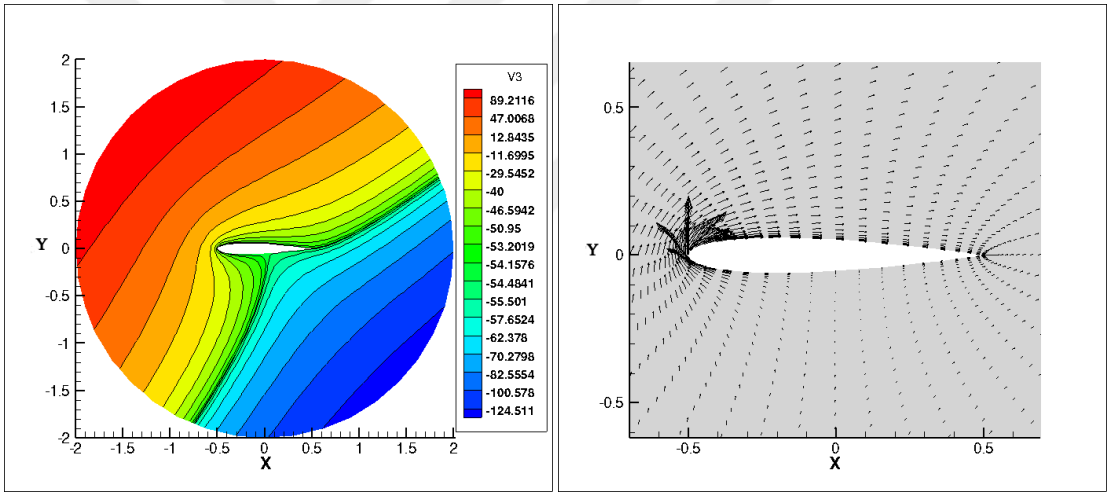

(a) (b)

Figure 4.8 : Stream lines (left hand side) and velocity vectors (right hand side) for 121×121 grid points, chord=1.0 m, $U_\infty = 70\ m/s$, and $AOA = 45\ ^\circ$.

Results show that in all cases the airflow wraps around the airfoil and smoothly leaves it.

Apart from what has been studied in this section so far, the proposed method can be easily developed in terms of the velocity potential ϕ instead of stream function ψ, and the velocity potential can be calculated over the domain, then the entire procedure can be also extended to the three-dimension cases (Mohebbi and Sellier, 2014).

5. CONVECTIVE HEAT TRANSFER COEFFICIENT

The convective heat transfer coefficient (h_{conv}) is one of the most important parameters used for the calculations of ice accretion in the simulation of aircraft icing. The temperature gradient at the body surface (wall) has a significant effect on the order of magnitude of the convective heat transfer coefficient. The temperature gradient itself is affected by the velocity gradient in the boundary layer. Therefore, in this section, we take a more detailed look at the momentum and energy equations in the momentum and thermal boundary layers.

Generally, there are two main approaches to evaluating the convective heat transfer coefficient which depend on the flow solver employed. When the potential flow solver (e.g. panel method or stream function method) is used, the viscous effects are not considered, hence, the approximate solution must be applied for the calculation of the convective heat transfer coefficient. However, when the boundary layer code or Navier-Stokes solver is utilized, it is possible to calculate the exact convective heat transfer coefficient by solving the energy equation (Lavoie, 2017).

5.1 Calculation of h_{conv} for Inviscid Airflow

It is often tried to look for approximate methods for complex and complicated flows. Among them, the integral equations of the boundary layer provide the proper approximation for lots of fluid problems (Kays, 2012; Schlichting and Gersten, 2016; Smith and Spalding, 1958; White and Corfield, 2006).

5.1.1 Concepts of momentum and thermal boundary layer thicknesses, and friction (c_f) and convective heat transfer (h_{conv}) coefficients

Integral Boundary Layer (IBL) equations should be solved to calculate a convective heat transfer rate (Q_{conv}). The IBL method should not be confused with the Interactive Boundary Layer method (Cebeci and Cousteix, 2005) which is in common use in combination with potential flow solvers. A description of the integral boundary layer

method is given by Fortin et al. (2006); Özgen and Canıbek (2009) and many others. Meanwhile, the velocities at the outer edge of boundary layer (U_e) are needed in advance for the calculation of convective heat transfer coefficient (h_{conv}). The airflow values which are calculated by the airflow solver module in the previous steps are not coupled with the IBL method to predict the exact boundary layer extent. There are two main approaches to evaluating the flow field values. When using a potential flow solver (e.g. panel method or stream function), the viscous effects are not considered and hence one must approximate the boundary layer characteristics. On the other hand, when using a boundary layer code or a Navier-Stokes solver, it is possible to compute the exact values (Lavoie, 2017).

Some of the most important articles which deal with the convective heat transfer coefficient on the body surface are the studies done by Bu et al. (2013); Cao et al. (2012); da Silva and de Mattos; Fortin et al. (2006); Özgen and Canıbek (2009); Sun et al. (2012), meanwhile the article by Gent et al. (2000) is the most comprehensive one.

In the following parts, first, the momentum integral equation of the boundary layer is developed to obtain the alternative forms of the momentum equation which reveal friction coefficient (c_f) and roughness Reynolds number (Re_k) utilizing displacement thickness (δ_1) and momentum thickness (δ_2) concepts. Then, the energy integral equation is used for deriving the alternating forms of the energy equation which explain local Stanton number (St) and convective heat transfer coefficient (h_{conv}) using the concepts of enthalpy thickness (Δ_2) and energy thickness (Δ_4).

Most of the icing studies use the Smith and Spalding (1958) approach in laminar flow, and the Kays (2012) approach in turbulent flow for the calculations of Integral Boundary Layer (IBL) equations.

5.1.1.1 Momentum boundary layer

In fluid dynamics, a boundary layer is a layer of fluid near a bounding surface where the effects of viscosity are significant. The concept of a boundary layer was first introduced by Ludwig Prandtl in a paper presented on August 12, 1904, at the third International Congress of Mathematicians in Heidelberg, Germany. Prandtl in his famous article says that: "A very satisfactory explanation of the physical process in the boundary

layer between a fluid and a solid body can be obtained by the hypothesis of adhesion of the fluid to the walls, that is, by the hypothesis of a zero relative velocity between fluid and wall. If the viscosity was very small and the fluid path along the wall was not too long, the fluid velocity ought to resume its normal value at a very short distance from the wall. In the thin transition layer, however, the sharp changes of velocity, even with a small coefficient of friction, produce marked results." It simplifies the equations of fluid flow by dividing the flow field into two areas: one inside the boundary layer, dominated by viscosity and creating the majority of drag experienced by this thin region which is called a boundary layer; and one outside the boundary layer, where viscosity can be neglected without significant effects on the solution and this region is called a shear layer. More practically speaking, the viscous boundary layer thickness (δ) is similarly the distance from the body at which the velocity of the flow is 99 % of the free-stream velocity.

There are also two other thickness concepts namely displacement and momentum thicknesses which play a very important role in the analyses of the viscous boundary layer (Anderson Jr, 2010).

The displacement thickness (δ_1) has two physical interpretations: the First one says the (δ_1) is the "missing mass flow" due to the presence of the viscous boundary layer. The second interpretation of (δ_1) gives rise to the concept of an effective body, then, the displacement thickness essentially modifies the shape of a body immersed in a fluid to allow a pure inviscid solution (Anderson Jr, 2010). Therefore, the displacement thickness will be:

$$\delta_1 = \int_0^{\delta} \Big[1 - \frac{\rho_b(y) U_b(y)}{\rho_e U_e}\Big] dy \tag{5.1}$$

which $\rho_b(y)$ and $U_b(y)$ are the density and x-velocity component of the fluid inside the viscous boundary layer, furthermore, ρ_e is the density of the fluid outside and just next to the viscous boundary layer and U_e equals the x component of the air velocity (U_x) outside the boundary layer which has been discussed and calculated in the previous chapters.

The momentum thickness (δ_2) is the index of "missing momentum" due to the presence of the viscous boundary layer or is the distance by which a surface has to

be moved from the reference plane in an inviscid fluid stream of velocity U_e to give the same total momentum as exists between the surface and the reference plane in a real fluid. The momentum thickness is defined as:

$$\delta_2 = \int_0^{\delta} \frac{\rho_b(y)U_b(y)}{\rho_e U_e}\Big[1 - \frac{U_b(y)}{U_e}\Big]dy \tag{5.2}$$

Evidently the momentum integral equation can be expressed in terms of the boundary-layer thickness parameters. After rearranging and simplifying, that will be (Kays, 2012):

$$\frac{\tau_0}{\rho_e U_e^2} + \frac{\rho_0 U_0}{\rho_e U_e} = \frac{d\delta_2}{dx} + \delta_2\Big[\big(2 + \frac{\delta_1}{\delta_2}\big)\frac{1}{U_e}\frac{dU_e}{dx} + \frac{1}{\rho_e}\frac{d\rho_e}{dx} + \frac{1}{R}\frac{dR}{dx}\Big] \tag{5.3}$$

Equation 5.3 is simply an ordinary differential equation for δ_2 as a function of x. This equation forms the basis for many approximate boundary-layer solutions.

The various particularization of equation 5.3 can be obtained by neglecting some terms. For example, for constant-density flow along a two-dimensional surface $R \to \infty$ with no suction or blowing $V_0 = 0$, we obtain the simpler form:

$$\frac{\tau_0}{\rho_e . U_e^2} = \frac{d\delta_2}{dx} + \delta_2\big(2 + \frac{\delta_1}{\delta_2}\big)\frac{1}{U_e}\frac{dU_e}{dx} \tag{5.4}$$

A still more restricted form results if there is no pressure gradient, so that U_e is a constant:

$$\frac{\tau_0}{\rho_e . U_e^2} = \frac{d\delta_2}{dx} \tag{5.5}$$

considering the definition of the local friction coefficient:

$$c_f = \frac{\tau_0}{\frac{1}{2}\rho_e U_e^2} \tag{5.6}$$

Substituting in equation 5.5, eventually the integral momentum equation will be:

$$\frac{c_f}{2} = \frac{d\delta_2}{dx} \tag{5.7}$$

5.1.1.2 Thermal boundary layer

Defining a thickness of the thermal boundary layer is similar to that explained for the momentum boundary layer. The thermal boundary layer thickness is the distance from the body at which the temperature of the flow is 99 % of the free-stream temperature. Again, we can define the integral thickness parameters, and use concepts of the enthalpy and the energy thicknesses.

The enthalpy thickness is defined as:

$$\Delta_2 = \int_0^{\delta} \frac{\rho_b(y) U_b(y) e}{\rho_e U_e e_0} dy \tag{5.8}$$

For a low-velocity constant-property flow of a perfect gas with no chemical reaction, Δ_2 can be expressed in terms of temperature as follows:

$$e = c_p(T - T_\infty) \tag{5.9}$$

which e is enthalpy of the flow. Therefore, the enthalpy thickness can restate as:

$$\Delta_2 = \int_0^{\delta} \frac{U_b(y)}{U_e} \frac{(T - T_\infty)}{(T_0 - T_e} dy \tag{5.10}$$

A energy thickness Δ_4 can be defined as:

$$\Delta_4 = \frac{k(T_0 - T_e)}{\dot{q}_0''} \tag{5.11}$$

which $\dot{q}_0''$ is heat flux from the surface. T_0 is surface temperature and T_e is temperature of the external inviscid flow next to the boundary layer.

k is the thermal conductivity of the fluid.

From the definition of the convective heat transfer coefficient:

$$h = \frac{\dot{q}_0''}{(T_0 - T_e)} \tag{5.12}$$

the energy thickness will be:

$$\Delta_4 = \frac{k}{h} \tag{5.13}$$

Both k and h are conductive and convective properties of the fluid.

Making use of the definition of the enthalpy and energy thicknesses of the boundary layer, we will obtain the alternative forms of the energy integral equation as (Cebeci and Bradshaw, 2012; Kays, 2012):

$$\frac{\dot{q}_0''}{\rho_e U_e e_0} + \frac{\rho_0 U_0}{\rho_e U_e} = \frac{d\Delta_2}{dx} + \Delta_2 \Big[\frac{1}{U_e}\frac{dU_e}{dx} + \frac{1}{\rho_e}\frac{d\rho_e}{dx} + \frac{1}{R}\frac{dR}{dx} + \frac{1}{e_0}\frac{de_0}{dx} \Big] \tag{5.14}$$

with a more restricted form of the energy integral equation, for example, low-velocity gas flow, no chemical reaction, $U_0 = 0$, and constant fluid properties across the boundary layer, and using the definition of Δ_2 with some simplifications again we have:

$$\frac{\dot{q}_0''}{\rho_e U_e e_0 c_p (T_0 - T_e)} = \frac{d\Delta_2}{dx} + \Delta_2 \Big[\frac{1}{U_e}\frac{dU_e}{dx} + \frac{1}{\rho_e}\frac{d\rho_e}{dx} + \frac{1}{R}\frac{dR}{dx} + \frac{1}{(T_0 - T_e)}\frac{d(T_0 - T_e)}{dx} \Big] \tag{5.15}$$

Let's now pay attention to what form the energy integral equation reduces for the simplest conceivable boundary-layer problem. Consider flow over a flat plate, $R \to \infty$, with constant pressure and free-stream velocity $\frac{dU_e}{dx} = 0$, constant properties $\frac{d\rho_e}{dx} = 0$, and constant fluid to surface temperature difference $\frac{d(T_0 - T_e)}{dx} = 0$. Equation 5.15 then becomes:

$$\frac{\dot{q}_0''}{\rho_e U_e c_p (T_0 - T_e)} = \frac{d\Delta_2}{dx} \tag{5.16}$$

knowing the definition of the local convective heat transfer coefficient 5.12 then equation 5.16 becomes:

$$\frac{h}{\rho_e U_e c_p} = \frac{d\Delta_2}{dx} \tag{5.17}$$

The group of variables on the left-hand side is dimensionless and is called the local Stanton number St. Therefore,

$$St = \frac{h_a}{\rho_e U_e c_p} \tag{5.18}$$

and,

$$St = \frac{d\Delta_2}{dx} \tag{5.19}$$

The analogous relation of the momentum integral equation 5.7 and the energy integral equation 5.19 is very clear.

5.1.2 Convective heat transfer coefficient for laminar $(h_{conv,lam})$ and turbulent $(h_{conv,turb})$ flows

The different treatments are implemented for boundary layer heat transfer calculations in laminar and turbulent regimes. But the most icing studies use the Smith and Spalding (1958) approach in laminar airflow, and the Kays (2012) approach in turbulent airflow for the calculations of Integral Boundary Layer (IBL) equations.

In the remaining parts of this section, the velocity of the airflow external and just next to the boundary layer is (U_e).

By applying the following procedure the convective heat transfer coefficient on the body will be found for laminar and turbulent flows.

Along with surface energy and wettability, the roughness plays a very important role in the ice-adhesion property of the bodies and consequently affects the ice accretion directly. The surface energy depends on the aerodynamic characteristics of the geometries of the body, whereas the wettability and roughness are both metallurgical properties of the material of the bodies. In the case of wettability, water condenses in a liquid form, leading to the formation of a thin continuous water layer on a hydrophilic surface. Meanwhile, separated rounded water droplets are formed on hydrophobic surfaces. As a result of slower heat exchange, the freezing of rounded water droplets on a hydrophobic surface occurs later than the freezing of the continuous water layer on a hydrophilic one. Moreover, the growth of ice on hydrophobic surfaces is slower than on the hydrophilic ones, because ice grows due to the condensation of water vapor on already formed ice crystals. The main disadvantage of hydrophobic and superhydrophobic surfaces is the pinning of water droplets on them after thawing (Chanda et al., 2015). On the other hand, it was concluded that a smooth surface with low surface energy has low ice-adhesion strength (Bharathidasan et al., 2014).

Furthermore, the surface roughness also influences the velocity distribution around the airfoil and consequently the convective heat transfer coefficient. It means again the roughness affects the ice accretion indirectly in this way.

Therefore, the sand-grain roughness height (k_s) which represents the actual roughness on the surface brought by the ice layer is one of the most important parameters in the study of convective heat transfer on the body surface is defined as (Bharathidasan et al., 2014; Cebeci, 1999; Mart, 2011; Smith and Kaups, 1968; Wright et al., 1997):

$$k_s = \left[\frac{4\sigma_w \mu_w^2}{\rho_w F \tau_{wall}}\right]^{\frac{1}{3}} \tag{5.20}$$

which, σ_w, τ_{wall} and F are surface tension of the water, shear stress on the wall and the length of wetted surface on the body, respectively. Thus,

$$\tau_{wall} = \mu_a \frac{\partial U_e}{\partial n}\Big|_{wall} \tag{5.21}$$

The order of magnitude of the k_s is about 1 ± 0.3 mm (Han, 2015; Han and Palacios, 2017).

The heat transfer model used in the LEWICE code makes use of an equivalent sand grain roughness k_s, expressed as a function of liquid water content (LWC), static temperature of the ambient air (T_{amb}), and median volume diameter. The numerical studies conducted by Shin showed that the roughness height does not depend on airspeed, but depends on the median volume diameter (MVD). As a result, the correction for the equation of the roughness height is (Shin and Bond, 1992):

$$k_s = 0.6839\left[\frac{\left(\frac{k_s}{chord}\right)}{\left(\frac{k_s}{chord}\right)_{base}}\right]_{LWC}\left[\frac{\left(\frac{k_s}{chord}\right)}{\left(\frac{k_s}{chord}\right)_{base}}\right]_{T_{amb}}\left[\frac{\left(\frac{k_s}{chord}\right)}{\left(\frac{k_s}{chord}\right)_{base}}\right]_{MVD}\left(\frac{k_s}{chord}\right)_{base} chord \tag{5.22}$$

which,

$$\left[\frac{\left(\frac{k_s}{chord}\right)}{\left(\frac{k_s}{chord}\right)_{base}}\right]_{LWC} = 0.5714 + 0.2457(LWC) + 1.2571(LWC)^2 \tag{5.23}$$

also,

$$\left[\frac{\left(\frac{k_s}{chord}\right)}{\left(\frac{k_s}{chord}\right)_{base}}\right]_{T_{amb}} = 0.0470 T_{amb} - 11.27 \tag{5.24}$$

and,

$$\left[\frac{\left(\frac{k_s}{chord}\right)}{\left(\frac{k_s}{chord}\right)_{base}}\right]_{MVD} = \begin{cases} 1, & for\ MVD \leq 20 \\ 1.667 - 0.0333 MVD, & for\ MVD > 20 \end{cases} \tag{5.25}$$

and, the original expression for $\left(\frac{k_s}{chord}\right)_{base}$ is:

$$\left(\frac{k_s}{chord}\right)_{base} = 0.001177 \tag{5.26}$$

Utilizing Thwaites method for the laminar flow $\boldsymbol{Re_{k,lam} < 600}$ (Gent et al., 2000; Schlichting and Gersten, 2016; Smith and Spalding, 1958; White and Corfield, 2006) the momentum thickness will be:

$$\delta_{2,lam} = \sqrt{\frac{0.45\nu_a}{U_e^6}\int_0^s U_e^5 ds} \tag{5.27}$$

which s=0 is the reference point of surface-distance for the stagnation point on the front surface of airfoil.

Multiple Stagnation Points are a main cause of error in the calculations of boundary layer thickness which lead to the calculations of friction and convective heat transfer coefficients. LEWICE also mentions to this problem (Wright, 2008). Here, the criteria are to select the value closest to the stagnation point from the previous time step. If it finds more than one stagnation point on the first time step, the point closest to the leading edge is used. If this is not satisfactory, the number of points on the airfoil should be increased to produce a single stagnation point value.

The the thickness of boundary layer is:

$$\delta = \frac{315}{37}\delta_{2,lam} \tag{5.28}$$

By assuming 4th order polinomial equation of the Pohlhausen method for the dimensionless velocity distribution of air on the maximum height of roughness, and applying the boundary condition on the body based on Pohlhausen pressure gradient parameter (Chang, 2014), consequently, the air velocity on the maximum height of roughness will be (Özgen and Canıbek, 2009, 2012):

$$\frac{U_{k,lam}}{U_e} = +2\left(\frac{k_s}{\delta}\right) - 2\left(\frac{k_s}{\delta}\right)^3 + \left(\frac{k_s}{\delta}\right)^4 + \frac{1}{6}\frac{\delta^2}{\nu_a}\frac{\partial U_e}{\partial s}\Big|_{wall}\left(\frac{k_s}{\delta}\right)\left[1-\left(\frac{k_s}{\delta}\right)\right]^3 \tag{5.29}$$

Anywhere that k_s becomes larger than δ it is physically meaningless because the roughness height can not exceed the thickness of the boundary layer, then in that

situation, the magnitude of the k_s will set to $k_s = \delta$, and obviously, from the equation 5.29 the velocity on the top of roughness will be $U_k = U_e$ (Gent et al., 2000).

The $\left(\frac{k_s}{\delta}\right) \leq 1$ and $\frac{U_k}{U_e} \leq 1$ conditions should be always satisfied.

Thus, the Reynolds number will be:

$$Re_{k,lam} = \frac{\rho_a U_{k,lam} k_s}{\mu_a} \tag{5.30}$$

Just to have a better prespective, it is good to know that friction coefficient for the laminar airflow can be expressed as (Fortin et al., 2006):

$$\frac{c_{f,lam}}{2} = 0.225 \frac{\nu_a}{\delta_{2,lam} U_e} \tag{5.31}$$

The friction coefficient for the turbulent airflow $c_{f,turb}$ is necessary for calculation of the $U_{k,turb}$, but for the laminar airflow the $U_{k,lam}$ is derived from the Pohlhausen dimensionless velocity distribution (equation 5.29).

eventually the **convective heat transfer coefficient for the laminar flow** is:

$$h_{conv,lam} = \frac{0.296 k_a U_e^{1.435}}{\sqrt{\nu_a \int_0^s U_e^{1.87} ds}} \tag{5.32}$$

where k_a and ν_a are the thermal conductivity and kinematic viscosity of the air, respectively.

On the other hand, for the turbulent flow i.e. $\boldsymbol{Re_{k,lam} \geq 600}$ (Cebeci and Bradshaw, 2012; Kays, 2012), the momentum thickness is:

$$\delta_{2,turb} = \delta_{2,lam}\big|_{s_{trans}} + \frac{0.036 \nu_a^{0.2}}{U_e^{3.29}} \Big[\int_{s_{trans}}^{s} U_e^{3.86} ds \Big]^{0.8} \tag{5.33}$$

which, s_{trans} is the distance of transient point on the upper and lower body surface with respect to stagnation point at the leading edge.

Besides, the Stanton number is defined as:

$$St_k = 1.92 Re_{k,turb}^{-0.45} Pr_{lam}^{-0.8} \tag{5.34}$$

which $Pr_{lam} = 0.7$, and

$$Re_{k,turb} = \frac{\rho_a U_{k,turb} k_s}{\mu_a} \tag{5.35}$$

for turbulent airflow the velocity of air on the maximum roughness height is calculated as:

$$U_{k,turb} = U_e \sqrt{\frac{c_{f,turb}}{2}} \tag{5.36}$$

besides, the friction coefficient for turbulent flow is:

$$\frac{c_{f,turb}}{2} = \frac{0.1681}{\left[ln\left(2.568 + \frac{864\delta_{2,turb}}{k_s}\right)\right]^2} \tag{5.37}$$

eventually, from the turbulent flow's heat transfer and momentum analogy, the Stanton number for the turbulent flow is (Cebeci and Bradshaw, 2012; Kays, 2012):

$$St_{turb} = \frac{\frac{c_{f,turb}}{2}}{Pr_{turb} + \frac{\sqrt{\frac{c_{f,turb}}{2}}}{St_k}} \tag{5.38}$$

which $Pr_{turb} = 0.9$

and finally the **convective heat transfer coefficient for the turbulent flow** will be:

$$h_{conv,turb} = \rho_a c_{p,a} U_e St_{turb} \tag{5.39}$$

Because, after just a very short distance of laminar airflow from the stagnation point, the flow pattern turns to turbulent airflow, it is also possible to assume that only the turbulent airflow exists after the stagnation point in both upper and lower surfaces of the airfoil.

5.1.3 Validation

The result of the present study for h_{conv} values has been validated for NACA 0012 airfoil with respect to Sun et al. (2012).

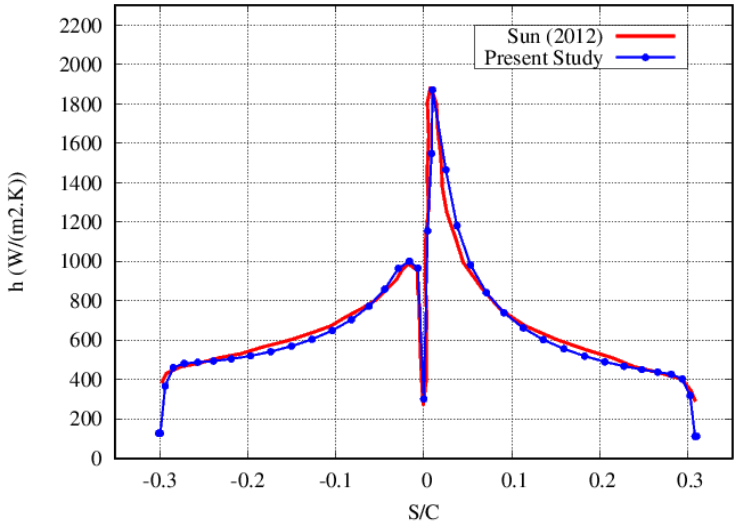

Figure 5.1 : Validation of h_{conv} value of present study for 121×121 grid points with respect to Sun et al. (2012), for chord=0.3 m, $U_\infty = 130\ m/s$, $AOA = 4\ ^\circ$, $T_{substrate} = 0\ ^\circ C$ and $T_\infty = -10\ ^\circ C$.

The mesh independence study shows that for the 121×121 grid size and $dn = 5\ mm$ (dn is the normal distance of the grid-loop just next to the body) results are in a good agreement with the literature (Figure 5.1).

5.1.4 Results

Results of the present study for convective heat transfer coefficient of the airflow have been shown in the following figures for different free air-stream velocities, angle of attack and ambient temperatures.

In all figures, the starting point for s is the stagnation point.

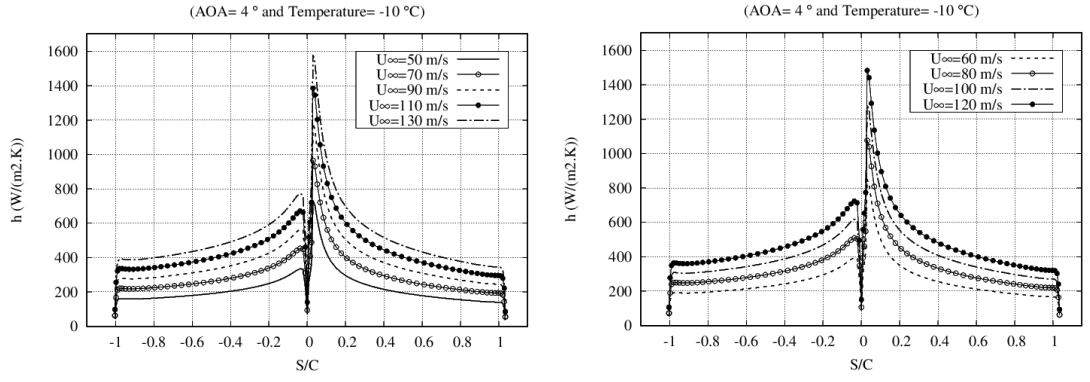

(a) (b)

Figure 5.2 : The variation of h_{conv} with respect to free stream velocity, for chord=1.0 m, $AOA = 4\ ^\circ$, $T_{substrate} = 0\ ^\circ C$ and $T_\infty = -10\ ^\circ C$.

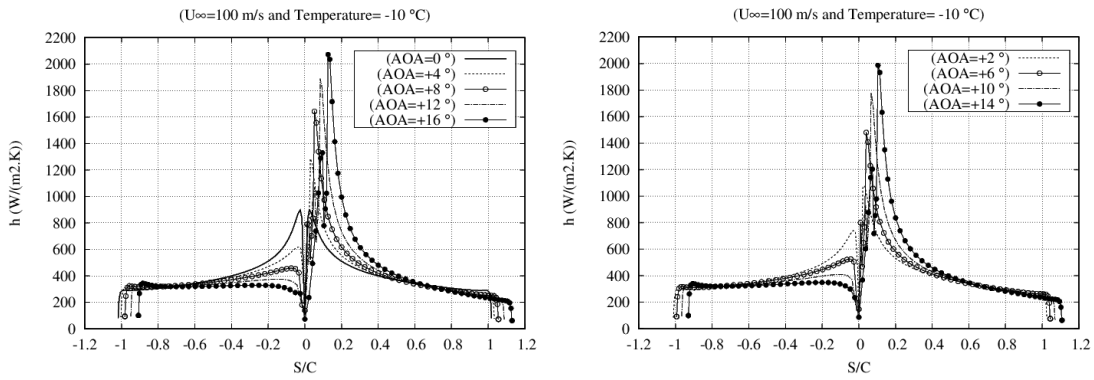

(a) (b)

Figure 5.3 : The variation of h_{conv} with respect to angle of attack, for chord=1.0 m, $U_\infty = 100\ m/s$, $T_{substrate} = 0\ ^\circ C$ and $T = -10\ ^\circ C$.

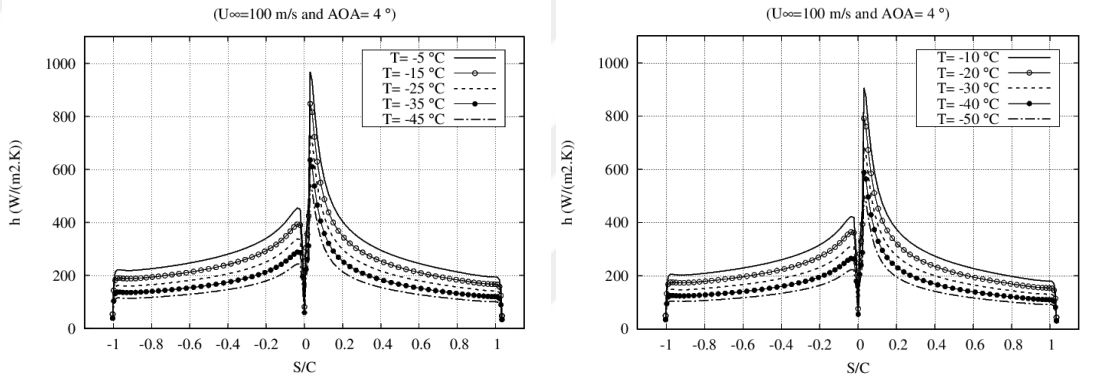

(a) (b)

Figure 5.4 : The variation of h_{conv} with respect to ambient temperature, for chord=1.0 m, $U_\infty = 100\ m/s$, $AOA = 4\ ^\circ$ and $T_{substrate} = 0\ ^\circ C$.

It is observed that convective heat transfer decreases with the increase of distance from the leading edge to the trailing edge due to the growth of boundary layer which plays a very important role in the augmentation of the thermal resistance. For each case, the highest convective heat transfer coefficient is seen in the stagnation point because there is a minimum thermal resistance.

The parametric study of results show that with the increase of both free air-stream velocities and angle of attacks, the convective heat transfer coefficient is raised because of the increase of Reynolds number. On the other hand, when the ambient temperature drops the convective heat transfer coefficient declines because the decrease in Reynolds number overcomes the increase of temperature difference.

6. COLLECTION EFFICIENCY

The study of two-phase flow could be a specialization field in the chemical, physical, mechanical, and aeronautical building. The term “two-phase flow” covers a wide extend of flow patterns. Two-phase streams are regularly categorized by the physical states of the constituent components and by the topology of the interfacing. In this way, a two-phase flow can be classified as gas-solid, gas-liquid, solid-liquid, or within the case of two immiscible fluids, liquid-liquid. Additionally, a two-phase flow can be broadly classified topologically as separated or immersed (Hayati, 2010; Rusche, 2002).

To numerically model two-phase flow, it is important to know if the different phases are separated or submerged (immersed). In a separated two-phase flow, the two phases are completely separated by the interface. On the other hand, in immersed two-phase flow, the broadest classification lies between dispersed and dense flows, indicating which coupling mechanism primarily determines particle motion. The secondary phase is composed of discrete or continuous bubbles, particles, or droplets, and the primary phase is the surrounding fluid which the secondary phase is generally immersed, and this primary phase is always a continuous phase. The secondary phase can be solid, liquid or gas, while the primary phase can be liquid or gas. The coupling between particle motion and its surrounding fluid can also be used to classify the character of immersed two-phase flow as one-way or two-way coupled. Two-phase flows can be considered dispersed if the effects of particle-surrounding phase interactions dominate the overall transport of the particles, as shown in the figure 6.1. The interaction between the primary and secondary fluids generally involves drag that impedes the relative velocity of the particles and therefore tends to direct the trajectory of the particles to the trajectories of the surrounding fluid. On the other hand, if particle-particle motion is dominant, the flow can be considered dense. Particle-particle interaction can refer to two separate mechanisms. The particle-particle collisions (where particles can bounce, split, or coalesce by colliding with each other)

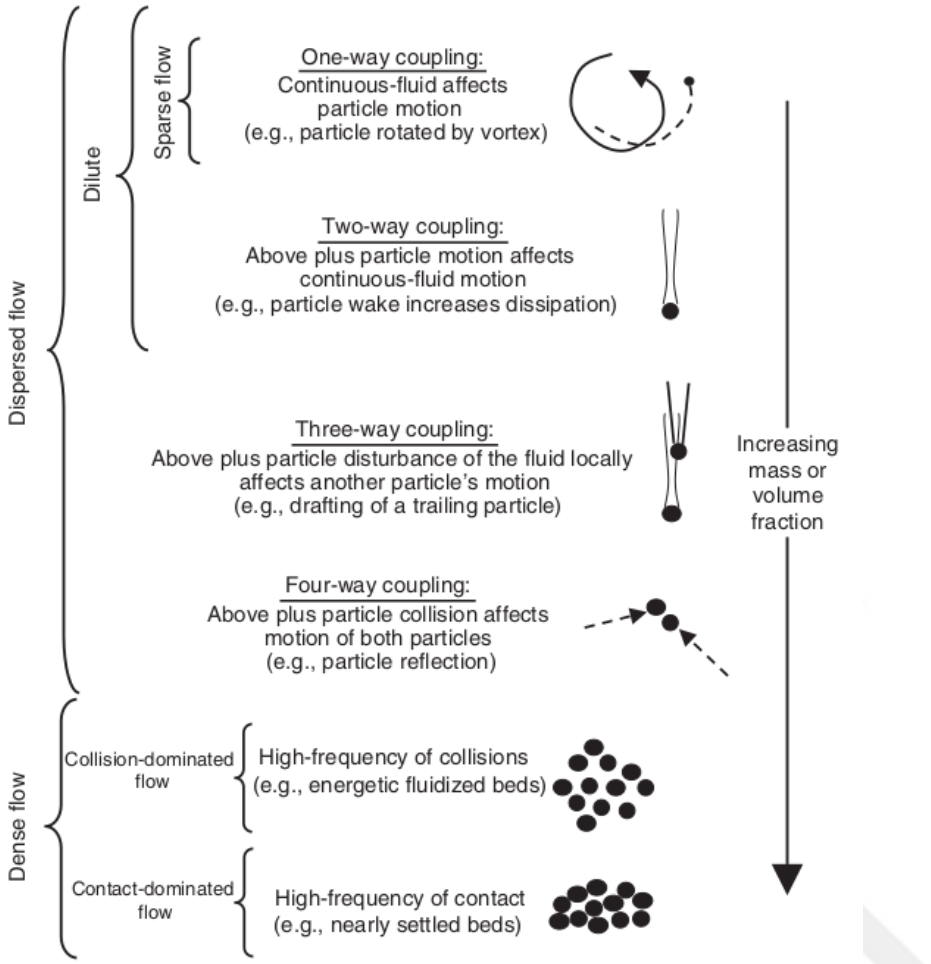

Figure 6.1 : Dilute, dispersed, and dense flow conditions based on various interphase and intraphase coupling (Loth et al., 2006).

and particle-particle dynamic interactions (the proximity of particles affects their fluids). Dispersed flows generally include one-way coupling (the movement of the dispersed phase is affected by the continuous phase, but not vice versa), two-way coupling (the dispersed phase also affects the continuous phase), Three-way coupling (particle wakes and other continuous phase perturbations affect the motion of other particle interactions) and four-way coupling (collisions and other particle-particle interactions affect but does not control the entire motion). Dense flow is commonly defined as a four-way coupling, but in some cases (for example, granular flow), the particle's effect on the continuous fluid is weak and often ignored. (Loth et al., 2006).

From a different perspective, the models of two-phase flows can be classified into homogeneous or non-homogeneous flow models. In the homogeneous flow model, it is assumed that the two phases are identical and share one set of governing equations. On

the other hand, the non-homogeneous flow model allows each phase to be designated a particular region in the flow field where it has its own velocity and temperature.

To solve problems involving non-homogeneous two-phase flows, the governing equations for each phase must be separately given, and the boundary conditions for each phase at the interface must be matched. Obviously, the development of a methodology that predicts the two-phase flow with considerable detail and sufficient accuracy is highly desirable. Such a methodology exists in the form of computational fluid dynamics (CFD). Three well-known CFD methodologies for the prediction of the dynamics of two-phase flows are namely direct numerical simulation (DNS), one-way coupled flow model, and two-way coupled flow model. In a Direct Numerical Simulation (DNS), the Navier-Stokes equations of a homogeneous two-phase flow are solved without additional assumptions and manipulations, and the topology of the interface between the two phases is determined as part of the solution. No additional modeling assumptions are introduced. DNS requires very high resolution to solve a broad range of temporal and spatial scales. Resolving these scales is computationally expensive both in terms of computer memory size and execution time. Therefore, most of the time, DNS is not an available solution. In the one-way coupled flow model, the secondary or dispersed phase is affected by the primary (surrounding) phase but not vice versa. Whereas, in the two-way coupled flow model the secondary phase does also affect the flow pattern of the primary phase. In both one-way and two-way coupled flow models primary (surrounding) phase is always considered a continuous phase, but the secondary (dispersed) phase can be treated either as a discrete or continuous phase, and the conservation equations are expressed in the Eulerian frame. The secondary (dispersed) phase is obtained either by replacing the conservation equations with a discrete formulation in a way that the dispersed phase is represented by individual partial differential equations (PDEs) which are tracked through the flow domain, by solving the equation of motion for each particle (Lagrangian formulation) or solving the momentum partial differential equations for the entire region (Eulerian formulation). Because of the early mentioned treatments of the one-way coupled and two-way coupled flow in two-phase flow models, the continuous-discrete or continuous-continuous models can be referred to as the Eulerian-Lagrangian or Eulerian-Eulerian models, respectively (Rusche, 2002).

The aircraft icing is a special case of two-phase flow. The airflow will affect the motion of water droplets around an airfoil. On the other hand, while the diameter of a water droplet is less than 50 μm, the motion of droplets does not affect the airflow (i.e. one-way coupled flow), but when the diameter of droplets is larger than 50 μm the motion of droplets does also influence the airflow, and there is an interaction between airflow and the motion of droplets (i.e. two-way coupled flow). In our study, it is assumed that the diameter of droplets is less than 50 μm, and consequently, the two-phase flow is treated as a one-way coupled flow model. While the airflow is solved by the Eulerian approach, both Lagrangian and Eulerian approaches can be applied for the motion of water droplets (Wu and Cao, 2015).

Apart from what has been mentioned so far, in the analysis of the Super-cooled Large Droplets (SLD), two different sets of equations are performed. While, one set of equations comprises the conventional forces (drag, gravity, and buoyancy), the other set should include the number of additional forces (Basset history force, virtual mass force, and Saffman lift force) (Hospers, 2013; van Eijkeren and Hoeijmakers, 2010).

The other effect that becomes noticeable for the super-cooled large droplets is due to droplet deformation. Larger shear forces in the flow can cause droplets to deform. It means that the assumption that a droplet behaves as a solid sphere is no longer valid (Hospers, 2013). If the stresses on a droplet are large enough (larger than the stresses needed to deform a droplet), or the deformation persists long enough; the droplet might break up into smaller droplets (Tan et al., 2005). Then, the deformation and breakup phenomena should be also considered for calculations of super-cooled large droplets. Breakup is a cascading process; droplets will continue to break up, under the stresses imposed by the flow on the droplet, until a certain critical diameter is reached. Droplets with a diameter smaller than this critical diameter are stable. The stresses on a droplet are determined mostly by the relative Weber number:

$$We_d = \frac{\rho_a \left|\vec{U} - \vec{V}\right|^2 d}{\sigma_w} \tag{6.1}$$

which ρ_a, $\vec{U}$, $\vec{V}$, d and σ_w are the air density, air velocity, droplet velocity, droplet diameter and droplet surface tension, respectively. For break up the critical Weber number, for cases neglecting droplet viscosity, is usually $We_{crit} = 12$ (Honsek et al.,

2008; Pilch and Erdman, 1987). Most models identify multiple types of breakup. For example, Pilch and Erdman (1987) identify five types, or modes, of breakup: vibrational breakup, bag breakup, bag-and-stamen breakup, sheet stripping, and wave crest stripping (followed by catastrophic breakup). These five breakup modes are illustrated in Figure 6.2.

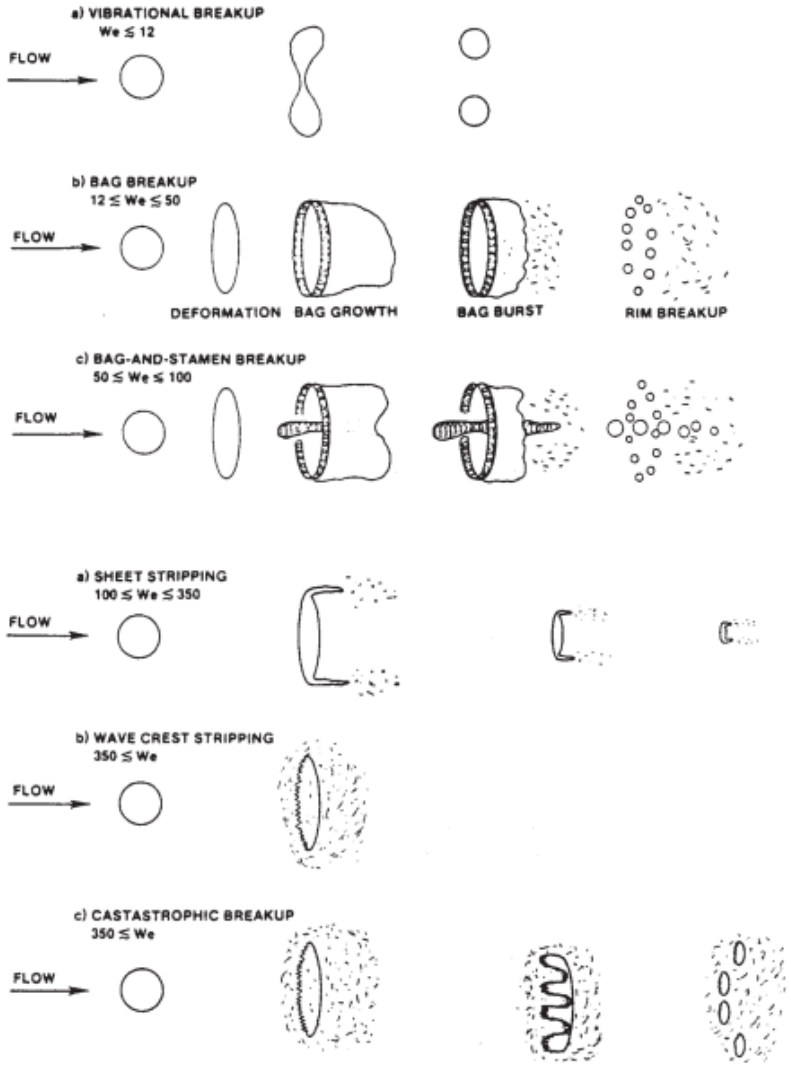

Figure 6.2 : Deformation and Breakup of Super-cooled Large Droplets (SLD) (Hospers, 2013).

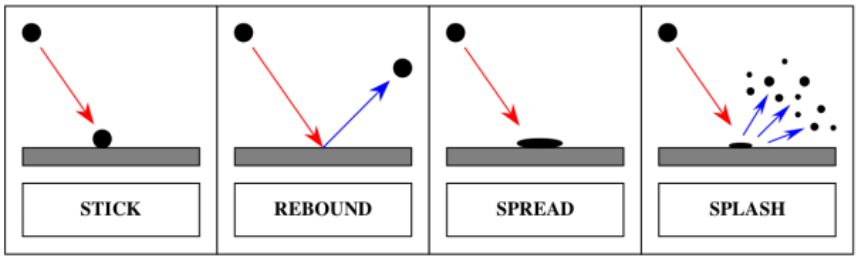

Figure 6.3 : Schematic representation of droplet-wall interactions (CAMAULI, 2018).

The other important factor for simulation of the impingement of SLD is that the droplet impact or the droplets-wall interactions (Figure 6.3) must be also included (Bilodeau et al., 2015; CAMAULI, 2018; Honsek, 2005; Honsek et al., 2008; Iuliano et al., 2011; Norde et al., 2019); it means that in addition to continuity and momentum equations, one more equation is also needed for conservation of the number of water droplets at the wall (Cao and Xin, 2019; Honsek et al., 2008; Hospers and Hoeijmakers, 2010; Jung and Myong, 2013; Kim et al., 2016).

6.1 Lagrangian (Droplets Trajectory) and Eulerian (Droplets Distribution) Approaches for Water Droplets in Aircraft-Icing Simulation

To know the magnitude of the collection efficiency, the water droplets flow field should be found. There are two main approaches namely Lagrangian and Eulerian methods to study the motion or distribution of water droplets around an airfoil.

The Lagrangian approach has been mostly used in the first ice accretion codes. In this method, Newton's second law of motion (force balance) is used for tracking the trajectory of water droplets. For each droplet it is checked to see whether the droplet collides with the surface of the airfoil or not. This can be a very time-consuming task. For 2D cases, the collision efficiency is defined as:

$$\beta = \frac{dy_0}{ds} \tag{6.2}$$

which dy_0 and ds determine the initial and respective impingement positioning of the droplets, respectively.

For 3D geometries, a similar trajectory equation for the z-direction is added to the system, consequently, the collision efficiency is:

$$\beta = \frac{A_0}{A_m} \tag{6.3}$$

where A_0 is the area formed by the initial position of four droplets and A_m is the area formed by their respective impingement positions at the body (Da Silveira et al., 2003).

LEWICE from the NASA Glenn Research Center is the most famous code for ice accretion simulation which uses the Lagrangian methodology, as can be seen in the

study by Wright (1995). In this code, the distribution of droplets of different sizes have be considered for the icing analysis, and very good agreement is achieved for different geometries. Other codes like CANICE (Morency et al., 1999) and ONERA (Hedde and Guffond, 1995) also use the Lagrangian method.

On the other hand, in the Eulerian approach, the continuity and momentum equations of water droplets are simultaneously solved for the entire grid-points around an airfoil. Since, instead of tracking individual particles, the average values of apparent density (or volume fraction) and velocity components of water-droplets are calculated in all points at the same time, the Eulerian approach is time-saving in comparison to the Lagrangian approach. The other advantages are to improve the ability to model unsteady flows over the body, and the automated treatment of shadow zones (zones with no impingement) (Kim et al., 2013). A further reason for developing the Eulerian method is the easy extension toward three-dimensional geometries (Hospers and Hoeijmakers, 2010).

For both 2D and 3D cases, the collision efficiency is defined as:

$$\beta = \frac{\rho_w . \alpha_{On\ the\ body}}{(LWC)_\infty} \left| \frac{V_{Normal,On\ the\ body}}{U_\infty} \right| \tag{6.4}$$

There are two main approaches for the Eulerian method namely, the full two-phase formulation (homogeneous approach) and non-homogeneous or discrete two-phase formulation (passive scalar transport approach) the last one can be itself seen as a one-way coupled flow or two-way coupled flow. The full two-phase formulation sees the mixture of air and droplets as a whole and tries to solve the Navier-Stokes equations for the entire mixture by DNS. In the non-homogeneous formulation, there are two approaches, which one-way coupled passive scalar transport approach assumes that the water droplets do not affect the airflow, and each air and droplet phase are solved independently, but the two-way coupled passive scalar transport approach assumes that the water droplets do also affect the airflow, and there is an interaction between air and droplets' flows (Da Silveira et al., 2003). A work by Bourgault et al. (1999) applies an Eulerian methodology to solve the distribution of water droplets in the FENSAP-ICE code. Such methodology has been successfully used for collision efficiency calculation in complex and 3D geometries (Da Silveira et al., 2003). The Eulerian approach

eliminates the seeding problems of the Lagrangian approach but it is limited to one droplet size per calculation (Wirogo and Srirambhatla, 2003).

All in all, the Eulerian approach can be considered a more general and desired formulation for calculating the distribution of water droplets. Therefore, in the present study, the Eulerian approach is utilized to find out the collision efficiency of the water droplets on the airfoil.

6.2 Explanation of Eulerian Method for Modeling of Distribution of Water Droplets

Even so, both Lagrangian and Eulerian methods are in use for the calculation of super-cooled water-droplet flowfield in aircraft icing, but the Eulerian method has some advantages. The Eulerian method can receive data of flow field from any available flow model e.g. potential flow or Navier-Stokes flow solvers. Also, the Eulerian method is more sensitive when dealing with complicated geometries, and also for 3D cases (Da Silveira et al., 2003; Wang et al., 2018). Besides, the Eulerian approach improves the quality of solution, the ability to model unsteady flows over bodies in relative motion, and the automated treatment of shadow zones (no impingement zones). By using the Eulerian approach, the interaction between the air particles and the droplets occurs through a drag force exerted by the mean airflow on the particles, and also, the presence of the droplet flow field can be felt by the mean airflow solver in the case of SLD (Kim et al., 2013).

Therefore, the Eulerian method is used in the present study to obtain the variation of volume fraction around the airfoil which leads to the calculation of the collection efficiency on the body.

6.2.1 Governing equations: continuity, x and y momentum equations of motion of droplet

Based on the multi-fluid model of droplets, the droplets distributed in the flow-field can be regarded as a kind of pseudo fluid that penetrates the real fluid in Eulerian coordinates. According to assumptions the fluctuation term, phase-change term, and Magnus force in the governing equations for droplets can be neglected. Furthermore, the energy equation does not need to be solved.

The mass conservation for the water phase by assuming a continuous phase approach in the physical coordinate is:

$$\frac{\partial \bar{\rho}}{\partial t} + \frac{\partial (\bar{\rho} V_x)}{\partial x} + \frac{\partial (\bar{\rho} V_y)}{\partial y} = 0 \tag{6.5}$$

which V is velocity of droplet, and $\bar{\rho}$ is apparent density (Liquid Water Content) which explained as:

$$\bar{\rho} = LWC = \rho_w \alpha \tag{6.6}$$

The momentum conservation for water phase in x direction by assuming continuous phase approach in the physical coordinate is:

$$\frac{\partial (\bar{\rho}.V_x)}{\partial t} + \frac{\partial (\bar{\rho} V_x.V_x)}{\partial x} + \frac{\partial (\bar{\rho} V_y.V_x)}{\partial y} = F_{D,x} \tag{6.7}$$

which $F_{D,x}$ is component of the drag force in x direction.

Eventually, the momentum conservation for water phase in y direction by assuming continuous phase approach in the physical coordinate is:

$$\frac{\partial (\bar{\rho}.V_y)}{\partial t} + \frac{\partial (\bar{\rho} V_x.V_y)}{\partial x} + \frac{\partial (\bar{\rho} V_y.V_y)}{\partial y} = F_{D,y} + F_{GB} \tag{6.8}$$

which $F_{D,x}$ and F_{GB} are drag and gravity & buoyancy forces, respectively, and will be explained as below (Cao et al., 2016b):

$$F_D = \frac{0.75 \bar{\rho} C_D Re_D \mu_a}{\rho_w D^2} (U - V) \tag{6.9}$$

$$F_{GB} = \bar{\rho} g \Big(1 - \frac{\rho_a}{\rho_w}\Big) \tag{6.10}$$

$$Re_D = \frac{\rho_a D}{\mu_a} |U - V| \tag{6.11}$$

$$\frac{C_D Re_D}{24} = \begin{cases} 1 + 0.197 Re_D^{0.63} + 2.6 \times 10^{-4} Re_D^{1.38} & , for\ Re_D \leq 3500 \\ 1.699 \times 10^{-5} Re_D^{1.92} & , for\ Re_D > 3500 \end{cases} \tag{6.12}$$

C_D and Re_D are the drag coefficient and Reynolds number of water-droplet, ρ_a, μ_a and U are density, viscosity, and velocity of air, respectively. Furthermore, D, ρ_w, α and

V are the diameter, density, volume fraction, and velocity of the droplet, respectively. Besides, g represents the gravity acceleration.

To simplify the solution of water droplets distribution, most of the time the governing equations are transferred from $x-y$ coordinate to the $\xi-\eta$ coordinate. The transformed equations can be found in lots of articles studied by Cao et al. (2016a,b, 2012, 2008).

The distribution of the water droplets is very sensitive especially next to the bodies, therefore, the vertex-centered finite volume method (FVM) will apply for solving the governing equations of the water droplets because FVM is both locally and globally conservative. Also, to get the high accurate solutions, the higher-order differentiating schemes are preferred for droplet impingement. In the present research, the Quadratic Upstream Interpolation for Convective Kinematics (QUICK) scheme has been applied which considers three-points upstream weighted quadratic interpolation for the cell-face values (Versteeg and Malalasekera, 1995).

By partial differentiating of the governing equations of the droplets with respect to ξ,η as:

continuity:

$$\frac{\partial \bar{\rho}}{\partial t}+\left(\frac{\partial(\bar{\rho}.V_x)}{\partial \xi}\frac{\partial \xi}{\partial x}+\frac{\partial(\bar{\rho}.V_x)}{\partial \eta}\frac{\partial \eta}{\partial x}\right)+\left(\frac{\partial(\bar{\rho}.V_y)}{\partial \xi}\frac{\partial \xi}{\partial y}+\frac{\partial(\bar{\rho}.V_y)}{\partial \eta}\frac{\partial \eta}{\partial y}\right)=0 \tag{6.13}$$

x momentum:

$$\begin{aligned}\frac{\partial(\bar{\rho}.V_x)}{\partial t}+\left[\left(\frac{\partial(\bar{\rho}V_x)}{\partial \xi}\frac{\partial \xi}{\partial x}+\frac{\partial(\bar{\rho}V_x)}{\partial \eta}\frac{\partial \eta}{\partial x}\right)V_x+\bar{\rho}V_x\left(\frac{\partial V_x}{\partial \xi}\frac{\partial \xi}{\partial x}+\frac{\partial V_x}{\partial \eta}\frac{\partial \eta}{\partial x}\right)\right]+\\ \left[\left(\frac{\partial(\bar{\rho}V_y)}{\partial \xi}\frac{\partial \xi}{\partial y}+\frac{\partial(\bar{\rho}V_y)}{\partial \eta}\frac{\partial \eta}{\partial y}\right)V_x+\bar{\rho}V_y\left(\frac{\partial V_x}{\partial \xi}\frac{\partial \xi}{\partial y}+\frac{\partial V_x}{\partial \eta}\frac{\partial \eta}{\partial y}\right)\right]=F_{D,x}\end{aligned} \tag{6.14}$$

y momentum:

$$\begin{aligned}\frac{\partial(\bar{\rho}.V_y)}{\partial t}+\left[\left(\frac{\partial(\bar{\rho}V_x)}{\partial \xi}\frac{\partial \xi}{\partial x}+\frac{\partial(\bar{\rho}V_x)}{\partial \eta}\frac{\partial \eta}{\partial x}\right)V_y+\bar{\rho}V_x\left(\frac{\partial V_y}{\partial \xi}\frac{\partial \xi}{\partial x}+\frac{\partial V_y}{\partial \eta}\frac{\partial \eta}{\partial x}\right)\right]+\\ \left[\left(\frac{\partial(\bar{\rho}V_y)}{\partial \xi}\frac{\partial \xi}{\partial y}+\frac{\partial(\bar{\rho}V_y)}{\partial \eta}\frac{\partial \eta}{\partial y}\right)V_y+\bar{\rho}V_y\left(\frac{\partial V_y}{\partial \xi}\frac{\partial \xi}{\partial y}+\frac{\partial V_y}{\partial \eta}\frac{\partial \eta}{\partial y}\right)\right]=F_{D,x}+F_{GB}\end{aligned} \tag{6.15}$$

By using coordinate transforming relationships (i.e. equations of 3.11 , 3.12 , 3.13 and 3.14) the transformed equations will be:

continuity:

$$\frac{\partial \bar{\rho}}{\partial t}+\left(\frac{\partial(\bar{\rho}.V_x)}{\partial \xi}\frac{y_\eta}{J}-\frac{\partial(\bar{\rho}.V_x)}{\partial \eta}\frac{y_\xi}{J}\right)+\left(-\frac{\partial(\bar{\rho}.V_y)}{\partial \xi}\frac{x_\eta}{J}+\frac{\partial(\bar{\rho}.V_y)}{\partial \eta}\frac{x_\xi}{J}\right)=0 \tag{6.16}$$

x momentum:

$$\frac{\partial(\bar{\rho}.V_x)}{\partial t}+\Big[(\frac{\partial(\bar{\rho}V_x)}{\partial\xi}\frac{y_\eta}{J}-\frac{\partial(\bar{\rho}V_x)}{\partial\eta}\frac{y_\xi}{J})V_x+\bar{\rho}V_x(\frac{\partial V_x}{\partial\xi}\frac{y_\eta}{J}-\frac{\partial V_x}{\partial\eta}\frac{y_\xi}{J})\Big]+$$
$$\Big[(-\frac{\partial(\bar{\rho}V_y)}{\partial\xi}\frac{x_\eta}{J}+\frac{\partial(\bar{\rho}V_y)}{\partial\eta}\frac{x_\xi}{J})V_x+\bar{\rho}V_y(-\frac{\partial V_x}{\partial\xi}\frac{x_\eta}{J}+\frac{\partial V_x}{\partial\eta}\frac{x_\xi}{J})\Big]=F_{D,x} \tag{6.17}$$

y momentum:

$$\frac{\partial(\bar{\rho}.V_y)}{\partial t}+\Big[(\frac{\partial(\bar{\rho}V_x)}{\partial\xi}\frac{y_\eta}{J}-\frac{\partial(\bar{\rho}V_x)}{\partial\eta}\frac{y_\xi}{\partial x})V_y+\bar{\rho}V_x(\frac{\partial V_y}{\partial\xi}\frac{y_\eta}{J}-\frac{\partial V_y}{\partial\eta}\frac{y_\xi}{J})\Big]+$$
$$\Big[(-\frac{\partial(\bar{\rho}V_y)}{\partial\xi}\frac{x_\eta}{\partial y}+\frac{\partial(\bar{\rho}V_y)}{\partial\eta}\frac{x_\xi}{\partial y})V_y+\bar{\rho}V_y(-\frac{\partial V_y}{\partial\xi}\frac{x_\eta}{J}+\frac{\partial V_y}{\partial\eta}\frac{x_\xi}{J})\Big]=F_{D,x}+F_{GB} \tag{6.18}$$

the governing equations of the droplets will be rearranged as:

continuity:

$$\frac{\partial\bar{\rho}}{\partial t}+\frac{1}{J}\frac{\partial\big(\bar{\rho}(V_x.y_\eta-V_y.x_\eta)\big)}{\partial\xi}+\frac{1}{J}\frac{\partial\big(\bar{\rho}(-V_x.y_\xi+V_y.x_\xi)\big)}{\partial\eta}=0 \tag{6.19}$$

x momentum:

$$\frac{\partial(\bar{\rho}.V_x)}{\partial t}+\frac{1}{J}\Big[\frac{\partial\big(\bar{\rho}(V_x.y_\eta-V_y.x_\eta)\big)}{\partial\xi}V_x+\big(\bar{\rho}(V_x.y_\eta-V_y.x_\eta)\big)\frac{\partial V_x}{\partial\xi}\Big]+$$
$$\frac{1}{J}\Big[\frac{\partial\big(\bar{\rho}(-V_x.y_\xi+V_y.x_\xi)\big)}{\partial\eta}V_x+\big(\bar{\rho}(-V_x.y_\xi+V_y.x_\xi)\big)\frac{\partial V_x}{\partial\eta}\Big]=F_{D,x} \tag{6.20}$$

y momentum:

$$\frac{\partial(\bar{\rho}.V_y)}{\partial t}+\frac{1}{J}\Big[\frac{\partial\big(\bar{\rho}(V_x.y_\eta-V_y.x_\eta)\big)}{\partial\xi}V_y+\big(\bar{\rho}(V_x.y_\eta-V_y.x_\eta)\big)\frac{\partial V_y}{\partial\xi}\Big]+$$
$$\frac{1}{J}\Big[\frac{\partial\big(\bar{\rho}(-V_x.y_\xi+V_y.x_\xi)\big)}{\partial\eta}V_y+\big(\bar{\rho}(-V_x.y_\xi+V_y.x_\xi)\big)\frac{\partial V_y}{\partial\eta}\Big]=F_{D,x}+F_{GB} \tag{6.21}$$

Knowing that the contra-variant velocity components of water droplets in ξ,η coordinate are explained as:

$$V_\xi=J\big(V_x.\xi_x+V_y.\xi_y\big)=V_x.y_\eta-V_y.x_\eta \tag{6.22}$$

$$V_\eta=J\big(V_x.\eta_x+V_y.\eta_y\big)=-V_x.y_\xi+V_y.x_\xi \tag{6.23}$$

the governing equations of the droplets are restated as:

continuity:

$$\frac{\partial\bar{\rho}}{\partial t}+\frac{1}{J}\frac{\partial\big(\bar{\rho}V_\xi\big)}{\partial\xi}+\frac{1}{J}\frac{\partial\big(\bar{\rho}V_\eta\big)}{\partial\eta}=0 \tag{6.24}$$

x momentum:

$$\frac{\partial(\bar{\rho}.V_x)}{\partial t}+\frac{1}{J}\frac{\partial\left(\bar{\rho}V_\xi.V_x\right)}{\partial\xi}+\frac{1}{J}\frac{\partial\left(\bar{\rho}V_\eta.V_x\right)}{\partial\eta}=F_{D,x} \tag{6.25}$$

y momentum:

$$\frac{\partial(\bar{\rho}.V_y)}{\partial t}+\frac{1}{J}\frac{\partial\left(\bar{\rho}V_\xi.V_y\right)}{\partial\xi}+\frac{1}{J}\frac{\partial\left(\bar{\rho}V_\eta.V_y\right)}{\partial\eta}=F_{D,x}+F_{GB} \tag{6.26}$$

Finally, the transformed equations of water droplets in ξ,η coordinate will be expressed as:

continuity:

$$J\frac{\partial\bar{\rho}}{\partial t}+\frac{\partial(\bar{\rho}V_\xi)}{\partial\xi}+\frac{\partial(\bar{\rho}V_\eta)}{\partial\eta}=0 \tag{6.27}$$

x momentum:

$$J\frac{\partial(\bar{\rho}.V_x)}{\partial t}+\frac{\partial(\bar{\rho}V_\xi.V_x)}{\partial\xi}+\frac{\partial(\bar{\rho}V_\eta.V_x)}{\partial\eta}=J(F_{D,x}) \tag{6.28}$$

y momentum:

$$J\frac{\partial(\bar{\rho}.V_y)}{\partial t}+\frac{\partial(\bar{\rho}V_\xi.V_y)}{\partial\xi}+\frac{\partial(\bar{\rho}V_\eta.V_y)}{\partial\eta}=J(F_{D,y}+F_{GB}) \tag{6.29}$$

The 2D Eulerian method will be applied via FVM in the computational domain (i.e. ξ-η coordinate) as:

continuity:

$$\int\int J\frac{(\bar{\rho}^n-\bar{\rho}^{n-1})}{\Delta t}d\xi d\eta+\int\int\Big[\frac{\partial(\bar{\rho}^nV_\xi^{n-1})}{\partial\xi}+\frac{\partial(\bar{\rho}^nV_\eta^{n-1})}{\partial\eta}\Big]d\xi d\eta=0 \tag{6.30}$$

x momentum:

$$\int\int J\frac{(\bar{\rho}^n.V_x^n-\bar{\rho}^{n-1}.V_x^{n-1})}{\Delta t}d\xi d\eta+\int\int\Big[\frac{\partial(\bar{\rho}^nV_\xi^{n-1}.V_x^n)}{\partial\xi}+\frac{\partial(\bar{\rho}^nV_\eta^{n-1}.V_x^n)}{\partial\eta}\Big]d\xi d\eta=\int\int J\big[F_{D,x}^n\big]d\xi d\eta \tag{6.31}$$

and y momentum:

$$\int\int J\frac{(\bar{\rho}^n.V_y^n-\bar{\rho}^{n-1}.V_y^{n-1})}{\Delta t}d\xi d\eta+\int\int\Big[\frac{\partial(\bar{\rho}^nV_\xi^{n-1}.V_y^n)}{\partial\xi}+\frac{\partial(\bar{\rho}^nV_\eta^{n-1}.V_y^n)}{\partial\eta}\Big]d\xi d\eta=\int\int J\big[F_{D,y}^n+F_{GB}\big]d\xi d\eta \tag{6.32}$$

which $n-1$ and n demonstrate the previous and present time steps, respectively. J is jacobian of the coordinate transformation, and V_x, V_y are the velocity components of the water droplets in x, y coordinate, and V_ξ, V_η are contra-variant velocity components in ξ, η coordinate which are calculated from the velocity components of V_x, V_y at the previous time step to linearize the governing equations of water droplets and expressed as:

$$V_\xi^{n-1} = +y_\eta V_x^{n-1} - x_\eta V_y^{n-1} \tag{6.33}$$

$$V_\eta^{n-1} = -y_\xi V_x^{n-1} + x_\xi V_y^{n-1} \tag{6.34}$$

By integration and discretization of these equations, the governing equations will be:

continuity equation:

$$J\frac{(\bar{\rho}^n - \bar{\rho}^{n-1})}{\Delta t}\Delta\xi\Delta\eta + (\bar{\rho}^n V_\xi^{n-1})_{west}^{east}\Delta\eta + (\bar{\rho}^n V_\eta^{n-1})_{south}^{north}\Delta\xi = 0 \tag{6.35}$$

x momentum equation:

$$J\frac{(\bar{\rho}^n.V_x^n - \bar{\rho}^{n-1}.V_x^{n-1})}{\Delta t}\Delta\xi\Delta\eta + (\bar{\rho}^n V_\xi^{n-1}.V_x^n)_{west}^{east}\Delta\eta + (\bar{\rho}^n V_\eta^{n-1}.V_x^n)_{south}^{north}\Delta\xi = J\Big[\frac{0.75\bar{\rho}C_D Re_D \mu_a}{\rho_w D^2}(U_x - V_x^n)\Big]\Delta\xi\Delta\eta \tag{6.36}$$

and y momentum equation:

$$J\frac{(\bar{\rho}^n.V_y^n - \bar{\rho}^{n-1}.V_y^{n-1})}{\Delta t}\Delta\xi\Delta\eta + (\bar{\rho}^n V_\xi^{n-1}.V_y^n)_{west}^{east}\Delta\eta + (\bar{\rho}^n V_\eta^{n-1}.V_y^n)_{south}^{north}\Delta\xi = J\Big[\frac{0.75\bar{\rho}C_D Re_D \mu_a}{\rho_w D^2}(U_y - V_y^n) + \bar{\rho}g\Big(1 - \frac{\rho_a}{\rho_w}\Big)\Big]\Delta\xi\Delta\eta \tag{6.37}$$

The main idea of transforming the governing equations of water-droplets from the x, y coordinate into ξ, η coordinate is that mass fluxes are calculated by using contra-variant velocity components of V_ξ, V_η for the control volume in the ξ, η coordinate.

The gravity acceleration is in -y direction i.e. $g = -9.8\ \frac{m}{s^2}$.

To be certain that the major effects that play an important role in the simulation of super-cooled large droplets (SLD) distributions are included, along with drag, gravity, and buoyancy forces, Basset history force and virtual mass force may be added into

momentum equations. The deformation and breakup effects should be also considered for super-cooled large droplets (SLD). It means that the entire water droplets can not be still assumed to be a sphere with a single diameter. When droplets with diameters larger than 50 μm i.e. super-cooled large droplets (SLD) (e.g.for heavy rains) exist, the interactions of droplets and the body surface (droplet impact) must be also included, which means in addition to continuity and momentum equations, one more equation is needed for the conservation of the number of water droplets.

By using 2nd order upwind QUICK scheme for convective terms the algebraic forms of the governing equations will be written as:

continuity:

$$
\begin{aligned}
&J(\xi,\eta)\frac{(\bar{\rho}^n(\xi,\eta)-\bar{\rho}^{n-1}(\xi,\eta))}{\Delta t}\Delta\xi\Delta\eta+\\
&\Big[\big(AA_1(\xi,\eta)(-\frac{1}{8}\bar{\rho}^n(\xi-\Delta\xi,\eta)V_\xi(\xi-\Delta\xi,\eta)+\\
&\frac{6}{8}\bar{\rho}^n(\xi,\eta)V_\xi(\xi,\eta)+\frac{3}{8}\bar{\rho}^n(\xi+\Delta\xi,\eta)V_\xi(\xi+\Delta\xi,\eta))\\
&-AA_2(\xi,\eta)(-\frac{1}{8}\bar{\rho}^n(\xi+2\Delta\xi,\eta)V_\xi(\xi+2\Delta\xi,\eta)\\
&+\frac{6}{8}\bar{\rho}^n(\xi+\Delta\xi,\eta)V_\xi(\xi+\Delta\xi,\eta)+\frac{3}{8}\bar{\rho}^n(\xi,\eta)V_\xi(\xi,\eta))\big)-\\
&\big(BB_1(\xi,\eta)(-\frac{1}{8}\bar{\rho}^n(\xi-2\Delta\xi,\eta)V_\xi(\xi-2\Delta\xi,\eta)\\
&+\frac{6}{8}\bar{\rho}^n(\xi-\Delta\xi,\eta)V_\xi(\xi-\Delta\xi,\eta)+\frac{3}{8}\bar{\rho}^n(\xi,\eta)V_\xi(\xi,\eta))\\
&-BB_2(\xi,\eta)(-\frac{1}{8}\bar{\rho}^n(\xi+\Delta\xi,\eta)V_\xi(\xi+\Delta\xi,\eta)+\\
&\frac{6}{8}\bar{\rho}^n(\xi,\eta)V_\xi(\xi,\eta)+\frac{3}{8}\bar{\rho}^n(\xi-\Delta\xi,\eta)V_\xi(\xi-\Delta\xi,\eta)))\Big]\Delta\eta+\\
&\Big[\big(CC_1(\xi,\eta)(-\frac{1}{8}\bar{\rho}^n(\xi,\eta-\Delta\eta)V_\eta(\xi,\eta-\Delta\eta)+\\
&\frac{6}{8}\bar{\rho}^n(\xi,\eta)V_\eta(\xi,\eta)+\frac{3}{8}\bar{\rho}^n(\xi,\eta+\Delta\eta)V_\eta(\xi,\eta+\Delta\eta))\\
&-CC_2(\xi,\eta)(-\frac{1}{8}\bar{\rho}^n(\xi,\eta+2\Delta\eta)V_\eta(\xi,\eta+2\Delta\eta)\\
&+\frac{6}{8}\bar{\rho}^n(\xi,\eta+\Delta\eta)V_\eta(\xi,\eta+\Delta\eta)+\frac{3}{8}\bar{\rho}^n(\xi,\eta)V_\eta(\xi,\eta))\big)-\\
&\big(DD_1(\xi,\eta)(-\frac{1}{8}\bar{\rho}^n(\xi,\eta-2\Delta\eta)V_\eta(\xi,\eta-2\Delta\eta)\\
&+\frac{6}{8}\bar{\rho}^n(\xi,\eta-\Delta\eta)V_\eta(\xi,\eta-\Delta\eta)+\frac{3}{8}\bar{\rho}^n(\xi,\eta)V_\eta(\xi,\eta))\\
&-DD_2(\xi,\eta)(-\frac{1}{8}\bar{\rho}^n(\xi,\eta+\Delta\eta)V_\eta(\xi,\eta+\Delta\eta)+\\
&\frac{6}{8}\bar{\rho}^n(\xi,\eta)V_\eta(\xi,\eta)+\frac{3}{8}\bar{\rho}^n(\xi,\eta-\Delta\eta)V_\eta(\xi,\eta-\Delta\eta)))\Big]\Delta\xi=0
\end{aligned}
\tag{6.38}
$$

x momentum:

$$
\begin{aligned}
&J(\xi,\eta)\frac{(\bar{\rho}(\xi,\eta)V_x^n(\xi,\eta)-\bar{\rho}(\xi,\eta)V_x^{n-1}(\xi,\eta))}{\Delta t}\Delta\xi\Delta\eta+\\
&\Big[\big(AA_1(\xi,\eta)(-\frac{1}{8}\bar{\rho}(\xi-\Delta\xi,\eta)V_\xi(\xi-\Delta\xi,\eta)V_x^n(\xi-\Delta\xi,\eta)+\\
&\frac{6}{8}\bar{\rho}(\xi,\eta)V_\xi(\xi,\eta)V_x^n(\xi,\eta)+\frac{3}{8}\bar{\rho}(\xi+\Delta\xi,\eta)V_\xi(\xi+\Delta\xi,\eta)V_x^n(\xi+\Delta\xi,\eta))\\
&-AA_2(\xi,\eta)(-\frac{1}{8}\bar{\rho}(\xi+2\Delta\xi,\eta)V_\xi(\xi+2\Delta\xi,\eta)V_x^n(\xi+2\Delta\xi,\eta)\\
&+\frac{6}{8}\bar{\rho}(\xi+\Delta\xi,\eta)V_\xi(\xi+\Delta\xi,\eta)V_x^n(\xi+\Delta\xi,\eta)+\frac{3}{8}\bar{\rho}(\xi,\eta)V_\xi(\xi,\eta)V_x^n(\xi,\eta)))-\\
&\big(BB_1(\xi,\eta)(-\frac{1}{8}\bar{\rho}(\xi-2\Delta\xi,\eta)V_\xi(\xi-2\Delta\xi,\eta)V_x^n(\xi-2\Delta\xi,\eta)\\
&+\frac{6}{8}\bar{\rho}(\xi-\Delta\xi,\eta)V_\xi(\xi-\Delta\xi,\eta)V_x^n(\xi-\Delta\xi,\eta)+\frac{3}{8}\bar{\rho}(\xi,\eta)V_\xi(\xi,\eta)V_x^n(\xi,\eta))\\
&-BB_2(\xi,\eta)(-\frac{1}{8}\bar{\rho}(\xi+\Delta\xi,\eta)V_\xi(\xi+\Delta\xi,\eta)V_x^n(\xi+\Delta\xi,\eta)+\\
&\frac{6}{8}\bar{\rho}^n(\xi,\eta)V_\xi(\xi,\eta)V_x^n(\xi,\eta)+\frac{3}{8}\bar{\rho}(\xi-\Delta\xi,\eta)V_\xi(\xi-\Delta\xi,\eta)V_x^n(\xi-\Delta\xi,\eta)))\Big]\Delta\eta+\\
&\Big[\big(CC_1(\xi,\eta)(-\frac{1}{8}\bar{\rho}(\xi,\eta-\Delta\eta)V_\eta(\xi,\eta-\Delta\eta)V_x^n(\xi,\eta-\Delta\eta)\\
&+\frac{6}{8}\bar{\rho}(\xi,\eta)V_\eta(\xi,\eta)V_x^n(\xi,\eta)+\frac{3}{8}\bar{\rho}(\xi,\eta+\Delta\eta)V_\eta(\xi,\eta+\Delta\eta)V_x^n(\xi,\eta+\Delta\eta))\\
&-CC_2(\xi,\eta)(-\frac{1}{8}\bar{\rho}(\xi,\eta+2\Delta\eta)V_\eta(\xi,\eta+2\Delta\eta)V_x^n(\xi,\eta+2\Delta\eta)\\
&+\frac{6}{8}\bar{\rho}(\xi,\eta+\Delta\eta)V_\eta(\xi,\eta+\Delta\eta)V_x^n(\xi,\eta+\Delta\eta)+\frac{3}{8}\bar{\rho}(\xi,\eta)V_\eta(\xi,\eta)V_x^n(\xi,\eta)))-\\
&\big(DD_1(\xi,\eta)(-\frac{1}{8}\bar{\rho}(\xi,\eta-2\Delta\eta)V_\eta(\xi,\eta-2\Delta\eta)V_x^n(\xi,\eta-2\Delta\eta)\\
&+\frac{6}{8}\bar{\rho}(\xi,\eta-\Delta\eta)V_\eta(\xi,\eta-\Delta\eta)V_x^n(\xi,\eta-\Delta\eta)+\frac{3}{8}\bar{\rho}(\xi,\eta)V_\eta(\xi,\eta)V_x^n(\xi,\eta))\\
&-DD_2(\xi,\eta)(-\frac{1}{8}\bar{\rho}(\xi,\eta+\Delta\eta)V_\eta(\xi,\eta+\Delta\eta)V_x^n(\xi,\eta+\Delta\eta)\\
&+\frac{6}{8}\bar{\rho}(\xi,\eta)V_\eta(\xi,\eta)V_x^n(\xi,\eta)+\frac{3}{8}\bar{\rho}(\xi,\eta-\Delta\eta)V_\eta(\xi,\eta-\Delta\eta)V_x^n(\xi,\eta-\Delta\eta)))\Big]\Delta\xi=\\
&J(\xi,\eta)\Big[\frac{0.75\bar{\rho}C_DRe_D\mu_a}{\rho_wD^2}\big(U_x(\xi,\eta)-V_x^n(\xi,\eta)\big)\Big]\Delta\xi\Delta\eta
\end{aligned}
\tag{6.39}
$$

y momentum:

$$
\begin{aligned}
&J(\xi,\eta)\frac{(\bar{\rho}(\xi,\eta)V_y^n(\xi,\eta)-\bar{\rho}(\xi,\eta)V_y^{n-1}(\xi,\eta))}{\Delta t}\Delta\xi\Delta\eta+\\
&\Big[\big(AA_1(\xi,\eta)(-\frac{1}{8}\bar{\rho}(\xi-\Delta\xi,\eta)V_\xi(\xi-\Delta\xi,\eta)V_y^n(\xi-\Delta\xi,\eta)\\
&+\frac{6}{8}\bar{\rho}(\xi,\eta)V_\xi(\xi,\eta)V_y^n(\xi,\eta)+\frac{3}{8}\bar{\rho}(\xi+\Delta\xi,\eta)V_\xi(\xi+\Delta\xi,\eta)V_y^n(\xi+\Delta\xi,\eta))\\
&-AA_2(\xi,\eta)(-\frac{1}{8}\bar{\rho}(\xi+2\Delta\xi,\eta)V_\xi(\xi+2\Delta\xi,\eta)V_y^n(\xi+2\Delta\xi,\eta)\\
&+\frac{6}{8}\bar{\rho}(\xi+\Delta\xi,\eta)V_\xi(\xi+\Delta\xi,\eta)V_y^n(\xi+\Delta\xi,\eta)+\frac{3}{8}\bar{\rho}(\xi,\eta)V_\xi(\xi,\eta).V_y^n(\xi,\eta))\big)-\\
&\big(BB_1(\xi,\eta)(-\frac{1}{8}\bar{\rho}(\xi-2\Delta\xi,\eta)V_\xi(\xi-2\Delta\xi,\eta)V_y^n(\xi-2\Delta\xi,\eta)\\
&+\frac{6}{8}\bar{\rho}(\xi-\Delta\xi,\eta)V_\xi(\xi-\Delta\xi,\eta)V_y^n(\xi-\Delta\xi,\eta)+\frac{3}{8}\bar{\rho}(\xi,\eta)V_\xi(\xi,\eta)V_y^n(\xi,\eta))\\
&-BB_2(\xi,\eta)(-\frac{1}{8}\bar{\rho}(\xi+\Delta\xi,\eta)V_\xi(\xi+\Delta\xi,\eta)V_y^n(\xi+\Delta\xi,\eta)\\
&+\frac{6}{8}\bar{\rho}^n(\xi,\eta)V_\xi(\xi,\eta)V_y^n(\xi,\eta)+\frac{3}{8}\bar{\rho}(\xi-\Delta\xi,\eta)V_\xi(\xi-\Delta\xi,\eta)V_y^n(\xi-\Delta\xi,\eta))\big)\Big]\Delta\eta+\\
&\Big[\big(CC_1(\xi,\eta)(-\frac{1}{8}\bar{\rho}(\xi,\eta-\Delta\eta)V_\eta(\xi,\eta-\Delta\eta)V_y^n(\xi,\eta-\Delta\eta)\\
&+\frac{6}{8}\bar{\rho}(\xi,\eta)V_\eta(\xi,\eta)V_y^n(\xi,\eta)+\frac{3}{8}\bar{\rho}(\xi,\eta+\Delta\eta)V_\eta(\xi,\eta+\Delta\eta)V_y^n(\xi,\eta+\Delta\eta))\\
&-CC_2(\xi,\eta)(-\frac{1}{8}\bar{\rho}(\xi,\eta+2\Delta\eta)V_\eta(\xi,\eta+2\Delta\eta)V_y^n(\xi,\eta+2\Delta\eta)\\
&+\frac{6}{8}\bar{\rho}(\xi,\eta+\Delta\eta)V_\eta(\xi,\eta+\Delta\eta)V_y^n(\xi,\eta+\Delta\eta)+\frac{3}{8}\bar{\rho}(\xi,\eta)V_\eta(\xi,\eta)V_y^n(\xi,\eta)))\big)-\\
&\big(DD_1(\xi,\eta)(-\frac{1}{8}\bar{\rho}(\xi,\eta-2\Delta\eta)V_\eta(\xi,\eta-2\Delta\eta)V_y^n(\xi,\eta-2\Delta\eta)\\
&+\frac{6}{8}\bar{\rho}(\xi,\eta-\Delta\eta)V_\eta(\xi,\eta-\Delta\eta)V_y^n(\xi,\eta-\Delta\eta)+\frac{3}{8}\bar{\rho}(\xi,\eta)V_\eta(\xi,\eta)V_y^n(\xi,\eta))\\
&-DD_2(\xi,\eta)(-\frac{1}{8}\bar{\rho}(\xi,\eta+\Delta\eta)V_\eta(\xi,\eta+\Delta\eta)V_y^n(\xi,\eta+\Delta\eta)\\
&+\frac{6}{8}\bar{\rho}(\xi,\eta)V_\eta(\xi,\eta)V_y^n(\xi,\eta)+\frac{3}{8}\bar{\rho}(\xi,\eta-\Delta\eta)V_\eta(\xi,\eta-\Delta\eta)V_y^n(\xi,\eta-\Delta\eta)))\big)\Big]\Delta\xi=\\
&J(\xi,\eta)\Big[\frac{0.75\bar{\rho}C_DRe_D\mu_a}{\rho_wD^2}\big(U_y(\xi,\eta)-V_y^n(\xi,\eta)\big)+\bar{\rho}g\big(1-\frac{\rho_a}{\rho_w}\big)\Big]\Delta\xi\Delta\eta
\end{aligned}
\tag{6.40}
$$

which the coefficients of (AA_1,AA_2), (BB_1,BB_2), (CC_1,CC_2) and (DD_1,DD_2) are indicators of directions of droplet-flow in right, left, up and down faces of each control volume, respectively, which equal to 0 or 1, and are explained as follows:

$$
AA_1(\xi,\eta)=Max\big(\frac{(V_\xi(\xi,\eta)+V_\xi(\xi+\Delta\xi,\eta))}{|V_\xi(\xi,\eta)+V_\xi(\xi+\Delta\xi,\eta)|},0\big) \tag{6.41}
$$

$$AA_2(\xi,\eta) = Max\Big(\frac{-(V_\xi(\xi,\eta)+V_\xi(\xi+\Delta\xi,\eta))}{|V_\xi(\xi,\eta)+V_\xi(\xi+\Delta\xi,\eta)|},0\Big) \tag{6.42}$$

$$BB_1(\xi,\eta) = Max\Big(\frac{(V_\xi(\xi-\Delta\xi,\eta)+V_\xi(\xi,\eta))}{|V_\xi(\xi-\Delta\xi,\eta)+V_\xi(\xi,\eta)|},0\Big) \tag{6.43}$$

$$BB_2(\xi,\eta) = Max\Big(\frac{-(V_\xi(\xi-\Delta\xi,\eta)+V_\xi(\xi,\eta))}{|V_\xi(\xi-\Delta\xi,\eta)+V_\xi(\xi,\eta)|},0\Big) \tag{6.44}$$

$$CC_1(\xi,\eta) = Max\Big(\frac{(V_\eta(\xi,\eta)+V_\eta(\xi,\eta+\Delta\eta))}{|V_\eta(\xi,\eta)+V_\eta(\xi,\eta+\Delta\eta)|},0\Big) \tag{6.45}$$

$$CC_2(\xi,\eta) = Max\Big(\frac{-(V_\eta(\xi,\eta)+V_\eta(\xi,\eta+\Delta\eta))}{|V_\eta(\xi,\eta)+V_\eta(\xi,\eta+\Delta\eta)|},0\Big) \tag{6.46}$$

$$DD_1(\xi,\eta) = Max\Big(\frac{(V_\eta(\xi,\eta-\Delta\eta)+V_\eta(\xi,\eta))}{|V_\eta(\xi,\eta-\delta\eta)+V_\eta(\xi,\eta)|},0\Big) \tag{6.47}$$

$$DD_2(\xi,\eta) = Max\Big(\frac{-(V_\eta(\xi,\eta-\Delta\eta)+V_\eta(\xi,\eta))}{|V_\eta(\xi,\eta-\Delta\eta)+V_\eta(\xi,\eta)|},0\Big) \tag{6.48}$$

6.3 Applying of Computational Method

6.3.1 Initial guess values for inner region

$$\begin{cases} \bar{\rho}(\xi,\eta) = \bar{\rho}_\infty \\ V_x(\xi,\eta) = U_x(\xi,1) \\ V_y(\xi,\eta) = U_y(\xi,1) \end{cases} \tag{6.49}$$

6.3.2 Outer boundary conditions for farfield ($j = j_{Max}$ or $\eta = 1$)

The far-field condition is implemented to outer boundary i.e. the last loop of grid is far enough in order to appoint the same flow properties and values as the ones for free stream;

$$\begin{cases} \bar{\rho}(\xi,1) = \bar{\rho}_\infty \\ V_x(\xi,1) = U_x(\xi,1) \\ V_y(\xi,1) = U_y(\xi,1) \end{cases} \tag{6.50}$$

6.3.3 Inner boundary conditions on airfoil ($j = 1$ or $\eta = 0$)

To implement the inner boundary condition i.e. the values on the surface of the airfoil (j=1 or $\eta = 0$), the permeable or switching boundary condition will be applied to the body. If the normal component of contra-variant droplet-velocity in the transformed coordinate is positive, it means that droplets just are about to leave the surface body of the airfoil. But if this normal velocity is negative, actually means droplets would

collide with the body surface. Therefore, when the iteration method is utilized to find out the droplet's apparent density and velocity components, once the calculations lead to the positive value of the normal contra-variant velocity, all flow properties will equal to zero (Dirichlet boundary condition) for truly satisfying the wall boundary condition on the airfoil, whereas while the normal velocity is negative, all flow properties equal to the equivalent values of the grid points just next to the body (Neumann boundary condition), and this is why the B.C. on the body is named switching boundary condition (Cao et al., 2016a,b, 2012; Sznajder, 2015). Then inner boundary condition will be:

$$for \quad V_\eta(\xi,\Delta\eta) \geq 0 \rightarrow \begin{cases} \bar{\rho}(\xi,0) = 0 \\ V_x(\xi,0) = 0 \\ V_y(\xi,0) = 0 \end{cases} \tag{6.51}$$

$$for \quad V_\eta(\xi,\Delta\eta) < 0 \rightarrow \begin{cases} \bar{\rho}(\xi,0) = \bar{\rho}(\xi,\Delta\eta) \\ V_x(\xi,0) = V_x(\xi,\Delta\eta) \\ V_y(\xi,0) = V_y(\xi,\Delta\eta) \end{cases} \tag{6.52}$$

6.3.4 Updating values on "branch cuts" (reentrants)

$$\bar{\rho}(0,\eta) = \frac{\bar{\rho}(\Delta\xi,\eta) + \bar{\rho}(1-\Delta\xi,\eta)}{2} \tag{6.53}$$

$$V_x(0,\eta) = \frac{V_x(\Delta\xi,\eta) + V_x(1-\Delta\xi,\eta)}{2} \tag{6.54}$$

$$V_y(0,\eta) = \frac{V_y(\Delta\xi,\eta) + V_y(1-\Delta\xi,\eta)}{2} \tag{6.55}$$

$$\bar{\rho}(1,\eta) = \frac{\bar{\rho}(\Delta\xi,\eta) + \bar{\rho}(1-\Delta\xi,\eta)}{2} \tag{6.56}$$

$$V_x(1,\eta) = \frac{V_x(\Delta\xi,\eta) + V_x(1-\Delta\xi,\eta)}{2} \tag{6.57}$$

$$V_y(1,\eta) = \frac{V_y(\Delta\xi,\eta) + V_y(1-\Delta\xi,\eta)}{2} \tag{6.58}$$

6.3.5 Calculations for inner region

The mass and momentum fluxes through the control volume in the ξ,η coordinate are needed for Cao's approach. Besides, to obtain more accurate results, QUICK scheme will be applied for the solution of governing equations of water droplets.

The probabilities of the mass fluxes through the 4 faces of a control volume in 2D and ξ, η coordinate are as explained below:

$$\begin{aligned} for \quad V_\xi\big|^{east} \geq 0 \ (AA_1(\xi,\eta)=1, AA_2(\xi,\eta)=0), \\ MassFlux = -\frac{1}{8}\big[\bar{\rho}^n(\xi-\Delta\xi,\eta)V_\xi^{n-1}(\xi-\Delta\xi,\eta)\big] + \\ \frac{6}{8}\big[\bar{\rho}^n(\xi,\eta)V_\xi^{n-1}(\xi,\eta)\big] + \frac{3}{8}\big[\bar{\rho}^n(\xi+\Delta\xi,\eta)V_\xi^{n-1}(\xi+\Delta\xi,\eta)\big] \end{aligned} \tag{6.59}$$

$$\begin{aligned} for \quad V_\xi\big|^{east} < 0 \ (AA_1(\xi,\eta)=0, AA_2(\xi,\eta)=1), \\ MassFlux = -\frac{1}{8}\big[\bar{\rho}^n(\xi+2\Delta\xi,\eta)V_\xi^{n-1}(\xi+2\Delta\xi,\eta)\big] + \\ \frac{6}{8}\big[\bar{\rho}^n(\xi+\Delta\xi,\eta)V_\xi^{n-1}(\xi+\Delta\xi,\eta)\big] + \frac{3}{8}\big[\bar{\rho}^n(\xi,\eta)V_\xi^{n-1}(\xi,\eta)\big] \end{aligned} \tag{6.60}$$

$$\begin{aligned} for \quad V_\xi\big|_{west} \geq 0 \ (BB_1(\xi,\eta)=1, BB_2(\xi,\eta)=0), \\ MassFlux = -\frac{1}{8}\big[\bar{\rho}^n(\xi-2\Delta\xi,\eta)V_\xi^{n-1}(\xi-2\Delta\xi,\eta)\big] + \\ \frac{6}{8}\big[\bar{\rho}^n(\xi-\Delta\xi,\eta)V_\xi^{n-1}(\xi-\Delta\xi,\eta)\big] + \frac{3}{8}\big[\bar{\rho}^n(\xi,\eta)V_\xi^{n-1}(\xi,\eta)\big] \end{aligned} \tag{6.61}$$

$$\begin{aligned} for \quad V_\xi\big|_{west} < 0 \ (BB_1(\xi,\eta)=0, BB_2(\xi,\eta)=1), \\ MassFlux = -\frac{1}{8}\big[\bar{\rho}^n(\xi+\Delta\xi,\eta)V_\xi^{n-1}(\xi+\Delta\xi,\eta)\big] + \\ \frac{6}{8}\big[\bar{\rho}^n(\xi,\eta)V_\xi^{n-1}(\xi,\eta)\big] + \frac{3}{8}\big[\bar{\rho}^n(\xi-\Delta\xi,\eta)V_\xi^{n-1}(\xi-\Delta\xi,\eta)\big] \end{aligned} \tag{6.62}$$

$$\begin{aligned} for \quad V_\eta\big|^{north} \geq 0 \ (CC_1(\xi,\eta)=1, CC_2(\xi,\eta)=0), \\ MassFlux = -\frac{1}{8}\big[\bar{\rho}^n(\xi,\eta-\Delta\eta)V_\xi^{n-1}(\xi,\eta-\Delta\eta)\big] + \\ \frac{6}{8}\big[\bar{\rho}^n(\xi,\eta)V_\xi^{n-1}(\xi,\eta)\big] + \frac{3}{8}\big[\bar{\rho}^n(\xi,\eta+\Delta\eta)V_\xi^{n-1}(\xi,\eta+\Delta\eta)\big] \end{aligned} \tag{6.63}$$

$$\begin{aligned} for \quad V_\eta\big|^{north} < 0 \ (CC_1(\xi,\eta)=0, CC_2(\xi,\eta)=1), \\ MassFlux = -\frac{1}{8}\big[\bar{\rho}^n(\xi,\eta+2\Delta\eta)V_\xi^{n-1}(\xi,\eta+2\Delta\eta)\big] + \\ \frac{6}{8}\big[\bar{\rho}^n(\xi,\eta+\Delta\eta)V_\xi^{n-1}(\xi,\eta+\Delta\eta)\big] + \frac{3}{8}\big[\bar{\rho}^n(\xi,\eta)V_\xi^{n-1}(\xi,\eta)\big] \end{aligned} \tag{6.64}$$

$$\begin{aligned} for \quad V_\eta\big|_{south} \geq 0 \ (DD_1(\xi,\eta)=1, DD_2(\xi,\eta)=0), \\ MassFlux = -\frac{1}{8}\big[\bar{\rho}^n(\xi,\eta-2\Delta\eta)V_\xi^{n-1}(\xi,\eta-2\Delta\eta)\big] + \\ \frac{6}{8}\big[\bar{\rho}^n(\xi,\eta-\Delta\eta)V_\xi^{n-1}(\xi,\eta-\Delta\eta)\big] + \frac{3}{8}\big[\bar{\rho}^n(\xi,\eta)V_\xi^{n-1}(\xi,\eta)\big] \end{aligned} \tag{6.65}$$

$$for \quad V_\eta\big|_{south} < 0 \ (DD_1(\xi,\eta)=0, DD_2(\xi,\eta)=1),$$
$$MassFlux = -\frac{1}{8}\big[\bar{\rho}^n(\xi,\eta+\Delta\eta)V_\xi^{n-1}(\xi,\eta+\Delta\eta)\big]+ \tag{6.66}$$
$$\frac{6}{8}\big[\bar{\rho}^n(\xi,\eta)V_\xi^{n-1}(\xi,\eta)\big]+\frac{3}{8}\big[\bar{\rho}^n(\xi,\eta-\Delta\eta)V_\xi^{n-1}(\xi,\eta-\Delta\eta)\big]$$

The probabilities of the ξ-momentum fluxes for a control volume which the mass fluxes pass through the 4 faces in 2D and ξ,η coordinate:

$$for \quad V_\xi\big|^{east} \geq 0 \ (AA_1(\xi,\eta)=1, AA_2(\xi,\eta)=0),$$
$$\xi - MomentumFlux = -\frac{1}{8}\big[\bar{\rho}^n(\xi-\Delta\xi,\eta)V_\xi^{n-1}(\xi-\Delta\xi,\eta)\big].V_x^n(\xi-\Delta\xi,\eta)+$$
$$\frac{6}{8}\big[\bar{\rho}^n(\xi,\eta)V_\xi^{n-1}(\xi,\eta)\big].V_x^n(\xi,\eta)+\frac{3}{8}\big[\bar{\rho}^n(\xi+\Delta\xi,\eta)V_\xi^{n-1}(\xi+\Delta\xi,\eta)\big].V_x^n(\xi+\Delta\xi,\eta) \tag{6.67}$$

$$for \quad V_\xi\big|^{east} < 0 \ (AA_1(\xi,\eta)=0, AA_2(\xi,\eta)=1),$$
$$\xi - MomentumFlux = -\frac{1}{8}\big[\bar{\rho}^n(\xi+2\Delta\xi,\eta)V_\xi^{n-1}(\xi+2\Delta\xi,\eta)\big].V_x^n(\xi+2\Delta\xi,\eta)+$$
$$\frac{6}{8}\big[\bar{\rho}^n(\xi+\Delta\xi,\eta)V_\xi^{n-1}(\xi+\Delta\xi,\eta)\big].V_x^n(\xi+\Delta\xi,\eta)+\frac{3}{8}\big[\bar{\rho}^n(\xi,\eta)V_\xi^{n-1}(\xi,\eta)\big].V_x^n(\xi,\eta) \tag{6.68}$$

$$for \quad V_\xi\big|_{west} \geq 0 \ (BB_1(\xi,\eta)=1, BB_2(\xi,\eta)=0),$$
$$\xi - MomentumFlux = -\frac{1}{8}\big[\bar{\rho}^n(\xi-2\Delta\xi,\eta)V_\xi^{n-1}(\xi-2\Delta\xi,\eta)\big].V_x^n(\xi-2\Delta\xi,\eta)+$$
$$\frac{6}{8}\big[\bar{\rho}^n(\xi-\Delta\xi,\eta)V_\xi^{n-1}(\xi-\Delta\xi,\eta)\big].V_x^n(\xi-\Delta\xi,\eta)+\frac{3}{8}\big[\bar{\rho}^n(\xi,\eta)V_\xi^{n-1}(\xi,\eta)\big].V_x^n(\xi,\eta) \tag{6.69}$$

$$for \quad V_\xi\big|_{west} < 0 \ (BB_1(\xi,\eta)=0, BB_2(\xi,\eta)=1),$$
$$\xi - MomentumFlux = -\frac{1}{8}\big[\bar{\rho}^n(\xi+\Delta\xi,\eta)V_\xi^{n-1}(\xi+\Delta\xi,\eta)\big].V_x^n(\xi+\Delta\xi,\eta)+$$
$$\frac{6}{8}\big[\bar{\rho}^n(\xi,\eta)V_\xi^{n-1}(\xi,\eta)\big].V_x^n(\xi,\eta)+\frac{3}{8}\big[\bar{\rho}^n(\xi-\Delta\xi,\eta)V_\xi^{n-1}(\xi-\Delta\xi,\eta)\big].V_x^n(\xi-\Delta\xi,\eta) \tag{6.70}$$

$$for \quad V_\eta\big|^{north} \geq 0 \ (CC_1(\xi,\eta)=1, CC_2(\xi,\eta)=0),$$
$$\xi - MomentumFlux = -\frac{1}{8}\big[\bar{\rho}^n(\xi,\eta-\Delta\eta)V_\xi^{n-1}(\xi,\eta-\Delta\eta)\big].V_x^n(\xi,\eta-\Delta\eta)+$$
$$\frac{6}{8}\big[\bar{\rho}^n(\xi,\eta)V_\xi^{n-1}(\xi,\eta)\big].V_x^n(\xi,\eta)+\frac{3}{8}\big[\bar{\rho}^n(\xi,\eta+\Delta\eta)V_\xi^{n-1}(\xi,\eta+\Delta\eta)\big].V_x^n(\xi,\eta+\Delta\eta) \tag{6.71}$$

$$for \quad V_\eta\big|^{north} < 0 \ (CC_1(\xi,\eta)=0, CC_2(\xi,\eta)=1),$$
$$\xi - MomentumFlux = -\frac{1}{8}\big[\bar{\rho}^n(\xi,\eta-2\Delta\eta)V_\xi^{n-1}(\xi,\eta-2\Delta\eta)\big].V_x^n(\xi,\eta-2\Delta\eta)+$$
$$\frac{6}{8}\big[\bar{\rho}^n(\xi,\eta-\Delta\eta)V_\xi^{n-1}(\xi,\eta-\Delta\eta)\big].V_x^n(\xi,\eta-\Delta\eta)+\frac{3}{8}\big[\bar{\rho}^n(\xi,\eta)V_\xi^{n-1}(\xi,\eta)\big].V_x^n(\xi,\eta) \tag{6.72}$$

$$for \quad V_\eta\big|_{south} \geq 0 \ (DD_1(\xi,\eta)=1, DD_2(\xi,\eta)=0),$$
$$\xi - MomentumFlux = -\frac{1}{8}\big[\bar{\rho}^n(\xi,\eta-2\Delta\eta)V_\xi^{n-1}(\xi,\eta-2\Delta\eta)\big].V_x^n(\xi,\eta-2\Delta\eta)+$$
$$\frac{6}{8}\big[\bar{\rho}^n(\xi,\eta-\Delta\eta)V_\xi^{n-1}(\xi,\eta-\Delta\eta)\big].V_x^n(\xi,\eta-\Delta\eta)+\frac{3}{8}\big[\bar{\rho}^n(\xi,\eta)V_\xi^{n-1}(\xi,\eta)\big].V_x^n(\xi,\eta) \tag{6.73}$$

$$for \quad V_\eta\big|_{south} < 0 \ (DD_1(\xi,\eta)=0, DD_2(\xi,\eta)=1),$$
$$\xi - MomentumFlux = -\frac{1}{8}\big[\bar{\rho}^n(\xi,\eta+\Delta\eta)V_\xi^{n-1}(\xi,\eta+\Delta\eta)\big].V_x^n(\xi,\eta+\Delta\eta)+$$
$$\frac{6}{8}\big[\bar{\rho}^n(\xi,\eta)V_\xi^{n-1}(\xi,\eta)\big].V_x^n(\xi,\eta)+\frac{3}{8}\big[\bar{\rho}^n(\xi,\eta-\Delta\eta)V_\xi^{n-1}(\xi,\eta-\Delta\eta)\big].V_x^n(\xi,\eta-\Delta\eta) \tag{6.74}$$

The probabilities of the η-momentum fluxes for a control volume which the mass fluxes pass through the 4 faces in 2D and ξ,η coordinate:

$$for \quad V_\xi\big|^{east} \geq 0 \ (AA_1(\xi,\eta)=1, AA_2(\xi,\eta)=0),$$
$$\eta - MomentumFlux = -\frac{1}{8}\big[\bar{\rho}^n(\xi-\Delta\xi,\eta)V_\xi^{n-1}(\xi-\Delta\xi,\eta)\big].V_y^n(\xi-\Delta\xi,\eta)+$$
$$\frac{6}{8}\big[\bar{\rho}^n(\xi,\eta)V_\xi^{n-1}(\xi,\eta)\big].V_y^n(\xi,\eta)+\frac{3}{8}\big[\bar{\rho}^n(\xi+\Delta\xi,\eta)V_\xi^{n-1}(\xi+\Delta\xi,\eta)\big].V_y^n(\xi+\Delta\xi,\eta) \tag{6.75}$$

$$for \quad V_\xi\big|^{east} < 0 \ (AA_1(\xi,\eta)=0, AA_2(\xi,\eta)=1),$$
$$\eta - MomentumFlux = -\frac{1}{8}\big[\bar{\rho}^n(\xi+2\Delta\xi,\eta)V_\xi^{n-1}(\xi+2\Delta\xi,\eta)\big].V_y^n(\xi+2\Delta\xi,\eta)+$$
$$\frac{6}{8}\big[\bar{\rho}^n(\xi+\Delta\xi,\eta)V_\xi^{n-1}(\xi+\Delta\xi,\eta)\big].V_y^n(\xi+\Delta\xi,\eta)+\frac{3}{8}\big[\bar{\rho}^n(\xi,\eta)V_\xi^{n-1}(\xi,\eta)\big].V_y^n(\xi,\eta) \tag{6.76}$$

$$for \quad V_\xi\big|_{west} \geq 0 \ (BB_1(\xi,\eta)=1, BB_2(\xi,\eta)=0),$$
$$\eta - MomentumFlux = -\frac{1}{8}\big[\bar{\rho}^n(\xi-2\Delta\xi,\eta)V_\xi^{n-1}(\xi-2\Delta\xi,\eta)\big].V_y^n(\xi-2\Delta\xi,\eta)+$$
$$\frac{6}{8}\big[\bar{\rho}^n(\xi-\Delta\xi,\eta)V_\xi^{n-1}(\xi-\Delta\xi,\eta)\big].V_y^n(\xi-\Delta\xi,\eta)+\frac{3}{8}\big[\bar{\rho}^n(\xi,\eta)V_\xi^{n-1}(\xi,\eta)\big].V_y^n(\xi,\eta) \tag{6.77}$$

$$for \quad V_\xi\big|_{west} < 0 \ (BB_1(\xi,\eta)=0, BB_2(\xi,\eta)=1),$$

$$\eta - MomentumFlux = -\frac{1}{8}\left[\bar{\rho}^n(\xi+\Delta\xi,\eta)V_\xi^{n-1}(\xi+\Delta\xi,\eta)\right].V_y^n(\xi+\Delta\xi,\eta)+$$
$$\frac{6}{8}\left[\bar{\rho}^n(\xi,\eta)V_\xi^{n-1}(\xi,\eta)\right].V_y^n(\xi,\eta)+\frac{3}{8}\left[\bar{\rho}^n(\xi-\Delta\xi,\eta)V_\xi^{n-1}(\xi-\Delta\xi,\eta)\right].V_y^n(\xi-\Delta\xi,\eta) \tag{6.78}$$

$$for \quad V_\eta\big|^{north} \geq 0 \ (CC_1(\xi,\eta)=1, CC_2(\xi,\eta)=0),$$

$$\eta - MomentumFlux = -\frac{1}{8}\left[\bar{\rho}^n(\xi,\eta-\Delta\eta)V_\xi^{n-1}(\xi,\eta-\Delta\eta)\right].V_y^n(\xi,\eta-\Delta\eta)+$$
$$\frac{6}{8}\left[\bar{\rho}^n(\xi,\eta)V_\xi^{n-1}(\xi,\eta)\right].V_y^n(\xi,\eta)+\frac{3}{8}\left[\bar{\rho}^n(\xi,\eta+\Delta\eta)V_\xi^{n-1}(\xi,\eta+\Delta\eta)\right].V_y^n(\xi,\eta+\Delta\eta) \tag{6.79}$$

$$for \quad V_\eta\big|^{north} < 0 \ (CC_1(\xi,\eta)=0, CC_2(\xi,\eta)=1),$$

$$\eta - MomentumFlux = -\frac{1}{8}\left[\bar{\rho}^n(\xi,\eta-2\Delta\eta)V_\xi^{n-1}(\xi,\eta-2\Delta\eta)\right].V_y^n(\xi,\eta-2\Delta\eta)+$$
$$\frac{6}{8}\left[\bar{\rho}^n(\xi,\eta-\Delta\eta)V_\xi^{n-1}(\xi,\eta-\Delta\eta)\right].V_y^n(\xi,\eta-\Delta\eta)+\frac{3}{8}\left[\bar{\rho}^n(\xi,\eta)V_\xi^{n-1}(\xi,\eta)\right].V_y^n(\xi,\eta) \tag{6.80}$$

$$for \quad V_\eta\big|_{south} \geq 0 \ (DD_1(\xi,\eta)=1, DD_2(\xi,\eta)=0),$$

$$\eta - MomentumFlux = -\frac{1}{8}\left[\bar{\rho}^n(\xi,\eta-2\Delta\eta)V_\xi^{n-1}(\xi,\eta-2\Delta\eta)\right].V_y^n(\xi,\eta-2\Delta\eta)+$$
$$\frac{6}{8}\left[\bar{\rho}^n(\xi,\eta-\Delta\eta)V_\xi^{n-1}(\xi,\eta-\Delta\eta)\right].V_y^n(\xi,\eta-\Delta\eta)+\frac{3}{8}\left[\bar{\rho}^n(\xi,\eta)V_\xi^{n-1}(\xi,\eta)\right].V_y^n(\xi,\eta) \tag{6.81}$$

$$for \quad V_\eta\big|_{south} < 0 \ (DD_1(\xi,\eta)=0, DD_2(\xi,\eta)=1),$$

$$\eta - MomentumFlux = -\frac{1}{8}\left[\bar{\rho}^n(\xi,\eta+\Delta\eta)V_\xi^{n-1}(\xi,\eta+\Delta\eta)\right].V_y^n(\xi,\eta+\Delta\eta)+$$
$$\frac{6}{8}\left[\bar{\rho}^n(\xi,\eta)V_\xi^{n-1}(\xi,\eta)\right].V_y^n(\xi,\eta)+\frac{3}{8}\left[\bar{\rho}^n(\xi,\eta-\Delta\eta)V_\xi^{n-1}(\xi,\eta-\Delta\eta)\right].V_y^n(\xi,\eta-\Delta\eta) \tag{6.82}$$

When the iteration method is implemented, there are two possibilities of mass fluxes (entering or exiting the face) for each face of the control volume. Therefore, in 2D, ξ,η coordinate there are 16 probabilities for 4 faces of each control volume as described in Table 6.1.

Table 6.1 : All 16 probabilities of the mass fluxes of each control volume in the 2D computational domain (i.e. ξ, η coordinate) based on the contra-variant velocity components through the 4 faces. It is assumed that zero possibilities are also included in the positive possibilities.

Possibilities	$V_\xi\big\vert^{east}$	$V_\xi\big\vert_{west}$	$V_\eta\big\vert^{north}$	$V_\eta\big\vert_{south}$
1	+	+	+	+
2	+	+	+	-
3	+	+	-	+
4	+	+	-	-
5	+	-	+	+
6	+	-	+	-
7	+	-	-	+
8	+	-	-	-
9	-	+	+	+
10	-	+	+	-
11	-	+	-	+
12	-	+	-	-
13	-	-	+	+
14	-	-	+	-
15	-	-	-	+
16	-	-	-	-

By rearranging of the transferred mass equation for applying Line Successive Over Relaxation (LSOR) method in η direction, it will be:

$$\begin{aligned} A_{SS9}(\eta)\bar{\rho}(\xi,\eta-2\Delta\eta)+A_{S9}(\eta)\bar{\rho}(\xi,\eta-\Delta\eta)+A_{P9}(\eta)\bar{\rho}(\xi,\eta)+ \\ A_{N9}(\eta)\bar{\rho}(\xi,\eta+\Delta\eta)+A_{NN9}(\eta)\bar{\rho}(\xi,\eta+2\Delta\eta)=b_9(\eta) \end{aligned} \tag{6.83}$$

The $A_{SS9}(\eta)$,$A_{S9}(\eta)$, $A_{P9}(\eta)$, $A_{N9}(\eta)$, $A_{NN9}(\eta)$ and $b_9(\eta)$ coefficients for different probabilities of Table 6.1 are as follows:

$$A_{SS9}(\eta)=\Big[DD_1(\xi,\eta)\frac{1}{8}V_\eta(\xi,\eta-2\Delta\eta)\Delta\xi\Big] \tag{6.84}$$

$$\begin{aligned} A_{S9}(\eta)=\big[&-CC_1(\xi,\eta)\frac{1}{8}V_\eta(\xi,\eta-\Delta\eta)\Delta\xi \\ &-DD_1(\xi,\eta)\frac{6}{8}V_\eta(\xi,\eta-\Delta\eta)\Delta\xi \\ &+DD_2(\xi,\eta)\frac{3}{8}V_\eta(\xi,\eta-\Delta\eta)\Delta\xi\big] \end{aligned} \tag{6.85}$$

$$
\begin{aligned}
A_{P9}(\eta) = \big[&\frac{J(\xi,\eta)}{\Delta t}\Delta\xi\Delta\eta \\
&+AA_1(\xi,\eta)\frac{6}{8}V_\xi(\xi,\eta)\Delta\eta - AA_2(\xi,\eta)\frac{3}{8}V_\xi(\xi,\eta)\Delta\eta \\
&-BB_1(\xi,\eta)\frac{3}{8}V_\xi(\xi,\eta)\Delta\eta + BB_2(\xi,\eta)\frac{6}{8}V_\xi(\xi,\eta)\Delta\eta \\
&+CC_1(\xi,\eta)\frac{6}{8}V_\eta(\xi,\eta)\Delta\xi - CC_2(\xi,\eta)\frac{3}{8}V_\eta(\xi,\eta)\Delta\xi \\
&-DD_1(\xi,\eta)\frac{3}{8}V_\eta(\xi,\eta)\Delta\xi + DD_2(\xi,\eta)\frac{6}{8}V_\eta(\xi,\eta)\Delta\xi\big]
\end{aligned} \tag{6.86}
$$

$$
\begin{aligned}
A_{N9}(\eta) = \big[&CC_1(\xi,\eta)\frac{3}{8}V_\eta(\xi,\eta+\Delta\eta)\Delta\xi \\
&-CC_2(\xi,\eta)\frac{6}{8}V_\eta(\xi,\eta+\Delta\eta)\Delta\xi \\
&-DD_2(\xi,\eta)\frac{1}{8}V_\eta(\xi,\eta+\Delta\eta)\Delta\xi\big]
\end{aligned} \tag{6.87}
$$

$$
A_{NN9}(\eta) = \big[CC_2(\xi,\eta)\frac{1}{8}V_\eta(\xi,\eta+2\Delta\eta)\Delta\xi\big] \tag{6.88}
$$

$$
\begin{aligned}
b_9(\eta) = &\frac{J(\xi,\eta)}{\Delta t}\Delta\xi\Delta\eta\bar{\rho}(\xi,\eta) \\
&-AA_1(\xi,\eta)\Big(-\frac{1}{8}\big(\bar{\rho}(\xi-\Delta\xi,\eta)V_\xi(\xi-\Delta\xi,\eta) \\
&+\frac{3}{8}\bar{\rho}(\xi+\Delta\xi,\eta)V_\xi(\xi+\Delta\xi,\eta)\Big)\Delta\eta \\
&+AA_2(\xi,\eta)\Big(-\frac{1}{8}\big(\bar{\rho}(\xi+2\Delta\xi,\eta)V_\xi(\xi+2\Delta\xi,\eta) \\
&+\frac{6}{8}\bar{\rho}(\xi+\Delta\xi,\eta)V_\xi(\xi+\Delta\xi,\eta)\Big)\Delta\eta \\
&+BB_1(\xi,\eta)\Big(-\frac{1}{8}\big(\bar{\rho}(\xi-2\Delta\xi,\eta)V_\xi(\xi-2\Delta\xi,\eta) \\
&+\frac{6}{8}\bar{\rho}(\xi-\Delta\xi,\eta)V_\xi(\xi-\Delta\xi,\eta)\Big)\Delta\eta \\
&-BB_2(\xi,\eta)\Big(-\frac{1}{8}\big(\bar{\rho}(\xi+\Delta\xi,\eta)V_\xi(\xi+\Delta\xi,\eta) \\
&+\frac{3}{8}\bar{\rho}(\xi-\Delta\xi,\eta)V_\xi(\xi-\Delta\xi,\eta)\Big)\Delta\eta
\end{aligned} \tag{6.89}
$$

for $j = 2$, always $DD_1 = 0$ then these coefficients are as:

$$
A_{SS9}(\eta) = \big[0\big] \tag{6.90}
$$

$$
A_{S9}(\eta) = \big[0\big] \tag{6.91}
$$

$$
\begin{aligned}
A_{P9}(\eta) = \big[&\frac{J(\xi,\eta)}{\Delta t}\Delta\xi\Delta\eta \\
&+AA_1(\xi,\eta)\frac{6}{8}V_\xi(\xi,\eta)\Delta\eta - AA_2(\xi,\eta)\frac{3}{8}V_\xi(\xi,\eta)\Delta\eta \\
&-BB_1(\xi,\eta)\frac{3}{8}V_\xi(\xi,\eta)\Delta\eta + BB_2(\xi,\eta)\frac{6}{8}V_\xi(\xi,\eta)\Delta\eta \\
&+CC_1(\xi,\eta)\frac{6}{8}V_\eta(\xi,\eta)\Delta\xi - CC_2(\xi,\eta)\frac{3}{8}V_\eta(\xi,\eta)\Delta\xi \\
&+DD_2(\xi,\eta)\frac{6}{8}V_\eta(\xi,\eta)\Delta\xi\big]
\end{aligned} \tag{6.92}
$$

$$
\begin{aligned}
A_{N9}(\eta) = \big[&CC_1(\xi,\eta)\frac{3}{8}V_\eta(\xi,\eta+\Delta\eta)\Delta\xi \\
&-CC_2(\xi,\eta)\frac{6}{8}V_\eta(\xi,\eta+\Delta\eta)\Delta\xi \\
&-DD_2(\xi,\eta)\frac{1}{8}V_\eta(\xi,\eta+\Delta\eta)\Delta\xi\big]
\end{aligned} \tag{6.93}
$$

$$
A_{NN9}(\eta) = \big[CC_2(\xi,\eta)\frac{1}{8}V_\eta(\xi,\eta+2\Delta\eta)\Delta\xi\big] \tag{6.94}
$$

$$
\begin{aligned}
b_9(\eta) = &\frac{J(\xi,\eta)}{\Delta t}\Delta\xi\Delta\eta\bar{\rho}(\xi,\eta) \\
&-AA_1(\xi,\eta)\Big(-\frac{1}{8}\big(\bar{\rho}(\xi-\Delta\xi,\eta)V_\xi(\xi-\Delta\xi,\eta) \\
&+\frac{3}{8}\bar{\rho}(\xi+\Delta\xi,\eta)V_\xi(\xi+\Delta\xi,\eta)\Big)\Delta\eta \\
&+AA_2(\xi,\eta)\Big(-\frac{1}{8}\big(\bar{\rho}(\xi+2\Delta\xi,\eta)V_\xi(\xi+2\Delta\xi,\eta) \\
&+\frac{6}{8}\bar{\rho}(\xi+\Delta\xi,\eta)V_\xi(\xi+\Delta\xi,\eta)\Big)\Delta\eta \\
&+BB_1(\xi,\eta)\Big(-\frac{1}{8}\big(\bar{\rho}(\xi-2\Delta\xi,\eta)V_\xi(\xi-2\Delta\xi,\eta) \\
&+\frac{6}{8}\bar{\rho}(\xi-\Delta\xi,\eta)V_\xi(\xi-\Delta\xi,\eta)\Big)\Delta\eta \\
&-BB_2(\xi,\eta)\Big(-\frac{1}{8}\big(\bar{\rho}(\xi+\Delta\xi,\eta)V_\xi(\xi+\Delta\xi,\eta) \\
&+\frac{3}{8}\bar{\rho}(\xi-\Delta\xi,\eta)V_\xi(\xi-\Delta\xi,\eta)\Big)\Delta\eta - \\
&\big(-CC_1(\xi,\eta)\frac{1}{8}V_\eta(\xi,\eta-\Delta\eta)\Delta\xi \\
&+DD_2(\xi,\eta)\frac{3}{8}V_\eta(\xi,\eta-\Delta\eta)\Delta\xi\big).\bar{\rho}(\xi,\eta-\Delta\eta)
\end{aligned} \tag{6.95}
$$

for $j = j_{Max} - 1$ the coefficients will be:

$$
A_{SS9}(\eta) = \big[DD_1(\xi,\eta)\frac{1}{8}V_\eta(\xi,\eta-2\Delta\eta)\Delta\xi\big] \tag{6.96}
$$

$$
\begin{aligned}
A_{S9}(\eta) = \big[& -CC_1(\xi,\eta)\frac{1}{8}V_\eta(\xi,\eta-\Delta\eta)\Delta\xi \\
& -DD_1(\xi,\eta)\frac{6}{8}V_\eta(\xi,\eta-\Delta\eta)\Delta\xi \\
& +DD_2(\xi,\eta)\frac{3}{8}V_\eta(\xi,\eta-\Delta\eta)\Delta\xi\big]
\end{aligned} \tag{6.97}
$$

$$
\begin{aligned}
A_{P9}(\eta) = \big[& \frac{J(\xi,\eta)}{\Delta t}\Delta\xi\Delta\eta \\
& +AA_1(\xi,\eta)\frac{6}{8}V_\xi(\xi,\eta)\Delta\eta - AA_2(\xi,\eta)\frac{3}{8}V_\xi(\xi,\eta)\Delta\eta \\
& -BB_1(\xi,\eta)\frac{3}{8}V_\xi(\xi,\eta)\Delta\eta + BB_2(\xi,\eta)\frac{6}{8}V_\xi(\xi,\eta)\Delta\eta \\
& +CC_1(\xi,\eta)\frac{6}{8}V_\eta(\xi,\eta)\Delta\xi - CC_2(\xi,\eta)\frac{3}{8}V_\eta(\xi,\eta)\Delta\xi \\
& -DD_1(\xi,\eta)\frac{3}{8}V_\eta(\xi,\eta)\Delta\xi + DD_2(\xi,\eta)\frac{6}{8}V_\eta(\xi,\eta)\Delta\xi\big]
\end{aligned} \tag{6.98}
$$

$$
A_{N9}(\eta) = \big[0\big] \tag{6.99}
$$

$$
A_{NN9}(\eta) = \big[0\big] \tag{6.100}
$$

$$
\begin{aligned}
b_9(\eta) = & \frac{J(\xi,\eta)}{\Delta t}\Delta\xi\Delta\eta\bar{\rho}(\xi,\eta) \\
& -AA_1(\xi,\eta)\Big(-\frac{1}{8}\big(\bar{\rho}(\xi-\Delta\xi,\eta)V_\xi(\xi-\Delta\xi,\eta) \\
& +\frac{3}{8}\bar{\rho}(\xi+\Delta\xi,\eta)V_\xi(\xi+\Delta\xi,\eta)\Big)\Delta\eta \\
& +AA_2(\xi,\eta)\Big(-\frac{1}{8}\big(\bar{\rho}(\xi+2\Delta\xi,\eta)V_\xi(\xi+2\Delta\xi,\eta) \\
& +\frac{6}{8}\bar{\rho}(\xi+\Delta\xi,\eta)V_\xi(\xi+\Delta\xi,\eta)\Big)\Delta\eta \\
& +BB_1(\xi,\eta)\Big(-\frac{1}{8}\big(\bar{\rho}(\xi-2\Delta\xi,\eta)V_\xi(\xi-2\Delta\xi,\eta) \\
& +\frac{6}{8}\bar{\rho}(\xi-\Delta\xi,\eta)V_\xi(\xi-\Delta\xi,\eta)\Big)\Delta\eta \\
& -BB_2(\xi,\eta)\Big(-\frac{1}{8}\big(\bar{\rho}(\xi+\Delta\xi,\eta)V_\xi(\xi+\Delta\xi,\eta) \\
& +\frac{3}{8}\bar{\rho}(\xi-\Delta\xi,\eta)V_\xi(\xi-\Delta\xi,\eta)\Big)\Delta\eta - \\
& \big(CC_1(\xi,\eta)\frac{3}{8}V_\eta(\xi,\eta+\Delta\eta)\Delta\xi \\
& -CC_2(\xi,\eta)\frac{6}{8}V_\eta(\xi,\eta+\Delta\eta)\Delta\xi \\
& -DD_2(\xi,\eta)\frac{1}{8}V_\eta(\xi,\eta+\Delta\eta)\Delta\xi\big).\bar{\rho}(\xi,\eta+\Delta\eta)
\end{aligned} \tag{6.101}
$$

consequently, by rearranging the transferred x-momentum equation for Line Successive Over Relaxation (LSOR) method in η direction, it will be:

$$A_{SS10}(\eta)V_x(\xi,\eta-2\Delta\eta)+A_{S10}(\eta)V_x(\xi,\eta-\Delta\eta)+A_{P10}(\eta)V_x(\xi,\eta)+ \\ A_{N10}(\eta)V_x(\xi,\eta+\Delta\eta)+A_{NN10}(\eta)V_x(\xi,\eta+2\Delta\eta)=b_{10}(\eta) \tag{6.102}$$

The $A_{SS10}(\eta)$, $A_{S10}(\eta)$, $A_{P10}(\eta)$, $A_{N10}(\eta)$, $A_{NN10}(\eta)$ and $b_{10}(\eta)$ coefficients for different probabilities of Table 6.1 are as follows:

$$A_{SS10}(\eta)=\left[DD_1(\xi,\eta)\frac{1}{8}\bar{\rho}(\xi,\eta-2\Delta\eta)V_\eta(\xi,\eta-2\Delta\eta)\Delta\xi\right] \tag{6.103}$$

$$\begin{aligned} A_{S10}(\eta)=\big[&-CC_1(\xi,\eta)\frac{1}{8}\bar{\rho}(\xi,\eta-\Delta\eta)V_\eta(\xi,\eta-\Delta\eta)\Delta\xi \\ &-DD_1(\xi,\eta)\frac{6}{8}\bar{\rho}(\xi,\eta-\Delta\eta)V_\eta(\xi,\eta-\Delta\eta)\Delta\xi \\ &+DD_2(\xi,\eta)\frac{3}{8}\bar{\rho}(\xi,\eta-\Delta\eta)V_\eta(\xi,\eta-\Delta\eta)\Delta\xi\big] \end{aligned} \tag{6.104}$$

$$\begin{aligned} A_{P10}(\eta)=\big[&\frac{J(\xi,\eta)}{\Delta t}\Delta\xi\Delta\eta\bar{\rho}(\xi,\eta) \\ &+AA_1(\xi,\eta)\frac{6}{8}\bar{\rho}(\xi,\eta)V_\xi(\xi,\eta)\Delta\eta-AA_2(\xi,\eta)\frac{3}{8}\bar{\rho}(\xi,\eta)V_\xi(\xi,\eta)\Delta\eta \\ &-BB_1(\xi,\eta)\frac{3}{8}\bar{\rho}(\xi,\eta)V_\xi(\xi,\eta)\Delta\eta+BB_2(\xi,\eta)\frac{6}{8}\bar{\rho}(\xi,\eta)V_\xi(\xi,\eta)\Delta\eta \\ &+CC_1(\xi,\eta)\frac{6}{8}\bar{\rho}(\xi,\eta)V_\eta(\xi,\eta)\Delta\xi-CC_2(\xi,\eta)\frac{3}{8}\bar{\rho}(\xi,\eta)V_\eta(\xi,\eta)\Delta\xi \\ &-DD_1(\xi,\eta)\frac{3}{8}\bar{\rho}(\xi,\eta)V_\eta(\xi,\eta)\Delta\xi+DD_2(\xi,\eta)\frac{6}{8}\bar{\rho}(\xi,\eta)V_\eta(\xi,\eta)\Delta\xi\big] \end{aligned} \tag{6.105}$$

$$\begin{aligned} A_{N10}(\eta)=\big[&CC_1(\xi,\eta)\frac{3}{8}\bar{\rho}(\xi,\eta+\Delta\eta)V_\eta(\xi,\eta+\Delta\eta)\Delta\xi \\ &-CC_2(\xi,\eta)\frac{6}{8}\bar{\rho}(\xi,\eta+\Delta\eta)V_\eta(\xi,\eta+\Delta\eta)\Delta\xi \\ &-DD_2(\xi,\eta)\frac{1}{8}\bar{\rho}(\xi,\eta+\Delta\eta)V_\eta(\xi,\eta+\Delta\eta)\Delta\xi\big] \end{aligned} \tag{6.106}$$

$$A_{NN10}(\eta)=\left[CC_2(\xi,\eta)\frac{1}{8}\bar{\rho}(\xi,\eta+2\Delta\eta)V_\eta(\xi,\eta+2\Delta\eta)\Delta\xi\right] \tag{6.107}$$

$$
\begin{aligned}
b_{10}(\eta) = \frac{J(\xi,\eta)}{\Delta t}\Delta\xi\Delta\eta\bar{\rho}(\xi,\eta).V_x(\xi,\eta) \\
-AA_1(\xi,\eta)\Big(-\frac{1}{8}\big(\bar{\rho}(\xi-\Delta\xi,\eta)V_\xi(\xi-\Delta\xi,\eta).V_x(\xi-\Delta\xi,\eta) \\
+\frac{3}{8}\bar{\rho}(\xi+\Delta\xi,\eta)V_\xi(\xi+\Delta\xi,\eta).V_x(\xi+\Delta\xi,\eta)\Big)\Delta\eta \\
+AA_2(\xi,\eta)\Big(-\frac{1}{8}\big(\bar{\rho}(\xi+2\Delta\xi,\eta)V_\xi(\xi+2\Delta\xi,\eta).V_x(\xi+2\Delta\xi,\eta) \\
+\frac{6}{8}\bar{\rho}(\xi+\Delta\xi,\eta)V_\xi(\xi+\Delta\xi,\eta).V_x(\xi+\Delta\xi,\eta)\Big)\Delta\eta \\
+BB_1(\xi,\eta)\Big(-\frac{1}{8}\big(\bar{\rho}(\xi-2\Delta\xi,\eta)V_\xi(\xi-2\Delta\xi,\eta).V_x(\xi-2\Delta\xi,\eta) \\
+\frac{6}{8}\bar{\rho}(\xi-\Delta\xi,\eta)V_\xi(\xi-\Delta\xi,\eta).V_x(\xi-\Delta\xi,\eta)\Big)\Delta\eta \\
-BB_2(\xi,\eta)\Big(-\frac{1}{8}\big(\bar{\rho}(\xi+\Delta\xi,\eta)V_\xi(\xi+\Delta\xi,\eta).V_x(\xi+\Delta\xi,\eta) \\
+\frac{3}{8}\bar{\rho}(\xi-\Delta\xi,\eta)V_\xi(\xi-\Delta\xi,\eta).V_x(\xi-\Delta\xi,\eta)\Big)\Delta\eta \\
+J(\xi,\eta)\Big[\frac{0.75\bar{\rho}C_D Re_D\mu_a}{\rho_w D^2}\big(U_x(\xi,\eta)-V_x^n(\xi,\eta)\big)\Big]\Delta\xi\Delta\eta
\end{aligned}
\tag{6.108}
$$

for $j=2$, always $DD_1=0$ then these coefficients are as:

$$A_{SS10}(\eta) = \big[0\big] \tag{6.109}$$

$$A_{S10}(\eta) = \big[0\big] \tag{6.110}$$

$$
\begin{aligned}
A_{P10}(\eta) = \big[\frac{J(\xi,\eta)}{\Delta t}\Delta\xi\Delta\eta\bar{\rho}(\xi,\eta) \\
+AA_1(\xi,\eta)\frac{6}{8}\bar{\rho}(\xi,\eta)V_\xi(\xi,\eta)\Delta\eta - AA_2(\xi,\eta)\frac{3}{8}\bar{\rho}(\xi,\eta)V_\xi(\xi,\eta)\Delta\eta \\
-BB_1(\xi,\eta)\frac{3}{8}\bar{\rho}(\xi,\eta)V_\xi(\xi,\eta)\Delta\eta + BB_2(\xi,\eta)\frac{6}{8}\bar{\rho}(\xi,\eta)V_\xi(\xi,\eta)\Delta\eta \\
+CC_1(\xi,\eta)\frac{6}{8}\bar{\rho}(\xi,\eta)V_\eta(\xi,\eta)\Delta\xi - CC_2(\xi,\eta)\frac{3}{8}\bar{\rho}(\xi,\eta)V_\eta(\xi,\eta)\Delta\xi \\
+DD_2(\xi,\eta)\frac{6}{8}\bar{\rho}(\xi,\eta)V_\eta(\xi,\eta)\Delta\xi\big]
\end{aligned}
\tag{6.111}
$$

$$
\begin{aligned}
A_{N10}(\eta) = \big[CC_1(\xi,\eta)\frac{3}{8}\bar{\rho}(\xi,\eta+\Delta\eta)V_\eta(\xi,\eta+\Delta\eta)\Delta\xi \\
-CC_2(\xi,\eta)\frac{6}{8}\bar{\rho}(\xi,\eta+\Delta\eta)V_\eta(\xi,\eta+\Delta\eta)\Delta\xi \\
-DD_2(\xi,\eta)\frac{1}{8}\bar{\rho}(\xi,\eta+\Delta\eta)V_\eta(\xi,\eta+\Delta\eta)\Delta\xi\big]
\end{aligned}
\tag{6.112}
$$

$$A_{NN10}(\eta) = \big[CC_2(\xi,\eta)\frac{1}{8}\bar{\rho}(\xi,\eta+2\Delta\eta)V_\eta(\xi,\eta+2\Delta\eta)\Delta\xi\big] \tag{6.113}$$

$$
\begin{aligned}
b_{10}(\eta) = \frac{J(\xi,\eta)}{\Delta t}\Delta\xi\Delta\eta\bar{\rho}(\xi,\eta).V_x(\xi,\eta) \\
-AA_1(\xi,\eta)\Big(-\frac{1}{8}\big(\bar{\rho}(\xi-\Delta\xi,\eta)V_\xi(\xi-\Delta\xi,\eta).V_x(\xi-\Delta\xi,\eta) \\
+\frac{3}{8}\bar{\rho}(\xi+\Delta\xi,\eta)V_\xi(\xi+\Delta\xi,\eta).V_x(\xi+\Delta\xi,\eta)\Big)\Delta\eta \\
+AA_2(\xi,\eta)\Big(-\frac{1}{8}\big(\bar{\rho}(\xi+2\Delta\xi,\eta)V_\xi(\xi+2\Delta\xi,\eta).V_x(\xi+2\Delta\xi,\eta) \\
+\frac{6}{8}\bar{\rho}(\xi+\Delta\xi,\eta)V_\xi(\xi+\Delta\xi,\eta).V_x(\xi+\Delta\xi,\eta)\Big)\Delta\eta \\
+BB_1(\xi,\eta)\Big(-\frac{1}{8}\big(\bar{\rho}(\xi-2\Delta\xi,\eta)V_\xi(\xi-2\Delta\xi,\eta).V_x(\xi-2\Delta\xi,\eta) \\
+\frac{6}{8}\bar{\rho}(\xi-\Delta\xi,\eta)V_\xi(\xi-\Delta\xi,\eta).V_x(\xi-\Delta\xi,\eta)\Big)\Delta\eta \\
-BB_2(\xi,\eta)\Big(-\frac{1}{8}\big(\bar{\rho}(\xi+\Delta\xi,\eta)V_\xi(\xi+\Delta\xi,\eta).V_x(\xi+\Delta\xi,\eta) \\
+\frac{3}{8}\bar{\rho}(\xi-\Delta\xi,\eta)V_\xi(\xi-\Delta\xi,\eta).V_x(\xi-\Delta\xi,\eta)\Big)\Delta\eta \\
+J(\xi,\eta)\Big[\frac{0.75\bar{\rho}C_D Re_D\mu_a}{\rho_w D^2}\big(U_x(\xi,\eta)-V_x^n(\xi,\eta)\big)\Big]\Delta\xi\Delta\eta- \\
\big(-CC_1(\xi,\eta)\frac{1}{8}\bar{\rho}(\xi,\eta-\Delta\eta)V_\eta(\xi,\eta-\Delta\eta)\Delta\xi \\
+DD_2(\xi,\eta)\frac{3}{8}\bar{\rho}(\xi,\eta-\Delta\eta)V_\eta(\xi,\eta-\Delta\eta)\Delta\xi\big).V_x(\xi,\eta-\Delta\eta)
\end{aligned}
\tag{6.114}
$$

for $j = j_{Max}-1$ the coefficients will be:

$$
A_{SS10}(\eta) = \Big[DD_1(\xi,\eta)\frac{1}{8}\bar{\rho}(\xi,\eta-2\Delta\eta)V_\eta(\xi,\eta-2\Delta\eta)\Delta\xi\Big] \tag{6.115}
$$

$$
\begin{aligned}
A_{S10}(\eta) = \big[&-CC_1(\xi,\eta)\frac{1}{8}\bar{\rho}(\xi,\eta-\Delta\eta)V_\eta(\xi,\eta-\Delta\eta)\Delta\xi \\
&-DD_1(\xi,\eta)\frac{6}{8}\bar{\rho}(\xi,\eta-\Delta\eta)V_\eta(\xi,\eta-\Delta\eta)\Delta\xi \\
&+DD_2(\xi,\eta)\frac{3}{8}\bar{\rho}(\xi,\eta-\Delta\eta)V_\eta(\xi,\eta-\Delta\eta)\Delta\xi\big]
\end{aligned}
\tag{6.116}
$$

$$
\begin{aligned}
A_{P10}(\eta) = \big[&\frac{J(\xi,\eta)}{\Delta t}\Delta\xi\Delta\eta\bar{\rho}(\xi,\eta) \\
&+AA_1(\xi,\eta)\frac{6}{8}\bar{\rho}(\xi,\eta)V_\xi(\xi,\eta)\Delta\eta - AA_2(\xi,\eta)\frac{3}{8}\bar{\rho}(\xi,\eta)V_\xi(\xi,\eta)\Delta\eta \\
&-BB_1(\xi,\eta)\frac{3}{8}\bar{\rho}(\xi,\eta)V_\xi(\xi,\eta)\Delta\eta + BB_2(\xi,\eta)\frac{6}{8}\bar{\rho}(\xi,\eta)V_\xi(\xi,\eta)\Delta\eta \\
&+CC_1(\xi,\eta)\frac{6}{8}\bar{\rho}(\xi,\eta)V_\eta(\xi,\eta)\Delta\xi - CC_2(\xi,\eta)\frac{3}{8}\bar{\rho}(\xi,\eta)V_\eta(\xi,\eta)\Delta\xi \\
&-DD_1(\xi,\eta)\frac{3}{8}\bar{\rho}(\xi,\eta)V_\eta(\xi,\eta)\Delta\xi + DD_2(\xi,\eta)\frac{6}{8}\bar{\rho}(\xi,\eta)V_\eta(\xi,\eta)\Delta\xi\big]
\end{aligned}
\tag{6.117}
$$

$$
A_{N10}(\eta) = \big[0\big] \tag{6.118}
$$

$$
A_{NN10}(\eta) = \big[0\big] \tag{6.119}
$$

$$
\begin{aligned}
b_{10}(\eta) = \frac{J(\xi,\eta)}{\Delta t}\Delta\xi\Delta\eta\bar{\rho}(\xi,\eta).V_x(\xi,\eta) \\
-AA_1(\xi,\eta)\Big(-\frac{1}{8}\big(\bar{\rho}(\xi-\Delta\xi,\eta)V_\xi(\xi-\Delta\xi,\eta).V_x(\xi-\Delta\xi,\eta) \\
+\frac{3}{8}\bar{\rho}(\xi+\Delta\xi,\eta)V_\xi(\xi+\Delta\xi,\eta).V_x(\xi+\Delta\xi,\eta)\Big)\Delta\eta \\
+AA_2(\xi,\eta)\Big(-\frac{1}{8}\big(\bar{\rho}(\xi+2\Delta\xi,\eta)V_\xi(\xi+2\Delta\xi,\eta).V_x(\xi+2\Delta\xi,\eta) \\
+\frac{6}{8}\bar{\rho}(\xi+\Delta\xi,\eta)V_\xi(\xi+\Delta\xi,\eta).V_x(\xi+\Delta\xi,\eta)\Big)\Delta\eta \\
+BB_1(\xi,\eta)\Big(-\frac{1}{8}\big(\bar{\rho}(\xi-2\Delta\xi,\eta)V_\xi(\xi-2\Delta\xi,\eta).V_x(\xi-2\Delta\xi,\eta) \\
+\frac{6}{8}\bar{\rho}(\xi-\Delta\xi,\eta)V_\xi(\xi-\Delta\xi,\eta).V_x(\xi-\Delta\xi,\eta)\Big)\Delta\eta \\
-BB_2(\xi,\eta)\Big(-\frac{1}{8}\big(\bar{\rho}(\xi+\Delta\xi,\eta)V_\xi(\xi+\Delta\xi,\eta).V_x(\xi+\Delta\xi,\eta) \\
+\frac{3}{8}\bar{\rho}(\xi-\Delta\xi,\eta)V_\xi(\xi-\Delta\xi,\eta).V_x(\xi-\Delta\xi,\eta)\Big)\Delta\eta \\
+J(\xi,\eta)\Big[\frac{0.75\bar{\rho}C_D Re_D\mu_a}{\rho_w D^2}\big(U_x(\xi,\eta)-V_x^n(\xi,\eta)\big)\Big]\Delta\xi\Delta\eta- \\
\big(CC_1(\xi,\eta)\frac{3}{8}\bar{\rho}(\xi,\eta+\Delta\eta)V_\eta(\xi,\eta+\Delta\eta)\Delta\xi \\
-CC_2(\xi,\eta)\frac{6}{8}\bar{\rho}(\xi,\eta+\Delta\eta)V_\eta(\xi,\eta+\Delta\eta)\Delta\xi \\
-DD_2(\xi,\eta)\frac{1}{8}\bar{\rho}(\xi,\eta+\Delta\eta)V_\eta(\xi,\eta+\Delta\eta)\Delta\xi\big).V_x(\xi,\eta+\Delta\eta)
\end{aligned}
\tag{6.120}
$$

and finally, by rearranging the transferred y-momentum equation for Line Successive Over Relaxation (LSOR) method in η direction, it will be as:

$$
\begin{aligned}
A_{SS11}(\eta)V_y(\xi,\eta-\Delta\eta)+A_{S11}(\eta)V_y(\xi,\eta-\Delta\eta)+A_{P11}(\eta)V_y(\xi,\eta)+ \\
A_{N11}(\eta)V_y(\xi,\eta+\Delta\eta)+A_{NN11}(\eta)V_y(\xi,\eta+\Delta\eta)=b_{11}(\eta)
\end{aligned}
\tag{6.121}
$$

The $A_{SS11}(\eta)$, $A_{S11}(\eta)$, $A_{P11}(\eta)$, $A_{N11}(\eta)$, $A_{NN11}(\eta)$ and $b_{11}(\eta)$ coefficients for different probabilities of Table 6.1 are as follows:

$$
A_{SS11}(\eta) = \big[DD_1(\xi,\eta)\frac{1}{8}\bar{\rho}(\xi,\eta-2\Delta\eta)V_\eta(\xi,\eta-2\Delta\eta)\Delta\xi\big] \tag{6.122}
$$

$$
\begin{aligned}
A_{S11}(\eta) = \big[-CC_1(\xi,\eta)\frac{1}{8}\bar{\rho}(\xi,\eta-\Delta\eta)V_\eta(\xi,\eta-\Delta\eta)\Delta\xi \\
-DD_1(\xi,\eta)\frac{6}{8}\bar{\rho}(\xi,\eta-\Delta\eta)V_\eta(\xi,\eta-\Delta\eta)\Delta\xi \\
+DD_2(\xi,\eta)\frac{3}{8}\bar{\rho}(\xi,\eta-\Delta\eta)V_\eta(\xi,\eta-\Delta\eta)\Delta\xi\big]
\end{aligned}
\tag{6.123}
$$

$$
\begin{aligned}
A_{P11}(\eta) = \big[&\frac{J(\xi,\eta)}{\Delta t}\Delta\xi\Delta\eta\bar{\rho}(\xi,\eta) \\
&+AA_1(\xi,\eta)\frac{6}{8}\bar{\rho}(\xi,\eta)V_\xi(\xi,\eta)\Delta\eta - AA_2(\xi,\eta)\frac{3}{8}\bar{\rho}(\xi,\eta)V_\xi(\xi,\eta)\Delta\eta \\
&-BB_1(\xi,\eta)\frac{3}{8}\bar{\rho}(\xi,\eta)V_\xi(\xi,\eta)\Delta\eta + BB_2(\xi,\eta)\frac{6}{8}\bar{\rho}(\xi,\eta)V_\xi(\xi,\eta)\Delta\eta \\
&+CC_1(\xi,\eta)\frac{6}{8}\bar{\rho}(\xi,\eta)V_\eta(\xi,\eta)\Delta\xi - CC_2(\xi,\eta)\frac{3}{8}\bar{\rho}(\xi,\eta)V_\eta(\xi,\eta)\Delta\xi \\
&-DD_1(\xi,\eta)\frac{3}{8}\bar{\rho}(\xi,\eta)V_\eta(\xi,\eta)\Delta\xi + DD_2(\xi,\eta)\frac{6}{8}\bar{\rho}(\xi,\eta)V_\eta(\xi,\eta)\Delta\xi\big]
\end{aligned} \tag{6.124}
$$

$$
\begin{aligned}
A_{N11}(\eta) = \big[&CC_1(\xi,\eta)\frac{3}{8}\bar{\rho}(\xi,\eta+\Delta\eta)V_\eta(\xi,\eta+\Delta\eta)\Delta\xi \\
&-CC_2(\xi,\eta)\frac{6}{8}\bar{\rho}(\xi,\eta+\Delta\eta)V_\eta(\xi,\eta+\Delta\eta)\Delta\xi \\
&-DD_2(\xi,\eta)\frac{1}{8}\bar{\rho}(\xi,\eta+\Delta\eta)V_\eta(\xi,\eta+\Delta\eta)\Delta\xi\big]
\end{aligned} \tag{6.125}
$$

$$
A_{NN11}(\eta) = \big[CC_2(\xi,\eta)\frac{1}{8}\bar{\rho}(\xi,\eta+2\Delta\eta)V_\eta(\xi,\eta+2\Delta\eta)\Delta\xi\big] \tag{6.126}
$$

$$
\begin{aligned}
b_{11}(\eta) = &\frac{J(\xi,\eta)}{\Delta t}\Delta\xi\Delta\eta\bar{\rho}(\xi,\eta).V_y(\xi,\eta) \\
&-AA_1(\xi,\eta)\Big(-\frac{1}{8}\big(\bar{\rho}(\xi-\Delta\xi,\eta)V_\xi(\xi-\Delta\xi,\eta).V_y(\xi-\Delta\xi,\eta) \\
&+\frac{3}{8}\bar{\rho}(\xi+\Delta\xi,\eta)V_\xi(\xi+\Delta\xi,\eta).V_y(\xi+\Delta\xi,\eta)\Big)\Delta\eta \\
&+AA_2(\xi,\eta)\Big(-\frac{1}{8}\big(\bar{\rho}(\xi+2\Delta\xi,\eta)V_\xi(\xi+2\Delta\xi,\eta).V_y(\xi+2\Delta\xi,\eta) \\
&+\frac{6}{8}\bar{\rho}(\xi+\Delta\xi,\eta)V_\xi(\xi+\Delta\xi,\eta).V_y(\xi+\Delta\xi,\eta)\Big)\Delta\eta \\
&+BB_1(\xi,\eta)\Big(-\frac{1}{8}\big(\bar{\rho}(\xi-2\Delta\xi,\eta)V_\xi(\xi-2\Delta\xi,\eta).V_y(\xi-2\Delta\xi,\eta) \\
&+\frac{6}{8}\bar{\rho}(\xi-\Delta\xi,\eta)V_\xi(\xi-\Delta\xi,\eta).V_y(\xi-\Delta\xi,\eta)\Big)\Delta\eta \\
&-BB_2(\xi,\eta)\Big(-\frac{1}{8}\big(\bar{\rho}(\xi+\Delta\xi,\eta)V_\xi(\xi+\Delta\xi,\eta).V_y(\xi+\Delta\xi,\eta) \\
&+\frac{3}{8}\bar{\rho}(\xi-\Delta\xi,\eta)V_\xi(\xi-\Delta\xi,\eta).V_y(\xi-\Delta\xi,\eta)\Big)\Delta\eta \\
&+J\Big[\frac{0.75\bar{\rho}C_D Re_D\mu_a}{\rho_w D^2}\big(U_y(\xi,\eta)-V_y^n(\xi,\eta)\big)+\bar{\rho}g\big(1-\frac{\rho_a}{\rho_w}\big)\Big]\Delta\xi\Delta\eta
\end{aligned} \tag{6.127}
$$

for $j=2$, always $DD_1=0$ then these coefficients are as:

$$
A_{SS11}(\eta) = \big[0\big] \tag{6.128}
$$

$$
A_{S11}(\eta) = \big[0\big] \tag{6.129}
$$

$$
\begin{aligned}
A_{P11}(\eta) = \big[&\frac{J(\xi,\eta)}{\Delta t}\Delta\xi\Delta\eta\bar{\rho}(\xi,\eta) \\
&+AA_1(\xi,\eta)\frac{6}{8}\bar{\rho}(\xi,\eta)V_\xi(\xi,\eta)\Delta\eta - AA_2(\xi,\eta)\frac{3}{8}\bar{\rho}(\xi,\eta)V_\xi(\xi,\eta)\Delta\eta \\
&-BB_1(\xi,\eta)\frac{3}{8}\bar{\rho}(\xi,\eta)V_\xi(\xi,\eta)\Delta\eta + BB_2(\xi,\eta)\frac{6}{8}\bar{\rho}(\xi,\eta)V_\xi(\xi,\eta)\Delta\eta \\
&+CC_1(\xi,\eta)\frac{6}{8}\bar{\rho}(\xi,\eta)V_\eta(\xi,\eta)\Delta\xi - CC_2(\xi,\eta)\frac{3}{8}\bar{\rho}(\xi,\eta)V_\eta(\xi,\eta)\Delta\xi \\
&+DD_2(\xi,\eta)\frac{6}{8}\bar{\rho}(\xi,\eta)V_\eta(\xi,\eta)\Delta\xi\big]
\end{aligned}
\tag{6.130}
$$

$$
\begin{aligned}
A_{N11}(\eta) = \big[&CC_1(\xi,\eta)\frac{3}{8}\bar{\rho}(\xi,\eta+\Delta\eta)V_\eta(\xi,\eta+\Delta\eta)\Delta\xi \\
&-CC_2(\xi,\eta)\frac{6}{8}\bar{\rho}(\xi,\eta+\Delta\eta)V_\eta(\xi,\eta+\Delta\eta)\Delta\xi \\
&-DD_2(\xi,\eta)\frac{1}{8}\bar{\rho}(\xi,\eta+\Delta\eta)V_\eta(\xi,\eta+\Delta\eta)\Delta\xi\big]
\end{aligned}
\tag{6.131}
$$

$$
A_{NN11}(\eta) = \big[CC_2(\xi,\eta)\frac{1}{8}\bar{\rho}(\xi,\eta+2\Delta\eta)V_\eta(\xi,\eta+2\Delta\eta)\Delta\xi\big] \tag{6.132}
$$

$$
\begin{aligned}
b_{11}(\eta) = &\frac{J(\xi,\eta)}{\Delta t}\Delta\xi\Delta\eta\bar{\rho}(\xi,\eta).V_y(\xi,\eta) \\
&-AA_1(\xi,\eta)\Big(-\frac{1}{8}\big(\bar{\rho}(\xi-\Delta\xi,\eta)V_\xi(\xi-\Delta\xi,\eta).V_y(\xi-\Delta\xi,\eta) \\
&+\frac{3}{8}\bar{\rho}(\xi+\Delta\xi,\eta)V_\xi(\xi+\Delta\xi,\eta).V_y(\xi+\Delta\xi,\eta)\big)\Delta\eta \\
&+AA_2(\xi,\eta)\Big(-\frac{1}{8}\big(\bar{\rho}(\xi+2\Delta\xi,\eta)V_\xi(\xi+2\Delta\xi,\eta).V_y(\xi+2\Delta\xi,\eta) \\
&+\frac{6}{8}\bar{\rho}(\xi+\Delta\xi,\eta)V_\xi(\xi+\Delta\xi,\eta).V_y(\xi+\Delta\xi,\eta)\big)\Delta\eta \\
&+BB_1(\xi,\eta)\Big(-\frac{1}{8}\big(\bar{\rho}(\xi-2\Delta\xi,\eta)V_\xi(\xi-2\Delta\xi,\eta).V_y(\xi-2\Delta\xi,\eta) \\
&+\frac{6}{8}\bar{\rho}(\xi-\Delta\xi,\eta)V_\xi(\xi-\Delta\xi,\eta).V_y(\xi-\Delta\xi,\eta)\big)\Delta\eta \\
&-BB_2(\xi,\eta)\Big(-\frac{1}{8}\big(\bar{\rho}(\xi+\Delta\xi,\eta)V_\xi(\xi+\Delta\xi,\eta).V_y(\xi+\Delta\xi,\eta) \\
&+\frac{3}{8}\bar{\rho}(\xi-\Delta\xi,\eta)V_\xi(\xi-\Delta\xi,\eta).V_y(\xi-\Delta\xi,\eta)\big)\Delta\eta \\
&+J(\xi,\eta)\Big[\frac{0.75\bar{\rho}C_D Re_D\mu_a}{\rho_w D^2}\big(U_y(\xi,\eta)-V_y^n(\xi,\eta)\big)+\bar{\rho}g\big(1-\frac{\rho_a}{\rho_w}\big)\Big]\Delta\xi\Delta\eta - \\
&\big(-CC_1(\xi,\eta)\frac{1}{8}\bar{\rho}(\xi,\eta-\Delta\eta)V_\eta(\xi,\eta-\Delta\eta)\Delta\xi \\
&+DD_2(\xi,\eta)\frac{3}{8}\bar{\rho}(\xi,\eta-\Delta\eta)V_\eta(\xi,\eta-\Delta\eta)\Delta\xi\big).V_y(\xi,\eta-\Delta\eta)
\end{aligned}
\tag{6.133}
$$

for $j = j_{Max} - 1$ the coefficients will be:

$$
A_{SS11}(\eta) = \big[DD_1(\xi,\eta)\frac{1}{8}\bar{\rho}(\xi,\eta-2\Delta\eta)V_\eta(\xi,\eta-2\Delta\eta)\Delta\xi\big] \tag{6.134}
$$

$$
\begin{aligned}
A_{S11}(\eta) = \big[& -CC_1(\xi,\eta)\frac{1}{8}\bar{\rho}(\xi,\eta-\Delta\eta)V_\eta(\xi,\eta-\Delta\eta)\Delta\xi \\
& -DD_1(\xi,\eta)\frac{6}{8}\bar{\rho}(\xi,\eta-\Delta\eta)V_\eta(\xi,\eta-\Delta\eta)\Delta\xi \\
& +DD_2(\xi,\eta)\frac{3}{8}\bar{\rho}(\xi,\eta-\Delta\eta)V_\eta(\xi,\eta-\Delta\eta)\Delta\xi\big]
\end{aligned} \tag{6.135}
$$

$$
\begin{aligned}
A_{P11}(\eta) = \big[& \frac{J(\xi,\eta)}{\Delta t}\Delta\xi\Delta\eta\bar{\rho}(\xi,\eta) \\
& +AA_1(\xi,\eta)\frac{6}{8}\bar{\rho}(\xi,\eta)V_\xi(\xi,\eta)\Delta\eta - AA_2(\xi,\eta)\frac{3}{8}\bar{\rho}(\xi,\eta)V_\xi(\xi,\eta)\Delta\eta \\
& -BB_1(\xi,\eta)\frac{3}{8}\bar{\rho}(\xi,\eta)V_\xi(\xi,\eta)\Delta\eta + BB_2(\xi,\eta)\frac{6}{8}\bar{\rho}(\xi,\eta)V_\xi(\xi,\eta)\Delta\eta \\
& +CC_1(\xi,\eta)\frac{6}{8}\bar{\rho}(\xi,\eta)V_\eta(\xi,\eta)\Delta\xi - CC_2(\xi,\eta)\frac{3}{8}\bar{\rho}(\xi,\eta)V_\eta(\xi,\eta)\Delta\xi \\
& -DD_1(\xi,\eta)\frac{3}{8}\bar{\rho}(\xi,\eta)V_\eta(\xi,\eta)\Delta\xi + DD_2(\xi,\eta)\frac{6}{8}\bar{\rho}(\xi,\eta)V_\eta(\xi,\eta)\Delta\xi\big]
\end{aligned} \tag{6.136}
$$

$$
A_{N11}(\eta) = \big[0\big] \tag{6.137}
$$

$$
A_{NN11}(\eta) = \big[0\big] \tag{6.138}
$$

$$
\begin{aligned}
b_{11}(\eta) = & \frac{J(\xi,\eta)}{\Delta t}\Delta\xi\Delta\eta\bar{\rho}(\xi,\eta).V_y(\xi,\eta) \\
& -AA_1(\xi,\eta)\Big(-\frac{1}{8}\big(\bar{\rho}(\xi-\Delta\xi,\eta)V_\xi(\xi-\Delta\xi,\eta).V_y(\xi-\Delta\xi,\eta) \\
& +\frac{3}{8}\bar{\rho}(\xi+\Delta\xi,\eta)V_\xi(\xi+\Delta\xi,\eta).V_y(\xi+\Delta\xi,\eta)\Big)\Delta\eta \\
& +AA_2(\xi,\eta)\Big(-\frac{1}{8}\big(\bar{\rho}(\xi+2\Delta\xi,\eta)V_\xi(\xi+2\Delta\xi,\eta).V_y(\xi+2\Delta\xi,\eta) \\
& +\frac{6}{8}\bar{\rho}(\xi+\Delta\xi,\eta)V_\xi(\xi+\Delta\xi,\eta).V_y(\xi+\Delta\xi,\eta)\Big)\Delta\eta \\
& +BB_1(\xi,\eta)\Big(-\frac{1}{8}\big(\bar{\rho}(\xi-2\Delta\xi,\eta)V_\xi(\xi-2\Delta\xi,\eta).V_y(\xi-2\Delta\xi,\eta) \\
& +\frac{6}{8}\bar{\rho}(\xi-\Delta\xi,\eta)V_\xi(\xi-\Delta\xi,\eta).V_y(\xi-\Delta\xi,\eta)\Big)\Delta\eta \\
& -BB_2(\xi,\eta)\Big(-\frac{1}{8}\big(\bar{\rho}(\xi+\Delta\xi,\eta)V_\xi(\xi+\Delta\xi,\eta).V_y(\xi+\Delta\xi,\eta) \\
& +\frac{3}{8}\bar{\rho}(\xi-\Delta\xi,\eta)V_\xi(\xi-\Delta\xi,\eta).V_y(\xi-\Delta\xi,\eta)\Big)\Delta\eta \\
& +J(\xi,\eta)\Big[\frac{0.75\bar{\rho}C_D Re_D\mu_a}{\rho_w D^2}\big(U_y(\xi,\eta)-V_y^n(\xi,\eta)\big)+\bar{\rho}g\big(1-\frac{\rho_a}{\rho_w}\big)\Big]\Delta\xi\Delta\eta - \\
& \big(CC_1(\xi,\eta)\frac{3}{8}\bar{\rho}(\xi,\eta+\Delta\eta)V_\eta(\xi,\eta+\Delta\eta)\Delta\xi \\
& -CC_2(\xi,\eta)\frac{6}{8}\bar{\rho}(\xi,\eta+\Delta\eta)V_\eta(\xi,\eta+\Delta\eta)\Delta\xi \\
& -DD_2(\xi,\eta)\frac{1}{8}\bar{\rho}(\xi,\eta+\Delta\eta)V_\eta(\xi,\eta+\Delta\eta)\Delta\xi\big).V_y(\xi,\eta+\Delta\eta)
\end{aligned} \tag{6.139}
$$

For the control volume on the airfoil (i.e. $j = 2$), always D_1 equals zero which means that the water droplets collide with the body surface or not, if yes the droplets would not reflect (rebound) from the surface.

The resulted matrix of coefficients of $\bar{\rho}$, V_x, and V_y will be solved for the inner region by utilizing Penta Diagonal Matrix Algorithm (PDMA) (Sebben and Baliga, 1995), see appendix 3.

6.4 Algorithm of Iterative Solution for Droplet Solver

The following algorithm is used in the computer program for the calculating of V_ξ, V_η and $\bar{\rho}$ values:

1. At the outer boundary, the values of droplets are set equal to the values of free streamflow.
2. On the airfoil, the switching boundary conditions are applied for the values of droplets.
3. The V_ξ, V_η and $\bar{\rho}$ values are updated on the branch cuts.
4. QUICK scheme will use for the discretization of governing equation. Then, the coefficient matrix of V_ξ, V_η and $\bar{\rho}$ values are formed in the inner region by applying "Line Successive Over Relaxation" (LSOR) in η direction, and these values are computed via Penta Diagonal Matrix Algorithm: PDMA, see appendix 3).
5. The convergence criteria are checked for the residuals of values, if the problem was not converged then the entire iteration method procedure is repeated from the second step (i.e. "switching boundary conditions on the body").

6.5 Collision and Collection Efficiencies

Here, special attention should be paid to defining some of the very important terms, namely collision efficiency and collection efficiency which are counted among the basic concepts of the aircraft icing (Soldevila Dalmau, 2018).

The definition of collision efficiency is the ratio between the number of droplets that impinge on the surface to the number of droplets on the windward side of the object

(Dobesch et al., 2005). The definition of collision efficiency (β) for the Eulerian droplet distribution approach will be:

$$\beta(\xi) = \frac{\alpha(\xi,0)}{\alpha_\infty}\left|\frac{V_N(\xi,0)}{U_\infty}\right| = \frac{\bar{\rho}(\xi,0)}{\bar{\rho}_\infty}\left|\frac{V_N(\xi,0)}{U_\infty}\right| \tag{6.140}$$

and consequently the droplet's mass rate that comes into the surface is:

$$\dot{m}_{drop} = \beta\bar{\rho}_\infty U_\infty = \beta(LWC)_\infty U_\infty \tag{6.141}$$

which $\bar{\rho}_\infty = (LWC)_\infty$ and U_∞ are the liquid water content and velocity of free-stream, respectively.

On the other hand, the collection efficiency is a product of two factors: (I) Collision efficiency determined by the aerodynamics properties of the flow, and (II) adhesion efficiency determined by the adhesive qualities of the component surface i.e. metallurgical properties of the surface body. Specifically, it is the fraction of the liquid water in the direct path of an aircraft component that is deposited as ice on that component whilst flying in icing conditions. Collection efficiency varies directly with both droplet size and aircraft speed and inversely with the surface area of icing.

Some important parameters affect collision and collection efficiencies. Droplet size determines where ice will form. If the droplets were small, ice formation is limited to the leading edge radius. As droplet size increases, ice formation will extend aft of the leading edge radius but medium-size droplets will not normally extend aft of surfaces normally protected by aircraft ice protection systems. Ice formation from large droplets can extend aft of the protected surfaces. Freezing rain or freezing drizzle can result in ice formation extending aft to the point of maximum component projection into the air stream. The faster the speed of the aircraft, the less chance there is for the droplets to be carried around the airfoil in the air stream. As a consequence, collection efficiency increases with aircraft speed. The rate at which ice accumulates on an aircraft depends upon the collection efficiency of the aircraft component involved. The collection efficiency bears an inverse relationship with the size of the surface area of an aircraft component and is described in terms of the curvature radius of its leading edge. Those components which have large curvature radii (canopies, windscreens, thick wings, etc.) collect only a small percentage of the cloud droplets, especially the smaller droplets,

and, therefore, have a low collection efficiency. Conversely, components that have small curvature radii (antenna masts, thin wings, etc.) deform the airflow less and permit a high proportion of droplets of all sizes to be caught. These components are said to have a high collection efficiency. Once the ice begins to form, the shape of the surface is modified by the ice itself, resulting in the curvature radius nearly always becoming smaller. Therefore, as ice accumulates, the collection efficiency increases leading to further and more rapid ice accumulation. On most aircraft, the curvature radius of the horizontal tail surface is smaller than that of the wing. This can lead to tail-plane icing before any ice accumulation on the wing and in some cases can lead to an ice-contaminated tail-plane stall.

In reality, the collection efficiency is dependent on the metallurgic properties of the body surface and different from the collision efficiency, but in this research, it is assumed that the collection efficiency equals the collision efficiency. Along with the convective heat transfer coefficient (h_{conv}), the collection efficiency (β) is the other one of the most important parameters used for the calculations of ice accretion in the simulation of aircraft icing.

6.6 Time Step

In a Navier-Stokes equations of airflow by applying finite-volume method; for global time stepping, the maximum time step is defined as follows (Hospers, 2013):

$$\Delta t_{max} = \frac{\Delta x_{min}}{\left|\vec{U}\right| + a} \tag{6.142}$$

where Δx is a characteristic length scale of a control volume, such as the distance or radius through a grid cell. The maximum time step can be described as the time needed for "information" to travel through the smallest cell possible, at the fastest speed possible. For local time-stepping the time step can be formulated as (Hospers, 2013):

$$\Delta t_{max,i} = \frac{\Delta x_{min,i}}{\left|\vec{U}_i\right| + a_i} \tag{6.143}$$

where i denotes the quantities belonging to the i-th grid-cell.

For the Eulerian droplet distribution method, this methodology cannot be employed. The considered field consists of a dispersed medium. The speed of sound has nothing to do with the speed at which information travels from one droplet to another; or from one grid-cell or control volume containing droplets to the next.

Analyzing the system of equations of water droplets, posed by equations 6.5, 6.7, 6.8, the maximum time step is related to the eigenvalues of this system. This means that for this system of equations the information velocity is V. For the Navier-Stokes equations of airflow, the speed of sound is introduced via the pressure-gradient term, which is not present in the governing equations of the water droplets. This gives the following relations for the maximum global time step and the maximum local time step, respectively (Hospers, 2013):

$$\Delta t_{max} = \frac{\Delta x_{min}}{\left|\vec{V}\right|} \tag{6.144}$$

$$\Delta t_{max,i} = \frac{\Delta x_{min,i}}{\left|\vec{V}_i\right|} \tag{6.145}$$

6.7 Assumptions

Since there are lots of parameters that affect the icing phenomenon in aircraft, therefore to be able to do an engineering analysis on the topic, does require taking some considerations, constraints, and limitations into account. Thus, some assumptions are included in our study as follows:

1. The aerodynamic effects of droplets on the airflow are neglected (i.e. one-way coupled flow).

2. The drag force caused by the airflow, self-gravity, and buoyancy forces are the only forces exerted on the water droplets.

3. There is no heat or mass exchange between the gas and liquid phases before droplets impinge on the body surface. Thus the physical properties of the water droplets are assumed not to be changed.

4. It is assumed that the diameter of water droplets is the same, and the sphere shape of droplets does not change.

5. The are no inter-droplet collisions, coalescence, distortion, evaporation, or any heat transfer for the droplets phase.

6. The droplet impact is neglected which means the droplet-wall interactions (i.e. stick, rebound, spread, and splashing) are not taken into account.

7. It is assumed that the surface of the body has no hydrophobic properties and so on, which means the collection efficiency equals the collision efficiency.

6.8 Validation

Here, the result of the present study is validated with respect to Da Silveira et al. (2003); Jung (2015) for zero angle of attack and 50 m/s velocities of air free stream.

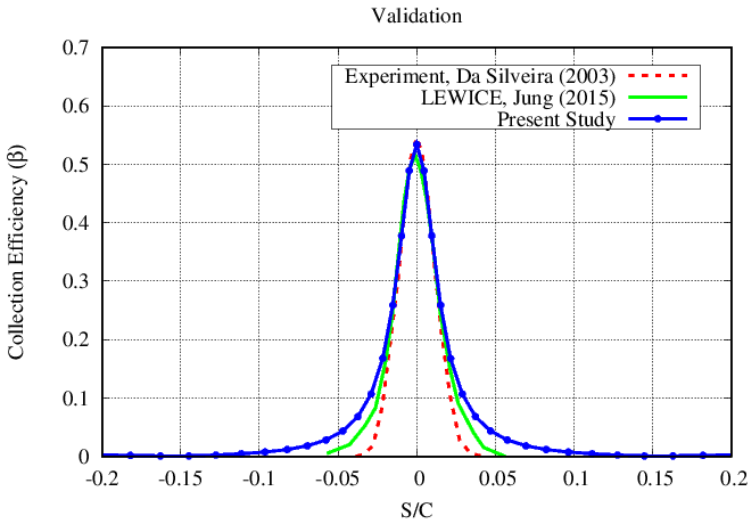

Figure 6.4 : Validation of Collection Efficiency β value of present study for 121×121 grid points with respect to Da Silveira et al. (2003); Jung (2015), for chord=1.0 m, $AOA = 0\ ^{\circ}$, $U_{\infty} = 44.4\ m/s$, $D = 20\ \mu m$ and $LWC_{\infty} = 0.78\ gr/m^3$.

The mesh independence study shows that for the 121×121 grid size and $dn = 5\ mm$ (dn is the normal distance of the grid-loop just next to the body) results are in a good agreement with the literature (Figure 6.4).

6.9 Results

Results of present study for collision efficiency of the water droplets have been shown in the following figures for different velocities of airflow, angle of attacks and droplets' size. In all figures, the starting point for s is the leading edge.

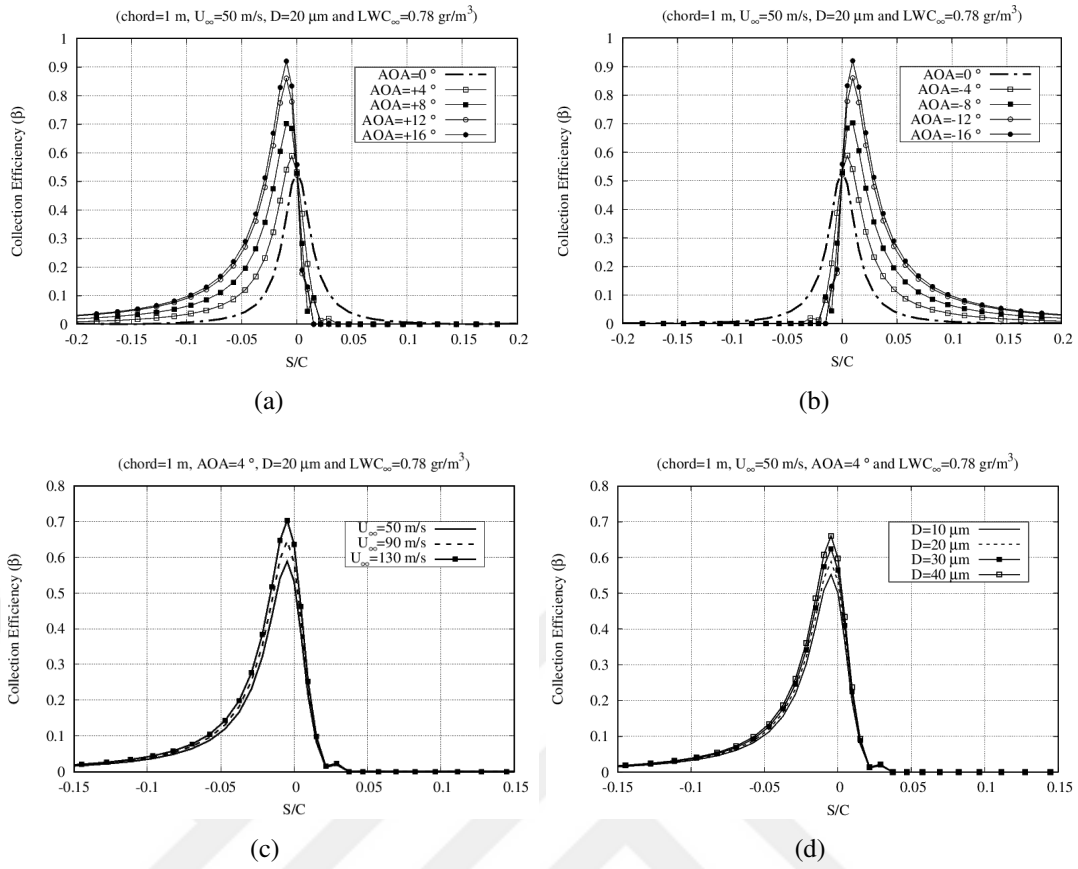

Figure 6.5 : The collection efficiency changes with varying: a,b) angle of attack, c)free-stream velocity, and d) diameter of water-droplets for 121×121 grid points.

The large-sized water droplets have greater inertia, which means their direction of motion is more difficult to change. On the other hand, larger droplets have a bigger gravity force, In the case of the free stream around the airfoil, results show that the larger droplets cause larger collection efficiencies. Results also show that the bigger velocities of free stream airflow and angle of attacks increase the collection efficiency.

The variation of liquid water content (LWC) or apparent density of droplets ($\bar{\rho}$) in the ambient does not effect the collection efficiency (β) (Chen et al., 2020).

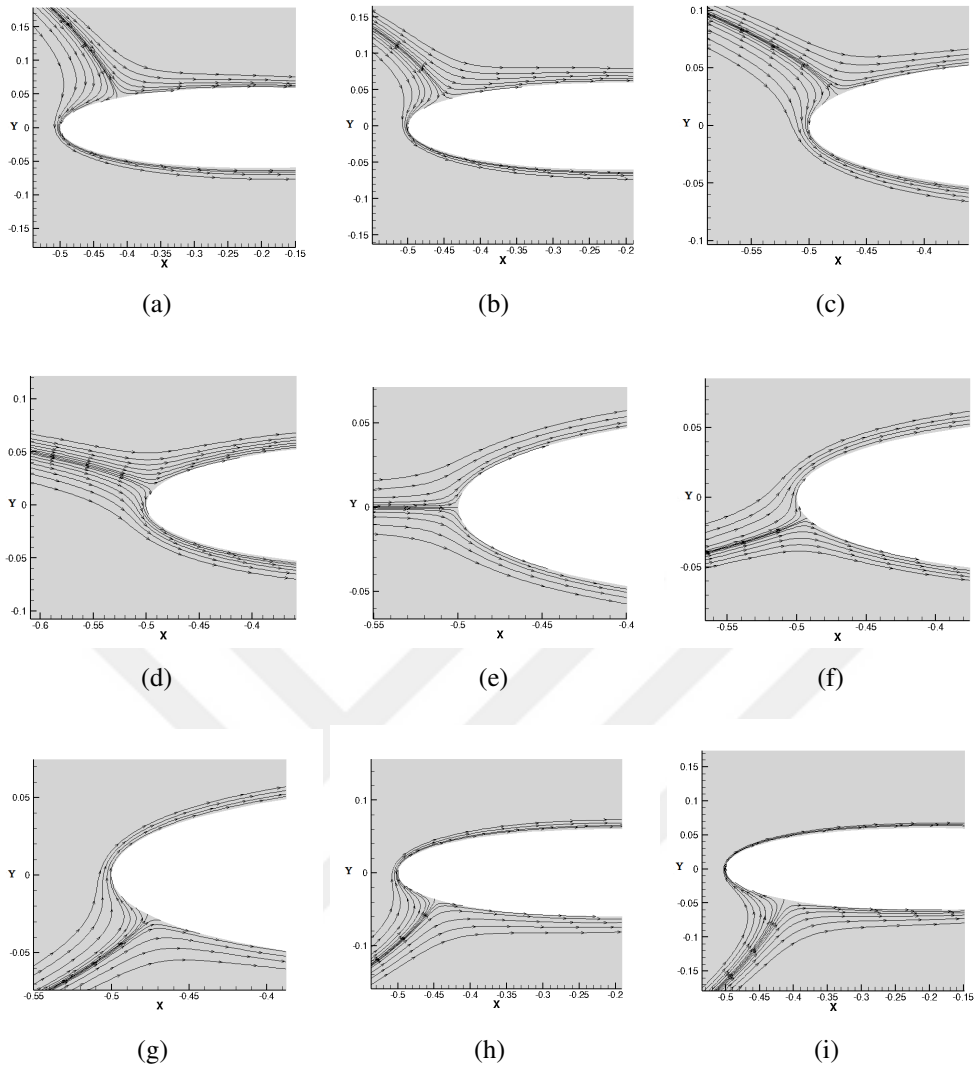

Figure 6.6 : The water-droplet trajectories for different angles of attack: a) $AOA = -16\ ^\circ$, b) $AOA = -12\ ^\circ$, c) $AOA = -8\ ^\circ$, d) $AOA = -4\ ^\circ$, e) $AOA = 0\ ^\circ$, f) $AOA = +4\ ^\circ$, g) $AOA = +8\ ^\circ$, h) $AOA = +12\ ^\circ$ and i) $AOA = +16\ ^\circ$ for chord=1.0 m, $U_\infty = 50\ m/s$, $D = 20\ \mu m$ and $LWC_\infty = 0.78\ gr/m^3$ at 121×121 grid points.

7. ICE ACCRETION

The ice accretion (Thermodynamic Calculations) is the last module of the computational procedure of the simulation of the aircraft icing. In this part, by using the conservation equations of mass and energy, the freezing fraction of the incoming super-cooled water droplets is calculated to know the thickness of the ice layer at each time step, and the final shape of the ice at specified exposure time. All terms of heat and energy sources should be included in the ice accretion to achieve a realistic simulation.

7.1 Multi-Layers and Predictor-Corrector Ice Accretion Methods

Since the ice is formed gradually in the nature, the geometry of airfoil changes continuously in aircraft icing. The reshaped geometry also alters the the airflow around the wing. In other words, the ice accretion is inherently an unsteady problem. Therefore, to solve the problem in quasi-steady state, the aircraft icing can be simulated via multi-layers approach (Lavoie, 2017).

The structure of a typical multi-layer icing simulation is shown in Figure 7.1. The general process goes as follows. The grid is generated using the geometry of the clean airfoil. Then, the airflow field is solved to obtain the velocity and pressure distributions around the body, and calculate the convective heat transfer coefficient (h_{conv}) on the body. Utilizing the airflow values, the droplets equations are solved to know the collection efficiency (β) on the body. Eventually, the thermodynamic mass and energy balances are performed to compute the surface temperature and thickness of the ice. Then, the new contaminated (iced) geometry is created and provided to the grid generator module to produce the new grid for the next time step. Finally, the whole procedure is repeated until the specified exposure time (Lavoie, 2017).

On the other hand, the predictor-corrector approach follows a slightly different philosophy (Mingione and Brandi, 1998; Verdin et al., 2009; Wright et al., 1997). In this approach, first, the calculations of ice accretion for the entire exposure time is performed. This is known as the predictor step. Then, by assuming a linear variation

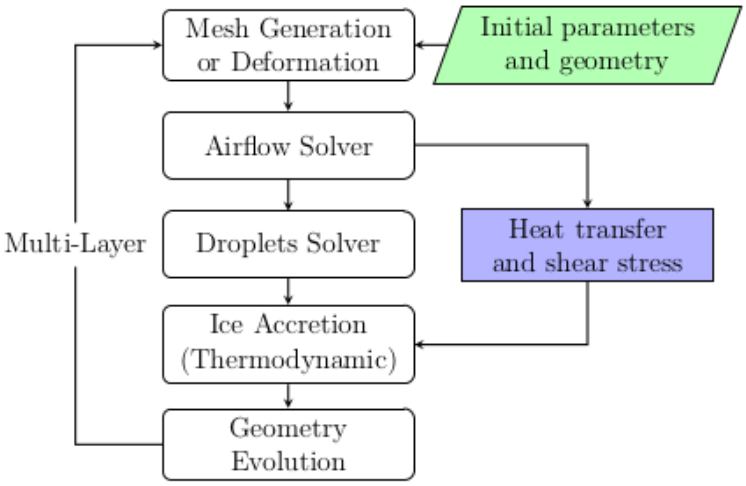

Figure 7.1 : Typical multi-layers icing simulation (Lavoie, 2017).

of the parameters between the solution of the clean airfoil and the iced geometry, the airflow and droplets solutions can be interpolated in time. Then, the final shape of ice is calculated by integrating from the beginning time (clean geometry) to exposure time (final ice shape). This step is known as the corrector step. Then, the solutions of flow and droplets can be re-evaluated on the corrected ice shape, consequently, a new linear interpolation can be computed and a new corrector step can be performed. This process will repeat until the difference between two corrector steps was negligible (Lavoie, 2017). The following list summarizes the predictor-corrector approach:

(a) evaluate a single ice layer spanning the full icing time (predictor step)

(b) compute the parameters on the new iced geometry (airflow, droplets, etc.)

(c) evaluate a new ice shape based on the interpolated time-dependent parameters and assume a linear variation of the parameters between the clean geometry and the iced shape (corrector step)

(d) repeat steps b and c until the desired convergence is achieved.

In the multi-layers icing simulation, more than two layers are usually employed. On the other hand, the predictor-corrector method generally requires only one ice accretion simulations and one correction step. Despite, the predictor-corrector is faster, but the multi-layers icing simulation is more accurate (Wright et al., 1997). The comparisons of the multi-layers and predictor-corrector approaches also show that the

predictor-corrector method provides acceptable results for the rime ice. But for the glaze ice, the multi-layers approach should be preferred (Huang et al., 2016; Lavoie, 2017; Verdin et al., 2009)

In present study, the multi-layers approach has been preferred.

7.2 Thermodynamic Models of Ice Accretion

Many icing softwares are using the algebraic model introduced by Messinger (1953).

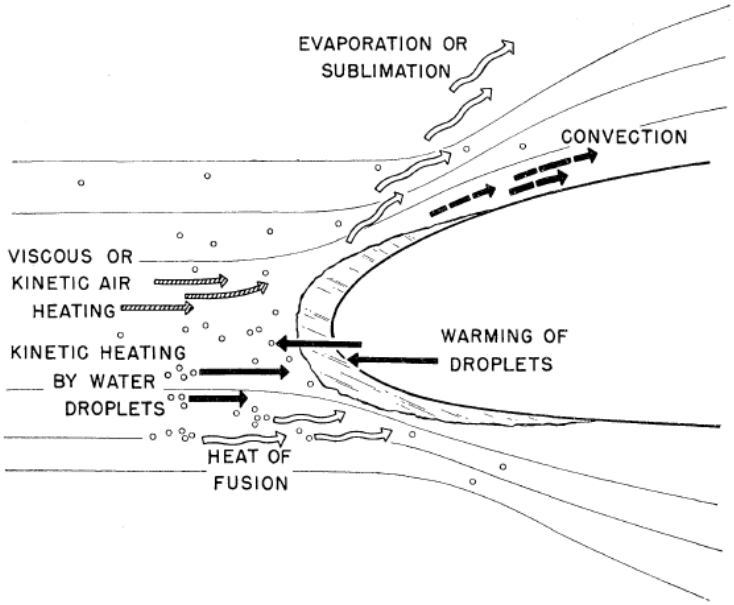

Figure 7.2 : Messinger Model, modes of energy transfer for an unheated airfoil in icing conditions (Messinger, 1953).

Messinger's model relies on mass and energy balances (Figure 7.2). However, the classical Messinger model can not simulate a continuous temperature profile in the ice and water interface in the glaze ice regime and is not able to take the heat conduction on the body surface into account. Due to the disadvantages of the classic Messinger model, Myers (2001) developed an extended Messinger model based on a Stefan problem that leads to a Messinger-like but more accurate model for the glaze ice. The extended Messinger model also considers the conduction through the ice layer by evaluating the temperature difference between the airfoil and the ice surface. Moreover, Myers et al. (2002) published a partial differential equation (PDE) version of their extended Messinger model to avoid the dependency of calculations on the stagnation point. This model also includes the water film that is driven by the air

shear stress. Myers and Charpin (2004) generalized this model for the curvilinear iced geometry. Chauvin (2015) also developed a PDE-based model considering the pressure gradients, shear stress, and gravity but neglecting the effect of surface tension. Raj et al. (2019) have also simulated the ice accretion using a PDE-based solver, instead of the commonly used control volume method. On the other hand, Cao et al. (2016b) used an iterative version of the extended Messinger model. Cao and Hou (2016) adapted the model presented by Myers and Charpin (2004), to non-orthogonal curvilinear coordinates. We may observe that the most important thermodynamic models for ice accretion are the Messinger model, extended Messinger model (Myers model), iterative models, and shallow water icing model (Lavoie et al., 2018). Many of the earlier studies simplify the rime and glaze ices as property-constant substances, and assumed that the rime ice had the same physical properties as the glaze ice (Al-Khalil et al., 1994; Myers and Thompson, 1998; Yanxia et al., 2010). On contrary, the research by Zhang et al. (2017) suggests that ice is actually a kind of porous medium and its properties are initially influenced by the parameters of the flow. Lian et al. (2018) introduced the modified spongy model that also considers droplet retention on the ice surface. Liu et al. (2019) developed a three-dimensional ice accretion model based on the unsteady Stefan problem assuming that the heat conduction within the ice layers is an unsteady process. Raj et al. (2020) have discussed that surface roughness, ice density, single or multi-shot solution, droplets' distribution, and evaporative heat transfer are the most important parameters that affect the ice accretion, among them, the surface roughness is the dominant parameter that controls the height and position of ice horn. All in all, in the conventional ice accretion models, the critical transient time and thickness are predicted at the very beginning of the calculations. These predictions are calculated based on the assumption that flow variables will not change until the formation of glaze ice. Then, either the rime ice or glaze ice calculations are implemented at each time step based on these critical transient criteria. In reality, the geometry of the body surface changes during the icing and affects the airflow and the distribution of water droplets around the airfoil. Consequently, the convective heat transfer coefficient and the collection efficiency play important roles in the ice accretion change, continuously. The main focus of the proposed approach of the present study is to make the progression of the ice accretion closer to the real physics of the icing phenomenon. In fact, without the need for the predictions of the critical

transient criteria, the calculations of the ice accretion begin with the rime ice until the temperature of the free surface of ice is equal to the melting (freezing) temperature of ice (water) in the ambient. After this point, the calculations are continued with the glaze ice.

7.2.1 Extended Messinger model (Myers model)

The general form of the energy balance in classic Messinger model with no heat transfer through the body (insulated wall) is written as:

$$\dot{Q}_{aero} + \dot{Q}_{kin} + \dot{Q}_{freezing} = \dot{Q}_{conv} + \dot{Q}_{evap/sub} + \dot{Q}_{drop} \tag{7.1}$$

The terms of the energy balance can be separated in two groups: cooling and heating effects.

There is cooling by convective heat transfer $\dot{Q}_{conv}$. The cooling by either evaporation for glaze ice (a liquid film) or sublimation for rime ice is denoted by $\dot{Q}_{evap/sub}$. There is also cooling by the incoming droplets $\dot{Q}_{drop}$ which is caused by the temperature change of the incoming droplets to the reference temperature.

For the heating effects, there is the kinetic heating $\dot{Q}_{kin}$ which is due to the change in momentum of the droplets. The release of latent heat while the water turns to ice is denoted by $\dot{Q}_{freezing}$, which means for the impacting water droplets to freeze, their latent heat of fusion must be released through the body surface and the surrounding air. $\dot{Q}_{aero}$ represents the aerodynamic heating of the surface which is related to the effects of compressibility and friction.

As it was discussed earlier Messinger model has some disadvantages, among them, the classic Messinger model does not allow to include the heat transfer on the body, but the extended Messinger model includes the heat transfer at the substrate as follows:

$$\dot{Q}_{aero} + \dot{Q}_{kin} + \dot{Q}_{freezing} = \dot{Q}_{conv} + \dot{Q}_{cond} + \dot{Q}_{evap/sub} + \dot{Q}_{drop} \tag{7.2}$$

which $\dot{Q}_{cond}$ represents the heat transfer through the substrate.

The radiation term of energy ($\dot{Q}_{rad}$) has been neglected for both Messinger and extended Messinger models. Extended Messinger model, does take the heat loss of sublimation into account.

For both Messinger and extended Messinger models, the general mass balance is written in the following form as:

$$\dot{m}_{drop} = \dot{m}_{freezing} \tag{7.3}$$

Mass is added to the cell by the mass of incoming droplets known as ($\dot{m}_{drop}$). This water can freeze leading to an ice accretion ($\dot{m}_{freezing}$) by releasing its latent heat. Mass loss is either by evaporation ($\dot{m}_{evap}$) for glaze-icing or sublimation ($\dot{m}_{sub}$) for rime-icing.

The Messinger and extended Messinger models do not include the mass and energy terms caused by the run-back water (moving film) in the continuity and energy equations. The Messinger and extended Messinger models do not take the mass of sublimation into account.

Based on the standard method of specifying a phase change, the Stefan problem is governed by four equations: heat equations in the ice and water, a mass balance, and a phase change or Stefan condition at the ice/water interface as (Myers, 2001):

$$\frac{\partial T}{\partial t} = \frac{k_i}{\rho_i c_i}\frac{\partial^2 T}{\partial z^2} \tag{7.4}$$

$$\frac{\partial \theta}{\partial t} = \frac{k_w}{\rho_w c_w}\frac{\partial^2 \theta}{\partial z^2} \tag{7.5}$$

$$\rho_i \frac{\partial B}{\partial t} + \rho_w \frac{\partial h}{\partial t} = \beta \bar{\rho}_\infty U_\infty \tag{7.6}$$

$$\rho_i L_f \frac{\partial B}{\partial t} = k_i \frac{\partial T}{\partial z} - k_w \frac{\partial \theta}{\partial z} \tag{7.7}$$

which B and h are ice and water-film thicknesses, and T and θ are the surface temperatures of ice and water-film, respectively.

The first and second equations are the conductive heat transfer equations in ice and water, respectively. The third equation is the conservative mass equation, and the fourth equation is the Stefan condition which is a straightforward energy balance. It may also be interpreted as stating that the velocity of the phase change boundary is proportional to the temperature gradients across the boundary. The Stefan condition is similar to the Messinger energy balance in the form of a differential equation. However, unlike the Messinger model, this approach requires knowledge of the temperature gradients in each layer. Hence, the heat equations 7.4 and 7.5 must be analyzed to solve the problem.

To determine the temperature, boundary and initial conditions must first be specified as the following assumptions:

1) The icing substrate temperature can be equal to or less than freezing temperature (Gent et al., 2000) as:

$$T(0,t) = T_{substrate} = \begin{cases} T_r & , T_r \leq T_{freezing} \\ T_{freezing} & , T_r > T_{freezing} \end{cases} \tag{7.8}$$

T_r is the dry adiabatic recovery temperature, which is evaluated from the following equation (Gent et al., 2000)

$$T_r(i) = \left(T_\infty + 273.15 + \frac{U_\infty^2}{2c_{p,a}}\right)\left(\frac{1 + r\frac{M^2(i)}{5}}{1 + \frac{M^2(i)}{5}}\right) - 273.15 \tag{7.9}$$

which U_∞, $c_{p,a}$, M and r are the air speed, air specific heat capacity, Mach number and recovery factor, respectively.

2) The temperature is continuous at the phase change boundary and equal to the freezing temperature:

$$T(B,t) = \theta(B,t) = T_{freezing} \tag{7.10}$$

This condition is not imposed for the case of rime ice.

3) The interface boundary conditions (see Figure 7.3) are as follows:

for rime ice, the interface boundary condition is:

$$z = B$$
$$-k_i \frac{\partial T}{\partial z} = (+\dot{Q}_{conv} + \dot{Q}_{sub} + \dot{Q}_{drop}) - (+\dot{Q}_{aero} + \dot{Q}_{kin}) \tag{7.11}$$

and for glaze ice, the interface boundary condition will be:

$$z = B + h$$
$$-k_w \frac{\partial \theta}{\partial z} = (+\dot{Q}_{conv} + \dot{Q}_{evap} + \dot{Q}_{drop}) - (+\dot{Q}_{aero} + \dot{Q}_{kin}) \tag{7.12}$$

4) The initial condition is:

$$t = 0$$
$$B = h = 0 \tag{7.13}$$

These conditions are sufficient to determine fully the temperature profiles and ice and water layer thicknesses.

The ice density (ρ_i) may take different values depending on whether rime or glaze ice forms.

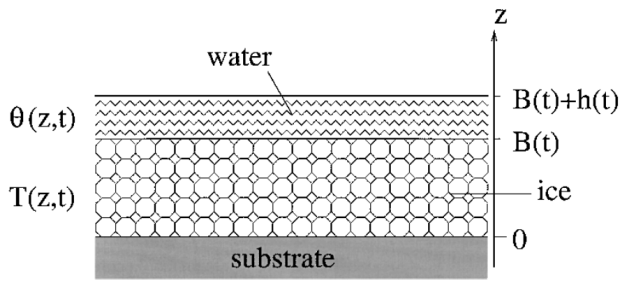

Figure 7.3 : Schematic of the ice and water thickness in Myers (2001) model.

The ice thickness in a rime calculation follows trivially from the mass balance, equation 7.6, with h set to zero:

$$B = \frac{\dot{m}_{freezing}}{\rho_{rime}}.t \tag{7.14}$$

The solution will be valid for ice thicknesses considerably less than 2.4 cm, otherwise, the time-step of ice accretion should be modified to repeat the solution.

Knowing that the energy equation is in the form of $\frac{\partial^2 T}{\partial z^2} = 0$ (Myers, 2001), by twice integrating and applying boundary conditions at the substrate and interface the surface temperature of the rime ice will be calculated by the following formula:

$$T = T_{substrate} + \frac{(+\dot{Q}_{aero} + \dot{Q}_{kin} + \dot{Q}_{freezing}) - (+\dot{Q}_{conv} + \dot{Q}_{drob} + \dot{Q}_{sub})}{k_i + B\frac{(+\dot{Q}_{conv}+\dot{Q}_{drob}+\dot{Q}_{sub})}{(T_{substrate}-T_{ambient})}}.z \qquad (7.15)$$

which z is an arbitrary thickness of ice ($0 \leqslant z \leqslant B$).

The freezing fraction (FF) for rime ice is defined as:

$$FF = \frac{\rho_r B}{(\dot{m}_{drop})t} \qquad (7.16)$$

Again knowing that the energy equations are in the form of $\frac{\partial^2 T}{\partial z^2} = 0$ and $\frac{\partial^2 \theta}{\partial z^2} = 0$ (Myers, 2001), by twice integrating and applying boundary conditions at the substrate and interfaces the surface temperatures of the glaze ice and water will be calculated by the following formulas:

$$T = T_{substrate} + \Big[\frac{(T_{freezing} - T_{substrate})}{B}\Big].z \qquad (7.17)$$

which z is an arbitrary thickness of ice plus water ($0 \leqslant z \leqslant B$).

and

$$\theta = T_{freezing} + \frac{(+\dot{Q}_{aero} + \dot{Q}_{kin}) - (+\dot{Q}_{conv} + \dot{Q}_{drob} + \dot{Q}_{evap})}{k_w + h\frac{(+\dot{Q}_{conv}+\dot{Q}_{drob}+\dot{Q}_{evap})}{(T_{freezing}-T_{ambient})}}.(z-B) \qquad (7.18)$$

which z is an arbitrary thickness of ice plus water ($B \leqslant z \leqslant (B+h)$).

these equations depend on the ice and water heights, which in turn depend on the temperature through equation 7.7.

To solve the coupled problem, first integrate the mass balance (equation 7.6) to obtain an expression for h as a function of B and t:

$$h = \frac{\dot{m}_{drop}(t - t_g) - \rho_{glaze}(B - B_g)}{\rho_w} \qquad (7.19)$$

This involves the constants of integration B_g and t_g, the ice thickness and time at which water first appears (transient point).

Differentiating equations 7.17, 7.18 provides expressions for the temperature gradients, which, together with equation 7.19 will be substituted into the Stefan condition, equation 7.7, to provide a first-order non-linear ordinary differential equation for the glaze-ice thickness:

$$\begin{aligned} \rho_{glaze} L_f \frac{\partial B}{\partial t} = \\ \frac{k_i(T_{freezing} - T_{substrate})}{B} - k_w \frac{(+\dot{Q}_{aero} + \dot{Q}_{kin}) - (+\dot{Q}_{conv} + \dot{Q}_{drob} + \dot{Q}_{evap})}{k_w + h\frac{(+\dot{Q}_{conv} + \dot{Q}_{drob} + \dot{Q}_{evap})}{(T_{freezing} - T_{ambient})}} = \\ \frac{k_i(T_{freezing} - T_{substrate})}{B} - \\ k_w \rho_w \frac{(+\dot{Q}_{aero} + \dot{Q}_{kin}) - (+\dot{Q}_{conv} + \dot{Q}_{drob} + \dot{Q}_{evap})}{k_w \rho_w + [\dot{m}_{drop}(t - t_g) - \rho_{glaze}(B - B_g)]\frac{(+\dot{Q}_{conv} + \dot{Q}_{drob} + \dot{Q}_{evap})}{(T_{freezing} - T_{ambient})}} \end{aligned} \tag{7.20}$$

For glaze ice, first B should be calculated to obtain the values of T, θ and h.

The 2.4 cm is a conservative estimate for the maximum limit of the ice thickness (B), otherwise, the time-step of ice accretion should be modified to repeat the solution. The thickness of the water layer (h), however, must remain thin (unless there is a slow buildup of water, which allows time for the temperature to adjust), with 3 mm being the lower value of the estimate.

The freezing fraction (FF) for glaze ice is defined as:

$$FF = \frac{\rho_r B + \rho_g (B - B_g)}{(\dot{m}_{drop})t} \tag{7.21}$$

7.2.2 Modified Myers model

The extended Messinger model does take the sublimation and evaporation heat fluxes into account in the energy equations but the regarded mass fluxes did not count in the mass equations, it assumes that all of the incoming droplets turn into the ice. Even so, the mass term of sublimation or evaporation may be negligible in conservative balances of mass this decrease leads to reducing the freezing mass, because the magnitude of the latent heat value of freezing water is high (see Table 7.3), the heat term of

freezing droplets will be reduced which is not negligible anymore. In fact, including the sublimation or evaporation mass does indirectly affect the entire icing simulation by reducing the latent heat released by freezing droplets. Therefore, the Modified Myers model aims to include the sublimation and evaporation mass fluxes in all of the calculations of conservation of mass as follows:

$$\dot{m}_{drop} = \dot{m}_{freezing} + \dot{m}_{evap/sub} \tag{7.22}$$

for rime icing it is:

$$\dot{m}_{drop} = \dot{m}_{freezing} + \dot{m}_{sub} \tag{7.23}$$

and for glaze icing it will be:

$$\dot{m}_{drop} = \dot{m}_{freezing} + \dot{m}_{evap} \tag{7.24}$$

which causes a notable difference in the calculations of conservation of energy.

The only difference between the extended Messinger model and the Modified Myers model is that in the Modified Myers model, the total amount of the incoming water droplets which formed into the ice (i.e. $\dot{m}_{freezing}$) is obtained by subtracting the sublimation/evaporation mass fluxes from the mass of incoming droplets, and consequently, the heat term of ice ($\dot{Q}_{freezing}$) is corrected in the Modified Myers model, then all of the calculations of the Modified Myers model will be as what was for the extended Messinger model via formulas of the previous section.

The difference between Myers and Modified Myers models is in the calculations of B_g, t_g. Because the heat term of $\dot{Q}_{freezing}$ does not correctly calculate in the extended Messinger model the transient point in the extended Messinger model will lag and lead to overestimations in the cases of mixed and glaze ices.

7.2.3 Run-back water (RW) model

In this section, the mass and energy terms caused by the run-back water (moving film) are added in the continuity and energy equations of the Modified Myers model to have more accurate prediction in the case of the glaze ice.

By adding extra terms of Modified Myers model and terms of water film, the equivalent mass balance for run-back water (RW) model are as follows:

$$\dot{m}_{in} + \dot{m}_{drop} = \dot{m}_{freezing} + \dot{m}_{evap/sub} + \dot{m}_{out} \tag{7.25}$$

for rime icing it is:

$$\dot{m}_{in} + \dot{m}_{drop} = \dot{m}_{freezing} + \dot{m}_{sub} \tag{7.26}$$

and for glaze icing it will be:

$$\dot{m}_{in} + \dot{m}_{drop} = \dot{m}_{freezing} + \dot{m}_{evap} + \dot{m}_{out} \tag{7.27}$$

The terms of the mass conservation can be separated in two groups of the adding and subtracting terms (see Table 7.1).

Table 7.1 : Mass terms involving in the ice accretion.

Term	Description	Unit	Formula	Effect
$\dot{m}_{in}$	The mass flux that enters the control volume via run-back water film when the previous control volume experiences the glaze ice condition	$\frac{kg}{s.m^2}$	$\dot{m}_{out,previous\ upstream\ cell}$	adding
$\dot{m}_{drop}$	The inlet mass flux by incoming water droplets	$\frac{kg}{s.m^2}$	$\beta\bar{\rho}_{\infty}U_{\infty} = \beta(LWC)_{\infty}U_{\infty}$	adding
$\dot{m}_f$	The amount of total inlet mass flux that turns into ice	$\frac{kg}{s.m^2}$	$FF(\dot{m}_{drop} + \dot{m}_{in})$	subtracting
$\dot{m}_{sub}$	The mass flux that exits the volume control because of sublimation in the case of rime ice	$\frac{kg}{s.m^2}$	$\frac{\dot{Q}_{sub}}{L_{sub}} = \frac{X_{sub}e_0(T_s-T_a)}{L_{sub}}$	subtracting
$\dot{m}_{evap}$	The mass flux that exits from the volume control because of evaporation in the case of glaze ice	$\frac{kg}{s.m^2}$	$\frac{\dot{Q}_{evap}}{L_{evap}} = \frac{X_{evap}e_0(T_s-T_a)}{L_{evap}}$	subtracting
$\dot{m}_{out}$	The amount of water mass flux that leaves the control volume via run-back water film in the case of glaze ice	$\frac{kg}{s.m^2}$	$(1-FF)(\dot{m}_{drop} + \dot{m}_{in}) - \dot{m}_{sub/evap}$	subtracting

On the other hand, the general form of the energy balance is written as:

$$\dot{Q}_{in} + \dot{Q}_{aero} + \dot{Q}_{kin} + \dot{Q}_{freezing} = \dot{Q}_{conv} + \dot{Q}_{cond} + \dot{Q}_{evap/sub} + \dot{Q}_{drop} + \dot{Q}_{out} \tag{7.28}$$

which for rime icing it is:

$$\dot{Q}_{in} + \dot{Q}_{aero} + \dot{Q}_{kin} + \dot{Q}_{freezing} = \dot{Q}_{conv} + \dot{Q}_{cond} + \dot{Q}_{sub} + \dot{Q}_{drop} \tag{7.29}$$

and for glaze icing it will be:

$$\dot{Q}_{in} + \dot{Q}_{aero} + \dot{Q}_{kin} + \dot{Q}_{freezing} = \dot{Q}_{conv} + \dot{Q}_{cond} + \dot{Q}_{evap} + \dot{Q}_{drop} + \dot{Q}_{out} \tag{7.30}$$

Similarly, the terms of the energy balance can be separated in two groups of the cooling and heating terms (see Table 7.2).

Table 7.2 : Heat terms involving in the ice accretion.

Term	Description	Unit	Formula	Effect
$\dot{Q}_{in}$	The entering energy into control volume via entering water film when the previous control volume experiences the glaze ice condition	$\frac{W}{m^2}$	$\dot{m}_{in}c_{p,w}(T_{in}-T_{ref})$	heating
$\dot{Q}_{aero}$	The heat gain associated to aerodynamic heating provided by the friction of the air over the surface	$\frac{W}{m^2}$	$\frac{1}{2}\frac{r_{rec}h_{conv}U_e^2}{c_{p,a}}$	heating
$\dot{Q}_{kin}$	The heat gain associated to the kinetic energy of the incomming droplets	$\frac{W}{m^2}$	$\frac{1}{2}\dot{m}_{drop}V^2$	heating
$\dot{Q}_f$	The heat gain associated to the release of the latent heat of fusion or solidification	$\frac{W}{m^2}$	$\dot{m}_{f,r}L_f$ *or* $\rho_g L_f\frac{\partial B}{\partial t}$	heating
$\dot{Q}_{conv}$	The convective heat loss exchanged between ice (rime regime) or water (glaze regime) with the surrounding air	$\frac{W}{m^2}$	$h_{conv}(T_s-T_a)$	cooling
$\dot{Q}_{cond}$	The conductive heat loss exchanged between ice and substrate	$\frac{W}{m^2}$	$k_{cond}\frac{dT}{dx}\|_{wall}$	cooling
$\dot{Q}_{drop}$	The cooling imposed by the incoming super-cooled droplets	$\frac{W}{m^2}$	$\dot{m}_{drop}c_{p,w}(T_a-T_d)$	cooling
$\dot{Q}_{sub}$	The sublimation heat loss between ice and the surrounding air in rime-icing	$\frac{W}{m^2}$	$\dot{m}_{sub}L_{sub}=X_{sub}e_0(T_s-T_a)$	cooling
$\dot{Q}_{evap}$	The evaporative heat loss between water and the surrounding air in glaze-icing	$\frac{W}{m^2}$	$\dot{m}_{evap}L_{evap}=X_{evap}e_0(T_s-T_a)$	cooling
$\dot{Q}_{out}$	The exiting energy from control volume via exiting water film in glaze-icing	$\frac{W}{m^2}$	$\dot{m}_{out}c_{p,w}(T_{out}-T_{ref})$	cooling

The involving terms of mass and heat conservation in the calculations of the rime and glaze ice are also shown in the Figure 7.4.

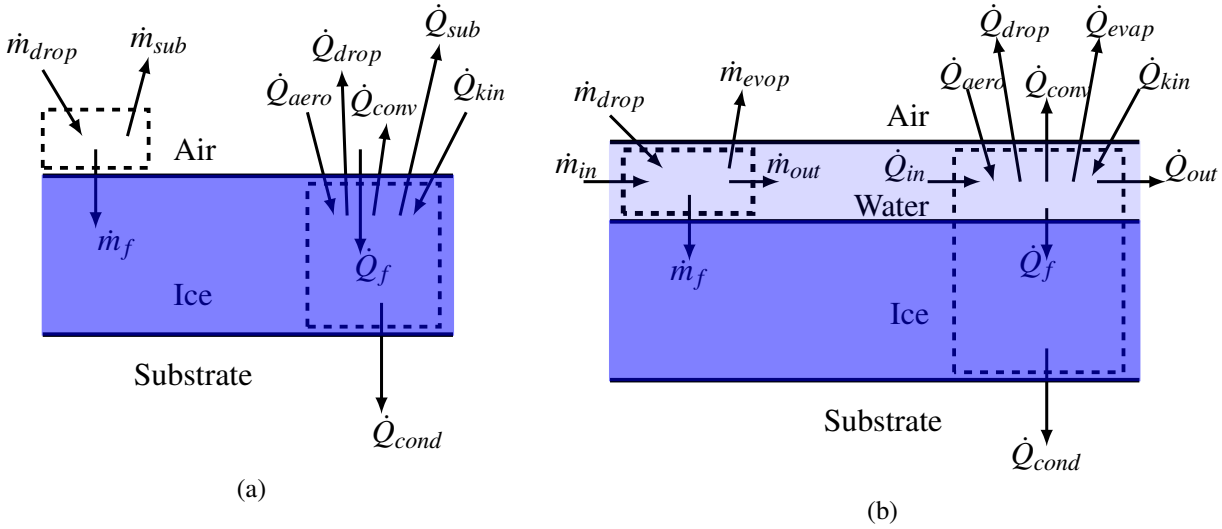

Figure 7.4 : The mass and heat terms involving in the calculations of ice accretion for the a) rime and b) glaze ice.

Schematic of the thicknesses of ice (B) and water film (h), and the temperatures of ice layer (T) and water film layer (θ) are shown in the Figure 7.5.

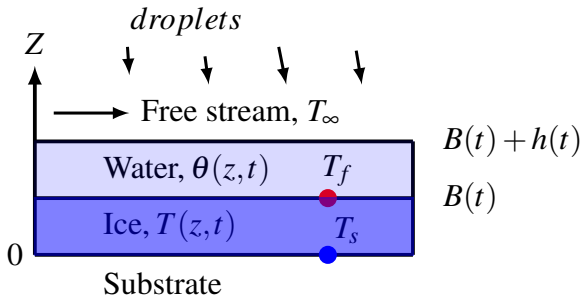

Figure 7.5 : The thicknesses of ice (B), water film (h), and the temperatures of ice layer (T), water film layer (θ).

For rime ice, the formulas of thickness and temperature are as:

$$B = \frac{\dot{m}_{drop} + \dot{m}_{in} - \dot{m}_{sub}}{\rho_{rime}} t \tag{7.31}$$

$$T = T_{substrate} + \frac{(+\dot{Q}_{in} + \dot{Q}_{aero} + \dot{Q}_{kin} + \dot{Q}_{freezing}) - (+\dot{Q}_{conv} + \dot{Q}_{drob} + \dot{Q}_{sub})}{k_i + B\frac{(+\dot{Q}_{conv}+\dot{Q}_{drob}+\dot{Q}_{sub})}{(T_{substrate}-T_{ambient})}} z \tag{7.32}$$

The freezing fraction for rime ice is defined as:

$$FF = \frac{\rho_r B}{(\dot{m}_{drop} + \dot{m}_{in})t} \tag{7.33}$$

Substituting relevant value of FF, the ice mass $(\dot{m}_{freezing})$ and outlet mass $(\dot{m}_{out})$ for rime ice are as:

$$\dot{m}_{freezing} = FF(\dot{m}_{drop} + \dot{m}_{in}) \tag{7.34}$$

and

$$\dot{m}_{out} = 0.0 \tag{7.35}$$

For glaze ice, the formulas of thicknesses and temperatures are as:

$$\rho_{glaze} L_f \frac{\partial B}{\partial t} = \frac{k_i (T_{freezing} - T_{substrate})}{B} - k_w \rho_w \frac{(+\dot{Q}_{in} + \dot{Q}_{aero} + \dot{Q}_{kin}) - (+\dot{Q}_{conv} + \dot{Q}_{drob} + \dot{Q}_{evap} + \dot{Q}_{out})}{k_w \rho_w + [(\dot{m}_{drop} + \dot{m}_{in} - \dot{m}_{evap} - \dot{m}_{out})(t - t_g) - \rho_{glaze}(B - B_g)] \frac{(+\dot{Q}_{conv} + \dot{Q}_{drob} + \dot{Q}_{evap} + \dot{Q}_{out})}{(T_{freezing} - T_{ambient})}} \tag{7.36}$$

$$T = T_{substrate} + \left[\frac{(T_{freezing} - T_{substrate})}{B}\right] z \tag{7.37}$$

$$h = \frac{(\dot{m}_{drop} + \dot{m}_{in} - \dot{m}_{evap} - \dot{m}_{out})(t - t_g) - \rho_{glaze}(B - B_g)}{\rho_w} \tag{7.38}$$

$$\theta = T_{freezing} + \frac{(+\dot{Q}_{in} + \dot{Q}_{aero} + \dot{Q}_{kin}) - (+\dot{Q}_{conv} + \dot{Q}_{drob} + \dot{Q}_{evap} + \dot{Q}_{out})}{k_w + h \frac{(+\dot{Q}_{conv} + \dot{Q}_{drob} + \dot{Q}_{evap} + \dot{Q}_{out})}{(T_{freezing} - T_{ambient})}} (z - B) \tag{7.39}$$

The freezing fraction for glaze ice is defined as:

$$FF = \frac{\rho_r B + \rho_g (B - B_g)}{(\dot{m}_{drop} + \dot{m}_{in}) t} \tag{7.40}$$

To solve the equations for glaze ice in RW model, the values of $\dot{m}_{out}$ and $\dot{Q}_{out}$ are allocated from the previous time step in computational procedure. After calculating all of the thicknesses and temperatures, these values are updated at the end of current time step.

Substituting relevant value of FF, the ice mass $(\dot{m}_{freezing})$ and outlet mass $(\dot{m}_{out})$ for glaze ice are as:

$$\dot{m}_{freezing} = FF(\dot{m}_{drop} + \dot{m}_{in}) \tag{7.41}$$

and

$$\dot{m}_{out} = (1 - FF)(\dot{m}_{drop} + \dot{m}_{in}) - \dot{m}_{evap} \tag{7.42}$$

Run-back Water (RW) model, does take the mass and heat of sublimation/evaporation into account for the calculations of thicknesses and temperatures. In our study,

the radiation heat term ($\dot{Q}_{rad}$) does not take into account in the thermodynamic calculations.

In the conventional ice accretion (extended Messinger and RW) models for a smooth transition from the rime to glaze models, the ice and water thicknesses and growth rates must be continuous. To determine when this occurs, the ice mass growth rate from the mass balance (equation 8.7) is substituted into the Stefan condition (equation 8.8) to give:

$$\begin{aligned} \dot{Q}_{gain} &= \dot{Q}_{in} + \dot{Q}_{aero} + \dot{Q}_{kin} + \dot{Q}_{freezing} \\ \dot{Q}_{lost} &= \dot{Q}_{conv} + \dot{Q}_{drob} + \dot{Q}_{evap} \\ B_g &= \frac{k_i(T_{freezing} - T_{substrate})}{\dot{Q}_{gain} - \dot{Q}_{lost}} \end{aligned} \tag{7.43}$$

Here, B_g is evaluated separately for each surface point. In transient point $\dot{Q}_{out} = 0$, but the upstream cell can be in rime or glaze condition then $\dot{Q}_{in}$ should be included.

The B_g is the ice thickness which glaze ice first appears. This explicit formula shows how B_g depends on the ambient conditions. An important feature of the equation is that it allows positive, negative, and even infinite values for B_g. These may be interpreted in the following way. If $0 < B_g < +\infty$, it indicates that the glaze ice might appear. An infinite or negative value for B_g indicates glaze ice will never appear. The B_g may have negative values when the numerator is negative $(T_{freezing} - T_{substrate}) < 0$. The negative numerator indicates that the substrate is too warm such that ice cannot form. Once, the denominator of equation 7.43 is less than or equal to zero, there will never be enough energy in the system to produce water, and the accretion is pure rime.

Because the ice thickness must be continuous between the two growth regimes, the time when glaze first appears is determined by comparison with equation 8.16 as:

$$t_g = \frac{\rho_r}{\dot{m}_{drop} + \dot{m}_{in} - \dot{m}_{evap}} B_g \tag{7.44}$$

If instead of initial rime ice growth, the glaze ice or water appears from the very beginning of the icing, then the initial conditions on the mass balance (equation 8.7) and the Stefan condition (equation 8.8) would be $B = h = 0$. equation 8.8 shows $\frac{\partial B}{\partial t} \to +\infty$, and the mass conservation (equation 8.7) indicates that $\frac{\partial h}{\partial t} \to -\infty$. Because

h is initially zero, this indicates that the water height immediately becomes negative, which is clearly non-physical, and the only reasonable assumption to be a draw when glaze ice first appears is $B_g \geqslant 0$.

$$\begin{cases} B_g \leqslant 0 \ \rightarrow \ rime\ ice\ regime \\ B_g > 0 \ \rightarrow \ ice\ accretion \begin{cases} time \leqslant t_g \ \rightarrow \ rime\ ice\ regime \\ time > t_g \ \rightarrow \ glaze\ ice\ regime \end{cases} \end{cases}$$

In general, the methodology for solving an ice accretion problem under the specific ambient condition proceeds as follows:

1) Calculate all of the necessary parameter values and determine the ice thickness and time which glaze first appear (B_g and t_g) via equations 7.43, 7.44.

2) If $B_g \leqslant 0$, this indicates the model assumptions are invalid and glaze ice never forms. Alternatively, if $B_g > 0$ and $time \leqslant t_g$, there would not be enough time for glaze ice to form. In either case, the ice thickness is determined by equation 8.16, and the temperature throughout the ice is given by equation 8.17.

3) If $B_g > 0$ and $time > t_g$, then glaze ice would occur during the icing. The ice thickness is determined by numerical integration of equation 8.24. Once, the ice thickness (B) is known, the water thickness (h) and the ice and water temperatures $(T \ and \ \theta)$ are given by equations 8.23, 8.21, 8.22, respectively.

7.3 Optimum Steps for Multi-Layers Ice-Accretion Approach

Because the nature of icing is accumulative and ice shapes gradually on the surface, it is anticipated that the multi-layers approach leads to better results in aircraft-icing simulation, then it is tried to solve the governing equations in multi-steps. While the fewer step numbers cause less accurate results, more numbers of steps do not guarantee more accurate results and do increase the round-off error. Therefore, there should be an optimum number of steps. To predict this optimum step number either the time-step or ice-thickness criteria can be used (Verdin and Charpin, 2013).

7.4 Regeneration of Iced Geometry

Once calculations of the ice accretion have been done for each time step the initial geometry of the airfoil will be changed because of icing contamination of the surface.

Thus, it is necessary to regenerate the grid for the new body surface and repeat the calculations from the very beginning module i.e. the elliptic grid generation (chapter 3).

$$\begin{aligned} X^n(i,1) &= X^{n-1}(i,1) + \\ Thickness^n_{TotalIce}(i)\frac{NormalVector_X(i,1)}{\sqrt{NormalVector_X(i,1)^2 + NormalVector_Y(i,1)^2}} \\ Y^n(i,1) &= Y^{n-1}(i,1) + \\ Thickness^n_{TotalIce}(i)\frac{NormalVector_Y(i,1)}{\sqrt{NormalVector_X(i,1)^2 + NormalVector_Y(i,1)^2}} \end{aligned} \tag{7.45}$$

which $n-1$ and n demonstrate the previous and present time steps, respectively.

7.5 Avoiding Multiple Stagnation Points

By progressing time in the multi-layers icing approach, more than one stagnation point will be revealed during each time step because of ice formation. Because the stagnation point is the benchmark in the aircraft-icing simulation, to avoid multiple stagnation points, a new geometry shape can be estimated by the curve fitting method or the average of velocities may be calculated to have one stagnation point by using the smoothing method (Gent et al., 2000; Gouttebroze et al., 2000).

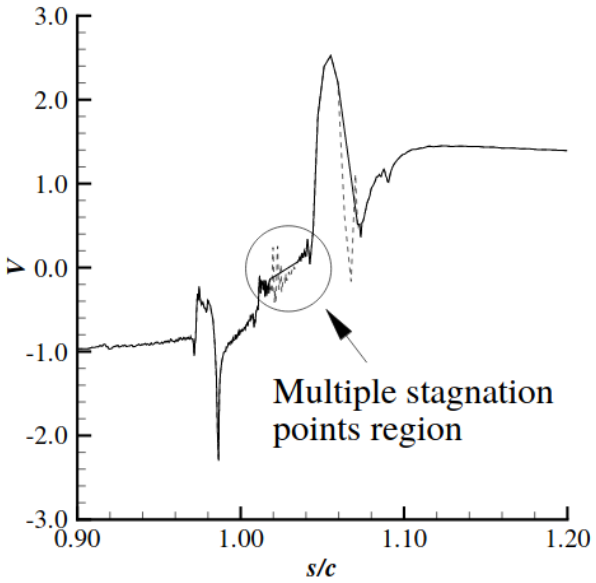

Figure 7.6 : The multiple stagnation points in the vicinity of the leading edge due to the formation of ice (Gouttebroze et al., 2000).

Although the use of small-time steps provides a consistent and smooth growth in ice, the presence of sharp corners near the stagnation region causes multiple stagnation points to appear as shown in Figure 7.6. The existence of multiple stagnation points presents a significant challenge to the solution of the boundary-layer equations and often leads to a breakdown of their solution. To overcome this problem, the velocity profile near the stagnation region is approximated with the help of a smooth curve. For example, to avoid multiple stagnation points, the tangential velocity V vs surface-arc length s curve is artificially smoothed. The choice of the stagnation point is then based on the location nearest to that of the stagnation point in the previous time step. Several curve-fitting schemes have been investigated to date and include: (a) least-squares fit, (b) linear interpolation, (c) B-spline, and (d) Bezier curve. Of these four techniques, the Bezier curve was found to yield the best results. Figure 7.7 shows the artificial smoothing as it is applied to correct for the multiple stagnation points (Saeed et al., 2001).

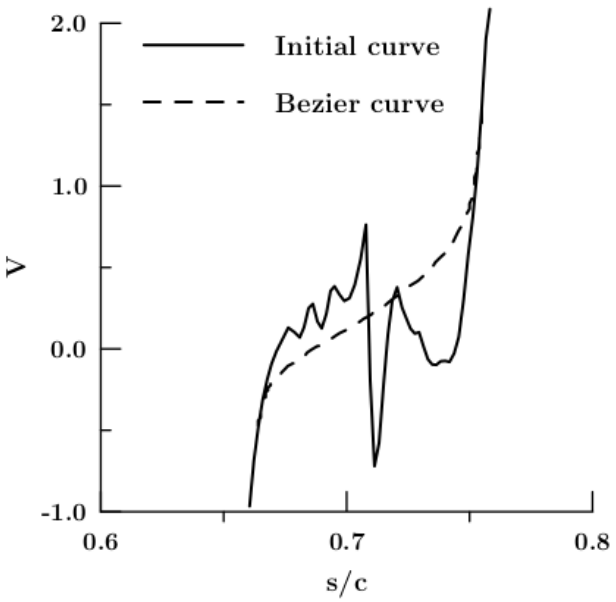

Figure 7.7 : The artificial smoothing applied to tanential velocity curve (Saeed et al., 2001).

The Bezier curve utilizes De Casteljau's algorithm to solve the problem. The geometric interpretation of De Casteljau's algorithm is straightforward.

- Consider a Bézier curve with control points $P_0, ..., P_n$. By connecting the consecutive points we create the control polygon of the curve.

- Subdivide now each line segment of this polygon with the ratio $r_{seg} : (1 - r_{seg})$ and connect the points. In this way, arrive at the new polygon having one fewer segment.
- Repeat the process until arrive at the single point, this is the point of the curve corresponding to the parameter r_{seg}.

Figure 7.8 shows this process for a cubic Bézier curve:

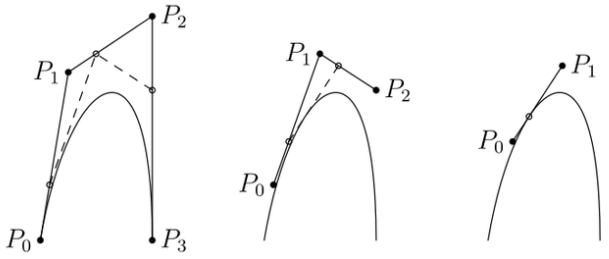

Figure 7.8 : Interpretation of De Casteljau's Algorithm.

The intermediate points that were constructed are in fact the control points for two new Bézier curves, both exactly coincident with the old one. This algorithm not only evaluates the curve at t, but also splits the curve into two pieces at t, and provides the equations of the two sub-curves in Bézier form.

Four points P_1, P_2, P_3 and P_4 in the plane or in higher-dimensional space define a cubic Bézier curve. The curve starts at P_1 going toward P_2 and arrives at P_4 coming from the direction of P_3. Usually, it will not pass through P_2 or P_3; these points are only there to provide directional information. The distance between P_2 and P_3 determines "how far" and "how fast" the curve moves towards P_2 before turning towards P_3.

Any series of 4 distinct points can be converted to a cubic Bézier curve that goes through all 4 points in order. The samples of 4 points Bézier curve are shown in Figure 7.9, Figure 7.10:

The concept of 4 points Bézier curve is as explained below:

- Connect control points by segments: $1 \rightarrow 2$, $2 \rightarrow 3$ and $3 \rightarrow 4$. There will be 3 brown segments.
- For each r_{seg} in the interval from 0 to 1, we take points on these segments on the distance proportional to r_{seg} from the beginning. These points are connected so that we have two green segments.

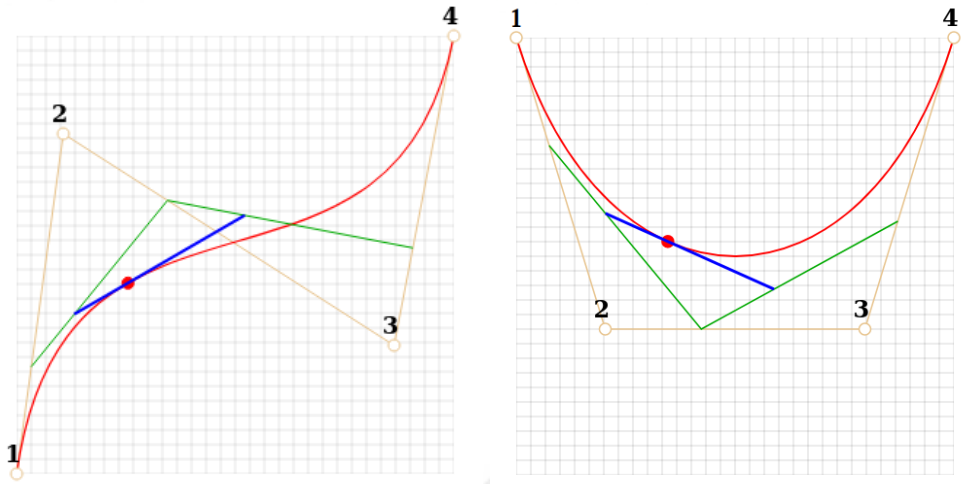

(a) (b)

Figure 7.9 : The concept of Cubic Bezier Curve.

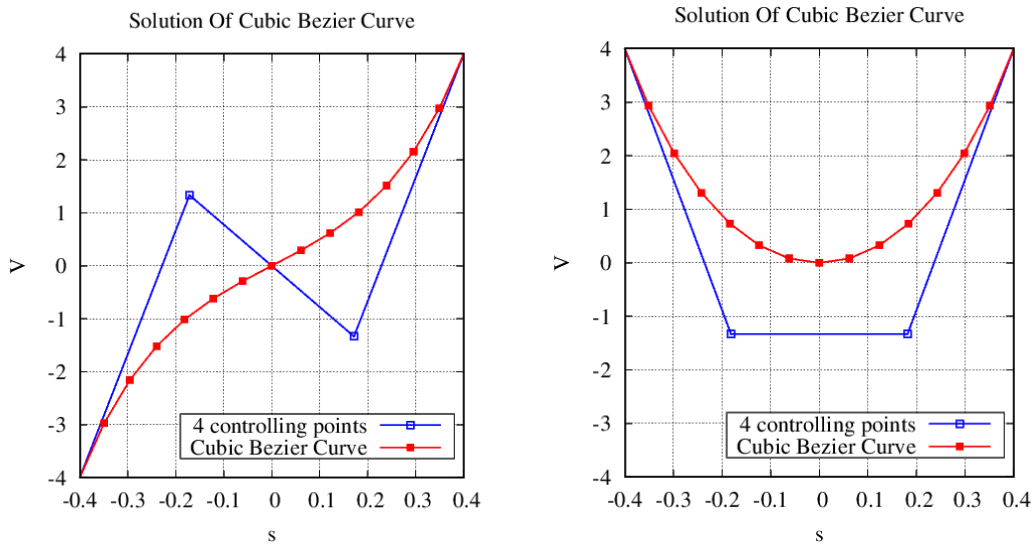

(a) (b)

Figure 7.10 : The results of Fortran-programing for Cubic Bezier Curve (see appendix 5).

- On these segments we take points proportional to r_{seg}. We get one blue segment.
- On the blue segment we take a point proportional to r_{seg}. In the example above it's red.
- These red points together form the smoothing curve.

The explicit form of the cubic Bezier curve is (also see appendix 5):

$$Be(r_{seg}) = (1-r_{seg})^3 P_1 + 3(1-r_{seg})^2 r_{seg} P_2 + 3(1-r_{seg}) r_{seg}^2 P_3 + r_{seg}^3 P_4 \qquad ,0 \leqslant r_{seg} \leqslant 1. \tag{7.46}$$

which P_1, P_2, P_3 and P_4 are 4 controlling points, r_{seg} is the independent segment ratio and $Be(r_{seg})$ is the dependent Bezier value.

The schematic of the conventional aircraft-icing simulation is shown in Figure 7.11.

7.6 Algorithm of Iterative Solution for Conventional Aircraft Icing Simulation

1. The grid is generated.
2. The airflow is solved by inviscid or viscous flow approaches. For the inviscid airflow, the stream function equation is solved, and for the viscous airflow the vorticity, stream function, and transport viscosity equations are solved.
3. The distribution of water droplets and collection efficiency is found using the calculated values of airflow in the current time-step (i.e. time marching concept) regardless of whether the inviscid or viscous airflow approaches have been used.
4. The convective heat transfer coefficient is calculated using the calculated values of airflow in the current time-step (i.e. time marching concept). For inviscid airflow, the Integral Boundary Layer method is applied, and for viscous airflow, the energy equation is solved alongside the vorticity, stream function, and transport viscosity equations.
5. The convergence criteria of the airflow, droplets' distribution, and energy equation will be checked during each time marching, if the problem was not converged then the time marching is continued from the second module (i.e. the airflow solution).

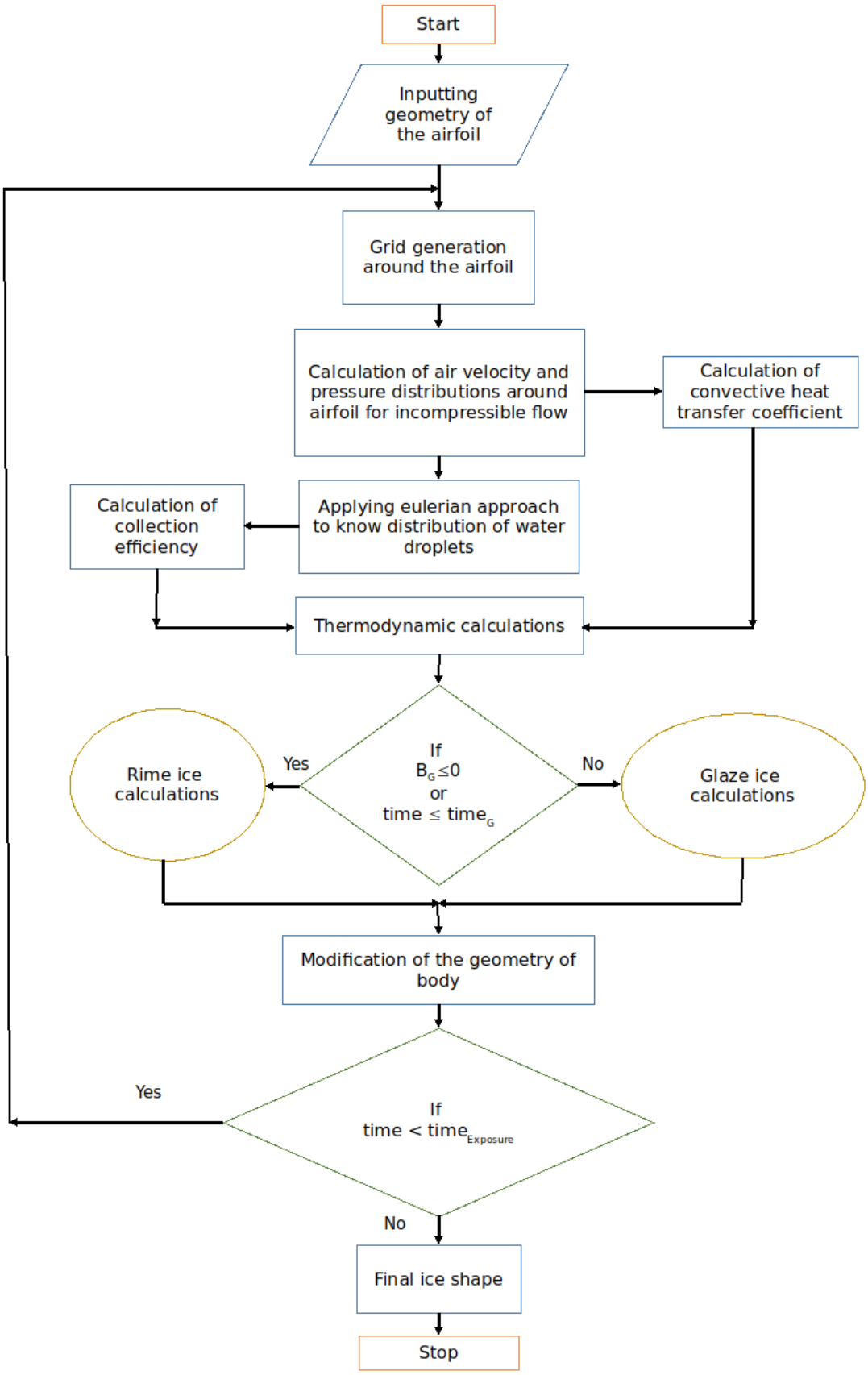

Figure 7.11 : Flowchart of the conventional aircraft-icing simulation.

6. Once the collection efficiency and convective heat transfer coefficient are found the thermodynamic calculations are implemented as follows to know the thickness of ice (ice accretion). The critical time and thickness of icing which water film is seen for the first time are calculated. For the negative B_g the rime ice model will be used. For the positive B_g the icing time which has started from the clean body (surface with no ice), is compared with the critical time (t_g), if the spending time was less than the critical time then the rime ice model is applied, otherwise, the glaze ice model will be used. In the rime ice model, the mass and energy equations will be separately solved for the calculation of ice thickness and temperature of the free surface, respectively. In the glaze ice model, based on the standard method of specifying a phase change or Stefan problem the combination of continuity and energy equations gives a first-order non-linear ordinary differential equation for the calculation of ice thickness, which is the Runge-Kutta method (see appendix 4) is used for solving this equation (Mathews and Fink, 2004). Then, the thickness of the water film, and the temperatures of the ice and water are obtained. In each icing time-step, if the accumulated thickness of the ice and water film during this time-step was larger than 2.4 cm and 3 mm, respectively, the time-step of icing is modified and the calculations of the ice accretion are repeated.

7. The geometry of the contaminated (iced) body is regenerated.

8. Because the geometry of the body changes during icing in each time step, the calculations will be restarted from the very beginning module of the aircraft-icing i.e. the grid generation. Then, all of the calculations will be continued until the final icing exposure time.

7.7 Assumptions

1. It is assumed that the collection efficiency equals to the collision efficiency.

2. The validations are implemented for $chord = 0.53\ m$ then the results are presented for $chord = 1.0\ m$.

3. The freezing temperature of water droplets is $0^{\circ}\ C$.

7.8 Validation

In this section, first, the extended Messinger model of ice accretion is validated for specific parameter values (Table 7.3) and different temperatures of the ambient and substrate (Figure 7.12, Figure 7.13). These are the validation of extended Messinger model only for one dimensional ice-accretion. In these figures, T_s and T_a are the substrate and ambient temperatures, respectively.

Table 7.3 : Parameter values used for the validation of extended Messinger model (Myers, 2001) in Figure 7.12 and Figure 7.13.

Parameter	Description	Unit	Value
$\mathbf{c_a}$	specific heat of air	$J/(kg.K)$	1014
$\mathbf{c_i}$	specific heat of ice	$J/(kg.K)$	2050
$\mathbf{c_w}$	specific heat of water	$J/(kg.K)$	4218
$\mathbf{e_0}$	vapor pressure constant	Pa/K	27.03
$\tilde{\rho}_\infty$	liquid water content of ambient	kg/m^3	0.001
$\mathbf{h_{conv,AirWater}}$	convective heat coefficient between air and water	$W/(m^2.K)$	500
$\mathbf{h_{conv,AirIce}}$	convective heat coefficient between air and ice	$W/(m^2.K)$	1000
$\mathbf{k_i}$	conductive heat coefficient of ice	$W/(m.K)$	2.18
$\mathbf{k_w}$	conductive heat coefficient of water	$W/(m.K)$	0.571
Le	Lewis number	—	13.4
$\mathbf{L_f}$	Latent heat of freezing	J/kg	3.344×10^5
$\mathbf{L_e}$	Latent heat of evaporation	J/kg	2.26×10^6
$\mathbf{L_s}$	Latent heat of sublimation	J/kg	2.26×10^6
$\mathbf{p_0}$	ambient pressure	Pa	6.3×10^4
β	collection efficiency	—	0.55
$\rho_\mathbf{r}$	density of rime ice	kg/m^3	880
$\rho_\mathbf{g}$	density of glaze ice	kg/m^3	917
$\rho_\mathbf{w}$	density of water	kg/m^3	1000
$\mathbf{X_s}$	sublimation coefficient	m/s	11.0
$\mathbf{X_e}$	evaporation coefficient	m/s	11.0
r	recovery coefficient	—	0.84

In Figure 7.12, the results of the extended Messinger model are shown for two different air temperatures of 263.15 K (-10 Celsius) and 270 K (-3 Celsius). The substrate temperature in both cases is assumed to be the same as the air temperature. As shown in this figure, dark-blue lines denote $T_a = 263.15K$, and the lines of ice thickness and ice plus water thickness are the same for small times since there is no water present. Two dark-blue lines diverge only when water appears. In this case, water and, hence, glaze ice first occurs after 45 seconds, when the ice height is about 2.6 mm. Light-blue lines in Figure 7.12 denote $T_a = 270K$, because the air is warmer, the glaze appears much more rapidly after 7 seconds and about 0.5 mm ice thickness.

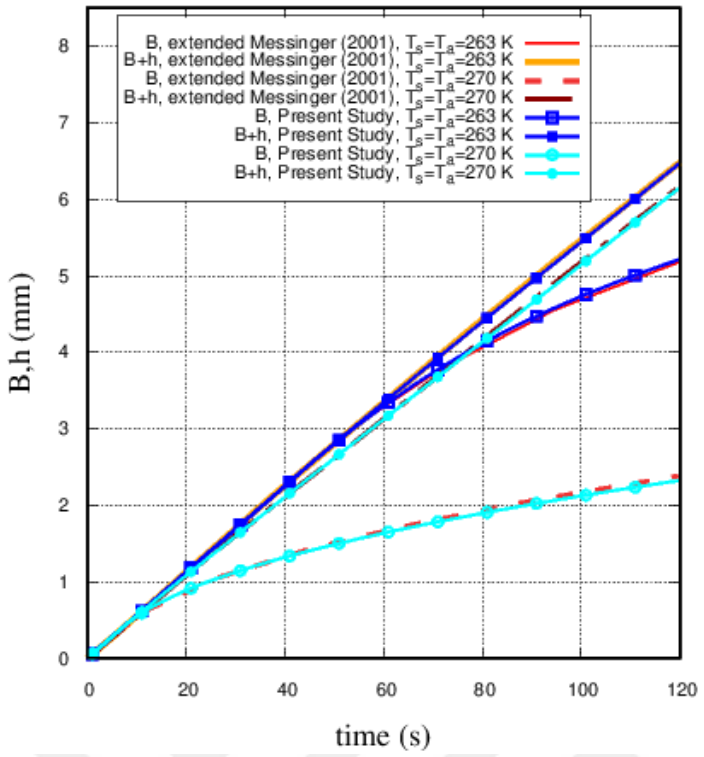

Figure 7.12 : The validation of extended Messinger model, B,h vs $time$ with respet to Myers (2001), for $\bar{\rho}_\infty = 0.001\ kg/m^3$, $\beta = 0.55$, $U_\infty = 90\ m/s$, and $AOA = 0\ ^\circ$, in different ambient temperatures of $T_s = T_a = 263\ K$ and $T_s = T_a = 270\ K$.

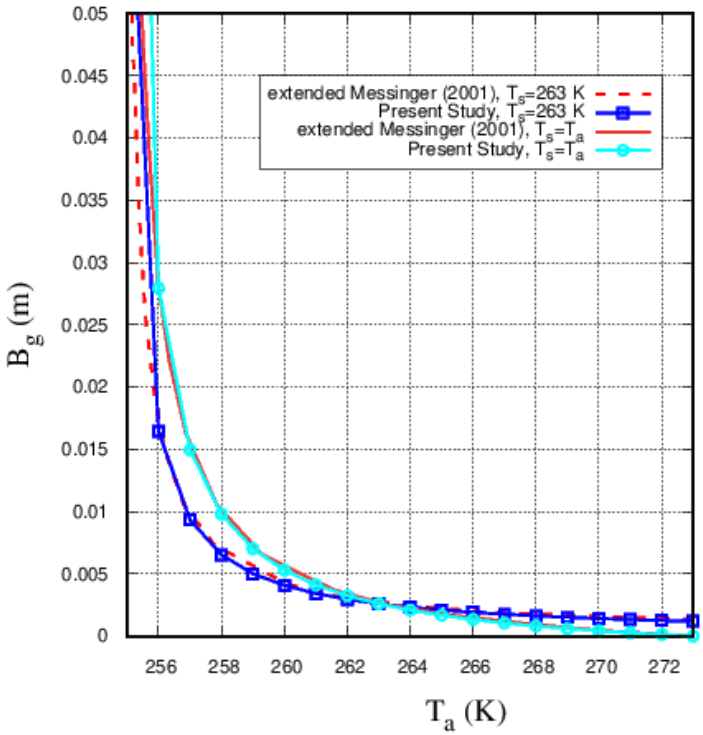

Figure 7.13 : The validation of extended Messinger model, B_g vs T_a with respet to Myers (2001), for $\bar{\rho}_\infty = 0.001\ kg/m^3$, $\beta = 0.55$, $U_\infty = 90\ m/s$, and $AOA = 0\ ^\circ$.

Figure 7.13 shows the variation of the critical transient time with ambient temperature. When the substrate temperature is the same as the air temperature, the light-blue line shows when $T_s = T_a = T_f$ (T_f is freezing temperature) the ice can not be accreted, consequently $B_g = 0$. Decreasing T_a increases the value of B_g until a singularity is reached about at $T_a = 255\ K$. This is the lowest temperature that glaze ice can occur under the present conditions. The dark-blue line in Figure 7.13 shows the value of B_g with a substrate temperature fixed at $T_s = 263.15\ K$. The value of the ambient temperature that glaze never occurs approximately equals the value for the light-blue line. However, when $T_a = T_f$, the dark-blue line displays a nonzero B_g, and indicates ice may grow even when the air temperature is above freezing temperature.

In the following part of this section, the different models of ice accretion will be verified by the experimental and computational results of DRA, NASA and ONERA collaboration during the entire aircraft-icing simulations (Figure 7.14, Figure 7.15, Figure 7.16).

Validation results show that the extended Messinger model gives more overestimated results in the cases of mixed and glaze ices because by using the value of collection efficiency at the zero time there will be a kind of exaggeration in the magnitude of the values of transient-point of rime into glaze ice (Figure 7.14).

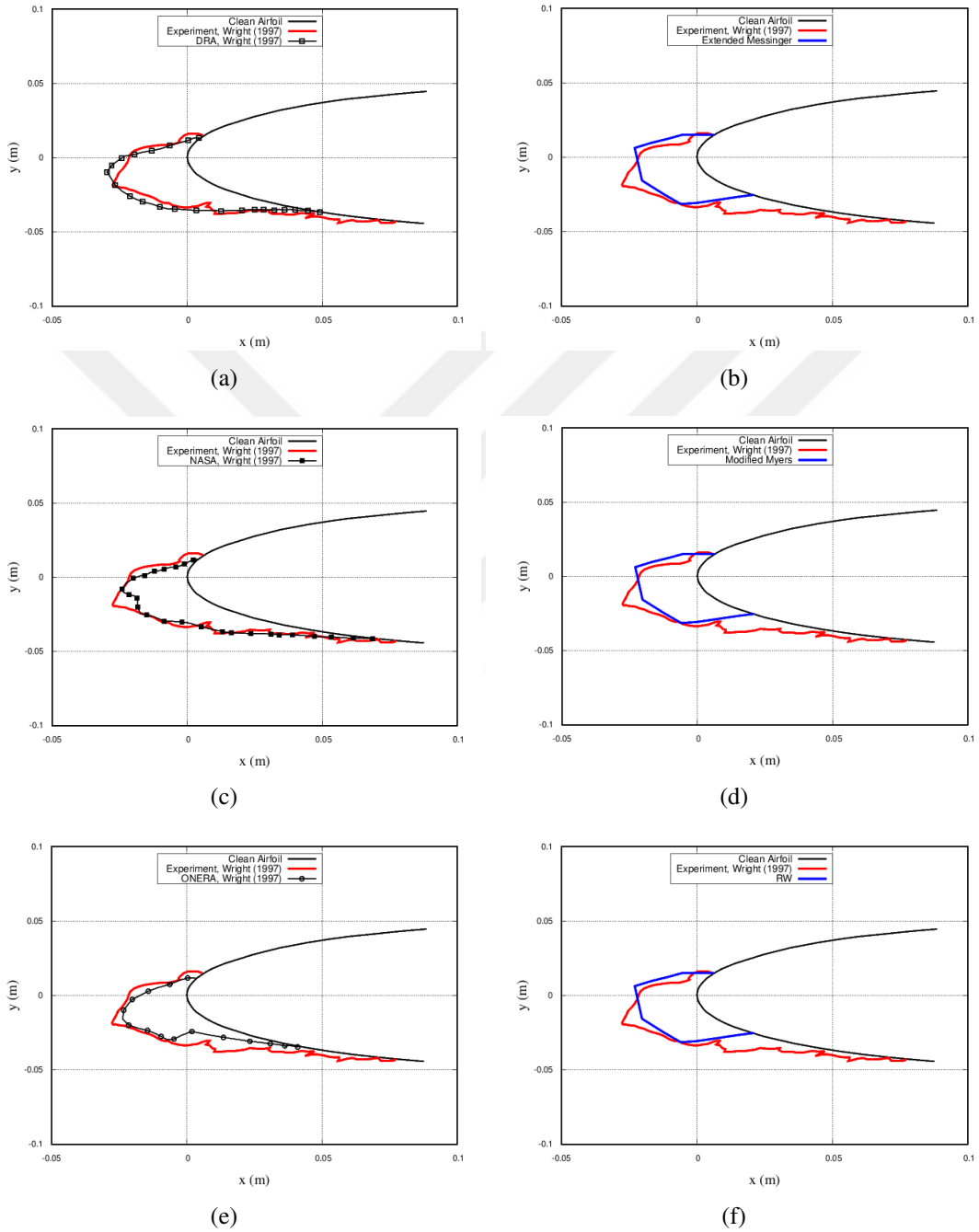

Figure 7.14 : The comparision of DRA, NASA and ONERA results and validation of conventional ice-accretion models (i.e. Extended Messinger, Modified Myers and RW models) with experimental results with respect to Wright et al. (1997) in the case of rime ice for $chord = 0.53\ m$, $U_\infty = 58.1\ m/s$, $AOA = 4\ ^\circ$, $D = 20\ \mu m$, $\bar{\rho}_\infty = 0.0013\ kg/m^3$, $T_a = -27.8\ ^\circ C$, and $time_{exposure} = 480\ s$.

The Modified Myers model gives better results in the cases of mixed and glaze ices since the mass terms of sublimation/evaporation are taken into account. But the results are still unreliable in both cases (Figure 7.15).

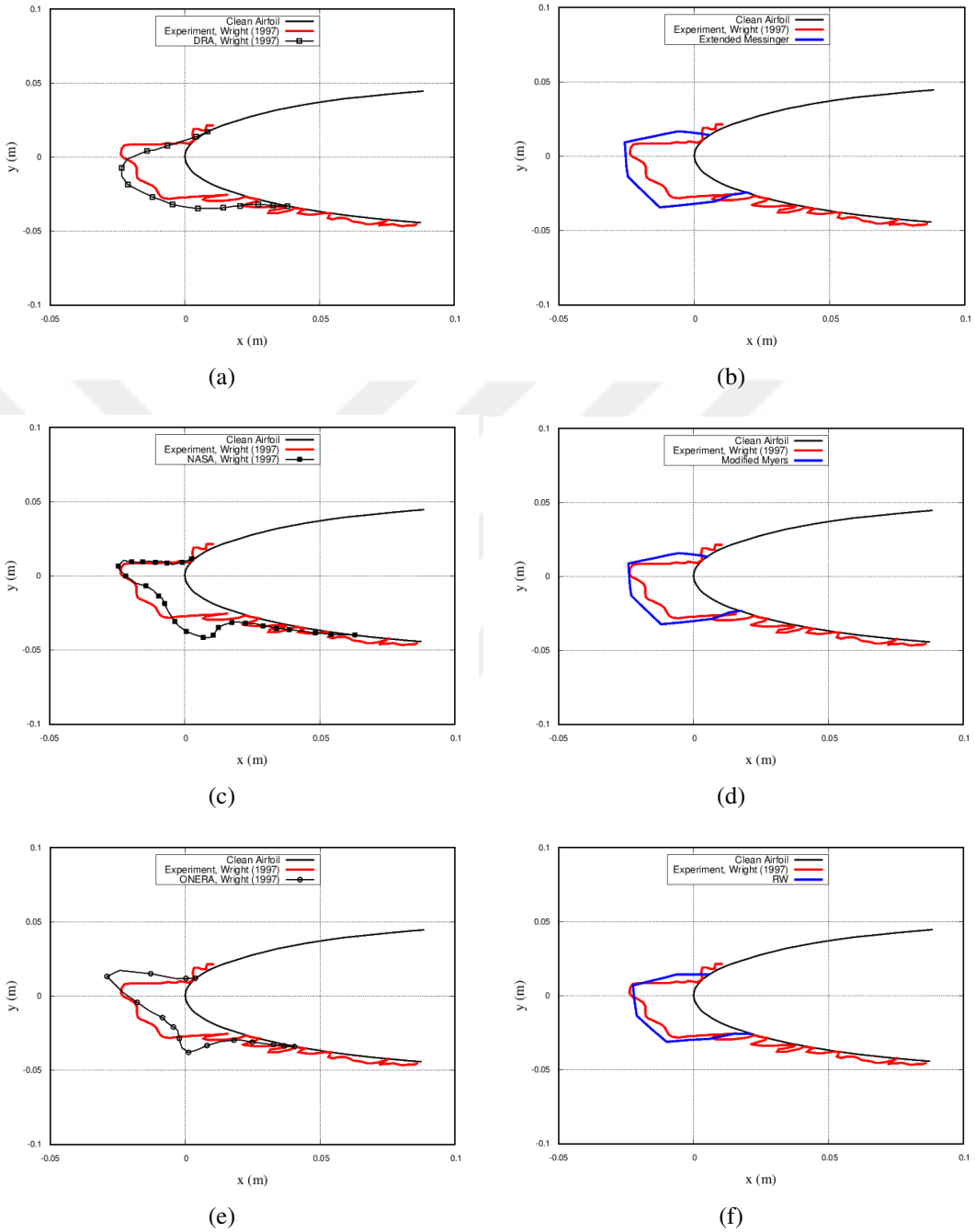

Figure 7.15 : The comparision of DRA, NASA and ONERA results and validation of conventional ice-accretion models (i.e. Extended Messinger, Modified Myers and RW models) with experimental results with respect to Wright et al. (1997) in the case of mixed ice for $chord = 0.53\ m$, $U_\infty = 58.1\ m/s$, $AOA = 4\ ^\circ$, $D = 20\ \mu m$, $\bar{\rho}_\infty = 0.0013\ kg/m^3$, $T_a = -13.9\ ^\circ C$, and $time_{exposure} = 480\ s$.

Finally, the RW model leads to more acceptable results in the cases of mixed and glaze ices, but it is still open to some improvements (Figure 7.16).

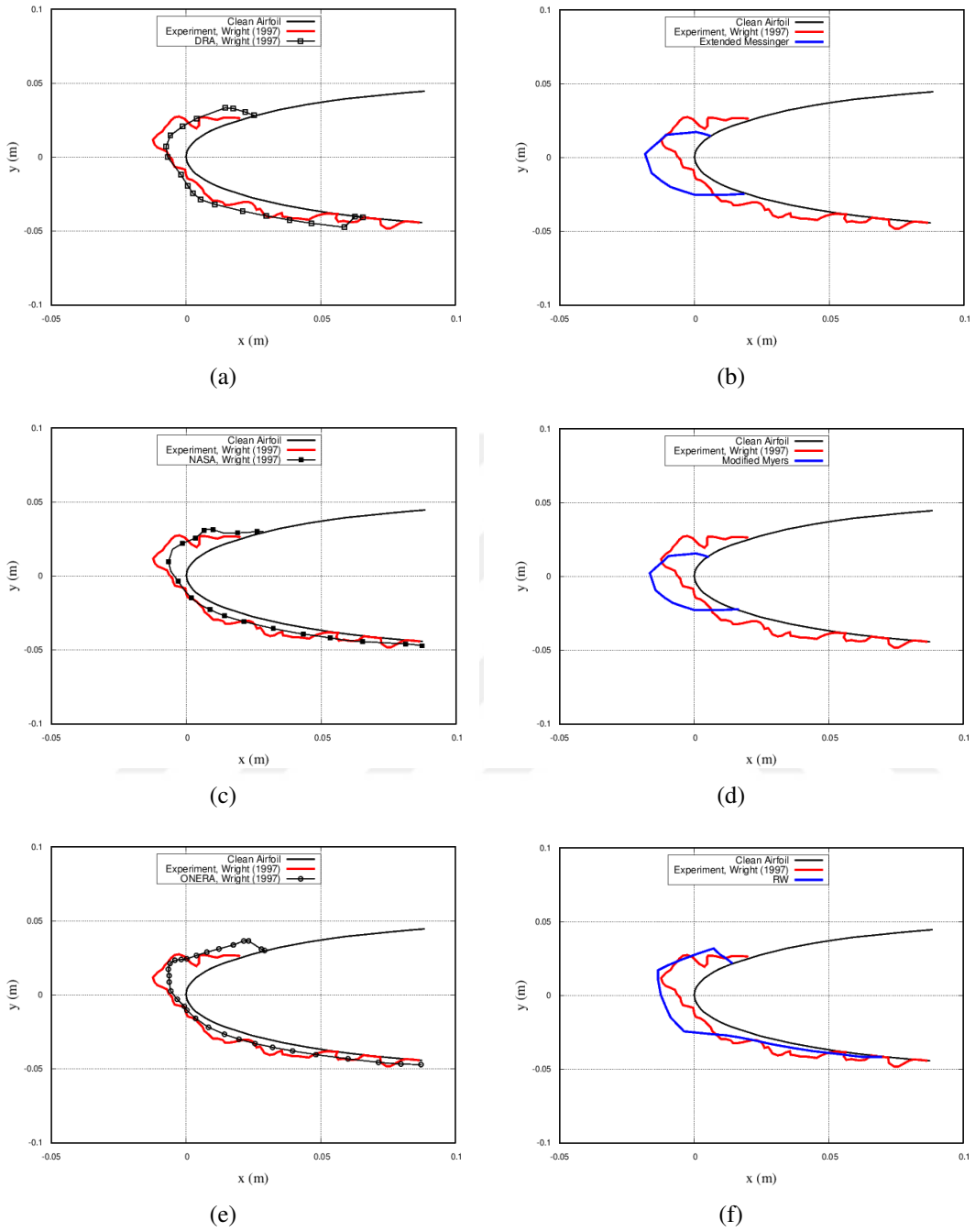

Figure 7.16 : The comparision of DRA, NASA and ONERA results and validation of conventional ice-accretion models (i.e. Extended Messinger, Modified Myers and RW models) with experimental results with respect to Wright et al. (1997) in the case of glaze ice for $chord = 0.53\ m$, $U_\infty = 58.1\ m/s$, $AOA = 4\ ^\circ$, $D = 20\ \mu m$, $\bar{\rho}_\infty = 0.0013\ kg/m^3$, $T_a = -3.9\ ^\circ C$, and $time_{exposure} = 480\ s$.

8. RESULTS

In the conventional models, the critical time and thickness are predicted at the very beginning of the calculations of ice accretion. These predictions are calculated based on the assumption that flow variables will not change until the formation of glaze ice. Then, the icing calculations have been performed based on these critical transient criteria. In reality, the geometry of the body surface changes during the icing and affects the airflow and the distribution of water droplets around the airfoil. Consequently, the convective heat transfer coefficient and the collection efficiency which play important roles in the ice accretion change, continuously. In the proposed approach without the need for the predictions of the critical transient criteria, the calculations of the ice accretion begin with the rime ice until the temperature of the free surface of ice is equal to the melting (freezing) temperature of ice (water) in the ambient. After this situation, the calculations are continued with the glaze ice. Therefore, the main focus of the adaptive approach of the present study is to model the ice accretion closer to the real physics of the icing phenomenon.

8.1 Proposed Model of Ice Accretion

The schematic of the proposed model of aircraft icing is shown in Figure 8.1. As has been shown in this figure, after the grid was generated, the convective heat transfer coefficient and the collection efficiency will be calculated in the air and droplet solvers. By utilizing these values, the calculations of the ice accretion are performed at the current time step and the new iced geometry of the body is determined. Then, the entire process from the grid generation to the ice accretion will be repeated until the specified exposure time to know the final shape of the ice.

The continuity equation of the ice accretion for proposed model is written in the following form (Lavoie, 2017; Lavoie et al., 2018):

for the rime ice,

$$\dot{m}_{in} + \dot{m}_{drop} = \dot{m}_{freezing} + \dot{m}_{sub} \tag{8.1}$$

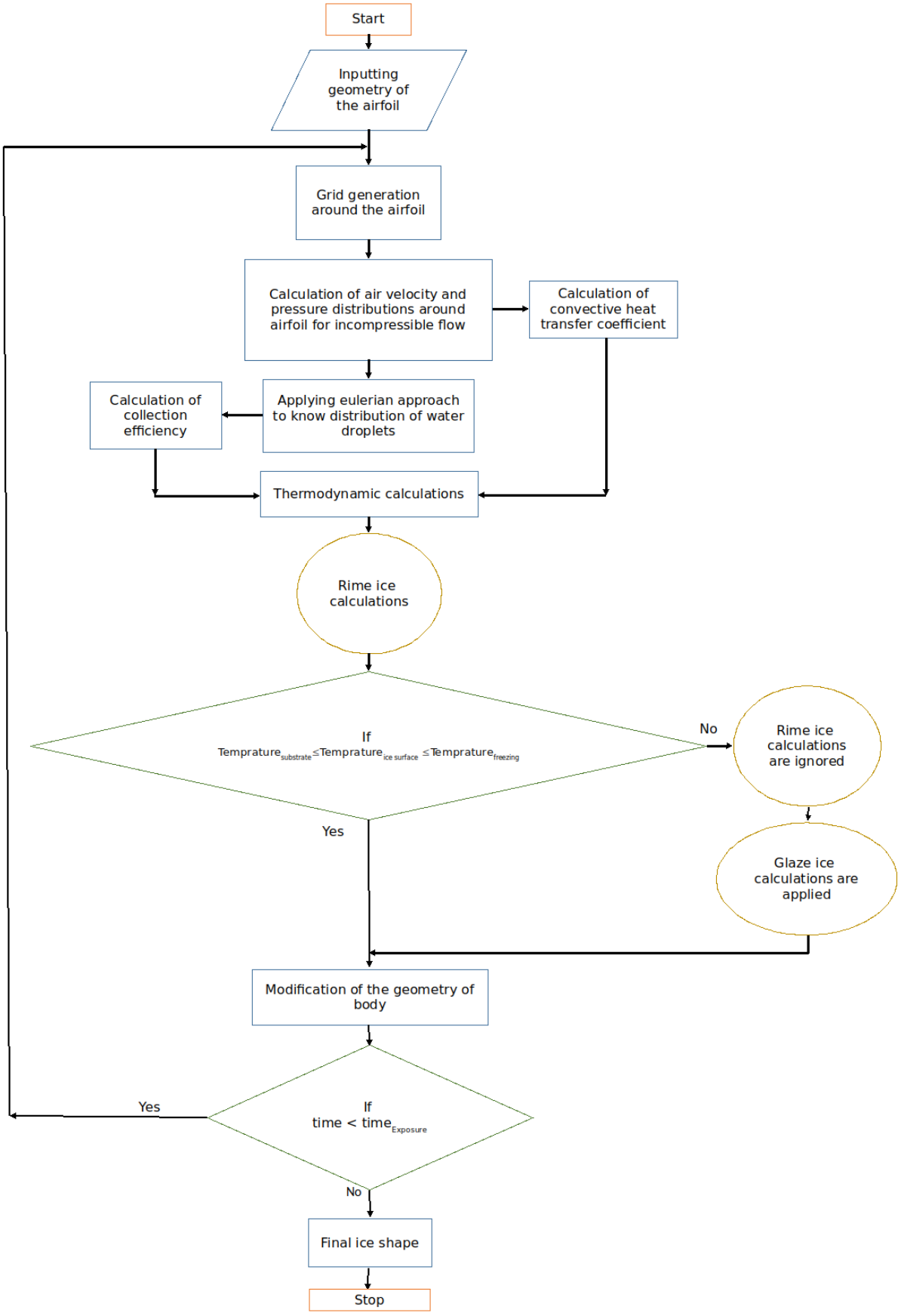

Figure 8.1 : Flowchart of the proposed aircraft icing simulation.

and for the glaze ice:

$$\dot{m}_{in} + \dot{m}_{drop} = \dot{m}_{freezing} + \dot{m}_{evap} + \dot{m}_{out} \tag{8.2}$$

On the other hand, the energy balance in proposed model for the rime ice is written as (Lavoie, 2017; Lavoie et al., 2018):

$$\dot{Q}_{in} + \dot{Q}_{aero} + \dot{Q}_{kin} + \dot{Q}_{freezing} = \dot{Q}_{conv} + \dot{Q}_{cond} + \dot{Q}_{sub} + \dot{Q}_{drop} \tag{8.3}$$

and, for the glaze ice is:

$$\dot{Q}_{in} + \dot{Q}_{aero} + \dot{Q}_{kin} + \dot{Q}_{freezing} = \dot{Q}_{conv} + \dot{Q}_{cond} + \dot{Q}_{evap} + \dot{Q}_{drop} + \dot{Q}_{out} \tag{8.4}$$

The thermodynamic calculations of the icing is formed by the following four equations given below:

$$\frac{\partial T}{\partial t} = \frac{k_i}{\rho_i c_i} \frac{\partial^2 T}{\partial z^2} \tag{8.5}$$

$$\frac{\partial \theta}{\partial t} = \frac{k_w}{\rho_w c_w} \frac{\partial^2 \theta}{\partial z^2} \tag{8.6}$$

$$\rho_i \frac{\partial B}{\partial t} + \rho_w \frac{\partial h}{\partial t} = \beta \bar{\rho}_\infty U_\infty + (\dot{m}_{in} - \dot{m}_{out}) - \dot{m}_{sub/evap} \tag{8.7}$$

$$\rho_i L_F \frac{\partial B}{\partial t} = k_i \frac{\partial T}{\partial z} - k_w \frac{\partial \theta}{\partial z} \tag{8.8}$$

The ice density (ρ_i) may take different values depending on whether the rime or glaze ice is formed.

The first and second equations are the conductive heat transfer equations in ice and water, respectively. The third equation is the conservative mass equation, and the fourth equation is the Stefan condition which is a straightforward energy balance.

To calculate the unknowns, the initial and boundary conditions must be specified with the following assumptions:

1) The ice is in perfect thermal contact with the substrate and has high conductivity and a thermal mass much greater than that of the ice accretion. The icing substrate temperature can be equal or less than freezing temperature (Gent et al., 2000) as:

$$T(0,t) = T_{substrate} = \begin{cases} T_{rec} \quad , for\ T_{rec} \leq T_{freezing} \\ T_{freezing}, for\ T_{rec} > T_{freezing} \end{cases} \tag{8.9}$$

The dry adiabatic recovery temperature (T_{rec}) is evaluated from the following equation (Gent et al., 2000):

$$T_{rec} = \left(T_{\infty} + 273.15 + \frac{U_{\infty}^2}{2c_{p,a}}\right)\left(\frac{1 + r\frac{M^2}{5}}{1 + \frac{M^2}{5}}\right) - 273.15 \tag{8.10}$$

U_{∞}, $c_{p,a}$, M, and r are the airspeed, air specific heat capacity, Mach number, and recovery factor, respectively.

The initial boundary condition (i.e. substrate temperature) for the ice accretion is the minimum of the ambient or recovery temperature. The boundary conditions for the next time steps will be the temperature of the ice surface that has been calculated in the previous iteration.

2) The temperature is continuous at the phase change boundary and equal to the freezing temperature:

$$T(B,t) = \theta(B,t) = T_{freezing} \tag{8.11}$$

This condition is not imposed in the case of rime ice.

3) The interface boundary conditions are as follows:

for rime ice, the interface boundary condition is:

$$-k_i \frac{\partial T}{\partial z}\Big|_{z=B} = (\dot{Q}_{conv} + \dot{Q}_{sub} + \dot{Q}_{drop}) - (\dot{Q}_{in} + \dot{Q}_{aero} + \dot{Q}_{kin} + \dot{Q}_{freezing}) \tag{8.12}$$

and for glaze ice, the interface boundary condition is:

$$\begin{aligned} z &= B+h \\ -k_w\frac{\partial\theta}{\partial z} &= (\dot{Q}_{conv}+\dot{Q}_{evap}+\dot{Q}_{drop}+\dot{Q}_{out})-(\dot{Q}_{in}+\dot{Q}_{aero}+\dot{Q}_{kin}) \end{aligned} \tag{8.13}$$

4) The initial condition is:

$$t = 0 \tag{8.14}$$

$$B = h = 0 \tag{8.15}$$

These conditions are sufficient to determine the temperature profiles and thicknesses of ice and water layer.

The ice thickness of rime ice is calculated from the mass balance, then equation 8.7 with h set to zero simplifies to:

$$B = \frac{\dot{m}_{drop}+\dot{m}_{in}-\dot{m}_{sub}}{\rho_{rime}}t \tag{8.16}$$

Knowing that the energy equation is in the form of $\frac{\partial^2 T}{\partial z^2} = 0$ (Myers, 2001), by twice integrating and applying boundary conditions at the substrate and interface, the temperature of rime ice is calculated by the following formula:

$$\begin{aligned} \dot{Q}_1 &= \dot{Q}_{in}+\dot{Q}_{aero}+\dot{Q}_{kin}+\dot{Q}_{freezing} \\ \dot{Q}_2 &= \dot{Q}_{conv}+\dot{Q}_{drob}+\dot{Q}_{sub} \\ T &= T_{substrate}+\frac{\dot{Q}_1-\dot{Q}_2}{k_i+B\frac{\dot{Q}_2}{(T_{substrate}-T_{amb})}}z \end{aligned} \tag{8.17}$$

The Freezing Fraction (FF) for rime ice is defined as:

$$FF = \frac{\rho_r B}{(\dot{m}_{drop}+\dot{m}_{in})t} \tag{8.18}$$

Substituting relevant value of FF, the ice mass $(\dot{m}_f)$ and outlet mass $(\dot{m}_{out})$ for rime ice are obtained as:

$$\dot{m}_{freezing} = FF(\dot{m}_{drop}+\dot{m}_{in}) \tag{8.19}$$

and

$$\dot{m}_{out} = 0.0 \tag{8.20}$$

Again, knowing that the energy equations are in the form of $\frac{\partial^2 T}{\partial z^2} = 0$ and $\frac{\partial^2 \theta}{\partial z^2} = 0$ (Myers, 2001), by twice integrating and applying boundary conditions at the substrate and interfaces, the temperatures of glaze ice and water are calculated by the following formulas:

$$T = T_{substrate} + \left[\frac{(T_{freezing} - T_{substrate})}{B}\right] z \tag{8.21}$$

z is an arbitrary thickness of ice plus water ($0 \leqslant z \leqslant B$).

and

$$\begin{aligned} \dot{Q}_3 &= \dot{Q}_{in} + \dot{Q}_{aero} + \dot{Q}_{kin} \\ \dot{Q}_4 &= \dot{Q}_{conv} + \dot{Q}_{drop} + \dot{Q}_{evap} + \dot{Q}_{out} \\ \theta &= T_{freezing} + \frac{\dot{Q}_3 - \dot{Q}_4}{k_w + h\frac{\dot{Q}_4}{(T_{freezing} - T_{amb})}}(z - B) \end{aligned} \tag{8.22}$$

here, z is an arbitrary thickness of ice plus water ($B \leqslant z \leqslant (B + h)$).

In the equations 8.21, 8.22, the ice and water temperatures depend on the ice and water thicknesses. Also, as expressed in the equation 8.8, the ice and water thicknesses inherently depend on the ice and water temperatures . Hence, the glaze ice calculation is a coupled problem.

The mass balance (equation 8.7) have to be integrated to obtain an expression for h as:

$$\begin{aligned} \dot{m} &= \dot{m}_{drop} + \dot{m}_{in} - \dot{m}_{evap} - \dot{m}_{out} \\ h &= \frac{\dot{m}(t - t_g) - \rho_g(B - B_g)}{\rho_w} \end{aligned} \tag{8.23}$$

In the proposed model, the ice calculations are initiated with the rime ice accretion. This assumption continues until the surface temperature of the ice reaches the freezing temperature of the water at the ambient. When the ice reaches the freezing temperature of the water, the total ice thickness and elapsed time are accepted as the B_g and t_g,

respectively. The values of B_g and t_g are used in the formulas of the glaze ice accretion later on.

Differentiating of the equations 8.21, 8.22 provide the expressions for the temperature gradients. When these expressions and equation 8.23 is substituted in the Stefan condition (equation 8.8) provide a first-order nonlinear ordinary differential equation for the glaze ice thickness as:

$$\rho_{glaze} L_f \frac{\partial B}{\partial t} = \frac{k_i (T_{freezing} - T_{substrate})}{B} - k_w \frac{\dot{Q}_3 - \dot{Q}_4}{k_w + h \frac{\dot{Q}_4}{(T_{freezing} - T_{amb})}} \tag{8.24}$$

this equation can be solved by Runge-Kutta method (Mathews and Fink, 2004).

Therefore, for glaze ice, first, B should be calculated via equation 8.24. Then, T, θ and h are obtained through the equation 8.21, 8.22, 8.23, respectively.

The Freezing Fraction (FF) for glaze ice is defined as:

$$FF = \frac{\rho_r B + \rho_g (B - B_g)}{(\dot{m}_{drop} + \dot{m}_{in}) t} \tag{8.25}$$

Substituting relevant value of FF, the ice mass $(\dot{m}_f)$ and outlet mass $(\dot{m}_{out})$ for glaze ice are obtained as:

$$\dot{m}_{freezing} = FF(\dot{m}_{drop} + \dot{m}_{in}) \tag{8.26}$$

and

$$\dot{m}_{out} = (1 - FF)(\dot{m}_{drop} + \dot{m}_{in}) - \dot{m}_{evap} \tag{8.27}$$

In general, the difference between the ice accretion approach in the proposed model with the conventional models is that calculations will be started with the rime ice. At each time step for each grid point, if $T_s \leqslant T \leqslant T_f$ and $B > 0$ then the results of the calculations of rime ice are accepted. Otherwise, these results are ignored and the calculations of glaze ice are applied.

If the accumulated thickness of the ice and water film during the current time step was larger than 2.4 cm and 3 mm, respectively, the magnitude of the time step of icing is

modified and the calculations of the ice accretion are repeated for the current time step (Myers, 2001).

Because the nature of icing is accumulative and the ice gradually shapes on the surface, it is anticipated that the implicit time marching method leads to better results in the icing simulation. While the fewer step numbers cause less accurate results, more numbers of steps do not guarantee more accurate results and do increase the round-off error. Therefore, there is an optimum number of steps. To predict this optimum step number either the time step or ice thickness criteria may be used (Verdin and Charpin, 2013).

8.2 Algorithm of Iterative Solution for Proposed Aircraft Icing Simulation

1. The grid is generated.

2. The airflow is solved by inviscid or viscous flow approaches. For the inviscid airflow, the stream function equation is solved, and for the viscous airflow the vorticity, stream function, and transport viscosity equations are solved.

3. The distribution of water droplets and collection efficiency is found using the calculated values of airflow in the current time-step (i.e. time marching concept) regardless of whether the inviscid or viscous airflow approaches have been used.

4. The convective heat transfer coefficient is calculated using the calculated values of airflow in the current time-step (i.e. time marching concept). For inviscid airflow, the Integral Boundary Layer method is applied, and for viscous airflow, the energy equation is solved alongside the vorticity, stream function, and transport viscosity equations.

5. The convergence criteria of the airflow, droplets' distribution, and energy equation will be checked during each time marching, if the problem was not converged then the time marching is continued from the second module (i.e. the airflow solution).

6. Once the collection efficiency and convective heat transfer coefficient are found the thermodynamic calculations (ice accretion) are implemented as follows. The rime ice model is applied which means the mass and energy equations will be used for the

calculation of ice thickness and temperature of the free surface until the free surface temperature equals the melting (freezing) temperature of water in the ambient. Just after that, the rime ice temperature at the surface equals the freezing temperature the glaze ice model is utilized based on the standard method of specifying a phase change or Stefan problem i.e. the combination of continuity and energy equations gives a first-order non-linear ordinary differential equation for the calculation of ice thickness, which the Runge-Kutta method is used for solving this mixed first-order equation (Mathews and Fink, 2004), (see appendix 4). In each icing time-step, if the accumulated thickness of the ice and water film during this time-step is larger than 2.4 cm and 3 mm, respectively, the time-step of icing is modified and the calculations of the ice accretion are repeated.

7. The geometry of the contaminated (iced) body is regenerated.

8. Because the geometry of the body is changed during icing in each time step calculations will be restarted from the beginning module of the aircraft-icing i.e. the grid generation. Then, the entire calculations will be continued until the final icing exposure time.

8.3 Results

In the following part of this section, the different models of ice accretion will be verified by the experimental results of DRA, NASA, and ONERA collaboration (Wright et al., 1997) for the entire aircraft icing simulations.

Figure 8.2 (a) shows that the results of rime ice are almost similar for conventional models, and Figure 8.2 (b), (c) show that the differences are more noticeable in the mixed and glaze ice regimes. The results of the extended Messinger model are modified by including the mass terms of evaporation and sublimation in the continuity equations because these terms change the latent heat term of the freezing droplets and indirectly affect the results of the ice accretion.

On the other hand, in Figure 8.2 (a), (b), (c) the results of the proposed approach to ice accretion are in perfect agreement with experimental results of Wright et al. (1997), and for all regimes are more accurate in comparison with the results of conventional models implemented in the present study.

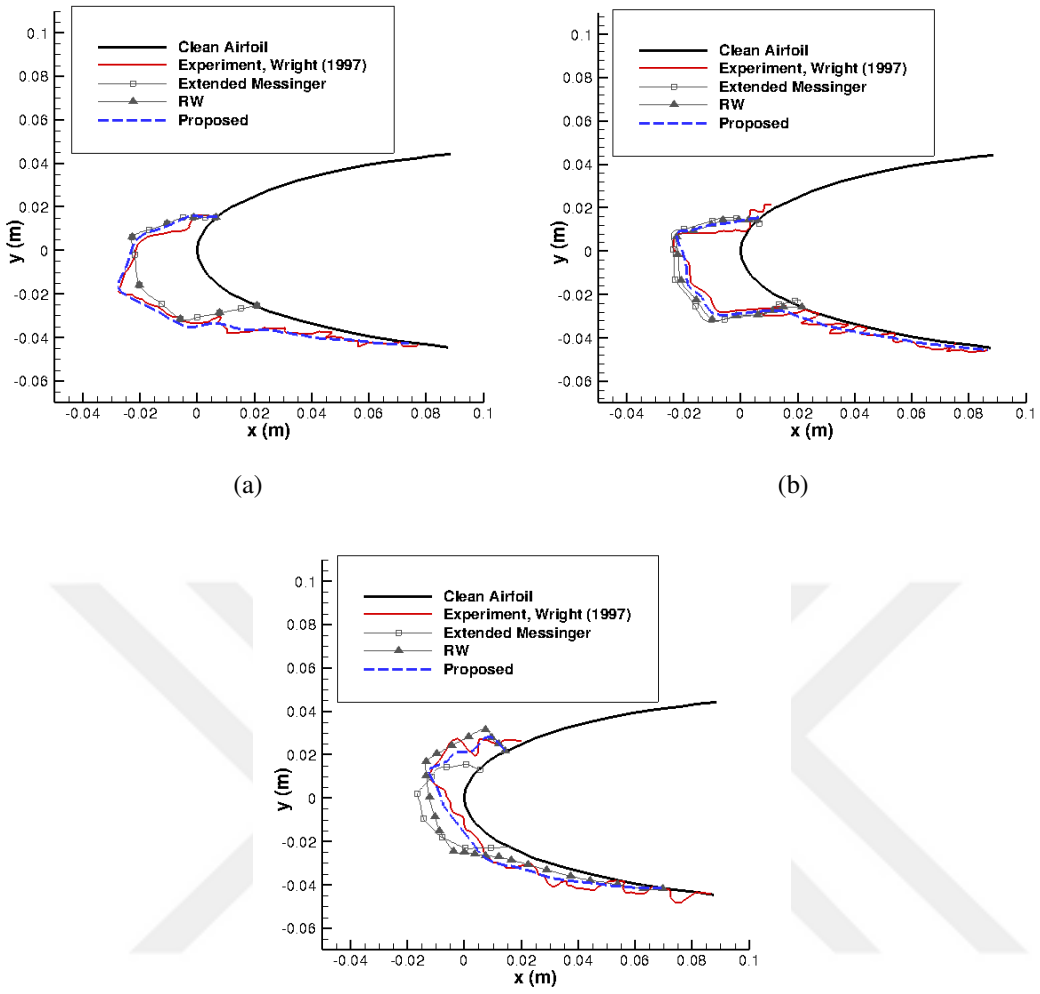

Figure 8.2 : The results of proposed ice accretion model with experimental results of Wright et al. (1997) and comparison with the results of conventional models implemented in the present study for $chord = 0.53\ m$, $U_\infty = 58.1\ m/s$, $AOA = 4\ ^\circ$, $D = 20\ \mu m$, $\bar{\rho}_\infty = 0.0013\ kg/m^3$, and $time_{exposure} = 480\ s$ in the cases of a) rime ($T_a = -27.8\ ^\circ C$), b) mixed ($T_a = -13.9\ ^\circ C$), and c) glaze ($T_a = -3.9\ ^\circ C$) ices.

Figure 8.2 (a) shows that moving away from the stagnation point, the results of the proposed model for the rime ice regime are more realistic than the conventional models implemented in the present study because the proposed model includes the changes of geometry, airflow and droplets' distribution in the calculations of ice accretion. These improvements are also observed in the cases of mixed and glaze ice regimes in Figure 8.2 (b), (c). Furthermore, Figure 8.2 (c) shows that the results of the proposed model for glaze ice are significantly better than the results of conventional models implemented in the present research.

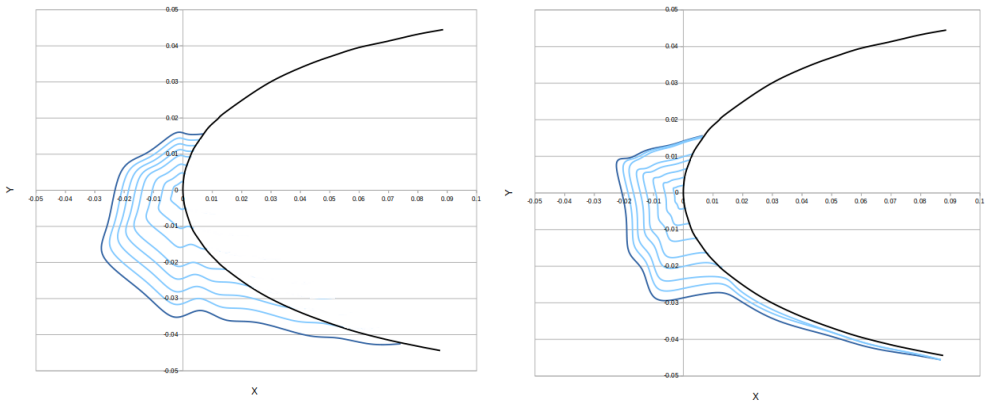

(a) (b)

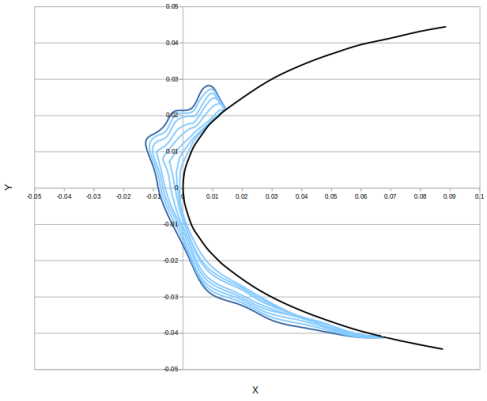

(c)

Figure 8.3 : The accumulative growth of ice using the proposed ice accretion model for $chord = 0.53\ m$, $U_\infty = 58.1\ m/s$, $AOA = 4\ ^\circ$, $D = 20\ \mu m$, $\bar{\rho}_\infty = 0.0013\ kg/m^3$, and $time_{exposure} = 480\ s$ in the cases of a) rime ($T_a = -27.8\ ^\circ C$), b) mixed ($T_a = -13.9\ ^\circ C$), and c) glaze ($T_a = -3.9\ ^\circ C$) ices.

The accumulative growth of the ice for the proposed model is shown in Figure 8.3 (a), (b), (c) for different cases of the rime, mixed, and glaze ices for every 60 seconds. As shown in Figure 8.3 (a), in the case of rime ice, the droplets immediately freeze when they impinge on the airfoil. Consequently, the wetted surface of the airfoil gradually increases. On the other hand, in the case of glaze ice as shown in Figure 8.3 (c), droplets do not freeze at the very first moment they collide with the surface, First, droplets wet the airfoil surface and then freeze, thus the wetted surface will approximately remain the same. In the case of mixed ice in Figure 8.3 (b), it is noticed that the growth pattern of mixed ice is the combination of the early mentioned patterns of the rime and glaze ices.

8.4 Recommended Alternative Simulation Method

It is anticipated that the results of our proposed ice accretion model would show more improvement if more accurate values use in the air solver module. In this regard, the Navier-Stokes equations for the viscous airflow can be solved. The Reynolds-Averaged Navier-Stokes (RANS) approach using Spalart-Allmaras (SA) model can be implemented for modeling turbulence flow around the airfoil. For the viscous air solver, the convective heat transfer coefficient will be calculated by solving the energy equation along with the Navier-Stokes equations. On the other hand, the droplet solver and ice accretion modules can be applied as the same as what were declared for the inviscid flow.

8.4.1 RANS approach

The continuity equation for 2D incompressible airflow would be:

$$\frac{\partial u_x}{\partial x} + \frac{\partial u_y}{\partial y} = 0 \tag{8.28}$$

u_x and u_y are the velocity components of the airflow in the x and y directions, respectively,

The corresponding Navier Stokes equations for laminar airflow in x and y directions are as:

$$\frac{\partial u_x}{\partial t} + u_x\frac{\partial u_x}{\partial x} + u_y\frac{\partial u_x}{\partial y} = -\frac{1}{\rho}\frac{\partial P}{\partial x} + \nu\left(\frac{\partial^2 u_x}{\partial x^2} + \frac{\partial^2 u_x}{\partial y^2}\right) \tag{8.29}$$

$$\frac{\partial u_y}{\partial t} + u_x\frac{\partial u_y}{\partial x} + u_y\frac{\partial u_y}{\partial y} = -\frac{1}{\rho}\frac{\partial P}{\partial y} + \nu\left(\frac{\partial^2 u_y}{\partial x^2} + \frac{\partial^2 u_y}{\partial y^2}\right) \tag{8.30}$$

ρ, P and ν are density, pressure and kinematic viscosity, respectively.

By definition of the time-averaging concept of the Reynolds-Averaged Navier-Stokes (RANS) model as:

$$u_i = U_i + u' \tag{8.31}$$

$$U_i = \lim_{T\to\infty} \frac{1}{T} \int_0^T u.dt \tag{8.32}$$

By using of the Reynolds time-averaging concept the mass and Navier-Stokes equations would be:

$$\frac{\partial U_x}{\partial x} + \frac{\partial U_y}{\partial y} = 0 \tag{8.33}$$

$$\frac{\partial U_x}{\partial t} + U_x \frac{\partial U_x}{\partial x} + U_y \frac{\partial U_x}{\partial y} = -\frac{1}{\rho}\frac{\partial P}{\partial x} + \nu\left(\frac{\partial^2 U_x}{\partial x^2} + \frac{\partial^2 U_x}{\partial y^2}\right) + \frac{\partial(-\overline{u'_x u'_x})}{\partial x} + \frac{\partial(-\overline{u'_x u'_y})}{\partial y} \tag{8.34}$$

$$\frac{\partial U_y}{\partial t} + U_x \frac{\partial U_y}{\partial x} + U_y \frac{\partial U_y}{\partial y} = -\frac{1}{\rho}\frac{\partial P}{\partial y} + \nu\left(\frac{\partial^2 U_y}{\partial x^2} + \frac{\partial^2 U_y}{\partial y^2}\right) + \frac{\partial(-\overline{u'_y u'_x})}{\partial x} + \frac{\partial(-\overline{u'_y u'_y})}{\partial y} \tag{8.35}$$

Boussinesq eddy viscosity hypothesis lies at the heart of the eddy viscosity turbulence models. Boussinesq postulated that momentum transfer caused by turbulent eddies can be modeled with an eddy viscosity (ν_t). This is in analogy with how the momentum transfer caused by the molecular motion in a gas can be described by a molecular viscosity. The Boussinesq assumption states that the Reynolds stress tensor ($-\rho\tau_{ij}$) is proportional to the trace-less mean strain rate tensor (S_{ij}), and can be written in the following way (Raje, 2015):

$$-\rho\overline{u'_i u'_j} = 2\mu_t S_{ij} - \frac{2}{3}\mu_t \frac{\partial U_k}{\partial x_k}\delta_{ij} - \frac{2}{3}k\delta ij \tag{8.36}$$

where k is the turbulence kinetic energy (TKE). The third term is included so as to balance the normal Reynolds stresses.

For incompressible flows, the second term of $\frac{\partial U_k}{\partial x_k} = 0$ is the continuity equation. Also, for the one-equation model, the third term could be neglected. Then, the Boussinesq hypothesis becomes:

$$-\rho\overline{u'_i u'_j} = 2\mu_t S_{ij} \tag{8.37}$$

or Reynolds stress could be restate as:

$$R_{ij} = -\overline{u'_i u'_j} = 2\nu_t S_{ij} \tag{8.38}$$

this equation shows that Boussinesq eddy viscosity hypothesis applies a simple linear relation between Reynolds stress (R_{ij}) and strain (S_{ij}). The regarding strain is expresses as:

$$S_{ij} = \frac{1}{2}\Big(\frac{\partial U_i}{\partial x_j} + \frac{\partial U_j}{\partial x_i}\Big) \tag{8.39}$$

Alternatively, by using the Boussinesq hypothesis for the closure problem of the turbulent flow, the corresponding continuity and Navier Stokes equations for turbulent airflow in x and y directions are as (Wilcox et al., 1998):

$$\frac{\partial U_x}{\partial x} + \frac{\partial U_y}{\partial y} = 0 \tag{8.40}$$

$$\frac{\partial U_x}{\partial t} + U_x\frac{\partial U_x}{\partial x} + U_y\frac{\partial U_x}{\partial y} = -\frac{1}{\rho}\frac{\partial P}{\partial x} + (\nu + \nu_t)\Big(\frac{\partial^2 U_x}{\partial x^2} + \frac{\partial^2 U_x}{\partial y^2}\Big) \tag{8.41}$$

$$\frac{\partial U_y}{\partial t} + U_x\frac{\partial U_y}{\partial x} + U_y\frac{\partial U_y}{\partial y} = -\frac{1}{\rho}\frac{\partial P}{\partial y} + (\nu + \nu_t)\Big(\frac{\partial^2 U_y}{\partial x^2} + \frac{\partial^2 U_y}{\partial y^2}\Big) \tag{8.42}$$

ρ, P, U, ν and ν_t are density, pressure, average velocity, kinematic viscosity and turbulent viscosity, respectively.

8.4.2 Transport Vorticity and stream function formulation

The vorticity stream-function formulation of the Navier-Stokes equations for 2D flows explains as (Salih, 2013; Thames et al., 1977; Thompson et al., 1977a):

$$\frac{\partial \omega}{\partial t} + \psi_y\frac{\partial \omega}{\partial x} - \psi_x\frac{\partial \omega}{\partial y} = (\nu + \nu_t)\Big[\frac{\partial^2 \omega}{\partial x^2} + \frac{\partial^2 \omega}{\partial y^2}\Big] \tag{8.43}$$

$$\frac{\partial^2 \psi}{\partial x^2} + \frac{\partial^2 \psi}{\partial y^2} = -\omega \tag{8.44}$$

The transport vorticity and stream function equations transformed into the computational domain (ξ, η coordinate) are:

$$\omega_t + \frac{\psi_\eta}{J}\omega_\xi - \frac{\psi_\xi}{J}\omega_\eta = (\nu + \nu_t)\Big[\frac{a}{J^2}\omega_{\xi\xi} - \frac{2b}{J^2}\omega_{\xi\eta} + \frac{c}{J^2}\omega_{\eta\eta} + P\omega_\xi + Q\omega_\eta\Big] \tag{8.45}$$

$$\frac{a}{J^2}\psi_{\xi\xi} - 2\frac{b}{J^2}\psi_{\xi\eta} + \frac{c}{J^2}\psi_{\eta\eta} + P\psi_{\xi} + Q\psi_{\eta} = -\omega \tag{8.46}$$

The coefficients of a, b, c, J, P and Q are the same as what were defined for the elliptic grid generation (see chapter 3).

By writing the Navier-Stokes equations in the form of vorticity and stream function equations (Eqs. 8.43 and 8.44), there would be two equations with three unknowns of ω, ψ and ν_t. Therefore, in the following parts the Spalart-Allmaras turbulent model would be explained, and gives one extra equation which is needed for the calculation of all three unknowns of the turbulent airflow.

8.4.3 Spalart-Allmaras turbulent model

The transport viscosity ($\tilde{\nu}$) could be defined as a function of the kinematic eddy turbulent viscosity (ν_t) via Spalart-Allmaras turbulent model.

The Spalart–Allmaras model is a one-equation model that solves a modelled transport equation for the kinematic eddy turbulent viscosity. The Spalart–Allmaras model is one equation turbulent model which has been developed for aerodynamic flows. In this model, the transport equation for the undamped eddy viscosity ($\tilde{\nu}$) is given as (Allmaras and Johnson, 2012; Aupoix and Spalart, 2003; Spalart and Allmaras, 1992):

$$\underbrace{\frac{\partial \tilde{\nu}}{\partial t}}_{\text{temporal term}} + \underbrace{U_x\frac{\partial(\tilde{\nu})}{\partial x} + U_y\frac{\partial(\tilde{\nu})}{\partial y}}_{\text{convection term}} = \underbrace{c_{b1}\tilde{S}\tilde{\nu}}_{\text{turbulence-generation term}} - \underbrace{c_{w1}f_w(\frac{\tilde{\nu}}{d})^2}_{\text{turbulence-distruction term}} + \underbrace{\frac{1}{\sigma}\Big[\frac{\partial}{\partial x}\Big((\nu+\tilde{\nu})\frac{\partial\tilde{\nu}}{\partial x}\Big) + \frac{\partial}{\partial y}\Big((\nu+\tilde{\nu})\frac{\partial\tilde{\nu}}{\partial y}\Big) + c_{b2}\Big((\frac{\partial\tilde{\nu}}{\partial x})^2 + (\frac{\partial\tilde{\nu}}{\partial y})^2\Big)\Big]}_{\text{diffusion term}} \tag{8.47}$$

The main idea of using this transport viscosity equation is the use of $\tilde{\nu}$ instead of ν_t because, unlike the eddy (turbulent) viscosity, the transport viscosity behaves in a nearly linear fashion near and far from the wall. The $\tilde{\nu}$ and ν_t are related as follows:

$$\begin{aligned} \chi &= \frac{\tilde{\nu}}{\nu} \\ f_{v1} &= \frac{\chi^3}{\chi^3 + c_{v1}^3} \\ \boldsymbol{\nu_t} &= \boldsymbol{f_{v1}\tilde{\nu}} \end{aligned} \tag{8.48}$$

and the other functions are:

$$f_{v2} = 1 - \frac{\chi}{1+\chi f_{v1}}$$
$$\tilde{S} = S + \frac{\tilde{\nu}}{K^2 d^2} f_{v2} \approx |\frac{\partial U_x}{\partial y}| + \frac{\tilde{\nu}}{K^2 d^2} f_{v2} = |\frac{\partial^2 \psi}{\partial y^2}| + \frac{\tilde{\nu}}{K^2 d^2} f_{v2} \tag{8.49}$$

$$r = Min(10, \frac{\tilde{\nu}}{\tilde{S} K^2 d^2})$$
$$q = r + c_{w2}(r^6 - r) \tag{8.50}$$
$$f_w = q(\frac{1+c_{w3}^6}{q^6 + c_{w3}^6})^{\frac{1}{6}}$$

The transformed transport viscosity equation into the computational domain (ξ, η coordinate) is:

$$\tilde{\nu}_t - \Big[\frac{c_{b1} f_{v2}}{K^2 d^2} - \frac{c_{w1} f_w \tilde{\nu}_{old}}{d^2}\Big]\tilde{\nu} +$$
$$\Big[\big(\psi_y - \frac{(1+c_{b2})}{\sigma}\tilde{\nu}_{x,old}\big)\frac{y_\eta}{J} + \big(\psi_x + \frac{(1+c_{b2})}{\sigma}\tilde{\nu}_{y,old}\big)\frac{x_\eta}{J} - \frac{(\nu+\tilde{\nu}_{old})}{\sigma}P\Big]\tilde{\nu}_\xi +$$
$$\Big[-\big(\psi_y - \frac{(1+c_{b2})}{\sigma}\tilde{\nu}_{x,old}\big)\frac{y_\xi}{J} - \big(\psi_x + \frac{(1+c_{b2})}{\sigma}\tilde{\nu}_{y,old}\big)\frac{x_\xi}{J} - \frac{(\nu+\tilde{\nu}_{old})}{\sigma}Q\Big]\tilde{\nu}_\eta -$$
$$\Big[\frac{(\nu+\tilde{\nu}_{old})}{\sigma}\frac{a}{J^2}\Big]\tilde{\nu}_{\xi\xi} + 2\Big[\frac{(\nu+\tilde{\nu}_{old})}{\sigma}\frac{b}{J^2}\Big]\tilde{\nu}_{\xi\eta} - \Big[\frac{(\nu+\tilde{\nu}_{old})}{\sigma}\frac{c}{J^2}\Big]\tilde{\nu}_{\eta\eta} -$$
$$c_{b1}|\psi_{yy}| = 0 \tag{8.51}$$

The coefficients of a, b, c, J, P and Q are the same as what were defined for the elliptic grid generation (see chapter 3).

If the transport viscosity equation is ignored (which means $\nu_t = 0$), the calculations of the current section can be considered for the laminar viscous airflow.

8.4.4 Velocity and pressure formulas

The velocity components of U_x and U_y in x, y coordinate would be calculated as:

$$U_x(x,y) = \frac{-[x_\eta(\xi,\eta)][\psi_\xi(\xi,\eta)] + [x_\xi(\xi,\eta)][\psi_\eta(\xi,\eta)]}{J(\xi,\eta)} \tag{8.52}$$

$$U_y(x,y) = \frac{-[y_\eta(\xi,\eta)][\psi_\xi(\xi,\eta)] + [y_\xi(\xi,\eta)][\psi_\eta(\xi,\eta)]}{J(\xi,\eta)} \tag{8.53}$$

consequently, the velocity distribution is:

$$U(x,y) = \sqrt{[U_x(x,y)]^2 + [U_y(x,y)]^2} \tag{8.54}$$

The pressure can be calculated through the Pressure Poisson's Equation (PPE) as:

$$-\frac{1}{\rho}\left(\frac{\partial^2 P}{\partial x^2} + \frac{\partial^2 P}{\partial y^2}\right) = -2\frac{\partial U_x}{\partial x}\frac{\partial U_y}{\partial y} + 2\frac{\partial U_y}{\partial x}\frac{\partial U_x}{\partial y} \tag{8.55}$$

In general, utilizing the values of the turbulence flow for the air solver module, our proposed icing model is expected to give better results.

9. CONCLUSIONS

In this chapter, a summary of the current research work is provided. The conclusions are announced, and suggestions for the future works are also revealed.

9.1 Summary

Due to the damages and malfunctioning effects of the icing on flaps, ailerons, rudders, elevators, and the other measuring and navigation devices, the icing can cause serious problems in the controllability of aircraft. On the other hand, the icing influences the aerodynamics of the wings and tail in a bad way that it will act far from the design point. Therefore, to overcome the safety and performance issues of the icing on the aircraft, first of all, better numerical and computational models are needed to simulate and understand the aircraft icing. These simulations can be also used in the pilot-training equipment or may be utilized in the deicing analyses by including the heating source term.

The main program of icing simulation in our study is based on the grid generation, air solver, droplet solver, and ice accretion modules.

First, the elliptic body-fitted curvilinear conformal coordinate transformation has been applied for generating the grid around the airfoil.

After grid generation, the stream function method is used for two-dimensional, steady-state, inviscid, incompressible, irrotational flow (potential flow) to calculate the velocity and pressure values around the airfoil.

Generally, two approaches namely Lagrangian and Eulerian approaches are applied for the calculation of the water-droplets field. In this research, the Eulerian approach has been performed. The Eulerian approach improves the speed of solution, the ability to model unsteady flows over the body, and the automated treatment of shadow zones with no impingement. Furthermore, this approach is more suitable for complicated 2D geometries and easier to extend toward 3D geometries.

Eventually, the traditional ice accretion models have been used for verifying our icing simulation, next, the proposed model is introduced. In the conventional ice accretion models, the critical transient time and thickness are predicted at the very beginning of the calculations. These predictions are calculated based on the assumption that flow variables will not change until the formation of glaze ice. Then, either the rime ice or glaze ice calculations are implemented at each time step based on these critical transient criteria. In reality, the geometry of the body surface changes during the icing and affects the airflow and the distribution of water droplets around the airfoil. Consequently, the convective heat transfer coefficient and the collection efficiency play important roles in the ice accretion change, continuously. The main focus of the proposed approach of the present study is to make the progression of the ice accretion closer to the real physics of the icing phenomenon. In fact, without the need for the predictions of the critical transient criteria, the calculations of the ice accretion begin with the rime ice until the temperature of the free surface of ice is equal to the melting (freezing) temperature of ice (water) in the ambient. After this point, the calculations are continued with the glaze ice.

9.2 Conclusions

One of the major deficits of the classic Messinger model is that the Messinger model only considers the energy balance between the released latent heat and heat transfer at the liquid-gas (water-air) interface, but ignores the heat conduction between the ice layer and body surface. Besides, the classical Messinger model does have not a good prediction of the equilibrium energy balance between water and air. On contrary, the extended Messinger model includes the conductive heat term of the ice and body surface in the thermodynamics' calculations and also gives more accurate results by including Stefan's condition in the water and air interface.

The Modified Myers model improves the predictions of critical transient criteria by taking the evaporation and sublimation mass terms into account, and correcting the latent heat transfer of freezing droplets. Although the evaporation and sublimation mass terms may be ignored in the mass balance equation, these masses indirectly affect the latent heat of freezing droplets and they should not be ignored in the energy balance

equation. Therefore, the extended Messinger model will be corrected by the Modified Myers model.

The problem with the Modified Myers model is that it does not include the mass and heat terms of the moving water film in the thermodynamics calculations yet. Therefore, the Run-back Water (RW) model eliminates the deficit of the Modified Myers model in the simulation of the glaze ice.

In the conventional ice accretion models (extended Messinger, Modified Myers, and Run-back Water models), the thickness (B_g) and time (t_g), at which the glaze ice appears for the first time, are predicted at the very beginning based on the thermodynamic calculations. These predictions are calculated based on the assumption that flow variables will not change until the formation of glaze ice. Then, these values are taken as critical transient criteria to apply either the rime ice or the glaze ice calculations at each time step. In reality, the geometry of the body surface changes during the icing and affects the airflow and the distribution of water droplets around the airfoil. Consequently, the convective heat transfer coefficient and the collection efficiency which play important roles in the ice accretion change, continuously. Therefore, in the proposed ice accretion model presented in this study, the calculations of the ice accretion are initiated with the rime ice. If the results were plausible they are accepted, otherwise, the glaze ice calculation is applied.

In the case of rime ice, the droplets immediately freeze when they impinge on the airfoil, consequently, the wetted surface of the airfoil will increase continuously. On the other hand, in the case of glaze ice droplets, first, droplets wet the airfoil surface and then freeze, thus, the wetted surface will approximately remain the same. Because the behavior of the rime and glaze ice accretions are completely different, the selected ice regime will strongly influence the icing simulation. In addition, since the icing simulation is an accumulative procedure, it is very important to more precisely catch the exact transient point of the rime into glaze ice formation. By including of the early mentioned expressions in thermodynamic calculations, the strength of our model is that it enables the course of numerical computations of the icing process to proceed in the same way as the real physics of the icing phenomenon.

The results of the present study show that the proposed ice accretion approach for all rime, mixed, and glaze ice regimes gives more accurate results than the conventional ice accretion models.

The research that has been undertaken for this dissertation has highlighted a number of topics on which further research would be beneficial.

The N-S equations for the viscous airflow can be solved. In this regard, the RANS approach using SA model can be implemented for modeling turbulence flow around the airfoil. For the viscous flow, the convective heat transfer coefficient will be calculated by solving the energy equation along with the N-S equations. On the other hand, the droplet solver and ice accretion modules can be applied as the same as what were declared for the inviscid flow.

The effect of water droplets on the airflow can be also considered for droplets larger than 50 μm i.e. two-way coupled flow for super-cooled large droplets (SLD) in the cases of heavy rains. The mixed Lagrangian-Eulerian (Arbitrary Lagrangian-Eulerian) method may be applied for these cases. To be certain that the major effects that play an important role in the simulation of super-cooled large droplets (SLD) distributions are included, along with drag, gravity, and buoyancy forces, Basset history force and virtual mass force can be added into momentum equations. The deformation and breakup effects should be also considered for super-cooled large droplets (SLD). It means that the entire water droplets can not be still assumed to be a sphere with a single diameter. The other important factor for simulation of the impingement of SLD is that the droplet impact or the droplets-wall interactions must be also included, it means that in addition to continuity and momentum equations, one more equation is also needed for the conservation of the number of water droplets at the wall (body).

The deicing models may be simulated by only adding the heat-source term in the ice accretion calculations which is usually provided by the exhaust gas of the jet engine.

The icing of different 2D geometries other than an airfoil, like icing in nacelles, engine intakes, air intake scoops, compressor blades in aircraft, rotor icing in helicopters, and icing of electrical power lines may be simulated.

The 2D approach of the Eulerian method in our study can be extended for 3D geometries (like finite wings and the the blades of the wind turbine) by including the induced drag.

REFERENCES

Aircraft accident report response of bureau enquetes-accidentsto safety board's draft report. (1996). National Transportation Safety Board, NTSB/AAR-96/02.

Aircraft accident report safety board report. (1996). National Transportation Safety Board, Safety Board, NTSB/AAR-96/01.

Acker, L. W. and Kleinknecht, K. S. (1950). Effects of inlet icing on performance of axial flow turbojet engine in natural icing conditions.

Al-Khalil, K. M., Keith Jr, T. G., and De Witt, K. J. (1994). Development of an improved model for runback water on aircraft surfaces. *Journal of aircraft*, 31(2):271–278.

Alemour, B., Badran, O., and Hassan, M. R. (2019). A review of using conductive composite materials in solving lightening strike and ice accumulation problems in aviation. *Journal of Aerospace Technology and Management*, 11.

Allmaras, S. R. and Johnson, F. T. (2012). Modifications and clarifications for the implementation of the spalart-allmaras turbulence model. In *Seventh international conference on computational fluid dynamics (ICCFD7)*, pages 1–11. Big Island, HI.

Anderson Jr, J. D. (2010). *Fundamentals of aerodynamics*. Tata McGraw-Hill Education.

Aupoix, B. and Spalart, P. (2003). Extensions of the spalart–allmaras turbulence model to account for wall roughness. *International Journal of Heat and Fluid Flow*, 24(4):454–462.

Beaugendre, H., Morency, F., and Habashi, W. G. (2003). Fensap-ice's three-dimensional in-flight ice accretion module: Ice3d. *Journal of Aircraft*, 40(2):239–247.

Bharathidasan, T., Kumar, S. V., Bobji, M., Chakradhar, R., and Basu, B. J. (2014). Effect of wettability and surface roughness on ice-adhesion strength of hydrophilic, hydrophobic and superhydrophobic surfaces. *Applied surface science*, 314:241–250.

Bilodeau, D. R., Habashi, W. G., Fossati, M., and Baruzzi, G. S. (2015). Eulerian modeling of supercooled large droplet splashing and bouncing. *Journal of Aircraft*, 52(5):1611–1624.

Bourgault, Y., Habashi, W. G., Dompierre, J., and Baruzzi, G. S. (1999). A finite element method study of eulerian droplets impingement models. *International Journal for Numerical methods in fluids*, 29(4):429–449.

Bragg, M., Hutchison, T., and Merret, J. (2000). Effect of ice accretion on aircraft flight dynamics. In *38th Aerospace Sciences Meeting and Exhibit*, page 360.

Bramantya, M. A. and Ginting, R. R. R. (2020). Study of the effect of 4-digit naca variation on airfoil performance using computation fluid dynamics. In *AIP Conference Proceedings*, volume 2248, page 020002. AIP Publishing LLC.

Broeren, A. P. and Bragg, M. B. (2005). Effect of airfoil geometry on performance with simulated intercycle ice accretions. *Journal of Aircraft*, 42(1):121–130.

Bu, X., Lin, G., Yu, J., Yang, S., and Song, X. (2013). Numerical simulation of an airfoil electrothermal anti-icing system. *Proceedings of the Institution of Mechanical Engineers, Part G: Journal of Aerospace Engineering*, 227(10):1608–1622.

Busch, G., Broeren, A., and Bragg, M. (2008). Aerodynamic fidelity of sub-scale two-dimensional ice accretion simulations. In *26th AIAA Applied Aerodynamics Conference*, page 7062.

Calay, R. K., Holdø, A. E., Mayman, P., and Lun, I. (1997). Experimental simulation of runback ice. *Journal of aircraft*, 34(2):206–212.

CAMAULI, G. (2018). Droplet-wall interaction modelling for in-flight ice accretion.

Cansdale, J. and Gent, R. (1983). Ice accretion on aerofoils in two-dimensional compressible flow-a theoretical model. *Royal Aircraft Establishment Technical Report*, 82128.

Cao, Y. and Hou, S. (2016). Extension to the myers model for calculation of three-dimensional glaze icing. *Journal of Aircraft*, 53(1):106–116.

Cao, Y. Huang, J. Xu, Z. and Yin, J. (2016a). Insight into rime ice accretion on an aircraft wing and corresponding effects on aerodynamic performance. *The Aeronautical Journal*, 120(1229):1101–1122.

Cao, Y. Huang, J. and Yin, J. (2016b). Numerical simulation of three-dimensional ice accretion on an aircraft wing. *International Journal of Heat and Mass Transfer*, 92:34–54.

Cao, Y. Ma, C. Zhang, Q. and Sheridan, J. (2012). Numerical simulation of ice accretions on an aircraft wing. *Aerospace Science and Technology*, 23(1):296–304.

Cao, Y. Tan, W. and Wu, Z. (2018). Aircraft icing: an ongoing threat to aviation safety. *Aerospace Science and Technology*, 75:353–385.

Cao, Y. and Xin, M. (2019). Numerical simulation of ice accretion in supercooled large droplet conditions. *Science China Technological Sciences*, 62(7):1191–1201.

Cao, Y. Zhang, Q. and Sheridan, J. (2008). Numerical simulation of rime ice accretions on an aerofoil using an eulerian method. *The aeronautical journal*, 112(1131):243–249.

Cebeci, T. (1999). *An engineering approach to the calculation of aerodynamic flows Springer Science & Business Media*.

Cebeci, T. and Bradshaw, P. (2012). *Physical and computational aspects of convective heat transfer*. Springer Science & Business Media.

Cebeci, T. and Cousteix, J. (2005). Interactive boundary-layer theory. *Modeling and Computation of Boundary-Layer Flows: Laminar, Turbulent and Transitional Boundary Layers in Incompressible and Compressible Flows*, pages 307–343.

Chanda, J. Ionov, L. Kirillova, A. and Synytska, A. (2015). New insight into icing and de-icing properties of hydrophobic and hydrophilic structured surfaces based on core–shell particles. *Soft matter*, 11(47):9126–9134.

Chang, P. K. (2014). *Separation of flow*. Elsevier.

Chauvin, R. (2015). *Un modèle unifié pour les phénomènes de givrage en aéronautique et les systèmes de protection thermiques*. PhD thesis, Toulouse, ISAE.

Chen, N. Du, J. Hu, Y. Ji, H. and Yuan, Y. (2020). Study of the flow and impingement of water droplets inside an inertial particle separator. *AIP Advances*, 10(4):045313.

Chengtao, W. M. W. L. H. (2008). Computational effects of ice accretion on aircraft longitudinal stability and control [j]. *Journal of Beijing University of Aeronautics and Astronautics*, 5.

COLE, J. and SAND, W. (1991). Statistical study of aircraft icing accidents. In *29th Aerospace Sciences Meeting*, page 558.

da Silva, G. A. L. and de Mattos, O. Aircraft wing anti-icing: thermal boundary-layer models comparison.

Da Silveira, R. A. Maliska, C. R. Estivam, D. A. and Mendes, R. (2003). Evaluation of collection efficiency methods for icing analysis. In *Proceedings of 17th International Congress of Mechanical Engineering*.

Dobesch, H. Nikolov, D. and Makkonen, L. (2005). Physical processes, modelling and measuring of icing effects in europe: Österreichische beiträge zu meteorologie und geophysik.

Final report. (2001). German Federal Bureau of Aircraft Accident Investigation (Bundesstelle für Flugunfalluntersuchung), BFU/5X011-0/98.

Fortin, G. Laforte, J. L. and Ilinca, A. (2006). Heat and mass transfer during ice accretion on aircraft wings with an improved roughness model. *International Journal of Thermal Sciences*, 45(6):595–606.

Gent, R. Dart, N. and Cansdale, J. (2000). Aircraft icing. *Philosophical Transactions of the Royal Society of London. Series A: Mathematical, Physical and Engineering Sciences*, 358(1776):2873–2911.

Gouttebroze, S., Saeed, F., and Paraschivoiu, I. (2000). Canice—capabilities and current status. In *NATO/RTO Workshop, Assessment of Icing Code Prediction Capabilities, at CIRA, Capua, Italy*.

Gray, V. H. and Von Glahn, U. H. (1953). Effect of ice and frost formations on drag of naca 65 (sub 1)-212 airfoil for various modes of thermal ice protection.

Gray, V. H. and vonGlahn, U. H. (1958). Aerodynamic effects caused by icing of an unswept naca 65a004 airfoil.

Green, S. (2006). A study of us inflight icing accidents and incidents, 1978 to 2002. In *44th AIAA Aerospace Sciences Meeting and Exhibit*, page 82.

Ground Icing. (2008). National defence, Canada.

Han, Y. (2015). Aerodynamics and thermal physics of helicopter ice accretion.

Han, Y. and Palacios, J. (2017). Surface roughness and heat transfer improved predictions for aircraft ice-accretion modeling. *AIAA Journal*, pages 1318–1331.

Hayati, A. (2010). Numerical study of 2d particle flow in a duct.

Hedde, T. and Guffond, D. (1995). Onera three-dimensional icing model. *AIAA journal*, 33(6):1038–1045.

Hoffmann, K. A. Chiang, S. T. (2000). *Computational Fluid Dynamics v1*. Engineering Equation System.

Honsek, R. (2005). *Development of a three-dimensional Eulerian model of droplet-wall interaction mechanisms*. PhD thesis, McGill University.

Honsek, R. Habashi, W. G. and Aubé, M. S. (2008). Eulerian modeling of in-flight icing due to supercooled large droplets. *Journal of aircraft*, 45(4):1290–1296.

Hospers, J. (2013). Eulerian method for super-cooled large-droplet ice-accretion on aircraft wings.

Hospers, J. and Hoeijmakers, H. (2010). Eulerian method for ice accretion on multiple-element airfoil sections. In *48th AIAA Aerospace Sciences Meeting Including the New Horizons Forum and Aerospace Exposition*, page 1236.

Huang, J. Nie, S. Cao, Y. Yao, Y. and Yao, J. (2016). Multistep simulation for three-dimensinal ice accretion on an aircraft wing. In *AIAA Modeling and Simulation Technologies Conference*, page 1918.

Iuliano, E. Mingione, G. Petrosino, F. and Hervy, F. (2011). Eulerian modeling of large droplet physics toward realistic aircraft icing simulation. *Journal of Aircraft*, 48(5):1621–1632.

Jung, S. (2015). A computational modeling for semi-coupled multiphase flow in atmospheric icing conditions. *Journal of Aerospace Technology and Management*, 7(3):351–364.

Jung, S. and Myong, R. (2013). Numerical modeling for eulerian droplet impingement in supercooled large droplet conditions. In *51st AIAA*

Aerospace Sciences Meeting including the New Horizons Forum and Aerospace Exposition, page 244.

Kanter, M. (1945). Flight performance on xb-25e aircraft in natural ice during february, march and april 1945. washington, d.c. Report No.: 42-32281.

Karev, A. R. Farzaneh, M. and Kollár, L. E. (2007). Measuring temperature of the ice surface during its formation by using infrared instrumentation. *International journal of heat and mass transfer*, 50(3-4):566–579.

Kays, W. M. (2012). *Convective heat and mass transfer*. Tata McGraw-Hill Education.

Kim, D. H. Yang, J. H. Chang, J. W. and Chung, J. (2009). Boundary layer and near-wake measurements of naca 0012 airfoil at low reynolds numbers. In *47th AIAA Aerospace Sciences Meeting including The New Horizons Forum and Aerospace Exposition*, page 1472.

Kim, I. Bachchan, N. and Peroomian, O. (2016). Supercooled large droplet modeling for aircraft icing using an eulerian–eulerian approach. *Journal of Aircraft*, 53(2):487–500.

Kim, J. Dennis, P. G. Sankar, L. and Kreeger, R. (2013). Ice accretion modeling using an eulerian approach for droplet impingement. In *51st AIAA Aerospace Sciences Meeting including the New Horizons Forum and Aerospace Exposition*, page 246.

Kong, W. and Liu, H. (2014). Development and theoretical analysis of an aircraft supercooled icing model. *Journal of Aircraft*, 51(3):975–986.

Landsberg, B. (2010). Aircraf icing. *Safety Advisor*.

Lavoie, P. (2017). *Modeling of thin water films on swept wings in icing condition*. PhD thesis, École Polytechnique de Montréal.

Lavoie, P. Pena, D. Hoarau, Y. and Laurendeau, E. (2018). Comparison of thermodynamic models for ice accretion on airfoils. *International Journal of Numerical Methods for Heat & Fluid Flow*.

Lee, S. and Bragg, M. B. (1999). Experimental investigation of simulated large-droplet ice shapes on airfoil aerodynamics. *Journal of Aircraft*, 36(5):844–850.

Lee, S. and Bragg, M. B. (2003). Investigation of factors affecting iced-airfoil aerodynamics. *Journal of Aircraft*, 40(3):499–508.

Lee, S. Ratvasky, T. Thacker, M. and Barnhart, B. (2005). Geometry and reynolds-number scaling on an iced business-jet wing. In *43rd AIAA Aerospace Sciences Meeting and Exhibit*, page 1066.

Li, X. Bai, J. Hua, J. Wang, K. and Zhang, Y. (2014). A spongy icing model for aircraft icing. *Chinese Journal of Aeronautics*, 27(1):40–51.

Lian, W. Zhao, L. Xuan, Y. and Shen, J. (2018). A modified spongy icing model considering the effect of droplets retention on the ice accretion process. *Applied Thermal Engineering*, 134:54–61.

Liseikin, V. D. (2017). *Grid generation methods*. Springer.

List, R. (1990). Physics of supercooling of thin water skins covering gyrating hailstones. *Journal of the atmospheric sciences*, 47(15):1919–1925.

Liu, T. Qu, K. Cai, J. and Pan, S. (2019). A three-dimensional aircraft ice accretion model based on the numerical solution of the unsteady stefan problem. *Aerospace Science and Technology*, 93:105328.

Loth, E. Tryggvason, G. Tsuji, Y. Elghobashi, S. Crowe, C. T. Berlemont, A. Reeks, M. Simonin, O. Frank, T. Onishi, Y. et al. (2006). 13.1 overview of multiphase modeling.

Mart, S. R. (2011). *The effect of roughness element thermal conductivity on turbulent convection.* PhD thesis.

Mathews, J. H. and Fink, K. D. (2004). Numerical methods using mathlab, prenctice. Hall Inc.

Messinger, B. L. (1953). Equilibrium temperature of an unheated icing surface as a function of air speed. *Journal of the aeronautical sciences*, 20(1):29–42.

Mingione, G. and Brandi, V. (1998). Ice accretion prediction on multielement airfoils. Journal of Aircraft, 35(2):240-246.

Mohebbi, F. and Sellier, M. (2014). On the kutta condition in potential flow over airfoil. Journal of A*erodynamics*.

Morency, F. Tezok, F. and Paraschivoiu, I. (1999). Anti-icing system simulation using canice. *Journal of Aircraft*, 36(6):999–1006.

Myers, T. Charpin, J. and Thompson, C. (2002). Slowly accreting ice due to supercooled water impacting on a cold surface. *Physics of Fluids*, 14(1):240–256.

Myers, T. G. (2001). Extension to the messinger model for aircraft icing. *AIAA journal*, 39(2):211–218.

Myers, T. G. and Charpin, J. P. (2004). A mathematical model for atmospheric ice accretion and water flow on a cold surface. *International Journal of Heat and Mass Transfer*, 47(25):5483–5500.

Myers, T. G. and Thompson, C. P. (1998). Modeling the flow of water on aircraft in icing conditions. *AIAA journal*, 36(6):1010–1013.

Norde, E. Senoner, J. M. Van Der Weide, E. T. A. Trontin, P. Hoeijmakers, H. W. M. and Villedieu, P. (2019). Eulerian and lagrangian ice-crystal trajectory simulations in a generic turbofan compressor. *Journal of Propulsion and Power*, 35(1):26–40.

Oleskiw, M. (2001). A review of 65 years of aircraft in-flight icing research at nrc. *Canadian Aeronautics and Space Journal*, 47(3):259–268.

Olsen, W. and Walker, E. (1986). Experimental evidence for modifying the current physical model for ice accretion on aircraft surfaces.

Özgen, S. and Canıbek, M. (2009). Ice accretion simulation on multi-element airfoils using extended messinger model. *Heat and Mass Transfer*, 45(3):305.

Özgen, S. and Canıbek, M. (2012). In-flight ice formation simulation on finite wings and air intakes. *The Aeronautical Journal*, 116(1178):337–362.

Papadakis, M. and Gile Laflin, B. (2001). Aerodynamic performance of a tail section with simulated ice shapes and roughness. In *39th aerospace sciences meeting and exhibit*, page 539.

Pilch, M. and Erdman, C. (1987). Use of breakup time data and velocity history data to predict the maximum size of stable fragments for acceleration-induced breakup of a liquid drop. *International journal of multiphase flow*, 13(6):741–757.

Politovich, M. (2003). Aircraft icing. *Encyclopedia of Atmospheric Sciences*, 358(1776):68–75.

Preston, G. M. and Blackman, C. C. (1948). Effects of ice formations on airplane performance in level cruising flight.

Raj, L. P. Lee, J. and Myong, R. (2019). Ice accretion and aerodynamic effects on a multi-element airfoil under sld icing conditions. *Aerospace Science and Technology*, 85:320–333.

Raj, L. P. Yee, K. and Myong, R. (2020). Sensitivity of ice accretion and aerodynamic performance degradation to critical physical and modeling parameters affecting airfoil icing. *Aerospace Science and Technology*, 98:105659.

Raje, P. V. (2015). Spalart-allmaras turbulence model for compressible flows.

Ranaudo, R. Mikkelsen, K. McKnight, R. and PERKINS, JR, P. (1984). Performance degradation of a typical twin engine commuter type aircraft in measured natural icing conditions. In *22nd Aerospace Sciences Meeting*, page 179.

Reehorst, A. Chung, J. Potapczuk, M. Choo, Y. Wright, W. and Langhals, T. (1999). An experimental and numerical study of icing effects on the performance and controllability of a twin engine aircraft. In *37th Aerospace Sciences Meeting and Exhibit*, page 374.

Rusche, H. (2002). *Computational fluid dynamics of dispersed two-phase flows at high phase fractions*. PhD thesis, University of London.

Saeed, F. Gouttebroze, S. and Paraschivoiu, I. (2001). Modified canice for improved prediction of airfoil ice accretion. In *8th Aerodynamic Symposium of 48th CASI Conference, Toronto, Canada, Apr*.

Salih, A. (2013). Streamfunction-vorticity formulation. *Department of Aerospace Engineering Indian Institute of Space Science and Technology, Thiruvananthapuram-Mach*, page 10.

Schlichting, H. and Gersten, K. (2016). *Boundary-layer theory*. Springer.

Sebben, S. and Baliga, B. R. (1995). Some extensions of tridiagonal and pentadiagonal matrix algorithms. *Numerical Heat Transfer, Part B Fundamentals*, 28(3):323–351.

Shin, J. and Bond, T. H. (1992). Experimental and computational ice shapes and resulting drag increase for a naca 0012 airfoil.

Smith, A. and Kaups, K. (1968). Aerodynamics of surface roughness and imperfections. *SAE Transactions*, pages 668–688.

Smith, A. and Spalding, D. (1958). Heat transfer in a laminar boundary layer with constant fluid properties and constant wall temperature. *The Aeronautical Journal*, 62(565):60–64.

Soldevila Dalmau, E. (2018). Study of the effects of in-flight icing on fixed wing uav's aerodynamic performance. B.S. thesis, Universitat Politècnica de Catalunya.

Spalart, P. and Allmaras, S. (1992). A one-equation turbulence model for aerodynamic flows. In *30th aerospace sciences meeting and exhibit*, page 439.

Steger, J. and Sorenson, R. (1979). Automatic mesh-point clustering near a boundary in grid generation with elliptic partial differential equations.

Sun, Z. Zhu, C. Fu, B. and Zhu, C. (2012). Study on thermodynamic characteristics of ice-layer accretion for airfoils. *Heat and Mass Transfer*, 48(3):427–438.

Sznajder, J. (2015). implementation of an eulerian method of determination of surface water collection efficiency for atmospheric icing problems. *Prace Instytutu Lotnictwa*, (1 (238)):91–105.

Tan, J. Papadakis, M. and Sampath, M. (2005). *Computational study of large droplet breakup in the vicinity of an airfoil*. US Department of Transportation, Federal Aviation Administration, Office of . . . .

Thames, F. C. Thompson, J. F. Mastin, C. W. and Walker, R. L. (1977). Numerical solutions for viscous and potential flow about arbitrary two-dimensional bodies using body-fitted coordinate systems. *Journal of computational Physics*, 24(3):245–273.

Thompson, J. F. Thames, F. C. and Mastin, C. W. (1974). Automatic numerical generation of body-fitted curvilinear coordinate system for field containing any number of arbitrary two-dimensional bodies. *Journal of computational physics*, 15(3):299–319.

Thompson, J. F. Thames, F. C. and Mastin, C. W. (1977a). Boundary-fitted curvilinear coordinate systems for solution of partial differential equations on fields containing any number of arbitrary two-dimensional bodies.

Thompson, J. F. Thames, F. C. and Mastin, C. W. (1977b). Tomcat—a code for numerical generation of boundary-fitted curvilinear coordinate systems on fields containing any number of arbitrary two-dimensional bodies. *Journal of Computational Physics*, 24(3):274–302.

Thompson, J. F. Warsi, Z. U. and Mastin, C. W. (1982). Boundary-fitted coordinate systems for numerical solution of partial differential equations—a review. *Journal of computational Physics*, 47(1):1–108.

Thompson, J. F. Warsi, Z. U. and Mastin, C. W. (1985). *Numerical grid generation: foundations and applications*, volume 45. North-holland Amsterdam.

van Eijkeren, D. F. and Hoeijmakers, H. W. M. (2010). Influence of the history term in a lagrangian method for oil-water separation (usb stick no. 6.. 2.1). In *7th International Conference on Multiphase Flow, ICMF 2010*, pages 1–9. University of Florida.

Verdin, P. F. Charpin, J. and Thompson, C. (2009). Multistep results in icecremo2. *Journal of Aircraft*, 46(5):1607–1613.

Verdin, P. G. and Charpin, J. P. (2013). Multi-stepping ice prediction on cylinders and other relevant geometries. *Journal of aircraft*, 50(3):871–878.

Versteeg, H. and Malalasekera, W. (1995). An introdution to computational fluid dynamics. *The finite volume method*.

Wang, Z. Zhao, N. and Zhu, C. (2018). Numerical simulation for three-dimensional rotor icing in forward flight. *Advances in Mechanical Engineering*, 10(4):1687814018772404.

Whalen, E. Broeren, A. and Bragg, M. (2006). Considerations for aerodynamic testing of scaled runback ice accretions. In *44th AIAA Aerospace Sciences Meeting and Exhibit*, page 260.

Whalen, E. Lee, S. Bragg, M. and Ratvasky, T. (2002). Characterizing the effect of ice on aircraft performance and control from flight data. *AIAA paper*, 816:2002.

Whalen, E. A. Broeren, A. P. and Bragg, M. B. (2008). Aerodynamics of scaled runback ice accretions. *Journal of Aircraft*, 45(2):591–603.

White, F. M. and Corfield, I. (2006). *Viscous fluid flow*, volume 3. McGraw-Hill New York.

Wilcox, D. C. et al. (1998). *Turbulence modeling for CFD*, volume 2. DCW industries La Canada, CA.

Wirogo, S. and Srirambhatla, S. (2003). An eulerian method to calculate the collection efficiency on two and three dimensional bodies. In *41st Aerospace sciences meeting and exhibit*, page 1073.

Wright, W. (2008). User's manual for lewice version 3.2.

Wright, W. B. (1995). Users manual for the improved nasa lewis ice accretion code lewice 1.6.

Wright, W. B. Gent, R. and Guffond, D. (1997). Dra/nasa/onera collaboration on icing research. part 2; prediction of airfoil ice accretion.

Wu, Z. and Cao, Y. (2015). Numerical simulation of flow over an airfoil in heavy rain via a two-way coupled eulerian–lagrangian approach. *International Journal of Multiphase Flow*, 69:81–92.

Yanxia, D. Yewei, G. Chunhua, X. and Xian, Y. (2010). Investigation on heat transfer characteristics of aircraft icing including runback water. *International Journal of Heat and Mass Transfer*, 53(19-20):3702–3707.

Yi, X. Gui, Y. Zhu, G., et al. (2010). Numerical method of a three-dimensional ice accretion model of aircraft. *Acta Aeronautica et Astronautica Sinica*, 31(11):152–158.

Zhang, Q. Liu, Y. and Gao, Z. H. (2011). Simulation of aircraft flight dynamics affected by ice accretion. *Flight Dynamics*, 29(3):4–7.

Zhang, X. Wu, X. and Min, J. (2017). Aircraft icing model considering both rime ice property variability and runback water effect. *International Journal of Heat and Mass Transfer*, 104:510–516.

APPENDICES

APPENDIX A : The Derivatives of Coordinate Transformation
APPENDIX B : Fortran Code for Tri Diagonal Matrix Algorithm (TDMA)
APPENDIX C : Fortran Code for Penta Diagonal Matrix Algorithm (PDMA)
APPENDIX D : Fortran Code for Runge-Kutta Method
APPENDIX E : Fortran Code for Cubic Bézier Curve (4-points Smoothing Curve)

APPENDIX A : The Derivatives of Coordinate Transformation

$$\xi_x = \frac{y_\eta}{J} \tag{A.1}$$

$$\xi_y = -\frac{x_\eta}{J} \tag{A.2}$$

$$\eta_x = -\frac{y_\xi}{J} \tag{A.3}$$

$$\eta_y = \frac{x_\xi}{J} \tag{A.4}$$

$$J = x_\xi y_\eta - x_\eta y_\xi \tag{A.5}$$

$$\begin{aligned} \xi_{xx} = (\xi_x)_x = \big(\frac{y_\eta}{J}\big)_x = \frac{(y_{\eta\xi}\xi_x + y_{\eta\eta}\eta_x)}{J} - \\ \frac{y_\eta}{J^2}\big[(x_{\xi\xi}\xi_x + x_{\xi\eta}\eta_x)y_\eta + x_\xi(y_{\eta\xi}\xi_x + y_{\eta\eta}\eta_x) - \\ (x_{\eta\xi}\xi_x + x_{\eta\eta}\eta_x)y_\xi - x_\eta(y_{\xi\xi}\xi_x + y_{\xi\eta}\eta_x)\big] \end{aligned} \tag{A.6}$$

$$\begin{aligned} \xi_{yy} = (\xi_y)_y = \big(-\frac{x_\eta}{J}\big)_y = -\frac{(x_{\eta\xi}\xi_y + x_{\eta\eta}\eta_y)}{J} + \\ \frac{x_\eta}{J^2}\big[(x_{\xi\xi}\xi_y + x_{\xi\eta}\eta_y)y_\eta + x_\xi(y_{\eta\xi}\xi_y + y_{\eta\eta}\eta_y) - \\ (x_{\eta\xi}\xi_y + x_{\eta\eta}\eta_y)y_\xi - x_\eta(y_{\xi\xi}\xi_y + y_{\xi\eta}\eta_y)\big] \end{aligned} \tag{A.7}$$

$$\begin{aligned} \xi_{xy} = (\xi_x)_y = \big(\frac{y_\eta}{J}\big)_y = \frac{(y_{\eta\xi}\xi_y + y_{\eta\eta}\eta_y)}{J} - \\ \frac{y_\eta}{J^2}\big[(x_{\xi\xi}\xi_y + x_{\xi\eta}\eta_y)y_\eta + x_\xi(y_{\eta\xi}\xi_y + y_{\eta\eta}\eta_y) - \\ (x_{\eta\xi}\xi_y + x_{\eta\eta}\eta_y)y_\xi - x_\eta(y_{\xi\xi}\xi_y + y_{\xi\eta}\eta_y)\big] \end{aligned} \tag{A.8}$$

$$\begin{aligned} \eta_{xx} = (\eta_x)_x = \big(-\frac{y_\xi}{J}\big)_x = -\frac{(y_{\xi\xi}\xi_x + x_{\xi\eta}\eta_x)}{J} + \\ \frac{y_\xi}{J^2}\big[(x_{\xi\xi}\xi_x + x_{\xi\eta}\eta_x)y_\eta + x_\xi(y_{\eta\xi}\xi_x + y_{\eta\eta}\eta_x) - \\ (x_{\eta\xi}\xi_x + x_{\eta\eta}\eta_x)y_\xi - x_\eta(y_{\xi\xi}\xi_x + y_{\xi\eta}\eta_x)\big] \end{aligned} \tag{A.9}$$

$$\begin{aligned} \eta_{yy} = (\eta_y)_y = \big(\frac{x_\xi}{J}\big)_y = \frac{(x_{\xi\xi}\xi_y + x_{\xi\eta}\eta_y)}{J} - \\ \frac{x_\xi}{J^2}\big[(x_{\xi\xi}\xi_y + x_{\xi\eta}\eta_y)y_\eta + x_\xi(y_{\eta\xi}\xi_y + y_{\eta\eta}\eta_y) - \\ (x_{\eta\xi}\xi_y + x_{\eta\eta}\eta_y)y_\xi - x_\eta(y_{\xi\xi}\xi_y + y_{\xi\eta}\eta_y)\big] \end{aligned} \tag{A.10}$$

$$\eta_{xy} = (\eta_x)_y = \Big(-\frac{y_\xi}{J}\Big)_y = -\frac{(y_{\xi\xi}\xi_y + x_{\xi\eta}\eta_y)}{J} + \frac{y_\xi}{J^2}\big[(x_{\xi\xi}\xi_y + x_{\xi\eta}\eta_y)y_\eta + x_\xi(y_{\eta\xi}\xi_y + y_{\eta\eta}\eta_y) - (x_{\eta\xi}\xi_y + x_{\eta\eta}\eta_y)y_\xi - x_\eta(y_{\xi\xi}\xi_y + y_{\xi\eta}\eta_y)\big] \tag{A.11}$$

$$\frac{\partial}{\partial x} = \Big(\frac{\partial}{\partial \xi}\frac{\partial \xi}{\partial x} + \frac{\partial}{\partial \eta}\frac{\partial \eta}{\partial x}\Big) \tag{A.12}$$

$$\frac{\partial^2}{\partial x^2} = \frac{\partial\left(\frac{\partial}{\partial \xi}\frac{\partial \xi}{\partial x} + \frac{\partial}{\partial \eta}\frac{\partial \eta}{\partial x}\right)}{\partial x} = \frac{\partial^2}{\partial \xi^2}\Big(\frac{\partial \xi}{\partial x}\Big)^2 + \frac{\partial^2}{\partial \xi \partial \eta}\frac{\partial \eta}{\partial x}\frac{\partial \xi}{\partial x} + \frac{\partial}{\partial \xi}\frac{\partial^2 \xi}{\partial x^2} + \frac{\partial^2}{\partial \eta \partial \xi}\frac{\partial \xi}{\partial x}\frac{\partial \eta}{\partial x} + \frac{\partial^2}{\partial \eta^2}\Big(\frac{\partial \eta}{\partial x}\Big)^2 + \frac{\partial}{\partial \eta}\frac{\partial^2 \eta}{\partial x^2} \tag{A.13}$$

$$\frac{\partial}{\partial y} = \Big(\frac{\partial}{\partial \xi}\frac{\partial \xi}{\partial y} + \frac{\partial}{\partial \eta}\frac{\partial \eta}{\partial y}\Big) \tag{A.14}$$

$$\frac{\partial^2}{\partial y^2} = \frac{\partial\left(\frac{\partial}{\partial \xi}\frac{\partial \xi}{\partial y} + \frac{\partial}{\partial \eta}\frac{\partial \eta}{\partial y}\right)}{\partial y} = \frac{\partial^2}{\partial \xi^2}\Big(\frac{\partial \xi}{\partial y}\Big)^2 + \frac{\partial^2}{\partial \xi \partial \eta}\frac{\partial \eta}{\partial y}\frac{\partial \xi}{\partial y} + \frac{\partial}{\partial \xi}\frac{\partial^2 \xi}{\partial y^2} + \frac{\partial^2}{\partial \eta \partial \xi}\frac{\partial \xi}{\partial y}\frac{\partial \eta}{\partial y} + \frac{\partial^2}{\partial \eta^2}\Big(\frac{\partial \eta}{\partial y}\Big)^2 + \frac{\partial}{\partial \eta}\frac{\partial^2 \eta}{\partial y^2} \tag{A.15}$$

$$\frac{\partial^2}{\partial x \partial y} = \frac{\partial\left(\frac{\partial}{\partial \xi}\frac{\partial \xi}{\partial x} + \frac{\partial}{\partial \eta}\frac{\partial \eta}{\partial x}\right)}{\partial y} = \frac{\partial^2}{\partial \xi^2}\frac{\partial \xi}{\partial y}\frac{\partial \xi}{\partial x} + \frac{\partial^2}{\partial \xi \partial \eta}\frac{\partial \eta}{\partial y}\frac{\partial \xi}{\partial x} + \frac{\partial}{\partial \xi}\frac{\partial^2 \xi}{\partial x \partial y} + \frac{\partial^2}{\partial \eta \partial \xi}\frac{\partial \xi}{\partial y}\frac{\partial \eta}{\partial x} + \frac{\partial^2}{\partial \eta^2}\frac{\partial \eta}{\partial y}\frac{\partial \eta}{\partial x} + \frac{\partial}{\partial \eta}\frac{\partial^2 \eta}{\partial x \partial y} \tag{A.16}$$

APPENDIX B : Fortran Code for Tri Diagonal Matrix Algorithm (TDMA)

```
!-------------------------------------------------------------
! There are lots of articles whom deal with the solution of tri-
! diagonal matrices in the literature,
! Here, the method introduced by Simone Sebben and B. Rabi Baliga
! (2007) is applied.
!-------------------------------------------------------------
program TriDimensionalMatrixAlgorithm
implicit none
integer :: i,iMax
parameter(iMax=5)
real(kind=8),dimension(iMax):: D,U,L,bb,x

open(unit=7,file='TDMAinputs.dat')
open(unit=8,file='TDMAoutputs.dat')

do i=1,iMax-1
U(i)=1
enddo
U(iMax)=0

do i=1,iMax
D(i)=2
enddo

L(1)=0
do i=2,iMax
L(i)=3
enddo

bb(1)=4
bb(2)=10
bb(3)=16
bb(4)=22
bb(5)=22

do i=1,iMax
write(7,*) 'U=',U(i),'D=',D(i),'L=',L(i),'b=',bb(i)
enddo
```

```
call TDMA(iMax,D,U,L,bb,x)

do i=1,iMax
write(8,*) 'U=',U(i),'D=',D(i),'L=',L(i),'b=',bb(i),'x=',x(i)
enddo

end program TriDimensionalMatrixAlgorithm
!-------------------------------------------------
!----------Thomas Algorithm (TDMA) subroutine----------
subroutine TDMA(Nodes,Diag,SuperD,SubD,b,Unknown)
implicit none
integer:: counter,Nodes
real(kind=8),dimension(Nodes):: Diag,SuperD,SubD,b,Unknown

do counter=1,Nodes-1,+1
if (Diag(counter).EQ.0) then
Diag(counter)=0.000000001
endif
SuperD(counter)=SuperD(counter)/Diag(counter)
b(counter)=b(counter)/Diag(counter)
Diag(counter)=Diag(counter)/Diag(counter)

Diag(counter+1)=Diag(counter+1)-SubD(counter+1)*SuperD(counter)
b(counter+1)=b(counter+1)-SubD(counter+1)*b(counter)
SubD(counter+1)=SubD(counter+1)-SubD(counter+1)*Diag(counter)
enddo

Unknown(Nodes)=b(Nodes)/Diag(Nodes)

do counter=Nodes-1,1,-1
Unknown(counter)=(b(counter)-SuperD(counter)*Unknown(counter+1))/
&Diag(counter)
enddo

return
end
!---------End of Thomas Algorithm (TDMA) subroutine---------
```

APPENDIX C : Fortran Code for Penta Diagonal Matrix Algorithm (PDMA)

```
!-------------------------------------------------------------
! There are lots of articles whom deal with the solution of penta-
! diagonal matrices in the literature, but lots of them fail to
! solve in special cases. Therefore, here the method introduced by
! Simone Sebben and B. Rabi Baliga (2007) is applied to overcome
! the solution-failure problems.
!-------------------------------------------------------------
program PentaDiagonalMatrixAlgorithm
implicit none
integer :: i,iMax
parameter(iMax=5)
real(kind=8),dimension(iMax):: D,U,UU,L,LL
real(kind=8),dimension(iMax):: bb,w,x


open(unit=7,file='PDMAinputs.dat')
open(unit=8,file='PDMAoutputs.dat')


do i=1,iMax-2
UU(i)=1
enddo
UU(iMax-1)=0
UU(iMax)=0


do i=1,iMax-1
U(i)=2
enddo
U(iMax)=0


do i=1,iMax
D(i)=3
enddo


L(1)=0
do i=2,iMax
L(i)=4
enddo


LL(1)=0
LL(2)=0
do i=3,iMax
```

```
LL(i)=5
enddo


bb(1)=10
bb(2)=20
bb(3)=35
bb(4)=44
bb(5)=46


do i=1,iMax
write(7,*) 'UU=',UU(i),'U=',U(i),'D=',D(i),'L=',L(i),'LL=',LL(i),
&'b=',bb(i)
enddo


call PDMA(iMax,D,U,UU,L,LL,bb,x)


do i=1,iMax
write(8,*) 'UU=',UU(i),'U=',U(i),'D=',D(i),'L=',L(i),'LL=',LL(i),
&'b=',bb(i),'x=',x(i)
enddo


end program PentaDiagonalMatrixAlgorithm
!————————————————————————————————-
!————-Penta Diagonal Matrix Algorithm (PDMA) subroutine————
subroutine PDMA(Nodes,Diag,SuperD,SuperSuperD,SubD,SubSubD,b,
&Unknown)
implicit none
integer:: counter,Nodes
real(kind=8),dimension(Nodes):: Diag,SubD,SubSubD
real(kind=8),dimension(Nodes):: SuperD,SuperSuperD,b
real(kind=8),dimension(Nodes):: Unknown


do counter=1,Nodes-1,+1
if (Diag(counter).EQ.0) then
Diag(counter)=0.000000001
endif
SuperSuperD(counter)=SuperSuperD(counter)/Diag(counter)
SuperD(counter)=SuperD(counter)/Diag(counter)
b(counter)=b(counter)/Diag(counter)
Diag(counter)=Diag(counter)/Diag(counter)


Diag(counter+1)=Diag(counter+1)-
&SubSubD(counter+1)*SuperSuperD(counter-1)-
&(SubD(counter+1)-SubSubD(counter+1)*SuperD(counter-1))*
&SuperD(counter)
b(counter+1)=b(counter+1)-
```

```
&SubSubD(counter+1)*b(counter-1)-
&(SubD(counter+1)-SubSubD(counter+1)*SuperD(counter-1))*
&b(counter)
SuperD(counter+1)=SuperD(counter+1)-
&(SubD(counter+1)-SubSubD(counter+1)*SuperD(counter-1))*
&SuperSuperD(counter)
SubD(counter+1)=SubD(counter+1)-
&SubSubD(counter+1)*SuperD(counter-1)-
&(SubD(counter+1)-SubSubD(counter+1)*SuperD(counter-1))*
&Diag(counter)
SubSubD(counter+1)=SubSubD(counter+1)-
&SubSubD(counter+1)*Diag(counter-1)-
&(SubD(counter+1)-SubSubD(counter+1)*SuperD(counter-1))*
&SubD(counter)
enddo

Unknown(Nodes)=b(Nodes)/Diag(Nodes)
Unknown(Nodes-1)=(b(Nodes-1)-SuperD(Nodes-1)*Unknown(Nodes))/
&Diag(Nodes-1)

do counter=Nodes-2,1,-1
Unknown(counter)=(b(counter)-SuperD(counter)*Unknown(counter+1)-
&SuperSuperD(counter)*Unknown(counter+2))/
&Diag(counter)
enddo

return
end
!———-End of Penta Diagonal Matrix Algorithm (PDMA) subroutine—-
```

APPENDIX D : Fortran Code for Runge-Kutta Method

```
!———————————Main Program———————————-
! The 5th order Runge-Kutta method is developed in this program.
! Reference is the book of 'Numerical methods using matlab 3th
! edition' by Mathews and Fink.
!————————————————————————————————-
PROGRAM RungeKutta
IMPLICIT None
REAL(KIND=8)time,y,Hstep,timeFinal

OPEN(UNIT=8,FILE='RungeKutta.dat')

! Time Step
Hstep=0.1
! Final Time
timeFinal=1.4
! Initial Condition
time=0.0
y=0.0
WRITE(8,55) time,y

! Beginning of the integration
DO WHILE (time.LE.timeFinal)
CALL RK5(time,y,Hstep)
WRITE(8,55) time,y
ENDDO
! End of the integration

55 FORMAT(3F14.7)

STOP
ENDPROGRAM RungeKutta
!———————————-End of Main Program———————————
!———————————subroutine KCoefficients———————————
SUBROUTINE Kcoefficients(time,y,Hstep,K)
IMPLICIT None
REAL(KIND=8)time,y,Hstep,K,dydt

dydt=(1+y**2)
K=Hstep*dydt
RETURN
```

```
ENDSUBROUTINE
!————————————end of subroutine KCoefficients————-
!————————————subroutine RK5————————————
SUBROUTINE RK5(time,y,Hstep)
IMPLICIT None
REAL(KIND=8)time,y,Hstep,K1,K2,K3,K4,K5,K6


! K1
CALL Kcoefficients(time,y,Hstep,K1)
! K2
CALL Kcoefficients(time+Hstep/4.0,y+K1/4.0,Hstep,K2)
! K3
CALL Kcoefficients(time+3.0/8.0*Hstep,y+3.0/32*K1+9.0/32.0*K2,
&Hstep,K3)
! K4
CALL Kcoefficients(time+12.0/13.0*Hstep,y+1932.0/2197.0*K1-
&7200.0/2197.0*K2+7296.0/2197.0*K3,Hstep,K4)
! K5
CALL Kcoefficients(time+Hstep,y+439.0/216.0*K1-8.0*K2+
&3680.0/513.0*K3-845.0/4104.0*K4,Hstep,K5)
! K6
CALL Kcoefficients(time+Hstep/2.0,y-8.0/27.0*K1+2.0*K2-
&3544.0/2565*K3+1859.0/4104.0*K4-11.0/40.0*K5,Hstep,K6)
! All K coefficients have been calculated.


! Finding of the new time and y values.
y=y+(16.0/135.0*K1+6656.0/12825*K3+
&28561.0/56430.0*K4-9.0/50.0*K5+2.0/55.0*K6)
time=time+Hstep


RETURN
ENDSUBROUTINE
!————————————end of subroutine RK5————————————
```

APPENDIX E : Fortran Code for Cubic Bézier Curve (4-Points Smoothing Curve)

```
!————————————Programming References————————————-
!https://javascript.info/bezier-curve
!https://rosettacode.org/wiki/Bitmap/Bezier_ curves/Cubic
!————————————————————————————————————————-
!————————————Main Program————————————
program SmoothingCurve
implicit none
integer :: iMax,jMax,SPOld,LP,UP,MLP,MUP,i
parameter(iMax=41,jMax=41)
REAL(KIND=8)ds
REAL(KIND=8),DIMENSION(iMax):: Surface,s,V
REAL(KIND=8),DIMENSION(iMax,jMax):: Vel1,Vel2


OPEN(UNIT=10,FILE='Vs1.dat')
OPEN(UNIT=11,FILE='Vs2.dat')


! SPOld is stagnation point which has been calculated in the old (previous) step.
SPOld=(iMax-1)/2+1


! 4 controlling points
! LP is lower smoothing point, and UP is upper smoothing point.
! MLP is middle lower smoothing point, and MUP is middle upper smoothing point.
LP=SPOld-int(SPOld/3.0)
UP=SPOld+int(SPOld/3.0)
MLP=SPOld-int((UP-LP)/4.0)
MUP=SPOld+int((UP-LP)/4.0)


Surface(LP)=-0.4
Surface(UP)=+0.4
ds=abs(Surface(UP)-Surface(LP))/(UP-LP)
do i=LP+1,UP-1
Surface(i)=Surface(LP)+(i-LP)*ds
enddo


Vel1(LP,1)=-4.0
Vel1(MLP,1)=+4.0/3.0
Vel1(MUP,1)=-4.0/3.0
Vel1(UP,1)=+4.0
```

```
call CubicBezier(LP,MLP,MUP,UP,
&Surface(LP),Surface(MLP),Surface(MUP),Surface(UP),
&Vel1(LP,1),Vel1(MLP,1),Vel1(MUP,1),Vel1(UP,1),
&s,V)

do i=LP,UP
Surface(i)=s(i)
Vel1(i,1)=V(i)
write(10,*) Surface(i),Vel1(i,1)
enddo

Vel2(LP,1)=+4.0
Vel2(MLP,1)=-4.0/3.0
Vel2(MUP,1)=-4.0/3.0
Vel2(UP,1)=+4.0

call CubicBezier(LP,MLP,MUP,UP,
&Surface(LP),Surface(MLP),Surface(MUP),Surface(UP),
&Vel2(LP,1),Vel2(MLP,1),Vel2(MUP,1),Vel2(UP,1),
&s,V)

do i=LP,UP
Surface(i)=s(i)
Vel2(i,1)=V(i)
write(11,*) Surface(i),Vel2(i,1)
enddo

CALL SYSTEM("gnuplot -p gnuplotVs1.txt")
CALL SYSTEM("gnuplot -p gnuplotVs2.txt")

end program SmoothingCurve
!————————————-End of Main Program————————————
!————————————subroutine CubicBezier————————————
subroutine CubicBezier(i1,i2,i3,i4,s1,s2,s3,s4,V1,V2,V3,V4,s,V)
implicit none
integer :: i1,i2,i3,i4,i
REAL(KIND=8)t,a,b,c,d,s1,s2,s3,s4,V1,V2,V3,V4
REAL(KIND=8),DIMENSION((i4-i1)+1):: s,V

do i=0,(i4-i1)
t=(1.0-0.0)/(i4-i1)*i
a=1.0*(1.0-t)**3.0
b=3.0*(1.0-t)**2.0*t**1.0
c=3.0*(1.0-t)**1.0*t**2.0
d=1.0*t**3.0
s(i+i1)=a*s1+b*s2+c*s3+d*s4
```

```
V(i+i1)=a*V1+b*V2+c*V3+d*V4
print *,'———————————'
print *,'i=',i
print *,'t=',t
print *,'s(i)=',s(i)
print *,'V(i)=',V(i)
print *,'———————————'
enddo


return
end subroutine CubicBezier
!————————————end of subroutine CubicBezier————————————-
```

The first text file which is called in the main program and used for plotting of the results is as follows:

```
set terminal latex
set terminal postscript 20 color enhanced font"Times-Roman.12"
set output "gnuplotVs1.eps"
set multiplot
set grid
set title "Solution Of Cubic Bezier Curve"
set xlabel 's'
set ylabel 'V'
set xrange [-0.4:+0.4]
set yrange [-4:+4]
set xtics 0.1
set ytics 1.0
set size ratio 1.1
set key box at 0.38,-2.8
set key box width -6


plot
"4points1.dat" using 1:2 title '4 controlling points' with linespoints linetype 4 linecolor "blue" linewidth 2,
"Vs1.dat" using 1:2 title 'Cubic Bezier Curve' with linespoints linetype 5 linecolor "red" linewidth 2,


unset multiplot
```

The second text file which is called in the main program and used for plotting of the results is as follows:

```
set terminal latex
set terminal postscript 20 color enhanced font"Times-Roman.12"
set output "gnuplotVs2.eps"
set multiplot
set grid
```

```
set title "Solution Of Cubic Bezier Curve"
set xlabel ’s’
set ylabel ’V’
set xrange [-0.4:+0.4]
set yrange [-4:+4]
set xtics 0.1
set ytics 1.0
set size ratio 1.1
set key box at 0.38,-2.8
set key box width -6


plot
"4points2.dat" using 1:2 title ’4 controlling points’ with linespoints linetype 4 linecolor "blue" linewidth 2,
"Vs2.dat" using 1:2 title ’Cubic Bezier Curve’ with linespoints linetype 5 linecolor "red" linewidth 2,


unset multiplot
```

CURRICULUM VITAE

Name Surname: Hadi SIYAHI

EDUCATION:

- **B.Sc.** 2005, Department of Mechanical Engineering, Faculty of Engineering, Urmia University, Iran
  Title of graduation project: 'Improvement of the performance of a sample turbo-machine by optimizing the angle of attack of inlet flow'
  Concept: The commercial CAE program was used to model fluid flow around the blades, and the velocity and pressure distributions were obtained to evaluate the performance of sample turbo-machine.
  Advisor: Prof. Iraj Mirzaee

- **M.Sc.** 2009, Department of Mechanical Engineering, Faculty of Mechanical Engineering, University of Tabriz, Iran
  Title of thesis: 'Thermodynamic (energetic & exergetic) analysis of the steam injected gas turbine with compressor's inlet air cooling by using the evaporative cooling technique'
  Concept: It is about the utilization of advanced cycles instead of combined cycles, which leads to improving the performance by increasing both specific work and efficiency of the gas turbine cycle. Then, I have appreciable knowledge and background about gas turbines and aircraft engines. Besides, I have used engineering equation solver (EES) software for thermodynamic assessment, and this led to the translation of the 'EES manual' into Persian.
  Advisor: Prof. Seyed Mohammad Seyed Mahmoudi

- Ph.D. 2022, Department of Aeronautics and Astronautics Engineering, Faculty of Aeronautics and Astronautics, Istanbul Technical University, Turkey
  Title of dissertation: 'Numerical simulation of aircraft icing with an adaptive thermodynamic model considering ice accretion'
  Concept: The main idea is to use the computational fluid dynamics (CFD) tools for writing a modular computer program to simulate the icing phenomenon in aircraft and predict the final shape of ice on the wings. First, the grid is generated around an airfoil. Then, the airflow is calculated, and the convective heat transfer coefficient is determined. Besides, the distribution of water droplets under the influence of airflow is specified by using the Eulerian method to obtain the collection efficiency of water droplets on the body. Eventually, by applying thermodynamic calculations, the ice accretion on the surface is found. Finally, the entire icing simulation is repeated from the first module (i.e. the grid generation) for the contaminated (iced) surface of airfoil to predict the final shape of ice on the surface.
  Advisor: Prof. A. Cihat Baytaş

COURSES WHICH HAVE BEEN TAKEN IN GRADUATE SCHOOLS:

- Advanced Thermodynamics
- Selected Topics in Energy
- Micro Scale Heat Transfer
- Advanced Heat-Exchanger Design
- Convection Phenomena in Aerospace Systems
- Advanced Fluid Dynamics
- Boundary Layer Theory
- Viscous Fluid Flow
- Aerodynamics
- Aero-Thermodynamics of Turbo-Machines
- Numerical Methods
- Engineering Mathematics
- Computational Fluid Dynamics (CFD)
- Continuum Mechanics
- Boundary Element Method

PROFESSIONAL EXPERIENCE AND REWARDS:

- Teaching & Research Assistant, 2006-2009, Department of Mechanical Engineering, University of Tabriz, Iran
- Supervisor and Design Engineer of HVAC and buildings' mechanical equipment, 2010-present, Construction Engineering Organization, Alborz Province, Iran
- Research Assistant, 2016-2017, TÜBİTAK project, Department of Aeronautical Engineering, Istanbul Technical University, Turkey
- Lead R&D Engineer, 2017-2018, Can Klima Teknik San. ve Tic, Turkey
- Senior Engineer, 2019-2020, Can Klima Teknik San. ve Tic, Turkey
- Research Assistant, 2018-2022, CFD Lab, Department of Aeronautical Engineering, Istanbul Technical University, Turkey

PUBLICATIONS, PRESENTATIONS AND PATENTS ON THE THESIS:

- **Siyahi, H.** and Bayta¸s, A.C. 2022 (Accepted for publication). An adaptive approach for modeling ice accretion on aircraft. *Progress in Computational Fluid Dynamics*. DOI: 10.1504/PCFD.2022.10048280.

OTHER PUBLICATIONS, PRESENTATIONS AND PATENTS:

- Fallah, M. **Siyahi, H.** Ghiasi, RA. Mahmoudi, SMS. Yari, M. Rosen, MA. 2016. Comparison of different gas turbine cycles and advanced exergy analysis of the most effective. *International Journal of Energy*, 116 part 1, 701-715. DOI: 10.1016/j.energy.2016.10.009

- **Siyahi, H.** Siyahi, M. Nahadi, S. 2008. Translation of the user manual of Engineering Equations Solver (EES) into Persian. ELMIRAN Publications.